University of Groningen

Nano-sized precipitated formations in irradiated NaCl

Sugonyako, Anton V.

IMPORTANT NOTE: You are advised to consult the publisher's version (publisher's PDF) if you wish to cite from it. Please check the document version below.

Document Version
Publisher's PDF, also known as Version of record

Publication date:
2007

Link to publication in University of Groningen/UMCG research database

Citation for published version (APA):
Sugonyako, A. V. (2007). *Nano-sized precipitated formations in irradiated NaCl*. [s.n.].

Copyright
Other than for strictly personal use, it is not permitted to download or to forward/distribute the text or part of it without the consent of the author(s) and/or copyright holder(s), unless the work is under an open content license (like Creative Commons).

The publication may also be distributed here under the terms of Article 25fa of the Dutch Copyright Act, indicated by the "Taverne" license. More information can be found on the University of Groningen website: https://www.rug.nl/library/open-access/self-archiving-pure/taverne-amendment.

Take-down policy
If you believe that this document breaches copyright please contact us providing details, and we will remove access to the work immediately and investigate your claim.

Downloaded from the University of Groningen/UMCG research database (Pure): http://www.rug.nl/research/portal. For technical reasons the number of authors shown on this cover page is limited to 10 maximum.

Download date: 06-06-2022

Nano-sized precipitated formations in irradiated NaCl

ANTON V. SUGONYAKO

Nano-sized precipitated formations in irradiated NaCl

A.V. Sugonyako

ISBN: 978-90-36729-54-3

Zernike Institute PhD thesis series 2007-10
ISSN 1570-1530

Print: Groningen University Press

University of Groningen
Zernike Institute
for Advanced Materials

The work described in this thesis has been carried out in the Ionic Materials group of the Zernike Institute for Advanced Materials at the University of Groningen, The Netherlands, with the financial support provided by Ubbo Emmius Scholarship for PhD research.

RIJKSUNIVERSITEIT GRONINGEN

Nano-sized precipitated formations in irradiated NaCl

Proefschrift

ter verkrijging van het doctoraat in de
Wiskunde en Natuurwetenschappen
aan de Rijksuniversiteit Groningen
op gezag van de
Rector Magnificus, dr. F. Zwarts,
in het openbaar te verdedigen op
vrijdag 30 maart 2007
om 16.15 uur

door

Anton V. Sugonyako

geboren op 6 maart 1978
te Kazan, Rusland

Promotor : Prof. dr. H. W. den Hartog

Beoordelingscommissie : Prof. dr. J. T. M. de Hosson
Prof. dr. ir. P. W. M. Blom
Prof. dr. D. Khomskii

ISBN: 978-90-36729-54-3

CONTENTS

CHAPTER I

INTRODUCTION

The formation of radiation damage in alkali halides and in particular, in NaCl, has attracted worldwide attention in the last decades, because of important industrial and environmental applications related with the storage of high-level waste (HLW) of nuclear power plants in stable geological formations. Since the 1950s, scientists and engineers have promoted the idea that rock salt is one of the most promising geological media to host radioactive waste repositories. Laid down by evaporating seas over a long time period, natural salt is rock-solid and essentially impermeable. Energy is stored in crystalline rock salt by introducing radiolytic products, among which colloidal sodium and molecular chlorine, as a result of the interaction between the ionizing radiation emitted by HLW, and the rock salt crystal. The accumulation of stored energy under irradiation was the subject of numerous investigations [1-14]. In some of these investigations it was concluded that the saturation level of the production of radiation damage with increasing irradiation dose occurs and it was assumed that the maximum amount of stored energy would be moderate and sufficiently small to warrant a sufficient degree of repository safety. On the other hand, more recent experiments on many heavily irradiated NaCl samples have led us to conclusions, which are completely opposite to this. In natural rock salt and synthetic pure and many doped NaCl samples the concentrations of precipitated sodium and chlorine have been found to increase with increasing dose without any sign of saturation. The amounts of radiolytic products may reach very high values. In NaCl samples irradiated to an extremely high dose of 2×10^3 GRad (2×10^{10} Gy or 8×10^{19} e^-/cm^2) the concentration of colloidal sodium in the NaCl sample was found to be as high as 20 at%, while it was still increasing without any sign of saturation as a function of the dose. Moreover, the possibility of explosive decomposition of salt as a result of spontaneous exothermic recombination of radiolytic Na and Cl has been demonstrated [10,13,14]. In addition, the formation of large voids, which initiate explosive fracture of the samples, has been observed in NaCl at high irradiation doses.

The above mentioned experimental facts leave us with the problem of energy storage and its consequences for safe waste disposal in rock salt and this information stimulates ongoing systematic experimental and theoretical investigations of heavily irradiated NaCl crystals. The question, which arises from the point of view of safety of HLW repositories, is: Can one exclude the possibility that large fractions of metallic Na and Cl_2 are formed at any stage of the storage of HLW in natural rock salt? This question is of extreme practical importance, because we have found that in principle rock salt is capable to accommodate very large fractions of radiation damage in its crystal structure and more importantly it appeared that this capability is not reduced by the presence of increasing fractions of Na and Cl_2. It has been observed in laboratory experiments that with increasing amount of precipitated Na and Cl_2 and consequently with increasing stored energy, the mechanical/chemical stability of many samples is reduced to the point that (explosive) decomposition takes place, which is accompanied by the release of large amounts of energy, produced by the back reactions $2Na+Cl_2\rightarrow2NaCl$. Eventual instability of irradiated rock salt is certainly not acceptable for the above mentioned applications.

It should be mentioned that an important complication associated with the safe storage of HLW is that, depending on the details of the storage strategy and the geometry of the storage site, the expected doses close to the waste containers are very high (typically about 25 GRad), while the relevant exposure time in storage facilities is very long (several 100 to 1000 years). On the other hand, the irradiation time, which can be reached under laboratory conditions, is typically a few months. This implies that it is impossible to imitate the radiological conditions that exist in repositories and we will have to increase the dose rate in the laboratory experiments by a factor of 1000-10000 compared with the conditions in real HLW storage sites. The gap between laboratory and storage conditions can be bridged by extrapolation. This was noticed by van Opbroek and den Hartog [11] and these authors have carried out for the first time the necessary extrapolation to translate the experimental observations to meaningful results under storage conditions. Similar extrapolations should be carried out by means of the state-of-the-art theoretical models describing the radiolytic processes in NaCl. Some of the available models predict rather strong dose rate effects, which lead to increasing efficiency of radiolysis with decreasing dose rate. This is also supported by experimental results obtained from two-stage irradiation runs carried out by Groote et al [15]. The discrepancy between the efficiency of damage formation observed in laboratory experiments and the values that one will be faced with under storage conditions may be very dramatic. This leads us to the next practical question: How can we avoid unexpected problems due to large fractions of radiolytic products, which develop during extremely long-term exposure to ionizing radiation of rock salt in a storage site? To exclude problems in the future one should perform sustained monitoring of the properties of rock salt in the vicinity of the waste containers during storage. These monitoring efforts should be aimed at controlling the production of radiation damage and achieving drastic reductions in the overall efficiency of the radiolysis process. This implies that the investigations carried out during the monitoring stage should enable us to prevent problems with the stability of rock salt in the immediate vicinity of the HLW containers.

It is clear that almost perfect understanding of the processes taking place during radiolysis and a very high quality of the theoretical model(s) is necessary to carry out the above mentioned extrapolations of the dose rate. At this moment these models are not available, although several efforts have been made to develop new and more sophisticated models to describe radiolysis in NaCl. For the understanding of the radiolytic processes, especially those, which take place in very advanced stages of radiolysis, it is necessary to pay special attention to the most heavily damaged NaCl crystals where very high concentrations of radiolytic products have been accumulated. The study of extremely heavily irradiated NaCl crystals is the core issue of this thesis. From scientific point of view several key questions arise in these investigations.

The first question is: What happens to the crystalline NaCl matrix, which is exposed to very high doses of ionizing radiation? It is known from many observations reported in the literature on several other inorganic materials [16,17] that quite often after exposure to very high irradiation doses the samples become amorphous or metamict. It turned out that this is not the case for NaCl. Therefore, it is of crucial interest to obtain information about the structure of our extremely heavily irradiated NaCl samples, where a large amount of precipitated sodium and chlorine particles is embedded in the NaCl host material. This structural information may help us to find answers to the question, why it is so easy to produce and accommodate the above mentioned, very high concentrations of radiation damage in NaCl.

The second key question is about the radiolytic precipitates: What are the shapes, sizes, and physical properties of these very small metallic and halogen formations, which are embedded in the crystalline ionic matrix; and how should the sodium and chlorine particles be arranged in order to avoid continuous back reactions in the host matrix when the concentration of these products becomes very high? Besides the practical interest from the point of view of radiolysis in NaCl, this question is closely connected with the research areas of both isolated nano-size objects and organized nano-structures, because radiolytic sodium and chlorine precipitates are in fact well-organized woven structures of nano-particles. However, it should be noted that in the case of irradiated NaCl crystals we are, compared with other nano-structured systems, dealing with highly defective systems. The latter property leads to a high degree complexity and this is the reason why it is often difficult to interpret the experimental results obtained for heavily damaged NaCl.

The third crucial question is: How do the systems of radiolytic defects develop with the irradiation dose and how does this development depend on the irradiation conditions? The first part of the question is connected with the problem of organization of sodium and chlorine precipitated structures, in particular when they become increasingly dense with increasing amounts of damage. An answer to this question may be obtained by comprehensive investigations of NaCl samples as a function of the irradiation dose, i.e. as a function of the concentrations of radiolytic products. The second part is connected with the question about differences in the structure of the precipitated systems and their growth rates, which depend on the parameters of the radiolysis experiment, such as the temperature, the dose rate and the impurity content.

1.1 Radiolysis in NaCl

During irradiation of NaCl the ions in the sample are transformed partly into sodium and chlorine atoms. This process of transformation and successive separation of sodium and chlorine atoms in NaCl by means of radiation is rather similar to the well known process called electrolysis. For this reason the production of radiation induced defects in NaCl and many other ionic compounds is often referred to as radiolysis.

The formation of primary radiolytic defects in alkali halides, which are exposed to ionizing radiation, is caused by electronic excitation of the lattice. The mechanism of defect formation in alkali halides has been proposed by Pooley [18]. He suggested that irradiation gives rise to self-trapped excitons, which are excitations (electron-hole pairs) trapped at a lattice site. The self-trapped exciton may relax via either luminescence emission or by forming a Cl^0 interstitial, leaving behind an electron trapped in an anion-vacancy. The latter mechanism leads to the formation of the two primary defects, which are characteristic for radiolysis in alkali halides: the *F*-center – a vacancy in the anion sub-lattice with a trapped electron, and the *H*-center, which is basically a Cl^0 interstitial, see figure 1.1.

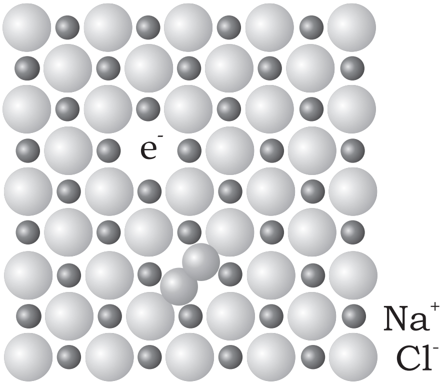

Figure 1.1. The *F*-center – a vacancy in the anion sub-lattice with a trapped electron, and the *H*-center – a Cl^0 interstitial.

The *F*-center may diffuse in the crystalline matrix as a result of hopping of one of its adjacent Cl^--ions into the vacancy. *H*-centers diffuse by switching between bonds, which are aligned along the available <110> axes. This is the reason why the migration energy of *H*-centers is very small compared with *F*-centers, and the associated mobilites of *F*- and *H*-centers show large differences. *H*-centers are highly mobile even at very low temperature, while *F*-centers become mobile at temperatures slightly below room temperature. Both primary point defects may be trapped at impurities or dislocations and annihilate when the electron and the hole center recombine. Reactions between point defects of the same type produce defect clusters. Ultimately clustering of *F*-centers leads to the formation of small particles of sodium metal, or *colloids*[1], see figure 1.2. In this thesis we will often use the term *sodium particle* or *sodium precipitate*; the word *colloid* is used more frequently in the theoretical chapters. Clustering of *H*-centers gives rise to molecular chlorine precipitates, which are usually referred to as *bubbles*.

The concentrations of the point defects in the crystal increase when the production rate of *F-H* pairs is higher than their recombination rate. With increasing concentrations of defects the probability of defect aggregation increases. This probability also depends strongly on the mobility of the defect centers. Because the mobility of the *F*-centers increases significantly with increasing temperature, there is a low-temperature limit for the effective production of

[1] The term *colloid* has been defined by Hughes [19] as follows: "A colloid is a particle whose size is sufficiently small that there is at least a possibility that its properties will differ from those of the bulk material. In practice particles are called colloids when their dimensions are of the order of 1 – 100 nm. Thus, a colloid may contain anything from a few tens to several million atoms, so that at the one extreme the properties may approach those of a large molecular cluster and at the other extreme those of bulk condensed matter."

the sodium precipitates. Evaporation of the *F*-centers from the particles at high temperatures leads to shrinkage of the colloids, which implies that there is some high-temperature limit for the production of colloids. Hence, there is certain temperature range where sodium colloids are produced with reasonable efficiency. Obviously the cut-off temperatures depend on the concentration of the *F*-centers in the sample, and consequently they depend on the dose rate. Therefore the temperature range, where effective colloid formation and effective accumulation of the stored energy take place depends on the dose rate. This effect has been described by Lidiard [6] in the theoretical radiolysis model for alkali halides. This model was modified by van Opbroek and den Hartog [11] for the purpose of applying it to predict the amounts of radiation damage formed under storage conditions. Later, calculations have been made in the framework of new models, developed by Dubinko, Turkin, Vainshtein and den Hartog [20,21]. Estimations with these models yield a temperature range from 0 to about 250 °C for a dose rate of 240 MRad/h, which corresponds to the values used in the laboratory experiments; for a dose rate of 0.15 MRad/h, which corresponds to the conditions in a nuclear waste repository the upper temperature limit for a positive growth rate of colloids has been found to be about 160 °C and the lower limit has been found to be well below 0 °C.

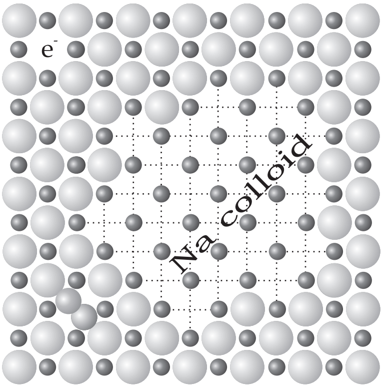

Figure 1.2. Clustering of the *F*-centers leads to the formation of small particles of sodium metal (colloids).

In addition, large numbers of dislocations and dislocation loops also develop in alkali halide matrix under ionizing radiation. Various mechanisms of radiation-induced dislocation climb in NaCl have been proposed to describe the radiolysis process in NaCl. Thus, in the model, proposed by Hobbs et al. [3], which was used by Lidiard in his kinetic model of radiolysis in NaCl [4,6], the dislocation climb mechanism was assumed to be complimentary to growth of Na colloids. Dislocation climb assumed to be accompanied by the creation of immobile molecular halogen centers, which are in fact two *H*-centers located in a stoichiometric vacancy pair in the vicinity of a dislocation line. However, this mechanism has turned out to be not suitable for explaining the formation of halogen bubbles (clusters of many halogen molecules) and nano- and micro-pores – voids, which have been observed in NaCl in advanced stages of radiolysis.

Another model of radiolysis in NaCl has been developed in our lab by by Dubinko et al [20,21]. Contrary to the Lidiard model, the formation of cation vacancies at dislocations as a result of their reaction with the excess *H*-centers has been proposed in the framework of the model. A detailed description of this model together with an analysis of the experimental data can be found in *chapter II.*

1.2 Outline of this thesis

Good understanding of the radiolysis process in alkali halides and its consequences for the materials, which are exposed to ionizing radiation for a very long time period, is crucial for safe storage of high-level nuclear waste in salt mines. This objective requires extensive investigations of the radiolysis process in crystalline NaCl in advanced stages, where very high concentrations of radiolytic products have been accumulated in the crystals. This thesis is devoted to comprehensive experimental observations of the natural rock salt and synthetic pure and doped NaCl samples, which have been irradiated to extremely high doses by means of electron beams. A detailed analysis of the structure and properties of radiolytic sodium and chlorine precipitates and the host crystalline matrix is helpful to explain behaviour of extremely heavily irradiated NaCl crystals. Together with theoretical modelling, these observations provide insight into the radiolysis process in NaCl from the beginning to very late stages.

Theoretical modelling of the radiolysis process and growth of the numbers of radiolytic defects in alkali halides together with a comparison between the results of modelling and those obtained experimentally has been helpful to improve our understanding of important aspects of the mechanisms of the formation radiolytic defects. The process of growth of radiolytic precipitates in NaCl crystal and the experimental information of the development of the sodium and chlorine fractions with increasing irradiation dose is discussed in *chapter II* in the framework of the model, developed by Dubinko, Turkin, Vainshtein and den Hartog [20,21].

The procedures used for the preparation of the NaCl crystalline samples and the irradiation facilities are described in *chapter III* together with the procedures used to calculate the irradiation dose.

A variety of experimental methods has been applied to study sodium and chlorine precipitate systems. The first and most important method, which provides us with information about the concentration and several physical properties of our precipitates, is Differential Scanning Calorimetry (DSC). The energy associated with the phase transition of sodium and chlorine in the precipitates is used as a probe for measuring the amount of metallic sodium and precipitated chlorine in the NaCl crystals. Moreover, an analysis of the features of the melting and freezing behavior of nano-sized sodium particles and chlorine bubbles may give us more detailed information about these objects, such as sizes and their structural organization. The melting properties of sodium precipitates are discussed in *chapter IV*. The melting and freezing behavior of chlorine bubbles is analyzed comprehensively in *chapter V*.

Microscopy techniques, such us Atomic Force and Scanning Electron Microscopy, are among the most powerful methods for the investigations of the small-sized objects and structures. These techniques have been applied in order to visualize small radiolytic objects in the NaCl matrix. *Chapter VI* is devoted to Atomic Force Microscopy (AFM) observations of the sodium precipitates. AFM provides us with direct information about the sizes and spatial distribution of the particles. This information is very useful for understanding the organization of the overall structure of the nano-particles in the crystalline matrix; it sheds light to the origin of the high capacity of NaCl to accumulate very large amounts of precipitated sodium and chlorine.

Scanning electron microscopy (SEM) has been applied for the investigation of other important class of radiolytic defects – the vacancy voids – nano- or micro-pores, which appear (or become visible) in the crystalline NaCl matrix in later stages of radiolysis as a result of highly localized back-reactions between precipitated sodium and chlorine. Voids are very important objects from the point of view of mechanical stability of irradiated NaCl. A comprehensive analysis of the sizes, concentrations and spatial distribution of voids in NaCl samples with a variety of impurities will be given. In addition, an evaluation of the results will be presented for these properties as a function of the irradiation dose. This enables us to assess the consequences with regard to the radiation stability of NaCl. Also it helps to understand the radiolysis process in very heavily damaged NaCl. The progress in this area is presented in *chapter VII*.

Detailed knowledge of the precipitated systems as a whole and their properties with the focus on the interactions with the damaged NaCl matrix have been obtained from the results of Conduction Electron Spin Resonance (CESR) and Raman Scattering (RS) experiments. X-Ray scattering observations yield the information about crystal structure of the sodium particles and frozen chlorine bubbles and their orientations with respect to the host matrix. In *chapter VIII* results of the investigations with these three methods are described in detail.

The questions about the differences in the structure and the evolution of the precipitated systems depending on the parameters of the radiolysis experiment are considered in *chapter IX*. The experimental observations along with the model simulations, presented in this chapter, show that the change of the irradiation temperature has a drastic effect on the evolution of the radiolytic nanoprecipitates. This information is very valuable for improving our understanding of the process of the formation of nanoprecipitates in alkali halides during exposure to ionizing radiation.

References

[1] H. Gies, W. Hild, T. Kuhle and J. Monig, *Radiation effects in rock salts*, Report: *GSF-Report 9/93*, GSF Munchen, (1994)

[2] L.W. Hobbs and A.E. Hughes, *Radiation Damage in Diatomic Materials at High Doses*, Report: *Harwell Report AERE – R 8092*, (1975)

[3] L.W. Hobbs, A.E. Hughes and D. Pooley, *Proc. R. Soc. Lond.* **A332** (1973), 167-185

[4] U. Jain and A.B. Lidiard, *Phil. Mag.* **35** (1977), 245-259

[5] A.B. Lidiard, *Comments Solid State Phys.* **8** (1978), 73

[6] A.B. Lidiard, *Phil. Mag.* **39** (1979), 647-659

[7] W.J. Soppe, H. Donker and A. Garcia Celma, *J. Prij, J. Nucl. Mater.* **217** (1994), 1

[8] J.C. Groote, J. Seinen, J.R.W. Weerkamp and H.W. den Hartog, *Radiat. Eff. & Def. Sol.* **119-121** (1991), 925

[9] H.W. den Hartog, J.C. Groote and J.R.W. Weerkamp, *Radiat. Eff. & Def. Sol.* **139** (1996), 1-19

[10] H.W. den Hartog and D.I. Vainshtein, *Mater. Sci. Forum.* **239-241** (1997), 611-614

[11] G. van Opbroek and H.W. den Hartog, *J. Phys. C.: Solid State Phys.* **18** (1985), 257-268

[12] J. Seinen, J.C. Groote, J.R.W. Weerkamp and H.W. den Hartog, *Radiat. Eff. & Def. Sol.* **124** (1992), 325

[13] D.I. Vainshtein, C. Altena and H.W. den Hartog, *Mater. Sci. Forum.* **239-241** (1997), 607-610

[14] D.I. Vainshtein and H.W. den Hartog, *Radiat. Eff. & Def. Sol.* **152** (2000), 23-37

[15] H.W. den Hartog, J.C. Groote and J.R.W. Weerkamp, *Stralingsschade in NaCl*, p. 27-28, Report: *OPLA programma: Rapportage REO-3*, Groningen, (September 1988)

[16] A. Benyagoub, *Nucl. Instr. and Meth. in Phys. Res. B* **225** (2004), 88-96

[17] C. Fillet, T. Advocat, F. Bart, G. Leturcq and H. Rabiller, *C. R. Chimie* **7** (2004), 1165-1172

[18] D. Pooley, *Proc. Phys. Soc. Lond.* **87** (1966), 245

[19] A.E. Hughes, *Radiat. Eff. & Def. Sol.* **74** (1983), 57-76

[20] H.W. den Hartog, D.I. Vainshtein, V.I. Dubinko, A.A. Turkin, V.V. Gann and J. Jacobs, *Radiation Damage in NaCl. Retrievability Smart Backfill Materials Monitoring*, Report: *CORA*, University of Groningen, Groningen, (1999)

[21] V.I. Dubinko, A.A. Turkin, D.I. Vainshtein and H.W. den Hartog, *Nucl. Instr. and Meth. in Phys. Res.* **B 166-167** (2000), 561-567

CHAPTER II

MODELING OF THE GROWTH OF EXTENDED DEFECTS IN NaCl UNDER ELECTRON IRRADIATION

2.1 Introduction and overview the basic concept

The earlier models of radiolysis in NaCl, which include colloid formation, are mostly based on the Jain-Lidiard (J-L) model [1,2]. This model has been extended and modified in [3] and [4] by taking into account the stage of colloid nucleation. The J-L model has been proposed analogous to that used for void growth in metals under irradiation. According to the model, clustering of *H*-centers leads to the growth of dislocation loops, the *F*-centers are assumed to aggregate to spherical colloids. Analogous to the void growth mechanism in metals, radiation-induced dislocation climb in NaCl was suggested to be complimentary to the growth of the colloids (as in an irradiated metal dislocation climb by accretion of interstitials (*H*-centers in our case) is complimentary to the growth of voids by accretion of vacancies (*F*-centers in NaCl)). According to the mechanism, suggested by Hobbs et al. [5], two *H*-centers meet in the vicinity of dislocations and 'dig their own hole' by displacing an electro-neutral pair of ions and end up in occupying the created stoichiometric vacancy pair. The displaced pair of ions joins a dislocation jog leaving behind an immobile halogen molecular center in a stoichiometric di-vacancy. Therefore, dislocations were suggested to attract the *H*-centers more strongly than *F*-centers, i.e. dislocations are assumed to be biased for *H*-centers. The difference between the flux of *H*-centers and the flux of *F*-centers to the dislocations is the driving force for the colloid growth in alkali halides.

Hence, the J-L model suggests three types of extended radiolytic defects (ED) – sodium colloids, halogen molecular centers and dislocation loops. Colloid growth was assumed to be limited according to the supposed saturation of the stored energy (SE), which is a measure of the extent of radiation-induced dissociation of NaCl into metallic Na colloids and *F*-centers on one hand and molecular chlorine and *H*-centers on the other hand. Thus, above some dose *F*-centers were supposed to recombine with the halogen molecular centers [2]. The J-L model was able to describe qualitatively several essential experimentally observed features of the temperature and dose rate dependences of the radiation-induced stored energy (SE): (i) the existence of a temperature where the stored energy as a function of T at a given dose and dose rate shows a maximum value; (ii) the existence of a maximum temperature, beyond which the stored energy is negligible (i.e., ED's are not created due to the high rate of mutual recombination between *F*- and *H*-centers).

However, the J-L model is not able to explain a number of important features of damage formation in NaCl, which we have found during extensive experimental investigations. In the earlier experiments carried out in our group it has been observed [6-8], that in heavily irradiated NaCl samples, (i) relatively large vacancy voids are formed together with radiolytic sodium, (ii) the chlorine precipitates, or bubbles of molecular chlorine, are present under high pressure and (iii) in most cases no saturation of the amount of damage radiation damage with the dose is observed. Differential scanning calorimetry (DSC) of relatively heavily irradiated samples has revealed the presence of chlorine precipitates, which are large enough to exhibit melting phenomena (see *chapter V*). X-ray crystallographic observations at temperatures below the chlorine melting temperature have shown the presence of well-oriented molecular chlorine bubbles showing a well-defined crystal structure (see *chapter VIII*). Voids with sizes of the order of hundred nanometers have been detected by means of scanning electron microscopy (SEM) [8]. The formation of voids is an essential feature of the radiolysis process, which could not be accounted for in the original J-L model.

In order to explain these experimentally observed features, a new model of radiolysis processes in ionic crystals has been proposed by Dubinko, Turkin, Vainshtein and den Hartog [9,10]. To describe void formation the new model needs to include the production of V_F-centers[1] (cation vacancy with a neighboring self-trapped hole) at dislocations as a result of their reaction with the excess *H*-centers. The V_F-center is a mobile "antimorph" of the *F*-center (an electron trapped in an anion vacancy), so their mutual recombination results in the production of a stoichiometric vacancy pair (in both anion and cation sub-lattices)[2]. Voids nucleate as a result of reactions between growing metallic colloids and halogen bubbles [7,9]. Subsequently, the voids continue to grow due to the formation of electro-neutral vacancy pairs, created during the reaction between F and V_F-centers arriving at the void surface. Interactions of voids with Na-colloids and chlorine precipitates is often followed by a powerful chemical back reaction between radiolytic sodium and chlorine, which results in sudden fracture of crystal and ultimately decomposition [7,14].

In the framework of the presented model all extended defects were supposed to be biased toward absorption of *H*-centers. Competition between bias factors controls the evolution of microstructure. The salient points of the model can be summarized in comparison with those of the J-L model in table 2.1. The scheme, presented in figure 2.2 illustrates the radiation-induced reactions between point defects (PD) and extended defects (ED) based on the presented model. Primary radiation-induced PD, *H*-centers and *F*-centers, separate ultimately into bubbles, dislocations and metal colloids, which results in the production of secondary PD (V_F-centers) and ED (vacancy voids).

---

[1] There exists a lot of experimental data on the production of cation vacancies in alkali halides under irradiation (see, e.g. [11,12]) and on the formation of vacancy pairs and their small aggregates [13].

[2] The following mechanism of V_F-center creation is proposed in [14]. The production of a V_F-center results from the absorption of *H*-centers by edge dislocations. When an *H*-center approaches the dislocation, it displaces a lattice cation and forms a stoichiometric interstitial pair, $i_A + i_C$, where i_A and i_C are the anion and cation interstitials, respectively and an *H*-center is $i_A + p$ (i.e. an interstitial anion plus a hole, *p*). A cation vacancy, V_C, and a hole are produced in the same reaction. The interstitial pair joins a dislocation jog leaving behind the hole trapped at the cation vacancy, which is in fact a V_F-center. See the scheme of the reactions in figure 2.1. Recombination of a V_F-center with an *F*-center produces a stoichiometric vacancy pair that restores the previous state of the dislocation.

Table 2.1: Comparison of the salient points of the Jain-Lidiard and Dubinko-Turkin-Vainshtein-den Hartog models.

Jain-Lidiard	***Dubinko-Turkin-Vainshtein-den Hartog***
Clustering of *H*-centers to form self-interstitial (sia)-loops and ***molecular centers***	Clustering of *H*-centers to form ***Halogen bubbles*** and a SIA-loops
Bias-driven growth of SIA-loops followed by generation of immobile ***molecular centers***, H_2V: $\mathit{H+H+SIAloop}\{n\}\rightarrow \mathit{SIAloop}\{n+1\}+H_2V$	Bias-driven growth of SIA-loops followed by generation of *mobile* ***V_F-centers*** (*cation vacancy with a trapped hole):* $\mathit{H+SIAloop}\{n\}\rightarrow \mathit{SIAloop}\{n+1\}+V_F$
Dislocations are biased toward absorption of *H*-centers. Metallic colloids are assumed to be neutral sinks	All extended defects are biased toward absorption of *H*-centers. Competition between bias factors controls the evolution of microstructure
Growth of colloids due to absorption of excess *F*-centers: $\mathit{F+Colloid}\{n\}\rightarrow \mathit{Colloid}\{n+1\}$	Growth of colloids due to absorption of excess *F*-centers. No absorption of ***V_F-centers*** by coherent colloids[1]
Accumulation of dispersed ***molecular centers***	Accumulation of halogen molecules in bubbles
	Void nucleation as a result of reactions between growing metallic colloids and halogen bubbles
Recombination of *molecular centers* with *F*-centers, which **suppresses** colloid growth.	Void growth due to absorption of V_F-centers and excess *F*-centers
	Collision of growing voids with *Hal*-bubbles and colloids followed by the **explosive *Me*+*Hal* reaction**, which gives rise to gas pressure increase in the void and to thermoelastic stresses in the surrounding matrix beyond the strength limit of the material [7,15]

---

[1] Since the colloids are formed by *F*-centers they are expected to be coherent with the host matrix as long as they are small, i.e. matrix and colloid crystal planes coincide with each other.

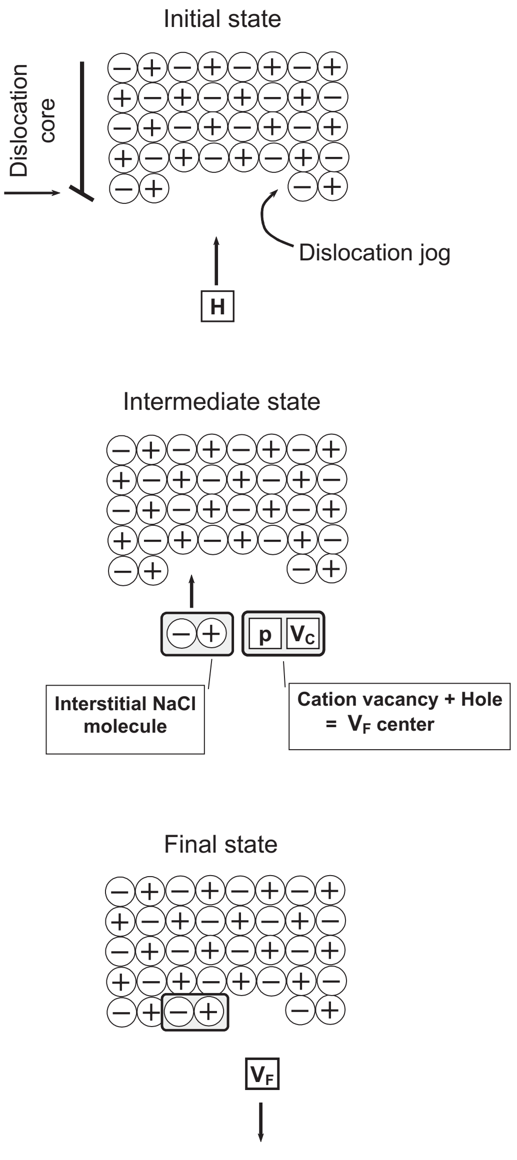

Figure 2.1: The scheme of V_F center creation.

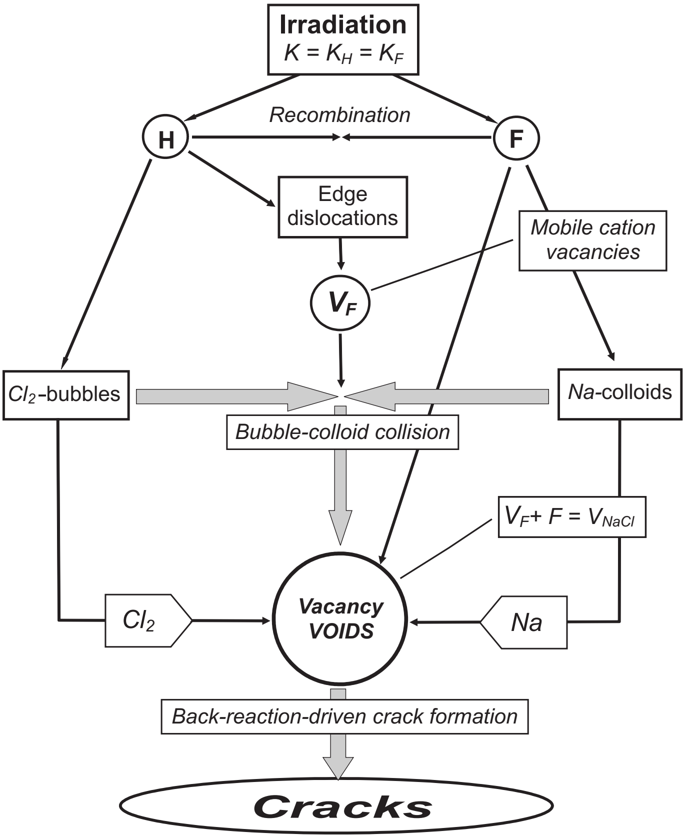

Figure 2.2: Diagram of radiation-induced reactions between point defects (*H*- and *F*-centers, and cation vacancies) and extended defects (bubbles, dislocations and colloids).

2.2 Details of the model

The results of the experimental studies presented in this thesis will be discussed in the framework of the recent theoretical model developed in Ionic Materials group at the University of Groningen [9,10]. The basic formulation of the model is considered below.

A mean field approach has been used to describe diffusion controlled clustering of radiation-induced *F*- and *H*-centers. In other words, a set of chemical rate equations has been formulated for the average concentrations of mobile *F*- and *H*-centers and clusters of these defects. The traps for *F*- and *H*-centers are introduced in the model. Trapping of *H*-centers is necessary to account for nucleation of chlorine bubbles, because the rate of homogeneous nucleation of chlorine bubbles is small due to the low concentration of highly mobile *H*-centers [3,4]. Experiments have shown that small amounts of impurities may have profound effects on the colloid formation in ionic crystals [6-8,14]. These effects can be modeled by taking into account traps for *F*-centers, which may provide additional (heterogeneous) nucleation sites, or recombination sites of *F*- and *H*-centers on the other hand. The nature of the individual traps is not specified. NaCl material may contain various types of traps with various binding energies with point defects. Crystal lattice defects, which may serve as traps for *H*- and *F*-centers, include impurity ions and complex defects, dislocation jogs, grain boundaries etc. At present we have no detailed information about the nature of trapping centers in NaCl. Possibly a series of special low dose irradiation experiments for samples with various concentrations of dopants could help to elucidate the question of the relation between defect traps and doping. However this task is a quite intricate problem, which is beyond the scope of this investigation. The trap concentration appears as one of the input parameters in this model.

The mean concentrations of the PD's, $\bar{c}_{F,H}$ are determined by the following rate equations

$$\frac{d\bar{c}_{F,H}}{dt} = K_{F,H} - k^2_{F,H} D_{F,H} (\bar{c}_{F,H} - \bar{c}^{th}{}_{F,H}) - \beta_r (D_F + D_H) \bar{c}_F \bar{c}_H \tag{2.1}$$

$$k^2_{F,H} = Z^d_{F,H} \rho_d + \sum_S Z^S_{F,H} 4\pi N_S \bar{R}_S$$

where $K_{F,H}$ is the production rate of *F*- and *H*-centers, usually expressed as displacements per atom per second (dpa/s)[1], $D_{F,H}$ are the diffusion coefficients for the PD's, β_r is the constant of their bulk recombination, $k^2_{F,H}$ are the sink strengths associated with the absorption and thermal emission of PD by extended defects (ED), $\bar{c}^{th}$ is the mean concentration of thermal PD, ρ_d is the dislocation density, N_S is the number density of "spherical" *S*-type ED's (colloids, bubbles and voids), and $\bar{R}_S$ is the corresponding mean radius; $Z^S_{F,H}$ are the sink

---

[1] The following dose relation has been used in the calculations: 6x10^{-2} dpa = 1 Grad = 10 MGy. This expression is based on an average amount of energy of 100 eV needed for the creation of one separated *F-H* pair [4].

capture efficiencies for the PD's, which determine the microstructure evolution under steady state conditions (i.e. for $d\bar{c}_{F,H}/dt = 0$).

The concentration of V_F -centers is determined by the V_F production at dislocations, bulk recombination and absorption by voids:

$$\frac{d\bar{c}_v}{dt} = K_v - k_v^2 D_v \bar{c}_v - 2\beta_r D_v \bar{c}_v{}^2 \tag{2.2}$$

$$K_v = (Z_H^d D_H \bar{c}_H - Z_F^d D_F \bar{c}_F)\rho_d\,, \qquad k_v^2 = 4\pi N_V \overline{R}_V$$

Mobile V_F -centers can recombine with each other to form a halogen molecule sitting in a double vacancy pair (i.e., in two adjacent stoichiometric vacancy pairs). This can be a nucleus of a halogen bubble that is formed by a subsequent absorption of *H*-centers.

Nucleation and growth of colloids

The time dependent size distribution function of clusters *f(n,t)*, i.e. the concentrations of the clusters of size *n* obey the following Master equation:

$$\frac{\partial f(n,t)}{\partial t} = J_{n-1,n} - J_{n,n+1} \tag{2.3}$$

$$J_{n-1,n} = W^+(n-1) f(n-1,t) - W^-(n) f(n,t) \tag{2.4}$$

$W^+(n)$ and $W^-(n)$ are the forward and backward reaction rates, i.e. the transition rates of n-mer to (n+1)-mer or (n-1)-mer, respectively. Under steady state conditions $\frac{\partial f(n,t)}{\partial t} = 0$ and $J_{n-1,n}$, i.e. the flux of clusters in the size space does not depend on time and size and can be evaluated to give the steady state nucleation rate in the following form [16];

$$J_N = \left\{ \sum_{m=1}^{\infty} \frac{1}{W^+(m) f_0(m)} \right\}^{-1}, \qquad f_0(n) = f_0(1)\exp\left\{-\frac{\Delta G(n)}{kT}\right\} \tag{2.5}$$

$$\frac{\Delta G(n)}{kT} = \sum_{m=1}^{n-1} ln \frac{W^-(m+1)}{W^+(m)} \tag{2.6}$$

where $\Delta G(n)$ is the kinetic analogue of the free energy of forming the n-mer from atoms in a supersaturated solution, known also as the nucleation barrier, kT is Boltzmann's constant times absolute temperature and $f_0(n)$ is the so called constraint equilibrium size distribution function, which describes the size distribution of hetero-phase fluctuations under zero nucleation rate conditions.

For metallic colloids formed by agglomeration of F-centers, the forward reaction rate is determined by the rate of F-center capture by a n-mer, $\beta_F(n)$[1], and the backward reaction rate is the sum of the rate of F-center loss, $\gamma_F(n)$, and H-center capture, $\beta_H(n)$:

$$W^+(n) = \beta_F(n) \ , \qquad W^-(n) = \gamma_F(n) + \beta_H(n) \tag{2.7}$$

These rates can be found by solving diffusion problem for a colloid with radius $R_C(n)$ taking into account its elastic interaction with PD's [10]

$$\beta_i(n) = \frac{4\pi}{\omega} Z_i^C(n) R_C(n) D_i \bar{c}_i , \quad R_C(n) = \left(\frac{3n\omega}{4\pi}\right)^{1/3}, \quad i = F, H \tag{2.8}$$

$$\gamma_F(n) = \frac{4\pi}{\omega} Z_F^C(n) R_C(n) D_F c_F^0 \exp\left(\frac{\sigma_r(n)\omega}{kT}\right) \tag{2.9}$$

where Z_i^C is the capture efficiency of precipitates of i-type PD, i = F, H correspond to F- and H-centers, respectively, ω is the atomic volume of the host matrix, D_i are the PD diffusivities, c_F^0 is the thermal equilibrium concentration of F-centers near the free surface, $\sigma_{rr}(n)$ is the normal stress at the colloid interface due to size misfit [4].

Using equations (2.7)-(2.9), equation (2.6), can be rewritten in the form

$$\frac{\Delta G(n)}{kT} = \sum_{m=1}^{n-1} ln\left\{ S_{FH}^{-1} \frac{Z_H^C(m+1)}{Z_F^C(m)} + S_F^{-1} \exp\left(\frac{\sigma_{rr}(m+1)\omega}{kT}\right)\right\}, \quad S_{FH} = \frac{D_F \bar{c}_F}{D_H \bar{c}_H} \tag{2.10}$$

where S_{FH} is the kinetic analogue of the supersaturation $S_F = \bar{c}_F / c_F^0$. Without irradiation ($\bar{c}_H = 0$ and $S_{FH} \to \infty$) equation (2.10) corresponds to the case of "classical" nucleation from supersaturated solid solution.

With increasing irradiation time (or dose), the microstructure changes and, generally, one has to solve the Master equation (2.3). Usually this equation is converted, by a Taylor series expansion up to the second order, into the Fokker-Planck equation for the continuous size coordinate

[1] The thermally activated loss of H centers from colloids (which would also increase their size) can be neglected due to their large binding energy, which is similar to the situation encountered for interstitial atoms in metals [16].

$$\frac{\partial f(n,t)}{\partial t} = -\frac{\partial}{\partial n}\left\{f(n,t)\left(W^{+}(n,t) - W^{-}(n,t)\right)\right\} + \frac{1}{2}\frac{\partial^2}{\partial n^2}\left\{f(n,t)\left[W^{+}(n,t) + W^{-}(n,t)\right]\right\} \tag{2.11}$$

where the first term corresponds to the “drift” flux in the size space and the second term describes “diffusion” in the size space due to the fluctuations. The second term is the most important one in the vicinity of the critical size determined by the equation $W^{+}(n) = W^{-}(n)$, where the drift flux is small.

In [10] equation (2.11) has been rewritten in terms of cluster radius R_C, and the second term has been replaced by the term describing the production of overcritical nuclei

$$\frac{\partial f(R_C,t)}{\partial t} = -\frac{\partial}{\partial R_C}\left\{f(R_C,t)\frac{dR_C}{dt}\right\} + \delta(R_C - R_{nucl})J_N(t) \tag{2.12}$$

The radius $R_{nucl} = R_{crit} + \Delta R$ of the newly formed particles is set to be slightly larger than the critical radius R_{crit} to enable these particles to grow, $\delta(R_C - R_{nucl})$ is a delta-function, dR_C/dt is the colloid growth (or shrinkage) rate.

$$\frac{dR_C}{dt} = \frac{\omega}{4\pi R_C^2}\left(W^{+} - W^{-}\right) \tag{2.13}$$

Formation of bubbles

In [10] nucleation of bubbles was not considered. Instead, their stable radius has been determined as a function of the mean bias of the evolving microstructure $\delta_{mean} \equiv k_H^2/k_F^2 - 1$. Chlorine bubbles are formed by agglomeration of *H*-centers and are allowed to grow as a result of dislocation loop punching [14], which is analogous to the loop punching by growing gas bubbles in metals [17,18]. Due to the extremely high pressure in small bubbles, they have a larger bias for *H* centers than for colloids or even dislocations, and therefore they absorb extra *H*-centers and grow during the initial stages of the irradiation [14]. With increasing bubble radius, i.e. beyond some threshold value $R^{th} \sim 1$ nm, their bias decreases very rapidly to the mean bias of the system (which is determined by the physical parameters of the dislocations and the sodium colloids) resulting in the formation of exceptionally large concentrations of stable bubbles [15] (see figures 2.3). The bubble volume fraction, $V_B(t)$ and number density, $N_B(t)$, increase steadily with increasing colloid volume fraction, $V_C(t)$, and are determined by the balance between the amounts of halogen molecules in the bubbles and metal atoms in the colloids

$$V_B(t) \approx \frac{\omega_{Gas}}{2\omega} V_C(t)\ , \qquad N_B(t) = \frac{3V_B(t)}{4\pi}\left(R^{th}\right)^{-3} \qquad (2.14)$$

where ω_{Gas} is the effective volume per halogen molecule in the bubble. This implies that by calculating the mean colloid parameters, the bubble parameters can be evaluated self-consistently.

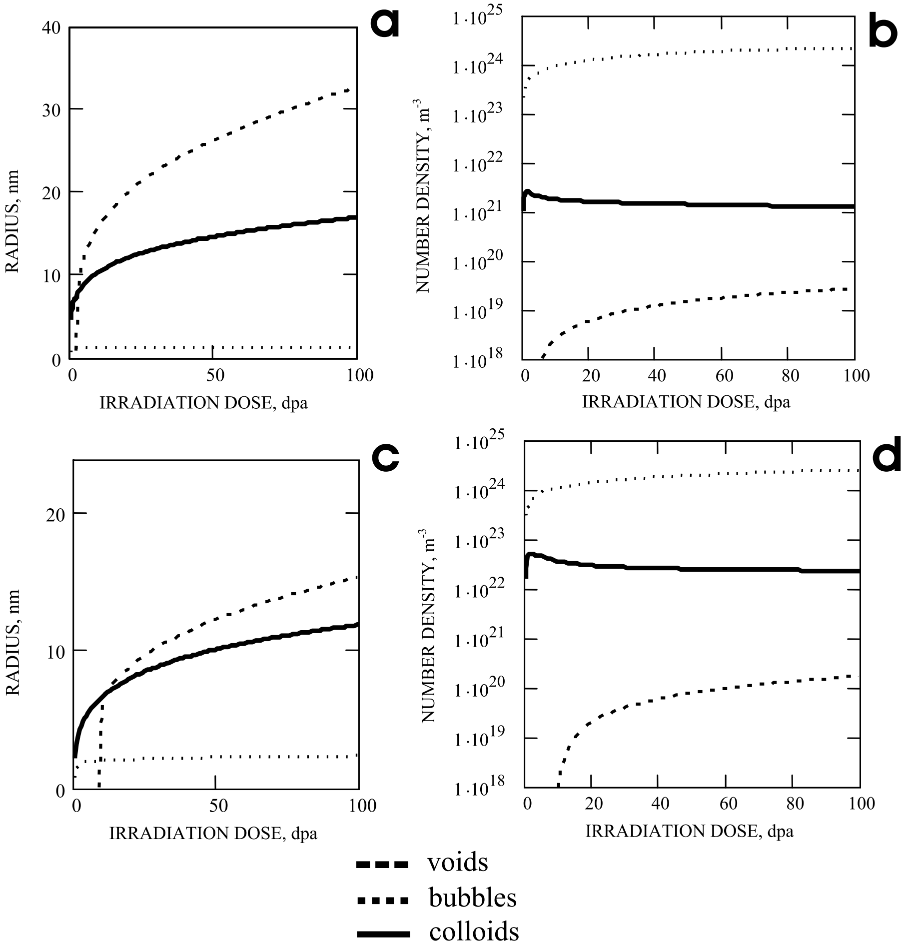

Figure 2.3: Calculated evolution of colloids, bubbles and voids at a dose rate K = 1.3x10^{-5}dpa/s, T = 100 °C. (a, b) low initial nucleation rate (no impurity *F*-center traps, dislocation density $\rho_d = 10^{13}$ m^{-2}); (c, d) high initial nucleation rate (100 ppm of impurity *F*-center traps, dislocation density $\rho_d = 10^{14}$ m^{-2}).

Formation of voids

The calculations of the mean radii and number densities of bubbles and colloids [19,20] show that in rather early stages colloids can grow to sizes exceeding the mean distance between the bubbles resulting in the direct collisions between colloids and bubbles. That would initiate a strong and highly localized back reaction between the radiolytic sodium and chlorine. The amount of released energy in the back reaction is proportional to the energy released due to the formation of one NaCl molecule, and to the number of molecules formed as a result of the collision. The latter is limited by the mean number of chlorine atoms in a bubble, which is about two orders of magnitude smaller than the number of sodium atoms accumulated in a colloid at the time of the collision. The energy released during the back reaction causes an increase of the temperature of the reaction products resulting in an instantaneous and highly localized temperature spike (about 10^4 K), which is accompanied by an increase of the local pressure up to several GPa [15]. Such a high pressure, although it is extremely short (in the picosecond range), will induce plastic expansion of the cavity filled with reaction products before it is cooled down. As a result, one expects the formation of an empty cavity (*void*) in the vicinity of the colloid with a radius exceeding the bubble radius before the collision. This process provides the possibility of explosive formation of voids, which can absorb more *F*-centers (as compared to *H*-centers) and grow as a result of their recombination with V_F -centers at the boundary of the voids. The growth rate of the voids is determined by the excess *F* center flux to the void [14]:

$$\frac{dR_V}{dt} = \frac{1}{R_V}\left(Z_F^V D_F \bar{c}_F - Z_H^V D_H \bar{c}_H\right) = \frac{1}{R_V} Z_F^V D_H \bar{c}_H \left(\bar{\delta} - \delta_V^{eff}\right) \tag{2.15}$$

where δ_V^{eff} is the void bias in the case that there are sufficient V_F-centers available for recombination with extra *F*-centers to produce stoichiometric vacancy pairs. In the opposite case, the flux of V_F -centers is the limiting factor of the void growth, which is then given by

$$\frac{dR_V}{dt} = \frac{1}{R_V} Z_v^V D_v \bar{c}_v \tag{2.16}$$

During collisions with chlorine bubbles the growing voids absorb chlorine gas. Collision of large voids, which are filled with chlorine and sodium colloids results in propagation of the cracks in the crystalline host NaCl material and ultimately explosive fracture of the sample. See for example the SEM images in figure 2.4. The above described steps of void nucleation and growth are illustrated in the scheme in figure 2.5. The kinetics of the back reaction processes, which includes chlorine bubbles, voids and colloids has been observed in [21,22]. The size, number density and volume fraction of the voids in the irradiated crystal is a measure of the mechanical and chemical stability of material. A detailed SEM investigation of voids in irradiated NaCl samples including a statistical treatment is presented in *chapter VII.*

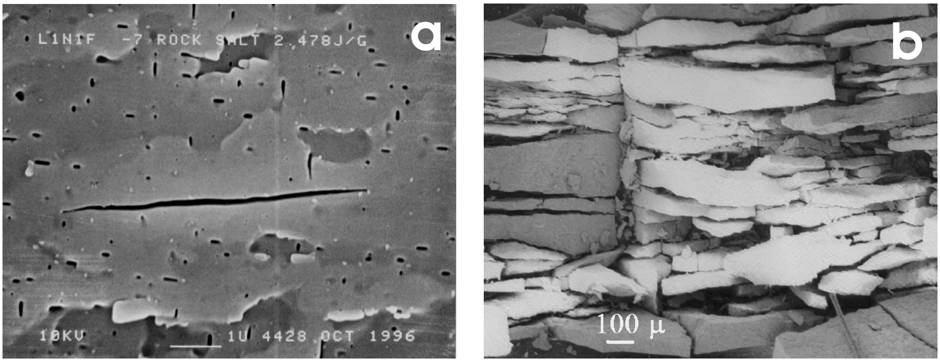

Figure 2.4: (a) SEM image showing vacancy voids and the crack in natural rock salt crystal irradiated with 0.5 MeV electrons at 100^0C. Long crack formed after irradiation to 300 Grad, LHM of metallic *Na* is 2.5 J/g. (b) Explosive fracture of NaCl+K (0.1mol%) samples irradiated with 0.5 MeV electrons to 300 Grad at 100^0C. SEM image of the exploded sample reveals large fragments and dust-like particles.

2.3 Simulation results and comparison with experimental data

The calculations with the model have been carried out in the same way as in [9] and [10], using a standard set of material parameters. The dose and dose rate in the simulations have been calculated in dpa (displacement per atom). We note that 1 Grad, the unit for the dose, which have been used in other parts of this thesis is equal to $6x10^{-2}$ dpa; this value is based on the average amount of energy of 100 eV needed for the creation of one separated *F-H* pair [4].

Figure 2.3 shows the dose dependence of the mean radii and the number densities of radiolytic ED-s, calculated for different values for the dislocation density and trap concentrations. According to the calculated results, the mean radii of the colloids and voids grow continuously, while the size of the bubbles shows saturation at a certain value, when the bias of the growing bubbles becomes equal to mean bias of the system (as it was discussed above). At the same time the calculation of the number densities shows a very short nucleation stage for colloids, when their number is growing to reach a fixed value. A similar assumption for the nucleation of the colloids can be found in earlier theoretical papers on radiolysis in NaCl [1,23]. The number densities of the bubbles and voids increase with the dose.

Hence, the volume fractions of each type of radiolytic precipitates grow unsaturated with increasing dose (figure 2.3). The model calculations for the volume fraction of the colloids are presented in figure 2.6 together with experimental DSC data. Variation of the material parameters (concentration of the dislocations and *F*-center traps) allows us to calculate different growth rates of the radiolytic ED-s, which cover the scatter of the experimental data (figure 2.6).

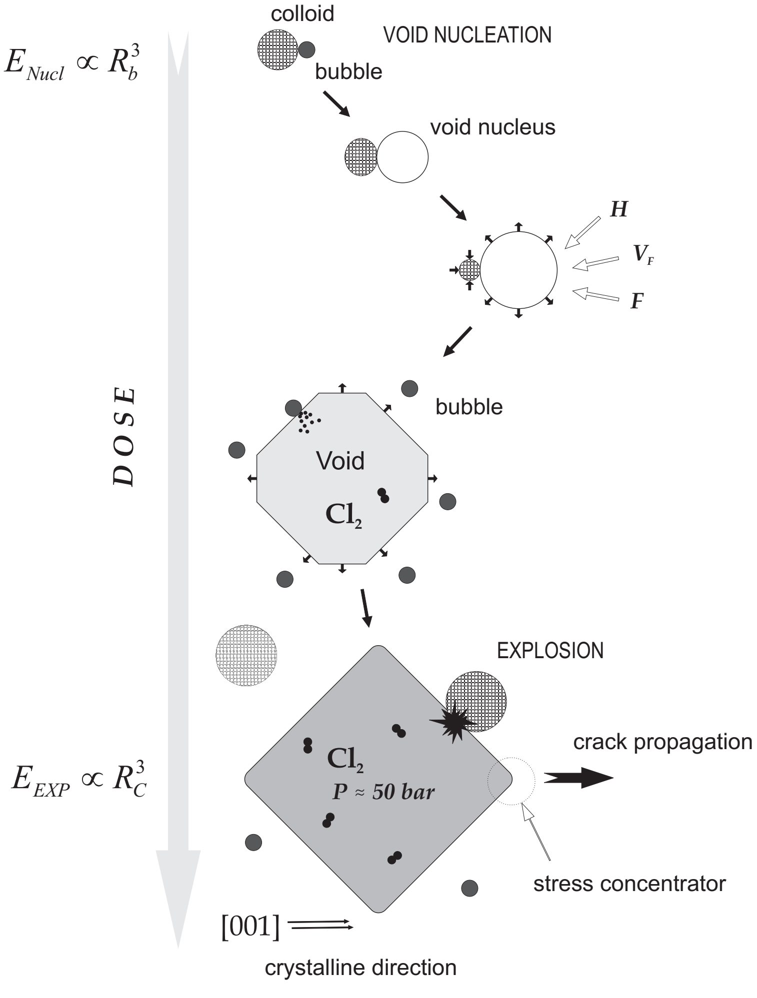

Figure 2.5: A scheme of void growth steps.

The results of the model calculations are in agreement with the experimentally observed behavior of the colloid volume fraction and the void growth dynamics (see *chapter VII*). The theoretical model, presented here, has been developed to operate with mean values of size for each type of radiolytic defects. The effects of the size distribution of the precipitates and the eventual inhomogeneity of the microstructure of the crystal, which becomes essential at ultra-high doses, have been not taken into account. The development of the size distribution of colloids and bubbles has been considered recently [24]. The observations have been presented in *chapter IX*.

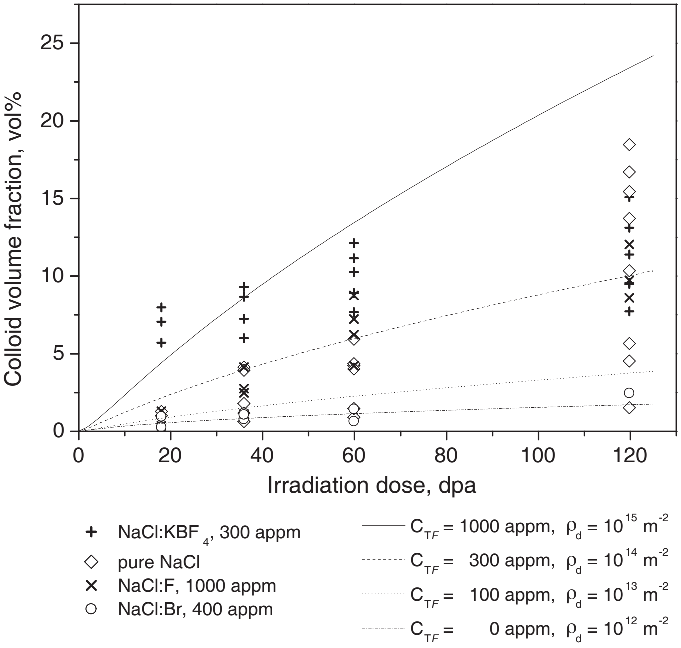

Figure 2.6: Comparison of the model calculations of the dose dependence of the colloid volume fraction at K=1Grad/h, 100 °C, for different traps and dislocations concentrations with experimental data, obtained for doped NaCl samples.

However, direct AFM observations of sodium colloids (*chapter VI*) and SEM observations of voids (*chapter VII*) have demonstrated appreciable inhomogeneity of the spatial distribution of colloids and voids in crystalline media. In addition, self-organized structures of nanoparticles have been detected in heavily-irradiated samples [25,26]. These structures may be caused by the interactions of closely spaced ED-s of the same type, and eventually by overlapping of strain fields of dislocations [25].

Although these features of the radiation-induced microstructural evolution have been neglected in the presented theoretical model, the results of the calculations show good qualitative and quantitative agreement with experimental data for the development of radiolytic defects in pure and doped NaCl crystals under irradiation.

The radiolysis model for NaCl, considered in this chapter, suggests the following scenario for the radiation-induced reactions between point defects (PD) and extended defects (ED). Primary radiation-induced PD, e.g. *H*- and *F*-centers, ultimately separate into bubbles, dislocations and metal colloids, which results in the production of secondary PD (V_F-centers) and ED (voids). The voids absorb fine chlorine bubbles during growth and accumulate a large number of chlorine molecules before the collision with colloids takes place for the first time, and which ultimately changes the scale of the back reaction from the atomic to a macroscopic one.

References

[1] U. Jain and A.B. Lidiard, *Phil. Mag.* **35** (1977), 245-259

[2] A.B. Lidiard, *Phil. Mag.* **39** (1979), 647-659

[3] J.C. Groote and J.R.W. Weerkamp, *Radiation damage in NaCl. Small particles*, PhD thesis, University of Groningen, (1990)

[4] J. Seinen, *Radiation damage in NaCl. The process of colloid formation*, PhD thesis, University of Groningen, (1994)

[5] L.W. Hobbs, A.E. Hughes and D. Pooley, *Proc. R. Soc. Lond.* **A332** (1973), 167-185

[6] H.W. den Hartog, J.C. Groote and J.R.W. Weerkamp, *Radiat. Eff. & Def. Sol.* **139** (1996), 1-19

[7] H.W. den Hartog and D.I. Vainshtein, *Mater. Sci. Forum.* **239-241** (1997), 611-614

[8] D.I. Vainshtein, C. Altena and H.W. den Hartog, *Mater. Sci. Forum.* **239-241** (1997), 607-610

[9] V.I. Dubinko, A.A. Turkin, D.I. Vainshtein and H.W. den Hartog, *J. Nucl. Mater.* **277** (2000), 184-198

[10] V.I. Dubinko, A.A. Turkin, D.I. Vainshtein and H.W. den Hartog, *J. Nucl. Mater.* **304** (2002), 117-128

[11] E.R. Hodgson, A. Delgado and F. Agullo-Lopez, *Radiat. Eff. & Def. Sol.* **74** (1983), 193

[12] Ch. Lushchik, N. Lushchik, A. Frorip and O. Nikiforova, *Phys. Stat. Sol. (b)* **168** (1991), 413

[13] A.V. Gektin, V.Ya. Serebryany and N. Shiran, *Radiat. Eff. & Def. Sol.* **134** (1995), 411

[14] D.I. Vainshtein and H.W. den Hartog, *Radiat. Eff. & Def. Sol.* **152** (2000), 23-37

[15] V.I. Dubinko, A.A. Turkin, D.I. Vainshtein and H.W. den Hartog, *J. Nucl. Mater.* **289** (2001), 86-95

[16] J.L. Katz and H. Wiedersich, *J. Chem. Phys.* **55** (1971), 1414

[17] V.I. Dubinko, V.V. Slezov, A.V. Tur and V.V. Yanovskij, *Radiat. Eff. & Def. Sol.* **100** (1986), 85

[18] G.W. Greenwood, A.J.E. Foreman and D.E. Rimmer, *J. Nucl. Mater.* **4** (1983), 305

[19] V.I. Dubinko, A.A. Turkin, D.I. Vainshtein and H.W. den Hartog, *Nucl. Instr. and Meth. in Phys. Res.* **B 166-167** (2000), 561-567

[20] D.I. Vainshtein, V.I. Dubinko, A.A. Turkin and H.W. den Hartog, *Nucl. Instr. and Meth. in Phys. Res.* **B 166-167** (2000), 550-555

[21] A.A. Turkin, V.I. Dubinko, D.I. Vainshtein and H.W. den Hartog, *J. Phys.: Condens. Matter.* **13** (2001), 203-216

[22] A.A. Turkin, V.I. Dubinko, D.I. Vainshtein and H.W. den Hartog, *Nucl. Instr. and Meth. in Phys. Res.* **B 191** (2002), 83-88

[23] A.E. Hughes and S.C. Jain, *Advances in Phys.* **28**: (6) (1979), 717-828

[24] A.A. Turkin, A.V. Sugonyako, D.I. Vainshtein and H.W. den Hartog, *J. Phys.: Condens. Matter.* **18** (2006), 5655-5668

[25] A.V. Sugonyako, A.A. Turkin, R. Gaynutdinov, D.I. Vainshtein, H.W. den Hartog and A.A. Bukharaev, *Phys. Stat. Sol.* **2**: (1) (2005), 289-293

[26] D.I. Vainshtein and H.W. den Hartog, *Appl. Radiat. Isot.* **47**: (11/12) (1996), 1503-1507

CHAPTER III

PREPARATION OF IRRADIATED SAMPLES

3.1 Introduction

This chapter is a brief review of the key elements of the procedures used for the preparation of the NaCl samples. In addition, a description of the irradiation facility will be given, along with the calculation of the irradiation dose.

Sodium chloride crystals doped with a variety of impurities have been used in the present investigations. In addition, we have investigated natural rock salt samples from salt dome formations in the province of Groningen (the Netherlands) and Asse (Germany). All synthetic crystals were grown earlier by our group. The electron irradiation of the samples has been carried out by means of electron beams from either a van de Graaff accelerator or a cascade generator. The irradiation setup allows us to control the temperature and the dose rate of samples during the irradiation run. In the calculations of the irradiation dose we have taken into account build-up phenomena of the energy deposition due to back scattering of electrons from the Al-target plate in which the samples are accommodated.

Gamma irradiation of the NaCl samples has been carried out in collaboration with the group of Dr. V.I. Dubinko at the NSC KIPT in Kharkov (Ukraine).

3.2 Crystal growth and sample preparation

The synthetic rock salt crystals, used for this investigation, have been grown earlier by our group by Groote et al [1] from the melt using suprapur NaCl powder (Merck). The impurities were added to the raw materials prior to crystal growth; the crystal growth procedure has been described in detail in [1]. The concentrations, mentioned in the present investigations are nominal concentrations, which were determined by the relative weight of the impurity compound compared with the weight of the NaCl powder. With the crystal growth technique used in this investigation, NaCl single crystal cylinders were obtained with a diameter of 6 mm and mostly with homogeneously distributed dopants. The crystal growth procedure is described in [1], and a more extensive description of the technique can be found in articles by den Hartog et al [2,3]. In the present work we have used pure, synthetic NaCl crystals and synthetic samples with the following impurities: KCl, NaF, NaBr and KBF_4. In addition, the above-mentioned natural rock-salt samples were used (these samples have been used for a variety of experiments, but they have been investigated most extensively with AFM, see *chapter VI*).

In order to prepare NaCl samples for irradiation the as grown crystal cylinders with lengths of about 6 cm have been cut into 30 disks by means of a cotton string saw, which was saturated with a mixture of water and alcohol. After cutting the samples they were polished to a thickness of about 0.5 mm. These thin disks were suitable for application in the multi-sample target, which was designed especially to carry out irradiation runs, where for efficiency reasons more than 300 samples could be exposed simultaneously.

Natural rock-salt samples were cleaved from large crystalline blocks taken from geological rock salt formations. These natural materials contain cm-sized, high quality single crystals, which could be cleaved and ‘machined’ to a reasonably cylindrical shape with a diameter of about 6 mm by chipping off small fragments from the sides. Shiny and plane-parallel samples with a thickness of about 0.5 mm were obtained by grinding and polishing.

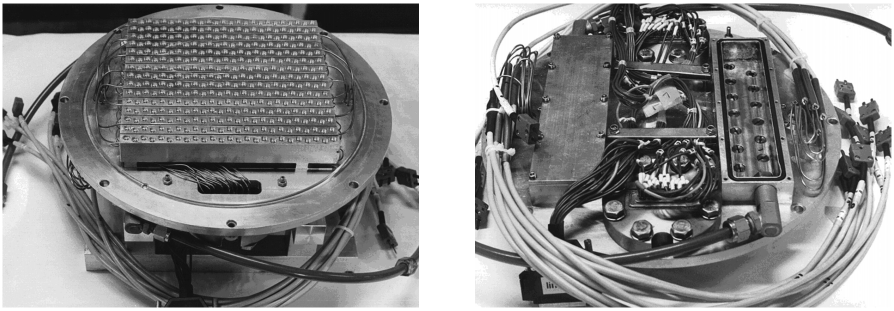

Figure 3.1: The front and back side of the new multi-sample target.

3.3 Electron irradiation

One of the purposes of this investigation was to study the characteristic properties of ultra-heavily damaged crystals with 20 at% or more radiolytic Na and Cl. To reach the required damage level very high irradiation doses up to 2 Tera Rad (TRad), which equals 20 Giga Gray (GGy)[1] were needed. These high doses were obtained for NaCl crystals with a 0.5 MeV electron beam from a cascade generator. The maximum dose reached with a 1.35 MeV beam from our van de Graaff accelerator was 0.15 TRad after an irradiation run that took 3-4 months. The irradiation setup was constructed earlier in our laboratory (important technical information about the setup and the irradiation procedures can be found in [5]). It should be noted, that according to our *de facto* established designation, irradiation doses of the NaCl crystals can be divided into four ranges: *low* – 100 MGy (or 10 GRad) and less, *moderate* – 200 to 1000 MGy (or 20-100 GRad), *high* – 1100 to 3000 MGy (or 110-300 GRad) and *ultra-high* – 6000 MGy (or 600 GRad) and higher.

---

[1] Different expressions for the dose are related in our case by: 1 Grad = 10 MGy = $4\text{x}10^{16}$ e^-/cm^2 = $6\text{x}10^{-2}$ dpa. The last expression is based on an average amount of energy of 100 eV needed for the creation of one separated *F-H* pair [4].

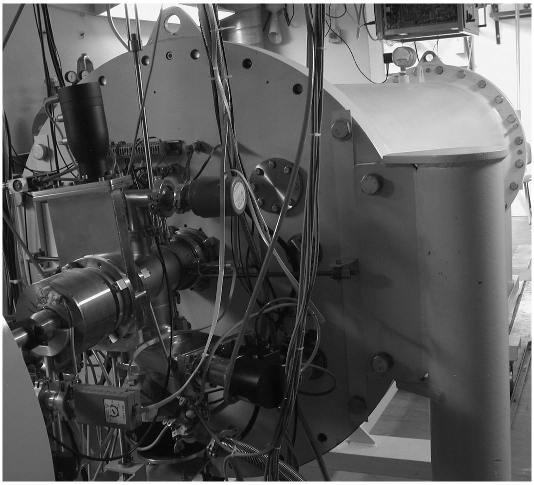

Figure 3.2: The van de Graaff electron accelerator.

Several modifications of the irradiation setup have been made to reach the ultra-high irradiation dose range. With the previous system we were able to irradiate a target area of 320 cm^2 at dose rates between 10 Mrad/hr and 1.5 Grad/hr. At high dose rates there are severe limitations due to the large heat production in the target plate caused by the energy losses of the stopped electrons. When too high dose rates are applied, the temperatures of the sub-targets cannot be controlled in the required temperature interval. In order to solve this problem, a new, strongly cooled sample holder has been constructed (see figure 3.1). A photograph of the accelerator is shown in figure 3.2.

The multi-sample aluminum target consists of 15 sub-targets; each of these sub-targets can accommodate more than 20 small disk-shaped samples with a diameter of 6 mm. The most important feature of this part of the setup is that it consists basically of one piece of aluminum metal. This is necessary in order to maintain a stable temperature at high dose rates during the very long non-stop irradiation runs. The temperature of each sub-target is measured and controlled separately. For the temperature adjustment each of the sub-targets is equipped with PDI temperature controlled electrical-heating device and a water-cooling system. The water flow in each of the sub-targets was adjusted individually; this was necessary in order to compensate the excessive heat production by the electron beam. With the fixed water flow and a temperature controlled electrical heating device it was possible to maintain the temperature of that particular sub-target at the correct value. At the highest dose rates used in this investigation it was possible to control the temperature in range 50-150 ^{o}C. In addition, it was also possible to keep the temperature of the sub-targets at about 20 ^{o}C, this temperature condition was used during the irradiation runs at low temperature (see *chapter VIII*). This low irradiation temperature was achieved by increasing the flow of the water-cooling system compared with the irradiation runs carried out at elevated temperatures.

In test experiments we have found that under the above-mentioned high dose rate conditions a significant fraction of the samples showed drastically reduced amounts of radiation damage. This was caused by a large difference between the temperature of the sample and the cooled sample holder. To avoid local heating by the electron beam due to poor temperature contact between the sample holder and the crystal we have applied a thin layer of Aquadag (a suspension of carbon in ethanol). The Aquadag layer fills eventual gaps between the sample and the surface of the sample holder. These gaps are caused by imperfections of either the surface of the sample holder or the sample. When Aquadag is used the temperature contact between the sample and the sample holder is improved drastically and only in a few cases the above-mentioned reduction of the amount of radiation damage is observed. A detailed picture of the sample in the sample holder has been given below in figure 3.3.

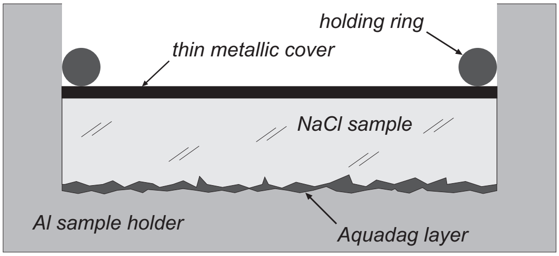

Figure 3.3: The NaCl sample in the sample holder.

The beam current of the 0.5 MeV cascade generator could in principle be varied up to maximum value of 1 mA, but in our investigations a maximum current of about 500 μA was used. With the effective target area of 320 cm^2 this corresponds to a dose rate ranging from 10 MRad/hr up to 1.5 Grad/hr, where the lower limit is determined by the problems encountered controlling the corresponding very low beam currents. To reach the maximum dose of 1 TRad the irradiation run lasted several (3-4) months. During irradiation the accelerator tube and the target area are kept under high vacuum (about 10^{-7} mbar).

In order to obtain sufficient numbers of samples simultaneously during one irradiation run, a specially constructed beam sweeping system (see ref. [5]) and a new version of a multi-sample target were used. The beam sweeping system was employed to obtain a homogeneous dose everywhere on the target area of approximately 18×18 cm^2.

It has been found from stored energy measurements (see, for instance, [6]), that the total amount of damage, accumulated in the samples, depends on the dose rate and the sample temperature during irradiation. According to earlier experiments, with dose rates ranging between 10 and 50 MRad/hr maximum concentrations of radiation-induced defects in rock-salt crystals are produced at about 100 ^{o}C. As mentioned above, we were forced to use significantly higher dose rates in order to reach the desired dose range. Theoretical models predict that the maximum damage at these higher dose rates is obtained at higher temperatures. However the expected temperature shift of the maximum is rather small. Hence, an irradiation temperature of 100 ^{o}C was adjusted in our experiments when the objective was to reach the required high damage levels for the characterization of these ultra-heavily damaged samples. The gamma irradiation runs have also been carried out at 100 ^{o}C (see below).

3.4 Calculation of the irradiation dose

The calculation of the dose, absorbed in our samples during irradiation, is based on the energy, dissipated by the high-energy electrons in a target with a certain thickness. We can express the dose rate in NaCl in terms of the current density as:

$$\dot{D}[rad/s] = \frac{1}{\rho}\left[\frac{dE}{dx}\right]\frac{J}{e} \tag{3.1}$$

where $\frac{dE}{dx}$ is the energy absorbed in matter per unit length, J is the current density and the density of NaCl $\rho = 2.16$ g/cm^3.

To obtain the average absorbed energy in thick target it is necessary to calculate the energy deposition profile. These calculations have been done by Gann et al [7,8].

The calculation of the energy losses by electrons in a thick target is a rather complex problem that requires a sophisticated approach. The main difficulty arises from the back scattering and multi-scattering of secondary electrons in matter. Hence, it is necessary to take into consideration the role of δ-electrons[1] in the process of the transfer of energy, when calculating the energy deposition profile. For a quick evaluation a simple semi-empirical method for the calculation of the electron beam energy deposition $Q(x)$ it has been developed, which is based on dependable, measured energy deposition profiles for a parallel electron beam in aluminum [7,8]. We point out that as explained by Groote and Weerkamp [1] the atomic Z-value of Al is approximately equal to the average Z-value of Na and Cl. In addition, the density of Al is about the same as the density of NaCl. The calculated average value of the deposited energy is plotted in figure 3.4 together with the energy loss, calculated with the Bethe-Bloch formula (broken line) using for the ionization energy $I = 175.3$ eV (see Seltzer and Berger [9]). By taking into account the build-up of the energy deposition due to back scattering and multi-scattering of the high-energy electrons, the dose increases by ~100% compared to the previous -at that time- 'state of the art' calculations (e.g. [4])[2].

---

[1] δ-electrons are electrons ejected in primary ionizing collisions between a charged particle and an atom.

[2] It should be noted, that the irradiation doses used in this thesis are doubled compared with those mentioned in the previous publications (before 2006), according to the present calculations. Because the build-up effect is assumed to take place in our irradiation set-up, we use corrected dose values.

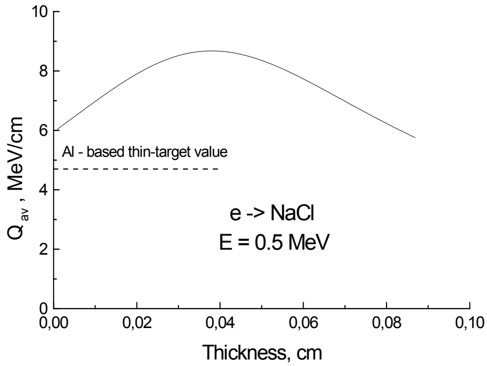

Figure 3.4: The average deposition profile with and without taking in to account the effect of the back scattering and multi-scattering electrons.

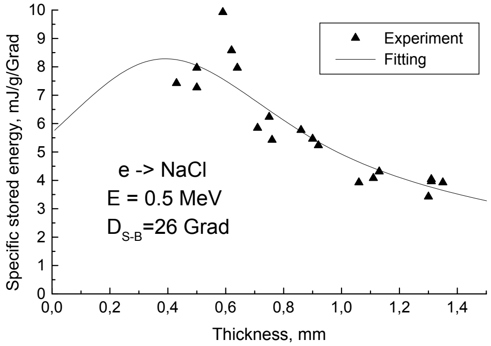

Figure 3.5: The average specific stored energy vs. the sample thickness.

Experimental investigations of the energy deposition profiles in NaCl platelets under $E = 0.5$ MeV electron irradiation have been performed. A set of synthetic NaCl samples with different values for the thickness were irradiated by the Groningen electron accelerator at 100°C up to a Seltzer and Berger dose of $D_{S\text{-}B}$= 26 GRad. Because the amount of energy absorbed in the sample at a certain depth varies with the depth, the average absorbed dose for each sample should depend on the overall thickness of the sample. The depth distribution of the absorbed dose was determined by measuring the stored energy associated with radiation damage, which was created in the NaCl sample during electron irradiation. The average specific stored energy W(t) is assumed to be proportional to the average absorbed dose, which depends on the sample thickness *t*:

$$W(t) = \frac{CD_{S-B}}{St}\int_0^t Q(x')dx' \tag{3.2}$$

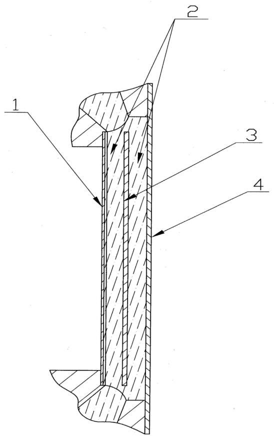

Figure 3.6: A schematic view of the electron to gamma-quanta converter, constructed at the NSC KIPT in Kharkov (see report [11]).

1 – stainless steel foil, through which the accelerated electron beam is put into the converter;
2 – cooling water layers;
3 – plate of tungsten, which converts electron into the gamma-quanta beam;
4 – output stainless steel plate, which absorbs the remaining energy of electron beam.

The converter total thickness is within 4mm.

Here S = 4.7 MeV/cm for an electron with energy E = 0.5 MeV, ρ is the density of the sample, C is a proportionality factor, which has been obtained by fitting of the W(t) curve to the measured stored energy data points (figure 3.5): C = 4.2 mJ/g/Grad.

The stored energy (SE) was calculated for each sample, after performing differential scanning calorimetry (DSC) experiments, see [10]. The experimental results are plotted in figure 3.5 together with the predicted average stored energy profile. The comparison of the experimental data with the calculated profile shows that the method proposed in [7,8] may serve as a basis for the evaluation of the absorbed dose in alkali halides under irradiation with electrons in the MeV-energy range.

3.5 The gamma irradiation runs and dose calculation

In order to compare the results for rock-salt samples irradiated with high-energy electrons and gamma-quanta, it was necessary to use a high-intensity source of gamma-quanta. The self-manufactured gamma-irradiation setup at the NSC KIPT in Kharkov was used in collaboration with the group of dr. V.I.Dubinko et al to irradiate our NaCl samples [11,12].

To obtain a bremsstrahlung-generated gamma-radiation spectrum that is similar to the one from real radioactive waste, a 3 MeV electron beam produced by the van de Graaff electrostatic electron accelerator ELIAS, model KS/3000 at the NSC KIPT in Kharkov, has been used. The electron beam was converted into an intense beam of gamma-quanta by a specially designed converter. The converter design was based on modeling results obtained for a 3 MeV electron beam interacting with the construction elements of the converter, taking into account the radiation and radiation-chemical stability of the converter construction elements. An optimal converter construction was designed based on modeling of the electron interaction with the converter construction elements by the Monte Carlo method (GEANT 3.16 program [13]).

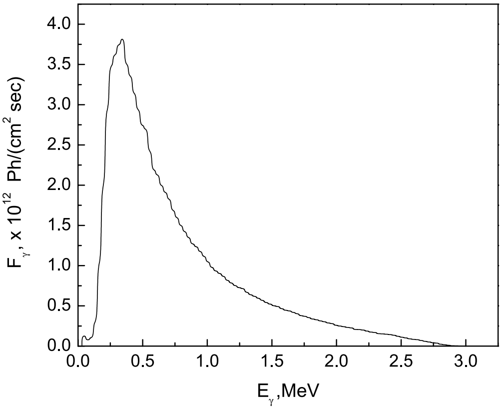

Figure 3.7: Spectrum of the gamma-quanta calculated for electron beam with energy 3 MeV and current density 150 μA/cm² [11].

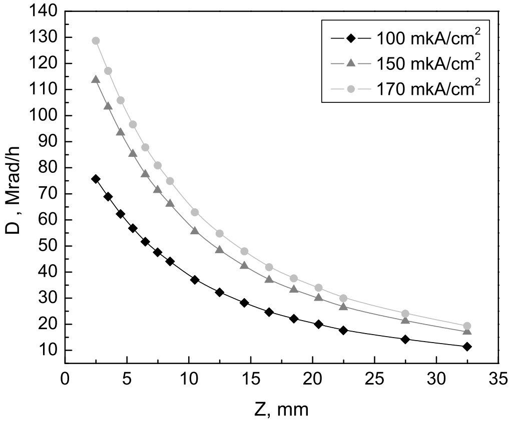

Figure 3.8: Dependence of the absorbed irradiation dose rate on the distance from converter in the air for the electron beam energy of 3 MeV and different current densities [11].

In addition to the bremsstrahlung gamma-radiation, the model has taken into account the ionization losses, the Compton effect, the photo effect and the creation of electron-positron pairs by gamma-quanta. Additional conditions such as the absence of electrons outside the converter, considerable stability during long non-stop irradiation runs, and the proximity of the samples to the converter have been taken into account. A schematic view of the converter, constructed at the NSC KIPT in Kharkov [11] is shown in figure3.6. In this way a 3 MeV electron beam with a current density of 150 μA/cm^2 was converted into beam of gamma-quanta with an intensity of about 10^{14} γ-quanta/cm^{2}sec.

The average energy of the resulting γ-quanta is 760 keV, which is close to the energy of the electrons, used for our irradiation runs with the high energy electrons from the Groningen cascade generator (500 keV). The calculated energy spectrum of the γ-quanta obtained by means of the accelerator at the NSC-KIPT is presented in figure 3.7.

A special temperature controlled chamber to irradiate our rock-salt specimens has been designed and manufactured together with the converter. This enabled us to irradiate four rolls of disk-shaped rock salt specimens with a diameter of 6.0 mm by gamma-quanta simultaneously at a constant temperature of 100 ºC. Each roll contained up to 25 specimens of one kind of (pure or doped) NaCl material with a thickness of 0.7 mm. During irradiation the temperature is stabilized in the range between 50 ºC and 150 ºC with an accuracy of 1 ºC. Along the specimen rolls, the intensity of gamma-quanta decreases monotonously, which allowed us to obtain specimens with various absorbed doses during one irradiation run. The dose absorbed by the first specimen in the roll exceeds the dose absorbed by the last specimen by a factor of 4.5 (figure 3.8) [11].

In this study 100 samples of synthetic crystals of NaCl (pure samples and doped ones with KBF_4, K, or Br; as mentioned we could accommodate 25 samples of each kind simultaneously) have been irradiated by γ-quanta at 100 ºC up to a total absorbed dose in the range from 12 to 78 Grad.

References

[1] J.C. Groote and J.R.W. Weerkamp, *Radiation damage in NaCl. Small particles*, PhD thesis, University of Groningen, (1990)

[2] H.W. den Hartog and J.C. Langevoort, *Phys. Rev. B* **24** (1981), 3547

[3] J. Meuldijk, H.H. Mulder and H.W. den Hartog, *Phys. Rev. B* **25** (1982), 5204

[4] J. Seinen, *Radiation damage in NaCl. The process of colloid formation*, PhD thesis, University of Groningen, (1994)

[5] J.C. Groote, J.R.W. Weerkamp and H.W. den Hartog, *Meas. Sci. Technol.* **2** (1991), 1187-1191

[6] H.W. den Hartog, J.C. Groote and J.R.W. Weerkamp, *Radiat. Eff. & Def. Sol.* **139** (1996), 1-19

[7] V.V. Gann, H.W. den Hartog and D.I. Vainshtein, *Problems of Atomic Science and Technology 2004, 1 Series: Nuclear Physics Investigations*: (42) (2004), 197-199

[8] V.V. Gann, A.V. Sugonyako, D.I. Vainshtein and H.W. den Hartog, *The Energy Deposition Profile of 0.1-3.0 MeV Electrons in NaCl*, Proc.: EPAC, p. 2756, Lucerne, Switzerland, 2004

[9] M.J. Berger and S.M. Seltzer, *Stopping power for electrons and positrons (ICRU-37)*, Washington D.C., (1984)

[10] J. Seinen, J.R.W. Weerkamp, J.C. Groote and H.W. den Hartog, *Phys. Rev. B* **50**: (14) (1994), 9793-9797

[11] V.I. Dubinko, *Experimental investigation of radiation damage in NaCl samples irradiated with gamma rays and electrons*, Report: *STCU #1761, T01 (or T07)*, (2005)

[12] V.I. Dubinko, A.N. Dovbnya, V.N. Borisenko, Yu.T. Petrusenko, V.M. Grytsyna, A.V. Sugonyako, D.I. Vainshtein and H.W. den Hartog, *The Use of Electron Accelerators for Simulation of Radiation Damage in Rock Salt Considered for Safe Storage of Nuclear Waste*, Proc.: The XIX Int. Workshop on Charge Particle Linear Accelerators, Alushta, 2005

[13] GEANT 3, *Detector description and simulation tool*, CERN program library, (1993)

CHAPTER IV

MELTING PROPERTIES OF SODIUM PRECIPITATES

4.1 Introduction

In moderate and high dose-irradiated NaCl samples the amount of metallic sodium and chlorine is usually large enough for detection, using the energy of the phase transition of sodium and chlorine in the precipitates as a probe. By measuring the total latent heat of melting of metallic sodium in the sample we can determine the extent of the damage in the irradiated crystals. The Latent Heat of Melting (LHM) value associated with the melting peak of Na can easily be recalculated into the percentage of radiation-induced metallic sodium.

Moreover, features of the melting and freezing behavior of nano-sized sodium and chlorine precipitates provide information about the properties of sodium-colloids and chlorine-bubbles. The relatively low melting temperature of metallic Na (97.72 ^{o}C) allows us to carry out LH measurements of the sodium colloid system, which does not cause annealing during the measurements. Measurements of Na melting peaks in the temperature range up to 150 ^{o}C are reproducible to high accuracy. This implies that these measurements are non-destructive and they have the advantage that after the LHM measurements the same sample can be used for further analysis.

In this chapter results of latent heat measurements of sodium precipitates are presented, along with a detailed analysis of their thermal properties and the dose and purity dependences. In the previous investigations (see for example [1,2]) thermal analysis of radiolytic Na particles has been carried out for low- and moderately irradiated NaCl samples. The present investigations are devoted to ultra-heavily irradiated samples as the main objects of our observations. The experimental results obtained for the most heavily damaged NaCl samples combined with a comprehensive analysis of the changes in the melting properties of the sodium particles with increasing dose provides insight into the development of the sodium precipitate systems in NaCl under ionizing radiation. Differential Scanning Calorimetry (DSC) was applied to measure the latent heat of melting and freezing of sodium colloids and chlorine bubbles. All measurements have been carried out with a Perkin Elmer DSC-7 instrument.

A typical example of a DCS ‘spectrum’ taken from an ultra-heavily irradiated NaCl sample is shown in figure 4.1. The raw DCS-curve was treated by background subtraction. The melting process appears as a peak in the heat flow curve during a heating run, and freezing can be recognized by the appearance of a dip during a DSC experiment in the cooling mode. The Latent Heat of Melting (LHM) and the Latent Heat of Freezing (LHF) (the energy, which is released during solidification) can easily be determined by calculating the area under the corresponding peak and the dip, respectively. Both the melting and freezing peak for sodium precipitates in the high temperature range and the corresponding ones for chlorine at low temperature are presented in figure 4.1. Obviously, the total amount of sodium produced during irradiation should be the same as the amount of chlorine, because F-centers and H-centers, which are the precursors of Na-colloids and chlorine precipitates, respectively, are produced in equal numbers. However, there could be an exception when a fraction of the

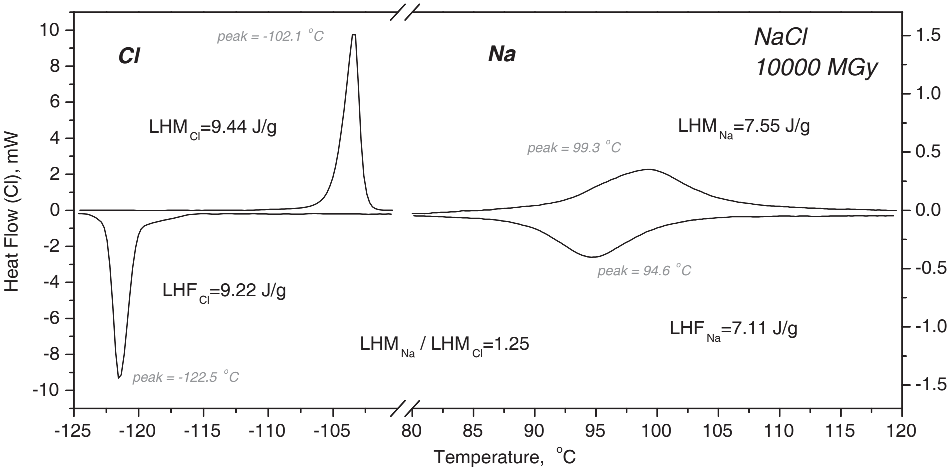

Figure 4.1: The full-range DSC-scan of the 5000 MGy electron-beam irradiated NaCl doped 300 ppm KBF4. The background of raw DSC spectrum was subtracted based on a second-order polynomial fit.

chlorine molecules escapes from the crystal during irradiation, after diffusion to the surface or to open micro-cracks. When the amount of sodium and chlorine is sufficient for detection by means of DSC, and when the numbers of Na and Cl atoms in the precipitates are the same, the LHM ratio should be equal to:

$$\frac{\mathrm{LHM}_{\mathrm{Na}}^{colloid}}{\mathrm{LHM}_{\mathrm{Cl}}^{bubble}} \sim \frac{\mathrm{LHM}_{\mathrm{Na}}^{bulk}}{\mathrm{LHM}_{\mathrm{Cl}}^{bulk}} = \frac{113.1 J/g}{90.3 J/g} \approx 1.25 \tag{4.1}$$

which is in perfect agreement with the results in figure 4.1. A detailed analysis of the LHM ratio of sodium and chlorine in the irradiated samples will be given in the next chapter. Here we will focus on the melting properties of the sodium precipitates.

4.2 Latent heat of melting, the atomic and volume fraction of the precipitates

For the observation the latent heat of melting of radiolytic sodium nano-particles in NaCl a standard procedure has been applied. NaCl samples were heated in a Perkin Elmer DSC-7 calorimeter from 50 to 150 °C at a heating rate of 10 °C/min. We have observed a variety of latent heat peaks in the DSC-curve, which are all associated with melting of the sodium nano-particles. The total LHM value is the sum of each of the individual LHM peaks, which are associated with Na. Here, we assume (i) that the LHM of sodium in nano-particles does not depend on the particle size and (ii) that it is equal to LHM of bulk sodium (see table 4.1).

Table 4.1: The material parameters.

Parameter		*Value*
Molar weight	NaCl, M_{NaCl}	58.442 g/mol
	Na, M_{Na}	22.990 g/mol
	Cl, M_{Cl}	35.453 g/mol
Volume density	NaCl, δ_{NaCl}	$\frac{1}{2\cdot 22.3543}$ at/Å
	Na, δ_{Na}	$\frac{1}{38.19}$ at/Å
	Cl, δ_{Cl}	$\frac{1}{28.016}$ at/Å
Latent Heat of Fusion of 1g	Na, LHM_{Na}	113.09 J/g
	Cl, LHM_{Cl}	90.3 J/g

Simple calculations allow us to estimate the atomic, mass and volume percentage of metallic Na in the sample by measured LHM of sodium.

The mass percentage of Na in the sample can be calculated directly from measured LHM/g value as:

$$m\%_{Na}=\frac{m_{Na}}{m_{Na}+m_{Cl}+m_{NaCl}}=\frac{\mathrm{LHM}_{Na}^{measured}}{\mathrm{LHM}_{Na}^{o}} \tag{4.2}$$

where LHM^{o}_{Na} is the latent heat of fusion of 1 gram pure sodium. Then, with $mol_{Na} = mol_{Cl}$,we have:

$$at\%_{Na}=\frac{N_{at_{Na}}}{N_{at_{Cl}}+N_{at_{Na}}+N_{at_{NaCl}}}=\frac{mol_{Na}}{2mol_{Na}+mol_{NaCl}}$$

and finally:

$$at\%_{Na}=\frac{1}{2-\frac{M_{Na}}{M_{NaCl}}\left(1+\frac{M_{Cl}}{M_{Na}}-\frac{LHM_{Na}^{o}}{LHM_{Na}^{meas.}}\right)}\cdot 100\% \tag{4.3}$$

where M_i is the molar weight of Na, Cl and NaCl respectively.

In the same way we calculate atomic percentage of chlorine in large chlorine precipitates:

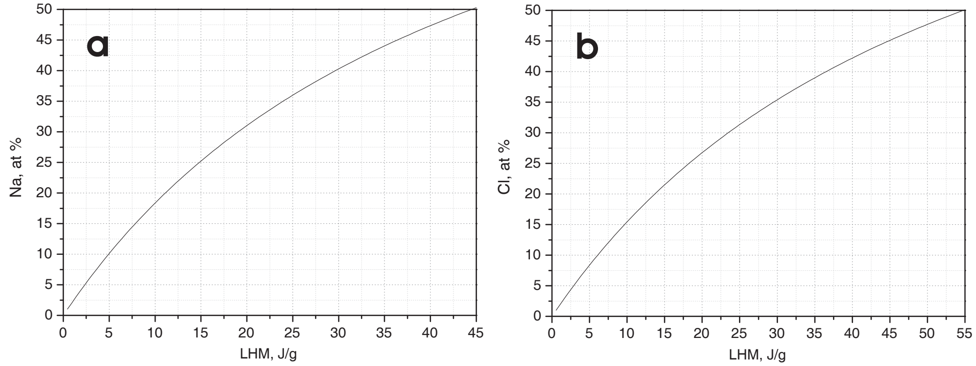

Figure 4.2: The correlations between atomic percentage and the LHM of a) precipitated metallic sodium, b) precipitated chlorine.

$$at\%_{Cl} = \frac{1}{2 - \frac{M_{Cl}}{M_{NaCl}}\left(1 + \frac{M_{Na}}{M_{Cl}} - \frac{LHM^{o}_{Cl}}{LHM^{meas.}_{Cl}}\right)} \cdot 100\% \tag{4.4}$$

The correlation curves between the LHM and the atomic percentages of Na and Cl are presented in figure 4.2, a and b, respectively. Using these calculations we can estimate amount of damage in the NaCl sample as a function of the percentage of the neutral Na and Cl atoms in the originally perfect NaCl matrix. It should be noted that this method yields an atomic percentage, which is lower than real one in the sample, because of presence of single *F*- and *H*-centers and very small sodium and chlorine precipitates, which are 'invisible' in melting experiments and can not be detected by calorimetry.

The volume percentage (or volume fraction) of sodium and chlorine precipitates can be calculated from the corresponding LHM values in a similar way. When δ_i is the volume density of Na, Cl, and NaCl respectively (we have used the material parameters for bulk sodium and solid molecular chlorine, see table 4.1), hence, the following expressions can be written:

$$Vol\%_{Na} = \frac{1}{1 - 2\frac{\delta_{Na}}{\delta_{NaCl}} + \frac{\delta_{Na}}{\delta_{Cl}} + \frac{\delta_{Na}}{\delta_{NaCl} \cdot at\%_{Na}}} \cdot 100\% \tag{4.5}$$

$$Vol\%_{Cl} = \frac{1}{1 - 2\frac{\delta_{Cl}}{\delta_{NaCl}} + \frac{\delta_{Cl}}{\delta_{Na}} + \frac{\delta_{Cl}}{\delta_{NaCl} \cdot at\%_{Cl}}} \cdot 100\% \tag{4.6}$$

The behavior of the LHM as a function of the volume percentage of the Na and Cl precipitates is presented in figure 4.3, a and b, respectively.

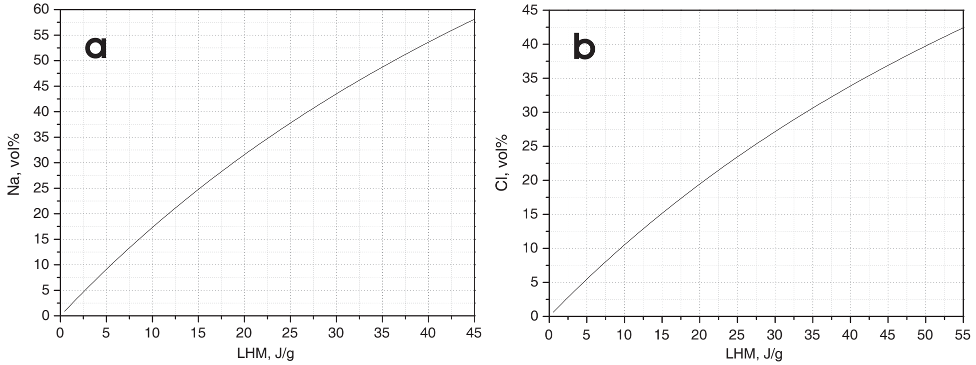

Figure 4.3: The correlations between volume percentage and the LHM of a) precipitated metallic sodium, b) precipitated chlorine.

4.3 The effects of the dose and impurities

In previous investigations, carried out by our group, it has been shown that in most cases impurities enhance the production of radiation damage centers [1-3]. Although the impurity concentration (a few 100 ppm) is much less than the radiolytical defect concentration, impurities often control the defect structure evolution, even for the most heavily irradiated NaCl samples with more than 20 at% metallic Na. Different impurities affect the amount of damage in different ways. Doping with KCl, KBF_4 and NaF leads to an appreciably higher production rate of radiation damage than in most other samples, whereas pure NaCl was quite resistant to ionizing radiation. Usually, the same or even higher resistance to ionizing radiation has been found for samples doped with small amounts of NaBr. For ultra-high doses (e.g. 20000 MGy) we have found that the radiation resistance of NaCl:Br was far better than for pure NaCl. At the same time in other heavily damaged materials (NaCl:KCl, NaCl:KBF_4) instantaneous exothermal back reactions are observed, resulting in instant transformation of the radiolytical Na and Cl into NaCl. Depending on the amount of damage and the organization of the defect structure these reactions may cause localized cracks in the sample (see *chapter VII*) or even lead to explosive decomposition of the irradiated material. The explosive reactions in irradiated NaCl have been described in detail in [4-7].

Irradiation up to ultra-high doses of e.g. 20000 MGy (2000 GRad) has shown that the differences persist for the most heavily damaged samples and some new features appear. It is the purpose of this section to investigate the effects of ultra-high doses up to 20000 MGy, which should be compared with the results obtained for 3000 MGy reached in the previous investigations carried out by our group [1-3]. This implies that the focus in this section will be at (i) the behavior of damage formation in the range of ultra-high doses and (ii) the effects caused by the presence of impurities.

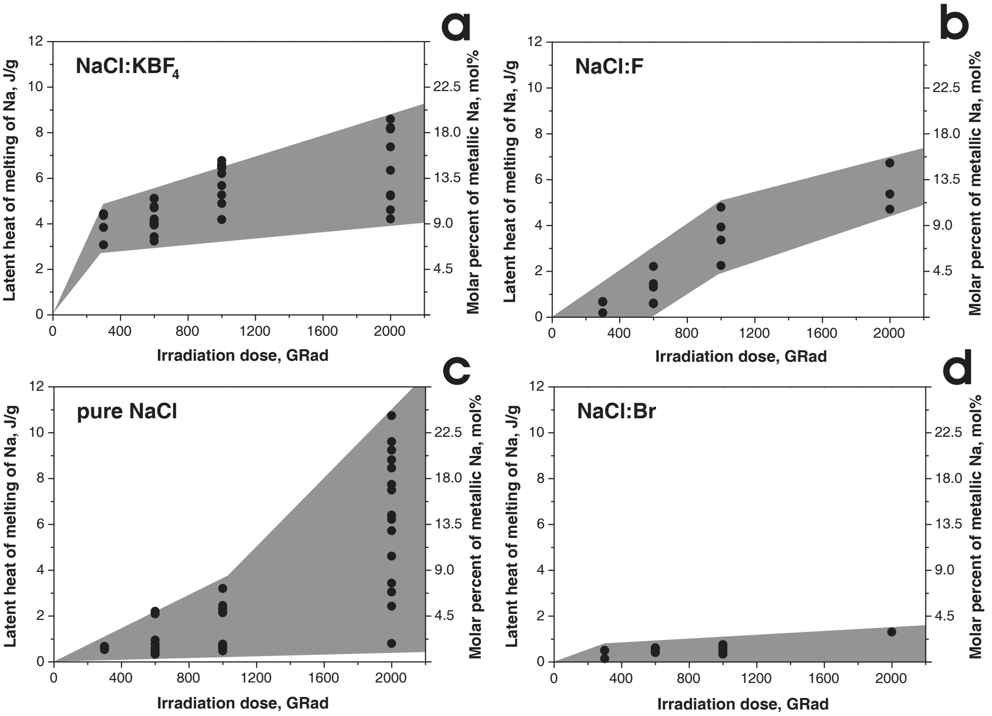

Figure 4.4: The LHM and the amount of metallic sodium inside NaCl crystals as a function of the irradiation dose. a) NaCl doped with 300ppm KBF$_4$, b) NaCl doped with 1000ppm NaF, c) nominally pure, and d) NaCl doped with 400ppm NaBr.

The efficiency of the production of radiolytic defects depends on the irradiation temperature, as shown in [3]. We have irradiated the samples at about 100 ºC to doses in the range 3000-20000 MGy (300 – 2000 GRad) in order to produce the most heavily damaged samples. We have applied a high-energy electron beam (0.5 MeV) as the irradiation source (see *chapter III*). The results of latent heat measurements of Na particles in heavily irradiated NaCl samples with various impurities are shown in figure 4.4. The LHM/dose dependencies up to ultra-high irradiation doses are presented.

In previous investigations [4,8-11] of heavily damaged NaCl samples doped with 1000 ppm KCl it has been shown that the presence of small amounts of this impurity enhances the formation of radiation damage dramatically. However, in the past we have also found that at very high doses the production of the usual forms of radiation damage in these materials (i.e. Na and Cl precipitates) is limited, because heavily damaged NaCl:K crystals are highly unstable. With increasing irradiation dose, i.e. with increasing amount of damage, more and more samples were destroyed and transformed sometimes into dust due to violent back reactions taking place during the irradiation run. For this type of samples the amount of radiolytic Na as a function of dose increases rapidly and usually it is impossible to produce very heavily damaged NaCl:K samples, because for doses higher than 2000 MGy (200 GRad) almost all samples were destroyed completely (for this reason no plot has been presented in figure 4.4 for NaCl:KCl).

For NaCl doped with 300ppm KBF_4 the efficiency of the damage formation process is very high in the early stage of irradiation. The radiolytical defect production rate is very high up to 300 GRad, and after that it drops to a substantially lower value, while the amount of metallic sodium keeps increasing almost linearly, without saturation. Even at the maximum dose of 20000 MGy (2000 GRad) the scatter of the data points is moderate (compared to several other samples); see figure 4.4a. It is remarkable that for samples with a very large amount of metallic sodium (~20 mol%) we have observed only in a few cases evidence for explosive reactions, which are initiated sometimes during the DSC-run by heating the sample to 150 ºC (see figure 4.5 for an illustration of the explosive reaction during heating). Probably, the reason for the increased stability of heavily irradiated NaCl:KBF_4 compared with NaCl:KCl should be found in the geometrical properties of the systems consisting of metallic nano-particles in combination with the chlorine nano-bubbles and vacancy voids.

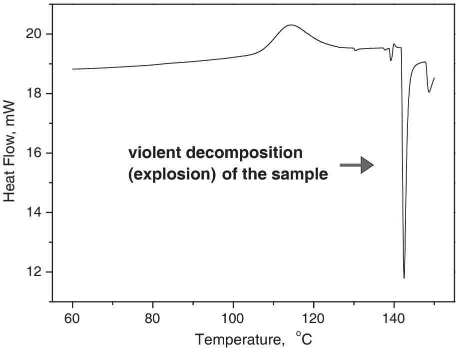

Figure 4.5: The DSC-scan of 3.000 MGy irradiated sample with explosion at about 140 ºC.

For the samples, doped with 1000ppm NaF the amount of damage associated with sodium nano-particles increases more slowly than for NaCl:KBF_4 and the dispersion of the LHM values and the corresponding percentages of metallic Na and chlorine are almost the same for the full dose range.

Among all ultra-heavily irradiated samples, which have been investigated up to now, nominally pure NaCl shows the most interesting results. The slope of the plot of the LHM of Na vs the dose is less than for NaCl:F and NaCl:KBF_4 up to about 10000 MGy (1000 GRad). Beyond this dose the amount of metallic sodium in pure NaCl increases steeply and reaches values of about 20 mol% at 20000 MGy (2000 GRad). There are two possible reasons for the appearance of these large concentrations of metallic Na and Cl, which increase without any sign of saturation. The first possible explanation is, that at very high concentrations chlorine can escape very easily from the sample during the irradiation run. However, this is not the case. As we will see below, low-temperature DSC measurements of chlorine inclusions yield within the accuracy of the measurements approximately the same numbers of precipitated chlorine and sodium atoms. The second explanation for the observations is that with increasing amount of damage the probability for back reactions to occur is reduced. This may occur as a result of self-organization of the Na colloids and Cl bubbles and the other forms of radiation damage in these heavily damaged crystals, such as dislocations, dislocation loops, dislocation forests and pile-ups, etc and vacancy voids. The situation might be similar to metals and alloys, where it is well-known, that dislocations are frequently decorated with a high density of small clusters of self-interstitial atoms in the form of dislocation loops (see for example [12,13]).

An important feature of the results for pure NaCl is that the scatter of the data is very large – for samples with 20000 MGy the scatter is one order of magnitude. Our explanation for the wide scatter is that in the absence of impurities other defects such as dislocations, grains boundaries and strain fields in the crystal play an important role in the formation and evolution of defect system [14-18]. The concentrations of these kinds of defects depend on the mechanical strain, produced in some of the steps in preparation procedure, e.g. grinding and polishing (see *chapter III*). Therefore in principle the variations in the observations for ultra-heavily damaged, pure NaCl might be caused by differences in the stress and strain situation within the samples or by small sample-to-sample variations of the amount of dislocations. Also this could be a consequence of the fact that the impurity concentrations in nominally pure NaCl (which should be only traces in this type of samples) vary from sample to sample.

Our experimental results show that the presence of small amounts of NaBr has a significant effect on the radiation resistance of NaCl in particular for ultra-high doses. The amount of precipitated Na in the 400ppm NaBr doped samples remains less than 4 mol% even for samples exposed to a ultra-high dose of 20000 MGy (2000 GRad). We note that this concentration is almost one order of magnitude less than the concentration of metallic Na for samples with any other impurity, which were irradiated under these conditions.

4.4 On the shape and position of the melting peaks

The shapes of the melting peaks and the temperature positions of the maxima of the peaks deviate strongly from the shape and position observed for bulk sodium, with its melting temperature of $T_m^0 = 97.72$ °C. Two relatively narrow peaks at fixed temperatures are observed for all samples irradiated up to low and moderate doses (a few MGy): peak I at 82±2 °C and peak II at 92±2 °C. The width of both peak I and II is typically in the range 3-5 °C. If we continue the irradiation, the third melting peak (Peak III) appears at 100-110°C, which is above bulk sodium melting temperature T_m^0. Peak III is quite broad, the width of this peak is usually several times that of peak I and II.

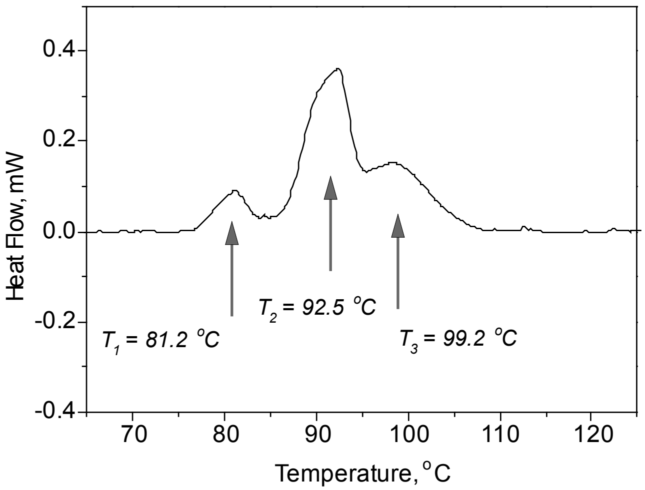

Figure 4.6: The DSC-scan of 1500 MGy irradiated sample showing all three melting peaks of sodium precipitates.

The intensity ratio of peak I, II, and III depends on the irradiation dose and the presence of impurities; its behavior is described in detail in [2]. For low irradiation doses (the exact dose value varies for different samples, because it depends on the presence of impurities and the irradiation temperature) only peak I and II are observed and peak I is dominant. With increasing dose peak II increases compared to peak I, and ultimately it exceeds the latter one. Then, at still higher doses peak III is observed. Peak III is the dominant one in the ultra-high dose range, and peak I and II disappear completely beyond some dose. This is not due to overlapping of peak I and II by peak III, or to the overwhelming intensity of peak III. Here, we are obviously dealing with the transformation of particles, associated with peak I and II, to the particles, giving rise to peak III.

Although the dominant LHM peak of Na in very heavily damaged NaCl is usually located around 100-110°C, we have found in several cases that this peak is located at 120-140°C. LHM peaks in the latter temperature range are significantly wider than the peaks in the range 100-110°C, observed in many other samples. We have found evidence for the existence in several samples of nano-particles of metallic Na, which show a LHM peak well beyond 140°C (e.g. 160°C and possibly even higher). When these samples are annealed during 30 min at 180°C the LHM peak, which could not be observed in as irradiated samples, is observed at temperatures around 100°C. This suggests that during annealing the nano-structured radiolytic Na-metal is modified, which leads to a large shift of the LHM peak to lower temperatures and appreciable narrowing of the peak. In addition, for some ultra-heavily irradiated samples several high-temperature peaks, with properties similar to those of peak III, can be observed located far beyond 97.72 °C. All superheated peaks are wide and in some cases they can not be distinguished clearly from the background. The DSC-scan showing all three melting peaks of sodium precipitates has been presented in figure 4.6.

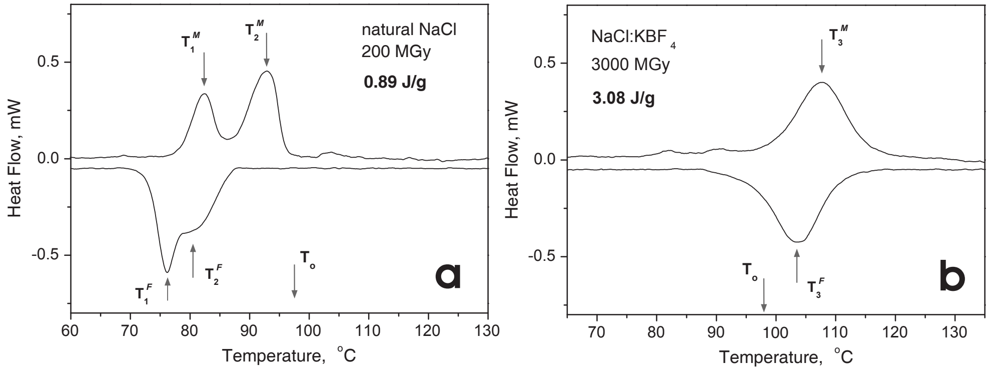

Figure 4.7: (a) The DSC-scan of a 100 MGy, electron-beam irradiated natural NaCl. Clearly defined two energy peaks are presented in both heating and cooling regimes. Temperatures of the melting peaks are: T^M_1=82.40 °C, T^M_2=92.87 °C, freezing peaks: T^F_1=76.05 °C, T^F_2=80.56 °C, T_0= 97.72 °C is the bulk melting temperature of sodium.
(b) The DSC-scan of the 1500 MGy, electron-beam irradiated NaCl doped with 300 ppm KBF_4. The temperature position of the superheated peak is: T^M_3=107.83 °C in heating regime and T^F_3=103.63 °C in cooling regime, T_0= 97.72 °C is the bulk melting temperature of sodium. The width of the peak is about 10 degrees, measured at half-height.

It should be mentioned, that the bulk sodium melting peak has been observed for irradiated NaCl crystals with a small and real excess amount of sodium only after long term irradiation and subsequent annealing at temperatures >500 °C by Groote and Weerkamp [1]. This peak is positioned at approximately bulk sodium melting temperature T_m^0 and it is very narrow compared with peaks I-III.

Let us additionally take into consideration the freezing counterparts of the melting peaks I, II and III. The peak onset values (which can be evaluated by extrapolating the leading edge of the peak of the heat-flow signal curve (corrected by background subtraction) back to the temperature value where the first sign of the presence of the latent heat peak appears) for peak I and II were found 20 and 10 degrees below the bulk melting temperature, respectively (figure 4.7a). The corresponding freezing peaks show the same onset temperatures within experimental accuracy. It seems that the observed change in intensity relation between peak I and II in the cooling run is simply due to an increased broadening of the type II freezing peak compared with the corresponding melting peak, combined with overlapping of peak II with the freezing peak I. To verify this conjecture we have carried out an additional experiment. The melting process was stopped just after passing the first peak, and then the sample was cooled down. The parameters like surface area under the peak, the height and width of the measured freezing peak were found to be the same as for the melting one within the accuracy of the measurement.

The high-temperature peak III (figure 4.7b) has its onset situated several degrees above the bulk melting temperature, i.e. $T_m > T_0$ for the particles associated with this peak. The onset of the freezing peak III is located at typically 10 ºC higher temperatures than during melting. It appears that here $T_m > T_f$. Unlike peak II but like peak I, the freezing and melting peak III have about the same shape.

Melting of embedded small particles

Let us consider the observed effects during melting of the sodium nanoparticles in terms of a model of finite-size particles embedded in the surrounding matrix. The Gibbs free energy of the solid and liquid phases may be written as

$$G_S = V_S\left(E_S + G_v^S\right) + A_S\gamma_{SM}$$
$$G_L = V_L\left(E_L + G_v^L\right) + A_L\gamma_M \tag{4.7}$$

where the subscripts and superscripts S and L refer respectively to the solid and liquid phases. V is the volume and A is the surface area of the particle, E is the average strain energy, G_v is the free energy per unit volume of bulk phase, and γ is the particle-matrix interfacial free energy.

Using the next expression for small undercooling/superheating ΔT:

$$\Delta G_v = \frac{L\Delta T}{T_m} \tag{4.8}$$

the change in Gibbs free energy associated with melting of the solid sphere may be expressed as

$$\Delta G = 4\pi r^2\left(\gamma_{LM} - \gamma_{SM}\right) + \frac{4}{3}\pi r^3\left(\frac{L\Delta T}{T_m^0} + \Delta E\right) \tag{4.9}$$

where ΔE is the change in the strain energy caused by melting, L is the latent heat of melting, T_m^0 is the equilibrium melting temperature. The volume change caused by melting is neglected. With the criterion that the free energy change due to melting $\Delta G = 0$, we find the following expression for the melting temperature

$$\frac{T_m}{T_m^0} = 1 - \left[3\frac{(\gamma_{SM} - \gamma_{LM})}{r} - \Delta E\right] \Big/ L \tag{4.10}$$

Due to the significant difference in lattice constant of NaCl and sodium, the Na precipitate lattice is ‘stretched’ by surrounding matrix, i.e. the solid Na particle shows a negative size misfit compared to the NaCl matrix. Assuming that the liquid particle has no or very small size misfit, the change of the strain energy on melting $\Delta E = E_L - E_S$ is negative[1], which causes the melting temperature T_m to decrease. As it has been suggested in [2,21], sodium precipitates may exist in two different structural states in the NaCl matrix. It is likely that the surrounding NaCl-matrix forces the small sodium particles to retain the *fcc* lattice of the Na-sublattice. When the small particle grows, its lattice or eventually the structure of the central part of the particle transforms into the *bcc* lattice structure of bulk Na. The size misfits are about -7% for *fcc* and -4% for *bcc* particles [2]. Hence, melting peak I, which has a lowest melting temperature, below bulk sodium melting temperature T_m^0, may correspond to the first-nucleated *fcc*-particles, which are large enough to exhibit melting behavior. Peak II, which grows with increasing of the amount of sodium, may be associated with larger particles, which are (partly) transformed into the *bcc* structure. A similar reasoning has been used in [21] in developing the phenomenological melting model (see also *chapter VI*).

In order to calculate the second term in equation 4.10 the values of the interfacial energies should be estimated. At this moment, there is no information available for the sodium-sodium chloride interfacial energy, but the following consideration might be helpful. It has been assumed, that the solid sodium precipitate has an outer layer, which is in the *fcc* state, while the particle-matrix interface is coherent. This leads to a relatively low value for the interfacial energy γ_{SM}. The interfacial energy in the liquid state can be estimated from the contact angle of a liquid sodium drop on a freshly cleaved NaCl surface. Then $\gamma_{LM} = \gamma_{MV} - \gamma_{LV}\cos\theta$, where θ is the contact angle, subscripts *M, L* and *V* refer to the NaCl matrix, liquid Na and Na vapor respectively. According to [2] the contact angle $\theta \approx 130^o$ and the liquid Na-NaCl interface energy γ_{LM} is estimated to be about twice of the liquid Na surface energy $2\gamma_{LV} = 200$ mJ/m^2 [22], which implies that $\gamma_{LM} \approx 400$ mJ/m^2. This is assumed to exceed γ_{SM} (according to [23], in general coherent interfacial energies range up to about 200 mJ/m^2). Thus, the difference in interfacial energy caused by melting of sodium precipitates is negative, which causes the melting temperature T_m to increase. Since the interfacial energy term in equation 4.10 is inversely proportional to the particle radius, the melting temperature for small particles is expected to increase.

We have observed that the melting peak above bulk sodium melting temperature T_m^0 grows with increasing amounts of metallic sodium. This can be explained if in the advanced stages of the irradiation the sodium precipitates are converted into very small particles or structures with ultrafine surface irregularities (where the strain energy E might be negligible). This explanation is supported by the vanishing melting peaks I and II in very heavily irradiated NaCl crystals. At the same time one-dimensional structures of fine metallic particles in heavily-irradiated NaCl samples have been revealed in ESR and AFM studies (see *chapters VI* and *VIII*). These modifications in the distribution of Na particles sizes are expected to lead to a significant broadening of melting peak III.

In the experiments of heavily irradiated samples [24] it has been found that peak III shifts during annealing at 180 °C almost to the position of peak II and ultimately peak I without

---

[1] Elasticity calculations for embedded particles [19,20] give ΔE proportional to the difference of misfit squares in the solid and liquid state $\Delta E \approx \varepsilon_L^2 - \varepsilon_S^2$.

significant loss of metal. This has been explained by short distance rearrangements of the surface of the particles (or structures) during annealing, when the finest details of the surface are annealed out [2]. We expect that with decreasing surface curvature the melting temperature decreases.

4.5 Moderately irradiated NaCl: electron and gamma irradiation

For applications, such as storage of high level nuclear waste in natural rock salt formations, the resistance of NaCl to different types of ionizing radiation is important. Because of the large penetration depth of gamma irradiation emitted by high level waste from nuclear power facilities, the resistance to this type of irradiation is important for practical applications.

Most of the samples investigated in this thesis have been irradiated by means of an electron beam of either 0.5 or 1.35 MeV. This irradiation source is very convenient and flexible for research of radiation damage in ionic materials. The maximum uniform dose rate over a surface area of 18×18 cm^2 reached with our irradiation facility is 10 MGy/hr (1000 MRad/hr). This is the reason why electron irradiation was used to study the most advanced stages of radiation induced defect formation (up to doses of 20000 MGy, or 2000 GRad). It is clear that with gamma irradiation the maximum doses, which can be reached under practical laboratory conditions, are much lower than for electron irradiation, because the maximum achievable laboratory dose rates are much lower in case of gamma irradiation. As a result, the irradiation run with γ-doses up to 750 MGy (75 GRad) lasted about two months, while the same dose is reached in our electron beam facility within one week. A disadvantage of the gamma irradiation carried out in the framework of this investigation is that due to the very long irradiation runs, the experiments had to be interrupted many times to allow other applications of the irradiation facility or maintenance. In this section we want to compare the features and the differences of the composition of radiolytic extended defects created by gamma and electron irradiation.

We have investigated gamma-irradiated NaCl samples by means of DSC to compare the latent heat effects of extended defects, created by two types of ionizing irradiation: gamma and electron irradiation. The gamma irradiation procedure is described in detail in *chapter III*. We have investigated four sets of samples with different impurities irradiated up to a maximum dose of 75 Grad: i) NaCl doped with 300ppm KBF$_4$, ii) NaCl doped with 1000ppm KCl, iii) NaCl with 100 ppm NaBr and iv) nominally pure NaCl. During the irradiation run the samples were kept at 100 ^{o}C. The measurements of the latent heat of melting yield small LHM values even for the most heavily irradiated samples of the last two sets. The LHM values less than 0.1 J/g were found very close to the noise level in these measurements.

The LHM measured for KCl and KBF$_4$ doped samples are presented in the two plots given in figure 4.8, showing the LHM/dose dependences for both gamma and electron irradiated crystals. It can be seen from the plots in figure 4.8 that the LHM of Na colloids (which is

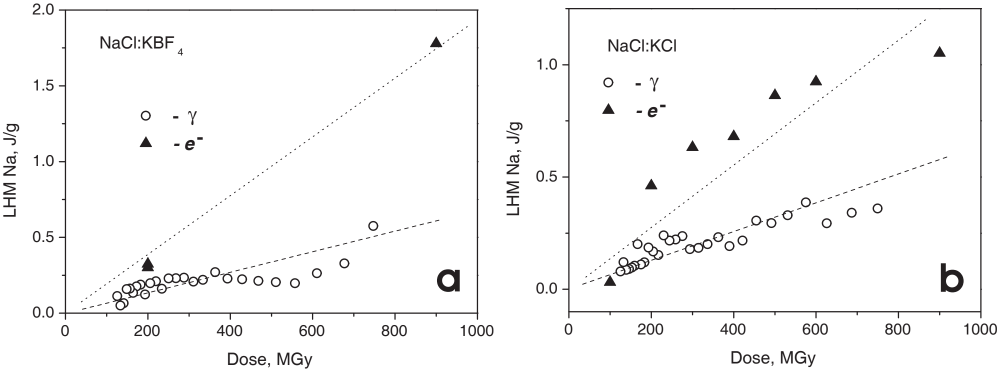

Figure 4.8: The LHM of metallic sodium particles inside NaCl crystals irradiated by gamma and electron beam. a) NaCl doped with 300ppm KBF_4, b) NaCl doped with 1000ppm KCl

proportional to the sodium precipitates volume fraction) produced by gamma irradiation at the maximum absorbed dose of 750 MGy is lower than that produced by electron irradiation by a factor of two. However, the dose rates for electron and gamma irradiation for these samples differ by a factor of 4 (2.4 MGy/hr in electron irradiation and 0.6 MGy/hr in gamma).

It has been observed experimentally by den Hartog et al. [3], that the total amount of damage, accumulated in the irradiation procedure, depends on the sample temperature during irradiation. These temperature dependencies of the sodium precipitates volume fraction in NaCl have a characteristic bell-shaped form. According to the theoretical models [14-18,25-33], this dependence calculated at different dose rates shifts to higher temperatures with increasing dose rate. The latest model calculations provided by Dubinko et al. [34] give the next dependencies, presented in figure 4.9. As both electron and gamma irradiation procedure were carried out at the same temperature of 100 °C, the experiments at different dose rates correspond to different points of the above mentioned bell-shaped curves. Hence, we can conclude that the observed difference in sodium precipitates production may be explained by the difference in the dose rates rather than the irradiation type.

We have compared the shape of the DSC-curves of gamma irradiated samples with similar ones observed after electron irradiation. These experiments provide information about eventual differences between gamma-generated sodium nano-particles and the ones obtained as a result of electron-irradiation. In figure 4.10 two typical DSC-curves, observed for gamma-irradiated NaCl, are shown. These plots have been obtained for gamma irradiated NaCl:KCl and NaCl:KBF_4 crystals in the high-dose range (531.4 and 470.7 MGy, respectively). The background of the raw DSC spectrum was approximated by a second-order polynomial fit to the measured data of the heat-flow signal in sections sufficiently far away from the latent heat peaks of interest. In order to obtain the latent heat peaks the background was subtracted from the raw signal. Comparison of gamma-irradiated samples DSC spectra with those for electron-irradiated NaCl gives the shapes of the peaks of the latent heat spectra and their positions are about the same, independently of irradiation type. (The variety of DSC-spectra of electron-irradiated NaCl with irradiation temperature, dose and impurity dependences can be found published, for instance, in [2]).

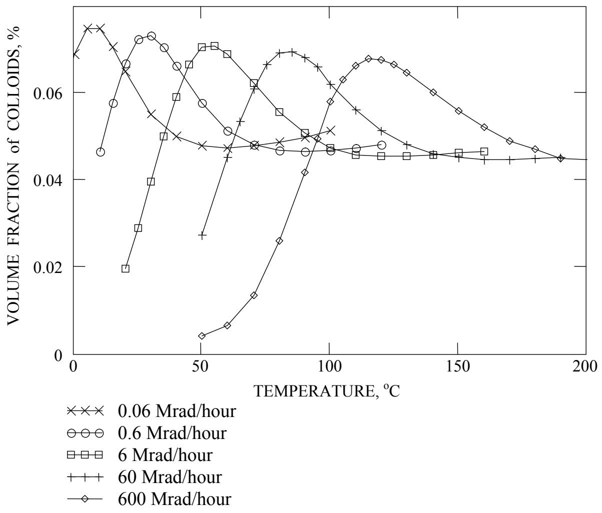

Figure 4.9: The temperature dependence of the sodium precipitates volume fraction in pure NaCl calculated at different dose rates for the total absorbed dose of 10 MGy.

Therefore, on the basis of this analysis, we can conclude that the same composition of extended defects exists for gamma-irradiated samples and electron-irradiated ones. This similarity proves the applicability of the results of our investigation using a high-energy electron beam to simulate practically relevant situations such as a storage site with high-level nuclear waste, where one is dealing with predominantly exposure to gamma's.

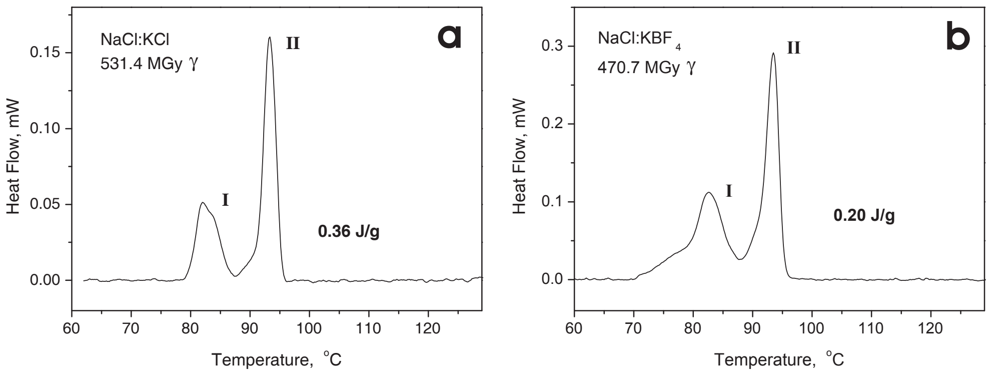

Figure 4.10: The DSC-scan of the NaCl crystals irradiated by gamma and electron beam. a) NaCl doped with 1000ppm KCl, b) NaCl doped with 300ppm KBF_4.

4.6 Conclusions

The energy of the phase transition of sodium serves as a good probe for measuring the amount of precipitated sodium in the irradiated NaCl crystal. A comparison of the latent heat of melting of bulk sodium with the experimentally measured energy, absorbed during melting of the precipitates in the irradiated sample allows us to calculate the percentage of the metallic sodium in the damaged NaCl matrix. The results, obtained in the calorimetry experiments have shown that the amount of precipitated sodium in the irradiated NaCl crystals increases continuously with the dose. This is the general trend for all of the NaCl samples; however in samples with different impurities the rate of the radiolysis process varies. For example, the radiolysis process is slowed down appreciably in Br-doped NaCl, and the percentage of precipitated sodium increases significantly in K and KBF_4 –doped crystals compared to pure NaCl samples. There is only exception for pure NaCl, irradiated up to 20000 MGy (2000 GRad), which is the highest dose reached in our investigation – the amount of metallic sodium in these samples increases steeply and reaches the highest values among all investigated NaCl samples. No saturation of the amount of precipitated Na in the sample with irradiation dose increasing has been observed for any of the different types of NaCl samples.

The appearance of a wide melting peak at temperatures higher than the bulk sodium melting temperature, which is a characteristic feature of the heavily irradiated samples, suggests that the curvature of the interface between Na particles and the host matrix is very high. It has led us to the conclusion, that in advanced stages of the irradiation the sodium precipitates are converted into very small particles or structures with ultra fine surface irregularities.

References

[1] J.C. Groote and J.R.W. Weerkamp, *Radiation damage in NaCl. Small particles*, PhD thesis, University of Groningen, (1990)

[2] J. Seinen, *Radiation damage in NaCl. The process of colloid formation*, PhD thesis, University of Groningen, (1994)

[3] H.W. den Hartog, J.C. Groote and J.R.W. Weerkamp, *Radiat. Eff. & Def. Sol.* **139** (1996), 1-19

[4] D.I. Vainshtein and H.W. den Hartog, *Radiat. Eff. & Def. Sol.* **152** (2000), 23-37

[5] A.A. Turkin, V.I. Dubinko, D.I. Vainshtein and H.W. den Hartog, *J. Phys.: Condens. Matter.* **13** (2001), 203-216

[6] H.W. den Hartog, D.I. Vainshtein, V.I. Dubinko and A.A. Turkin, *Nucl. Instr. and Meth. in Phys. Res.* **B 191** (2002), 168-172

[7] A.A. Turkin, V.I. Dubinko, D.I. Vainshtein and H.W. den Hartog, *Nucl. Instr. and Meth. in Phys. Res.* **B 191** (2002), 83-88

[8] H.W. den Hartog and D.I. Vainshtein, *Mater. Sci. Forum.* **239-241** (1997), 611-614

[9] D.I. Vainshtein, C. Altena and H.W. den Hartog, *Mater. Sci. Forum.* **239-241** (1997), 607-610

[10] D.I. Vainshtein, V.I. Dubinko, A.A. Turkin and H.W. den Hartog, *Radiat. Eff. & Def. Sol.* **150** (1999), 173-177

[11] D.I. Vainshtein, V.I. Dubinko, A.A. Turkin and H.W. den Hartog, *Nucl. Instr. and Meth. in Phys. Res.* **B 166-167** (2000), 550-555

[12] N.M. Ghoniem, B.N. Singh, L.Z. Sun and T. Diaz de la Rubia, *J. Nucl. Mater.* **276** (2000), 166-177

[13] H. Trinkaus, B.N. Singh and A.J.E. Foreman, *J. Nucl. Mater.* **251** (1997), 172-187

[14] A.E. Hughes, *Radiat. Eff. & Def. Sol.* **2** (1978), 57-76

[15] U. Jain and A.B. Lidiard, *Phil. Mag.* **35** (1977), 245-259

[16] A.B. Lidiard, *Comments Solid State Phys.* **8** (1978), 73

[17] A.B. Lidiard, *Phil. Mag.* **39** (1979), 647-659

[18] A.E. Hughes and S.C. Jain, *Advances in Phys.* **28**: (6) (1979), 717-828

[19] N.F. Mott and F.R.N. Nabarro, *Proc. Phys. Soc. Lond.* **52** (1940), 86

[20] F.R.N. Nabarro, *Proc. Phys. Soc. Lond.* **52** (1940), 90

[21] A.V. Sugonyako, D.I. Vainshtein, A.A. Turkin, H.W. den Hartog and A.A. Bukharaev, *J. Phys.: Condens. Matter.* **16** (2004), 785-798

[22] A.R. Miedema and J.A. den Broeder, *Z. Metallkde.* **70** (1979), 14

[23] D.A. Porter and K.E. Easterling, *Phase Transitions in Metals and Alloys*, (1992)

[24] J. Seinen, D.I. Vainshtein, H.C. Datema and H.W. den Hartog, *J. Phys.: Condens. Matter.* **7** (1995), 705-716

[25] V.I. Dubinko, A.A. Turkin, D.I. Vainshtein and H.W. den Hartog, *Radiat. Eff. & Def. Sol.* **150** (1999), 145-149

[26] V.I. Dubinko, A.A. Turkin, D.I. Vainshtein and H.W. den Hartog, *J. Appl. Phys.* **86**: (11) (1999), 5957-5960

[27] V.I. Dubinko, A.A. Turkin, D.I. Vainshtein and H.W. den Hartog, *Nucl. Instr. and Meth. in Phys. Res.* **B 153** (1999), 163-166

[28] V.I. Dubinko, A.A. Turkin, D.I. Vainshtein and H.W. den Hartog, *J. Nucl. Mater.* **277** (2000), 184-198

[29] V.I. Dubinko, A.A. Turkin, D.I. Vainshtein and H.W. den Hartog, *Nucl. Instr. and Meth. in Phys. Res.* **B 166-167** (2000), 561-567

[30] V.I. Dubinko, A.A. Turkin, D.I. Vainshtein and H.W. den Hartog, *J. Nucl. Mater.* **289** (2001), 86-95

[31] D.I. Vainshtein, V.I. Dubinko, A.A. Turkin and H.W. den Hartog, *Radiat. Eff. & Def. Sol.* **156** (2001), 51-57

[32] V.I. Dubinko, A.A. Turkin, D.I. Vainshtein and H.W. den Hartog, *J. Nucl. Mater.* **304** (2002), 117-128

[33] V.I. Dubinko, D.I. Vainshtein and H.W. den Hartog, *Radiat. Eff. & Def. Sol.* **158**: (10) (2003), 705-719

[34] V.I. Dubinko, A.N. Dovbnya, V.N. Borisenko, Yu.T. Petrusenko, V.M. Grytsyna, A.V. Sugonyako, D.I. Vainshtein and H.W. den Hartog, *The Use of Electron Accelerators for Simulation of Radiation Damage in Rock Salt Considered for Safe Storage of Nuclear Waste*, Proc.: The XIX Int. Workshop on Charge Particle Linear Accelerators, Alushta, 2005

CHAPTER V

MELTING AND FREEZING OF CHLORINE BUBBLES

5.1 Introduction

Bubbles of halogen gas atoms are formed in irradiated alkali halide crystals as a result of agglomeration of *H*-centers. Halogen gas bubbles are the counter part of the other radiolytic product, sodium colloids, which are agglomerates of *F*-centers. Because of the accumulation of *H*-centers, which are in fact interstitial chlorine atoms, halogen bubbles occupy interstitial positions in the crystalline matrix. Similar systems of gas bubbles at interstitial positions of the crystalline matrix exist in metals after implantation of noble gas atoms [1-4]. The gas atoms in these bubbles are usually present under abnormal conditions (see for instance [3]). Transmission microscopy, spectroscopy and thermal analysis are helpful techniques in the investigations of these intricate objects. Vom Felde et al [2] have studied several rare gas bubbles in Al by means of electron-energy-loss spectroscopy (EELS) and transmission electron microscopy (TEM). It was concluded that at room temperature Ne bubbles are in the liquid state whereas Ar and Xe bubbles are solid. When the bubbles are in the solid state, it is possible to monitor the melting behavior by heating the samples to sufficiently high temperatures. Rossouw and Donnelly [3] have observed with electron microscopy melting of solid Ar bubbles in their implanted Al samples at 730 K, which should be compared with the equilibrium bulk melting temperature of 250 K. In addition to these observations, investigations carried out by Andersen et al [1] on implanted Al-Kr by means of combination of XRD (X-ray diffraction) and RBS (Rutherford Backscattering) have shown that a dual size distribution of Kr bubbles exists. These inclusions were found to be solid in a wide range of temperatures. After annealing the samples at 620 K the larger bubbles with an average size of 9 nm show melting related phenomena in the vicinity of the bulk melting temperature (116 K at 0.72 bar). The pressure in these annealed bubbles is approximately equal to the ambient pressure. The smaller bubbles with an average size of 3.5 nm were found to remain in the solid state during heating to at least 620 K. The pressure in these bubbles was estimated to be about 10-20 kbar (1-2 GPa) [1].

Other systems of confined materials, which demonstrate extraordinary melting behavior, are gases and liquids, which are embedded in porous matter. Various independent experimental techniques have been used to obtain information about these interesting inclusions [5-8]. In porous samples one is dealing with connected nano-pores filled with for instance condensed systems consisting of rare gas atoms, which were transported along these pores until they reached saturation concentrations everywhere in the sample. It is well established that the freezing and melting points of a variety of materials, among which cryogenic liquids, water and metals are reduced considerably when these materials are embedded in nano-sized pores. The downward shift of the freezing temperature of confined materials increases with decreasing pore size [8]. Phase transition experiments also demonstrate appreciable temperature hysteresis between the melting and solidification processes. In addition, measurements of the specific heat of gas inclusions in both the heating and cooling mode show large differences between the latent heat of melting and the corresponding value for freezing [5-7].

The difference between these porous samples on one hand and heavily damaged NaCl with chlorine and the samples with implanted rare gas bubbles on the other hand is that the bubbles in the latter samples are closed individual systems which are isolated from each other. However, similar tendencies of the temperature hysteresis and difference in the specific heat in melting and solidification processes are found in both cases.

The DSC-spectra of heavily irradiated NaCl samples, taken in wide range of temperatures from -150 ºC (123 K) up to 150 ºC (423 K), show a single well-defined melting peak at about -102 ºC (171 K) in addition to the sodium melting peaks at high temperatures, which have been presented and discussed in the previous chapter. Because the Low-Temperature peak (LT-peak) is observed close to the melting point of bulk chlorine (-101.5 °C or 171.5 K), it is natural to associate this peak with the liquid-to-solid phase transition of chlorine, which is accumulated in the bubbles. At the same time direct X-ray diffraction measurements at low temperature have confirmed the presence of solid chlorine inclusions in heavily irradiated NaCl [9]. The fact, that we have not observed any evidence for specific heat effects associated with condensation or evaporation of chlorine in the bubbles population, indicates that the pressure in the chlorine bubbles should be higher than the critical value for chlorine (i.e. 76 bar); the chlorine in these bubbles is expected to be in the liquid state. A more detailed study of the phase transition of chlorine bubbles reveals several interesting details, which are discussed below.

5.2 LHM of chlorine and sodium precipitates

The atomic concentration of radiolytic chlorine and sodium, in irradiated NaCl crystals, should be the same, because during radiolysis equal numbers of atomically dispersed *F* and *H*-centers are produced. This leads to a proportional relationship between the LHM of chlorine and the corresponding sodium values. The above-described relationship yields a ratio of the LHM_{Na} and LHM_{Cl}, which is equal to 1.25 (see equation 4.1 in the previous chapter). However, in early stages of the irradiation experiment, when the concentration of metallic Na is equal to about 1 mol% or less, the latent heat of melting of chlorine is much smaller than expected on the basis of the amount of metallic Na calculated from the corresponding LHM peak. The graph showing the relationship between $LHM_{Na}^{colloid}$ and LHM_{Cl}^{bubble} is presented in figure 5.1 and shows that there are three different ranges from relatively low up to heavily irradiated samples [10,11].

(i) For LHM_{Na} < 0.7 mol% the latent heat of melting of chlorine is reduced drastically compared with the expected value. This result have been interpreted by assuming that for samples with rather small amounts of damage a significant fraction of the radiolytic chlorine atoms does not melt and consequently, it is not observed by means of LHM measurements. The reason for this might be that in the earliest stages of the irradiation the pressure in these extremely small chlorine precipitates is very high, and under this condition they do not melt in temperature range of the DSC experiment. On the other hand the large relative size variations of these extremely small particles might lead to appreciable broadening of the melting peak, which might be the reason why the melting phenomena cannot be detected compared with the background.

(ii) When 0.7 J/g < LHM_{Na} < 1.5 J/g the slope of the curve increases and the ratio $\delta^{Cl}_{Na} \equiv \frac{LHM_{Cl}}{LHM_{Na}}$ increases rapidly with increasing amounts of damage.

(iii) The plot in figure 5.1 behaves linearly when the LHM_{Na} is above 1.5 J/g, which means that the concentration of chlorine > 3.5 at%. For this region the ratio $\delta^{Cl}_{Na} \approx 1.25$, which is equal to the 'ideal' ratio, mentioned above.

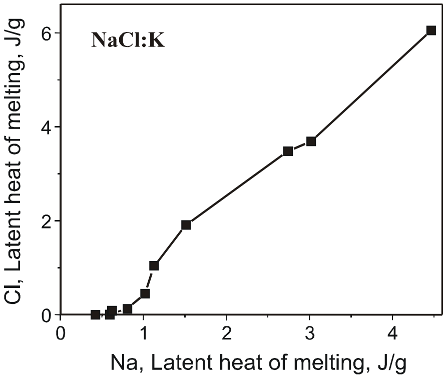

Figure 5.1: The LHM of chlorine bubbles vs. LHM of sodium nano-particles. The latent heat both of sodium and chlorine is (in most cases) proportional to the irradiation dose. The irradiation dose increases from the left to the right and from the bottom to the top of the plot.

We assume that the physical properties of the chlorine atoms in the interfacial layer are influenced strongly by covalent interactions, which exist between these atoms and the nearest Cl^--ions residing in the host NaCl crystal lattice. As a result of these covalent interactions the formation of interfacial chlorine atoms is energetically more favorable compared with bulk chlorine. So, it is likely that small chlorine precipitates are platelets, with large interfacial regions, which might exceed volume of the inner regions, and this could be the reason why most of the chlorine atoms are bound strongly to the host NaCl lattice. This is similar to the well known situation in metals with implanted rare gas atoms, where often the formation of planar extended defects is favored in early stages of damage formation. Since coherent interfaces have a lower energy than incoherent ones [12], usually the precipitates are coherent (or at least semi-coherent) during the early stages of precipitate nucleation and growth. Coherent precipitates have been observed in many alloys, and their morphology (platelets, spheres, needles) depends on the interfacial energy and the coherence dependent strain energy [13,14].

The discrepancy between the latent heat results of Na and chlorine for samples with less than 1 mol% Na and chlorine is reduced substantially by annealing the sample during several minutes up to half an hour at moderate temperatures (up to 180°C). This indicates that chlorine atoms/molecules, which could not be observed by means of latent heat effect measurements in 'as-irradiated' samples, can be detected after annealing [15,16]. In the context of our interpretation this means that the inner part of the chlorine bubbles increases during heating by either the transformation of planar defects into spherical ones, or by increasing the average size of the bubbles due to coarsening during the above-mentioned thermal treatment, or both.

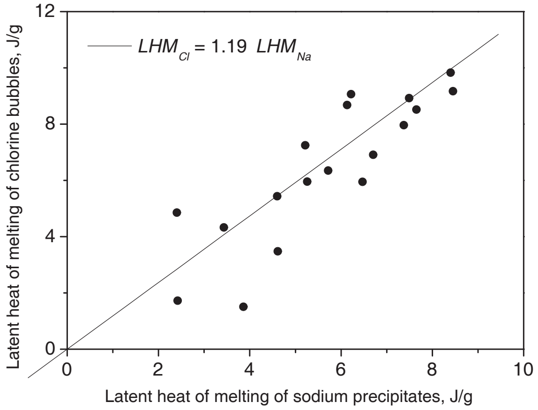

Figure 5.2: The LHM of chlorine bubbles versus LHM of sodium nano-particles for samples, irradiated up to 6000, 10000 and 20000 MGy. The linear fit of the experimental data points yields a coefficient of 1.19, which is in good agreement with the 'ideal' value 1.25

Approximately the same ratio of the latent heat of melting of chlorine and sodium as in figure 5.1 is observed in figure 5.2 for very heavily irradiated NaCl samples. In spite of the large scatter of the data points, the linear fit yields a mean ratio δ_{Na}^{Cl} of 1.19, which is rather close to the above-mentioned value of 1.25. We can hardly see any dependence of the ratio δ_{Na}^{Cl} on the presence of impurities or the irradiation dose in this dose range. It is most likely that the scatter of the data points is caused by errors, which are common for all heavily irradiated samples. Significant errors are made in measuring the LHM of sodium for heavily and ultra-heavily irradiated samples, because of the difficulty to distinguish the wings of the melting peak from the background. In addition, a fraction of the chlorine atoms might escape from the sample through cracks or other macro-defects and the surface of the sample, during the very long irradiation runs. This situation has been observed for several samples in stored energy measurements (DSC at high temperatures). Some NaCl crystals even after full annealing kept a blue color or are even black because of the presence of sodium precipitates, which did not recombine with chlorine. The third reason for the reduced quality of the fitted value for the ratio is the presence of chlorine, which is ‘invisible’ in melting experiments. This means that unequal fractions of radiolytic sodium and chlorine contribute to the melting phenomena. These fractions may differ from sample to sample.

5.3 Melting and solidification of chlorine bubbles

DSC measurements have been carried out on samples with a clearly detectable LT-peak in the heating mode close to the triple point of chlorine. Also the corresponding experiments in the cooling mode have been carried out. The peak in the heating mode, situated at about -100 ^{o}C is due to melting of solid chlorine inclusions. In the cooling mode the peak, which should correspond to solidification of chlorine, has been found at about -122 °C, i.e. it is shifted by almost 20 ^{o}C to lower temperature compared with the melting peak position. We note that the phase transition temperature is determined from DSC spectrum as the onset of the peak, i.e. by extrapolating the leading edge of the peak of the heat-flow signal curve (corrected by background subtraction) back to the temperature value where the first sign of the presence of the latent heat peak appears. In accordance with the mean temperature difference between the onsets of the melting and solidification peaks, we find that the difference between the melting and freezing temperature is about 17°C. Experimentally, the positions for the melting and freezing peaks and their onsets may deviate for different samples by ±2 ^{o}C from the above mentioned temperatures. The error in the determination of the difference between melting and freezing temperatures may be the result of a temperature lag between the actual sample temperature and the measured calorimeter temperature. A test experiment to detect the phase transition of mercury in the heating and cooling mode (T^{Hg}_{melt} = -38.83 °C) yields a difference between the melting and freezing temperature less than 2 degrees, which corresponds with a relative error about 10% in the measurement of the temperature difference. Repeated melting and freezing experiments yield reproducible latent heat values and temperature positions of the respective specific heat peaks.

Typical chlorine melting and solidification DSC spectra for pure NaCl samples and samples with a variety of impurities, irradiated up to 6000, 10000 and 20000 MGy, are shown in figure 5.3. The spectra have been obtained by means of second-degree background line subtraction; the y-axis – i.e. heat flow signal – is not scaled in order to be able to distinguish small features of the spectra. The width at half height of both the well-defined melting and freezing peaks is about 0.6 ^{o}C, i.e. they are rather narrow. For many of the measured samples the freezing peak appears to have a wide high-temperature shoulder and in some cases a wide additional peak is clearly distinguished, whereas for several other samples only one well-defined peak is observed in cooling mode (figure 5.3). The DSC spectra obtained for two of the 20000 MGy irradiated samples are presented in more detail in (figure 5.4). Measurements of the LHM and the Latent Heat of Freezing (LHF) (the energy, which is emitted during solidification) of chlorine precipitates show that the LHF value is typically 10% less than the LHM value of the same sample. A plot showing the value of the LHM as a function of the LHF is presented in figure 5.5. The linear fit of the datapoints yields the ratio LHM=1.09LHF. The same ratio has been obtained earlier in [17].

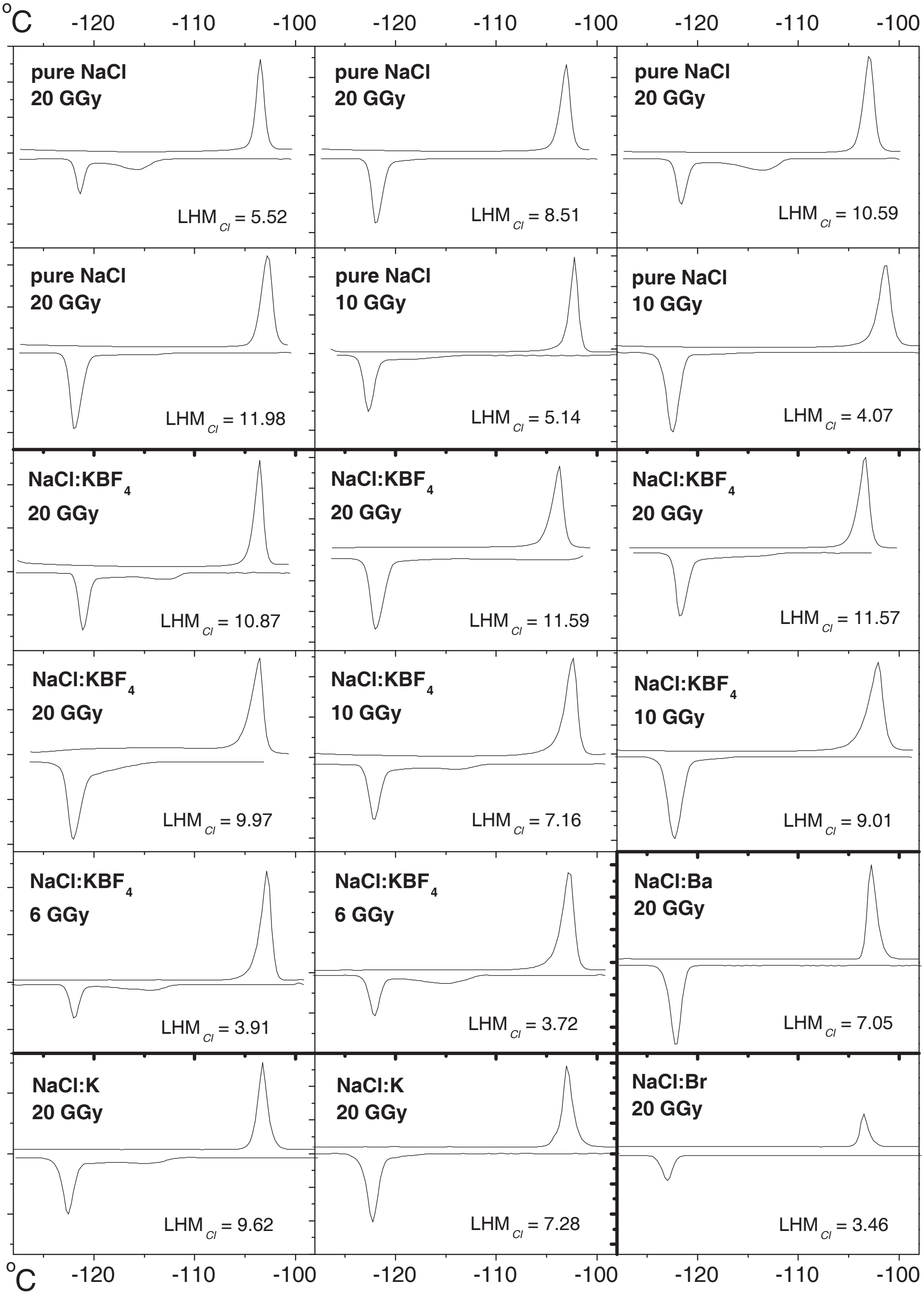

Figure 5.3: Survey of the DSC-scans showing the melting and solidification signal of chlorine in pure and doped NaCl samples irradiated at 100°C up to doses 6, 10 and 20 GGy. The Y-axis is the heat flow signal (the axis is not scaled in order to have small features of the spectra distinguishable. The differences in the signal intensities are large for spectra presented in this figure). The X-axis is the temperature in °C.

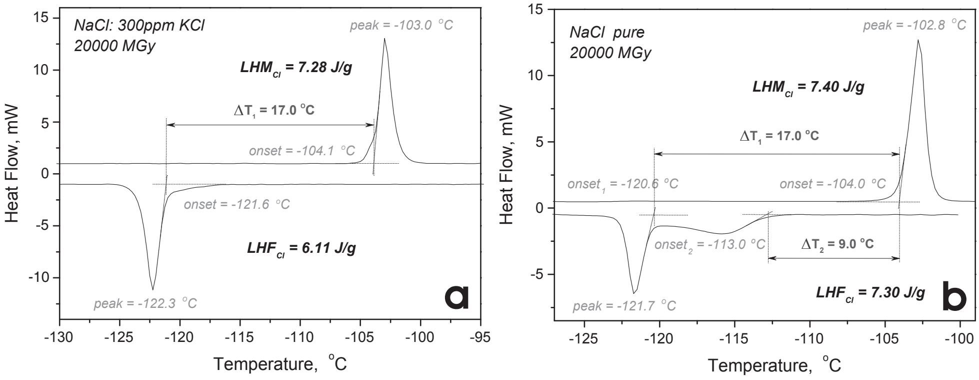

Figure 5.4: The low-temperature DSC-scan of the ultra-heavily irradiated NaCl. a) only one narrow freezing peak is obtained, and b) an additional wide peak (AD-peak) is observed in cooling mode. The background has been subtracted from the DSC curves. The heat flow coordinate range is not reduced to the sample weight and corresponding numbers along the y-axis should be considered as arbitrary values.

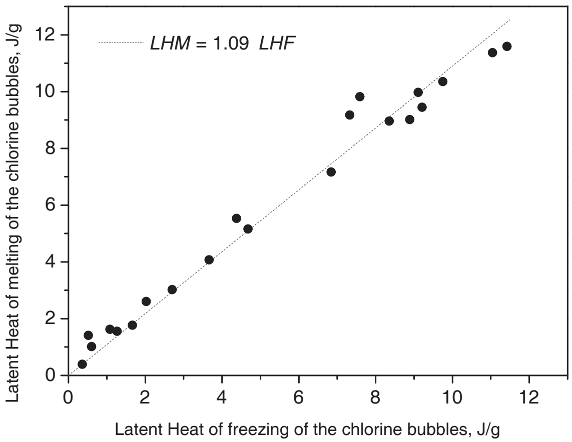

Figure 5.5: The latent heat of melting of the chlorine bubbles versus the latent heat of freezing for the samples, irradiated up to 6000, 10000 and 20000 MGy. The linear approximation gives *LHM* = 1.09*LHF*.

5.4 Temperature hysteresis of melting and solidification

Let us now discuss the possible reasons for the observed difference between the latent heat results for the melting and freezing peaks of chlorine in irradiated NaCl. First of all one has to take into account that chlorine precipitates are embedded in the NaCl matrix, i.e. during heating/cooling cycle stresses may affect the melting/solidification behavior. In the heating mode, the melting process is accompanied by a significant expansion of the precipitates, which should be accommodated by an appropriate relaxation of the NaCl matrix. In the cooling mode, shrinkage of the chlorine bubble after solidification results in a reduction of the pressure. We can express the LHM in terms of the LHF and the expansion contribution, $\Delta P \Delta V$ where ΔP is the pressure difference in the bubble before and after the phase transition and $\Delta V = \Delta V_L - \Delta V_S$ is the difference between the specific volumes of the chlorine bubbles in the liquid and solid state at the triple point temperature. We assume that we can use the bulk values for molecular chlorine V_L = 41.2 cm^3/mol and V_S = 34.8 cm^3/mol. The relationship between the latent heat of melting and freezing can be approximated by $LHM = LHF + \Delta P \Delta V$. The measured difference in the latent heat yields $\Delta P \Delta V \approx 0.09 LHF$, with the latent heat of freezing of bulk chlorine LHF = 90.2 J/g-Cl$_2$ the pressure difference in chlorine bubbles in the liquid and solid state at the triple point temperature is $\Delta P \approx 0.9$ kbar[1].

An immediate consequence of the different pressure conditions during melting and freezing is that a difference between the melting and freezing temperature is observed. The transition from the solid to the liquid state and vice versa takes place under the condition that the difference of the Gibbs free energy of the two aggregate states is zero, i.e.

$$\Delta G_{S\to L} = \int_{V_S}^{V_L} P_S(V)dV + \Delta U_{S\to L} - T_{S\to L}\Delta S_{S\to L} = 0 \qquad (5.1)$$

$$\Delta G_{L\to S} = \int_{V_L}^{V_S} P_L(V)dV + \Delta U_{L\to S} - T_{L\to S}\Delta S_{L\to S} = 0 \qquad (5.2)$$

Here, $P_{S,L}$ are the pressure values in the bubbles at the melting point after equilibrium is reached in the solid and liquid state, respectively.

Assuming equality of the enthalpy change during melting and solidification $\Delta U_{S\to L} \approx -\Delta U_{L\to S}$ and using $T_{S\to L} = T_{L\to S} + \Delta T$, where ΔT is the difference between the melting temperatures obtained from the latent heat peaks in the heating and cooling mode, we can write:

---

[1] It should be noted, that the accuracy of the latent heat measurement in the cooling mode is significantly less than in the heating mode because of the curvature of the background and the presence of additional wide freezing peaks. However, a careful statistical analysis of the measured LHF data shows that the LHM/LHF ratio is relevant and an essential feature of the chlorine bubble system, and are not due to experimental errors.

Table 5.1 The material parameters.

Parameter	*Value*
Molar volume of liquid Cl_2, V_L, cm^3/mol	41.2
Molar volume of solid Cl_2, V_S, cm^3/mol	34.8
Entropy change during melting of Cl_2, $\Delta S_{S\to L}$, J/mol K	37.2
Burger's vector of dislocation loops, b, nm	0.398
Dislocation core radius, r_0	$2b$
Shear modulus of NaCl, μ, GPa (× 10 kbar)	12.61
Poisson ratio of NaCl, ν	0.252
van der Waals constant, A, $Nm^4\ mol^{-2}$	0.6497
van der Waals constant, B, $m^3\ mol^{-1}$	$5.624x10^{-5}$
Volume per atom in liquid Cl_2, Ω_{Cl}^{L}, m^{-3}	$3.421x10^{-29}$
Volume per atom in solid Cl_2, Ω_{Cl}^{S}, m^{-3}	$2.898x10^{-29}$
Bulk modulus of liquid Cl_2, K_{Cl}, GPa (×10 kbar)	1.1
Bubble surface energy, γ, J/m^2	0.456
Melting temperature of Cl_2, T_m, K	171.6
Latent heat of melting of Cl_2, L, J/m^3	$1.55x10^{8}$

$$\int_{V_S}^{V_L} P_S(V)dV + \int_{V_L}^{V_S} P_L(V)dV \approx \Delta T \Delta S_{S\to L} \tag{5.3}$$

that yields the following simple relation: ΔT is proportional to the pressure difference in the chlorine bubbles in the solid and liquid state (implying that is $\Delta V_{S\to L}$ constant):

$$\Delta P(V_L - V_S) = \Delta P \Delta V \approx \Delta T \Delta S_{S\to L} \tag{5.4}$$

With equation 5.4 we can again estimate the lower limit of the pressure difference in the chlorine bubbles in the solid and liquid state using the measured temperature difference. With the above-mentioned assumption that the thermodynamical parameters of bulk chlorine, like the entropy change $\Delta S_{S\to L}$=37.2 J/mol K (see table 5.1) can be used, the pressure difference ΔP is estimated to be 0.83±0.1 kbar (see figure 5.6). Within experimental accuracy the estimates on the basis of the observed difference in the amounts of LHM and LHF on one hand and on the basis of the observed shifts of the latent heat peaks, calculated with equation (5.4) on the other hand, yield the approximately same pressure difference ΔP in the chlorine bubbles in solid and liquid state.

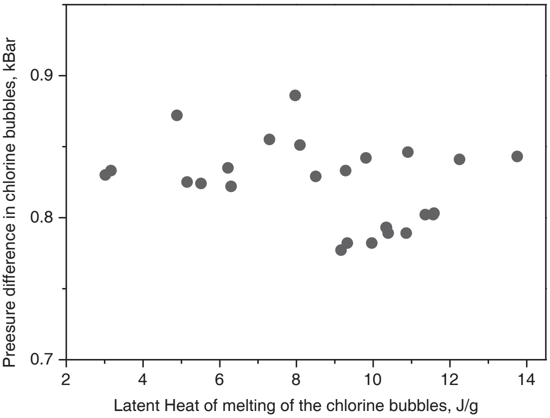

Figure 5.6: Pressure difference ΔP between solid and liquid states in chlorine bubbles, calculated using equation 5.4, versus latent heat of melting of chlorine bubbles for the samples, irradiated up to 6000, 10000 and 20000 MGy.

Elastic stress

We can also estimate the pressure change in the chlorine bubble due to melting in terms of the elastic strain generated in the matrix by an inclusion. According to the classical formalism, the contribution to the normal stress at the cluster-matrix interface is given by

$$\sigma_n = \frac{12\mu K_{Cl}}{4\mu + 3K_{Cl}}\varepsilon \tag{5.5}$$

where K_{Cl} is the bulk modulus of chlorine, μ is the shear modulus of the NaCl matrix. For ε we will use the change in the bubble-matrix misfit due to melting:

$$\varepsilon = \frac{\Omega_{Cl}^{L} - \Omega_{Cl}^{S}}{3\Omega_{Cl}^{L}} \tag{5.6}$$

where Ω_{Cl}^{L} and Ω_{Cl}^{S} are the volume per atom in liquid and solid chlorine, respectively. These parameters can be obtained from the molar volumes of Cl_2. With the values, presented in (table 5.1), equation5.6 and 5.5 we obtain $\varepsilon = 0.052$ and $\sigma_n \approx 1.6$ kbar. σ_n can be treated as the pressure difference in the chlorine bubble in the solid and liquid state. The calculated value is of the same order of magnitude as the pressure difference ΔP obtained from calorimetry data.

However, we note that the estimates given here are rather crude. It has been shown in theoretical papers (see for example [18]), that at nanolength scales, due to the increasing surface-to-volume ratio, surface effects become important and induce a size dependency in the otherwise size-independent classical elasticity solutions for embedded inclusions. Hence, the pressure in the chlorine bubble and the pressure difference in solid and liquid state may depend on the curvature of the bubble surface.

Another possible contribution to the temperature difference between the melting and freezing peaks of chlorine in irradiated NaCl can be attributed to supercooling, i.e. the solidification process occurs below the corresponding equilibrium melting temperature. The reason for supercooling is that solidification should start with the formation of small solid particles, which are called nuclei. These solid nuclei may be formed either homogeneously in the liquid volume or at the boundary of the precipitates by catalyzation of the formation of nuclei by the presence of the interface between the NaCl matrix and the liquid Cl_2-precipitate. The minimum radius of a stable nucleus is inversely proportional to the temperature decrease below the melting temperature. Therefore, in the case of liquid precipitates the shift of the freezing temperature with respect to the melting temperature is size-dependent [12]. For nucleation at the cavity wall the interface energies and the cavity curvature are crucial parameters.

Melting and solidification at temperatures, different from the equilibrium melting temperatures is usually observed in systems of particles with finite-sizes, which are embedded in a solid matrix [19-22] as well as for liquids in porous materials [5-8]. Often the observed hysteresis of the melting and freezing phenomena in these systems is explained by interface effects. Apparently, in case of liquid chlorine nanoparticles embedded in the NaCl matrix nucleation processes should take place, which affect the observed shift of the freezing temperature.

The interesting feature of the DSC spectra, mentioned in section 5.2, is that the additional wide freezing peak has been observed for many very heavily damaged NaCl samples. The behavior of this additional peak, which is situated at temperatures slightly higher than the well-defined freezing peak, has been carefully studied by measuring DSC spectra of various samples. A survey of the DSC-scans showing the melting and solidification signal of chlorine in pure and doped irradiated NaCl samples is presented in figure 5.3. It has been observed from the analysis of many spectra that the magnitude of this additional peak (AD-Peak) changes randomly from sample to sample: for one part of the samples there is only the well-defined peak, while for the second part well-defined peak has an additional high-temperature shoulder of different sizes, for the third part of the samples there is an additional wide peak with varying integral intensities; the proportion of the intensity of this peak to the main well-defined one can be as high as 50% for some of the samples. There is no dependence between the magnitude of the AD-Peak and the amount of damage (determined by the LHM) or the type of impurity in the NaCl sample. No dependence between these parameters and presence or absence of the AD-Peak was found either. However, the overall number of samples, where the AD-Peak was detected, is larger for more heavily irradiated samples. Also it should be noticed that the most intense AD-Peak, along with the most extensive scatter of the AD-Peak magnitudes was observed for pure NaCl samples.

Table 5.2: Temperature values of the maxima and the onsets of the melting and freezing chlorine peaks. The sub- and superscripts *1* and *2* corresponds to the 'main' narrow freezing peak and 'additional' wide high temperature freezing peak respectively. See figure 5.4 for two examples.

Sample type	**LHM Cl_2 (J/g_{NaCl})**	**Dose (Gy)**	**Peaks**		**Onsets**			**ΔT_1 (°C)**	**ΔT_2 (°C)**
			T_{melt} (°C)	**T_{freez} (°C)**	**T_{melt} (°C)**	**T_{freez}^{1} (°C)**	**T_{freez}^{2} (°C)**		
NaCl:KBF_4	9.97	$2x10^{10}$	103.5	122.0	105.2	120.5		15.3	
NaCl:KBF_4	11.57	$2x10^{10}$	103.3	121.8	104.7	120.4	111.6	15.7	6.9
NaCl:KBF_4	9.01	$1x10^{10}$	102.1	122.2	104.0	120.8		16.8	
NaCl:KBF_4	3.72	$6x10^{9}$	102.8	122.0	104.3	121.0	111.6	16.7	7.3
NaCl pure	5.52	$2x10^{10}$	103.5	121.3	104.4	120.5	113.6	16.1	9.2
NaCl pure	8.51	$2x10^{10}$	103.0	122.0	104.5	120.7		16.2	
NaCl pure	5.14	$1x10^{10}$	102.2	122.7	103.9	121.6	114.1	17.7	10.2
NaCl:Br	3.46	$2x10^{10}$	103.5	123.0	104.4	122.0		17.6	
NaCl:Ba	7.05	$2x10^{10}$	102.7	122.3	103.7	121.1		17.4	
NaCl:K	9.62	$2x10^{10}$	103.2	122.5	104.4	121.4	111.5	17.1	7.1
NaCl:K	7.28	$2x10^{10}$	103.0	122.3	104.1	121.0		17.0	

The analysis of the onset position of the AD-Peak (when it is large enough to measure its onset with reasonable accuracy) shows that the onset temperature is about the same for all measured samples. The observed variation of the onset temperatures of 3-4 °C seems to be the error of the measurements. The temperature values of the maxima and the onsets of the melting and freezing peaks of chlorine and the temperature difference between them for several samples are presented in table 5.2.

Because the AD-Peak is located at a fixed temperature and its magnitude varies from sample-to-sample, it is most likely that this peak is associated with bubbles, which are attached to defects in the matrix. The concentration and arrangement of these defects may change from sample to sample (i.e. impurity atoms and dislocations). If the defect is located in the bubble-matrix interface, it may locally change the interface energy, which may reduce the energy needed for the formation of the solid nuclei, and therefore reduce the downward shift of the solidification compare to the melting temperature. With the present experimental data it is not possible to establish exactly what sort of defects are involved. However, we assume that the chlorine bubbles contributing the AD-Peak are coupled to dislocations. Indeed, in those samples, irradiated up to the highest doses in the set, the concentration of dislocation increases considerably, which leads to an increase of the number of samples, showing the AD-Peak. At the same time the number of bubbles attached to the dislocations may differ from sample to sample, which might lead to differences in the magnitude or even the absence of the AD-Peak.

In conclusion, we assume that both phenomena discussed above, (i) the pressure difference between the solid and liquid state of the chlorine bubble and (ii) the influence of bubble-matrix interface, may affect the shift of phase-transition temperature simultaneously. A detailed study of the influence of each mechanism separately would necessitate additional investigations of the phase transition in embedded particles, using systems, less complicated than heavily rradiated NaCl. This task is beyond the scope of the present work.

5.5 Loop punching provided by chlorine bubbles

Chlorine precipitates grow due to agglomeration of H-centers, which are in fact interstitial chlorine atoms. We assume that the chorine atoms inside the bubbles are present under high pressure. This situation is well-known in metals implanted with rare gas atoms, where the pressure in the gas bubbles has been found to be higher than 10-20 kbar (1-2 GPa, see for instance [2,4,23]). Similar to implanted gas bubbles in metals and metallic nanoparticles embedded in a solid matrix (see [24,25]), we suppose that after prolonged exposure to ionizing radiation chlorine bubbles in NaCl release their excess pressure and that in this way by means of inelastic processes associated with dislocation loop punching extra room is created to allow further growth of these bubbles.

Let us consider loop punching initiated by the chlorine bubbles in irradiated NaCl crystals. According to [26] the threshold pressure for loop punching by a bubble of radius r filled with chlorine-gas molecules is given by

$$P_{th}(r) = \frac{\mu b}{2\pi r_L (1-\nu)} \ln \frac{8 r_L}{r_0 \sqrt{e}} + \frac{2\gamma}{r} \tag{5.7}$$

where μ is the shear modulus of the NaCl matrix, ν is the Poisson ratio, b is the Burger's vector of the dislocation loop, r_0 is the dislocation core radius and is the most probable radius of the punched loop, γ is the interface energy of the embedded bubble. If the pressure in the bubble is larger than the threshold pressure $r_L = r/\sqrt{2}$ the loop punching process results in a decrease of the energy of the system. The increase of the bubble radius is small

$$\Delta r = r\left(1 + \frac{3b}{8r}\right)^{1/3} - r \approx \frac{b}{8}, \quad r > \ b \tag{5.8}$$

To estimate the decrease of the pressure in the bubble due to one loop-punching event we use the van der Waals equation of state

$$P(n,r) = \frac{n k_b T}{V - nB} - A\left(\frac{n}{V}\right)^2 \tag{5.9}$$

where n is the number of chlorine molecules in the bubble, $V=\frac{4\pi}{3}r^3$ is the bubble volume, A and B are the van der Waals constants. The number of gas atoms, which need to be accumulated in the bubble, to initiate the loop-punching event, is determined by the relation $P_{th}(r) = P(n,r)$. Using this relation together with eqs. (5.8) and (5.9) one can find the drop in pressure of the bubble due to loop punching. The calculated threshold pressure in the chlorine bubble and the pressure after one loop-punching event are plotted in figure 5.7 as a function of the bubble radius. The parameters, which were used for the calculations are presented in table 5.1. The interface energy of the embedded bubble, γ, was set equal to the sodium particle interface energy [27], as a more or less randomly chosen, reasonable value

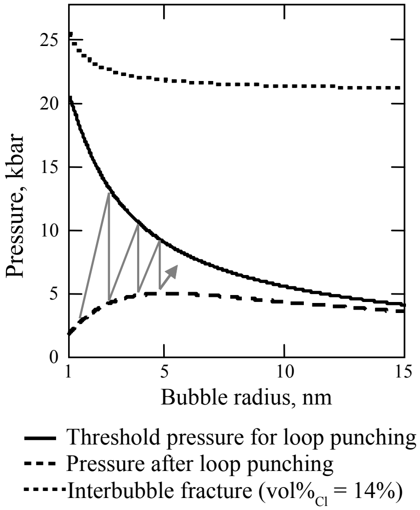

Figure 5.7: The dependence of the threshold pressure for loop punching on bubble radius (solid line) and the pressure in the bubble after punching of one loop (dashed line). The line with arrow shows the pressure oscillation during bubble growth. The temperature is 100 °C. The other parameters are listed in Table 5.1.

This choice is only arbitrary, however, it was found that variations of one order of magnitude in the γ value results only in minor contribution to the calculated pressure value $P_{th}(r)$. For this reason γ is not a critical parameter in our calculations and its value is not important. After the loop punching event and the associated drop in pressure, the bubble continues to accumulate new H-centers, which leads again to an increase of the pressure. Hence, during bubble growth we can expect that the pressure in the chlorine bubble oscillates between two pressure curves, as presented in figure 5.7. It can be seen that for a mean size of the chlorine bubble of about 2 nm (computed in [28]), the calculated threshold pressure is about 15 kbar, after the loop punching event the pressure drops by about a factor of 3 to the new value of

4 kbar. Both pressure values are quite high, which is in agreement with our assumtion that chlorine bubbles in heavily irradiated NaCl are present under high pressure.

In addition, the threshold pressure for interbubble fracture has been estimated using:

$$P_{bf} = \sigma_f \left[\frac{1}{(\pi r^2 C_b^{2/3})} - 1 \right] + \frac{2\gamma}{r} \qquad (5.10)$$

where σ_f is the fracture stress and C_b is the bubble concentration [29,30]. Calculations have shown that for those values of the volume fraction of chlorine, which had been measured for our samples, P_{bf} significantly exceeds the threshold pressure for loop punching process for all bubble sizes (figure 5.7).

5.6 Conclusions

Differential scanning calorimetry experiments on irradiated NaCl samples at low temperature allowed us to detect melting and solidification processes in very small chlorine bubbles. Measurements of the ratio of the latent heat of melting of the chlorine precipitates and the latent heat of melting of the sodium particles for the same irradiated samples have revealed a very important feature of the development of the system of chlorine bubbles. For relatively low damaged samples a large fraction of the radiolytic chlorine in the NaCl matrix does not exhibit melting behavior. On the other hand, when the overall fraction of radiolytic Na (and Cl_2) in the sample reaches values of about 3-4 mol% about the full amount of Cl_2 is ‘visible’ in melting experiments. This could be deduced from the above mentioned ratio of the latent heat of melting of Na and Cl_2. The results of these experiments on heavily damaged materials indicate that i. the numbers of chlorine and Na atoms in heavily damaged NaCl are the same and ii. the chlorine in the bubbles represents almost all the radiolytic Cl in the sample. It is likely that we have system of fine particles of molecular chlorine separated from each other rather than system of connected pores, like what one has in the porous media. Moreover, these chlorine particles are well separated from the sodium precipitated particles. The fact that NaCl crystal can accumulate quite high concentrations of metallic sodium and molecular chlorine indicate that even in ultra-heavily irradiated samples sodium and chlorine is effectively separated. In order to have this separation in the case of crystal with well-organized structure of fine sodium precipitated particles (see *chapter IV*), we can assume that chlorine bubbles also form highly organized systems.

The difference between the latent heat of melting and solidification of the chlorine bubbles observed for the same sample during heating and cooling, respectively, along with the difference in temperature positions of the peaks associated with melting and solidification are assumed to be due to the pressure difference when the phase transition takes place in the solid and liquid states of the bubbles during the two different types of experiments. For the estimated pressure increase due to melting of the embedded bubbles we have obtained a value of about 1 kbar. The calculation of the elastic strain generated in the matrix by the solid-liquid phase transition in the inclusion -which wants to expand due to melting- yields a pressure difference of about 1.6 kbar. The experimental values, deduced the experimental results are rather close to this theoretical value, even though the theory is based on a crude model.

At the same time the thermal hysteresis of the melting and solidification processes can be related to nucleation processes in the small chlorine particles. As a result one expects a lower temperature for the liquid-solid transition (i.e. supercooling) in the chlorine nano-bubbles. This implies, that also on the bases of this phenomenon we can explain the additional wide freezing peak, which has been observed for many ultra-heavily irradiated NaCl samples. Thus, the temperature decrease, which is necessary for the formation of solid nuclei at the wall of the cavity filled with the liquid, depends on the wall/liquid interface. We assume that the chlorine bubbles, which contribute to the additional freezing peak, are coupled to some defects, most probably dislocations or dislocation structures.

In addition, we have made calculations for the dislocation loop punching process, which might be initiated in the crystalline matrix by the over pressured bubbles. These calculations allowed us to obtain the critical pressure values for the chlorine bubble in the NaCl matrix, which depend on the bubble size. The maximum pressure in a bubble with a radius of 2 nm (which is the most probable size of the bubbles, according to the theoretical calculations) is found to be about 15 kbar. This estimate is of the same order of magnitude as the one obtained for halogen bubbles in metals, which suggests that the approach used in our calculations is quite appropriate.

References

[1] H.H. Andersen, J. Bohr, A. Johansen, E. Johnson, L. Sarholt-Kristensen and V. Surganov, *Phys. Rev. Lett.* **59** (1987), 1589-1592

[2] A. vom Felde, J. Fink, Th. Mueller-Heinzerling, J. Pflueger, B. Scheerer, G. Linker and D. Kaletta, *Phys. Rev. Lett.* **53** (1984), 922-925

[3] C.J. Rossouw and S.E. Donnelly, *Phys. Rev. Lett.* **55** (1985), 2960-2963

[4] C. Templier, C. Jaouen, J.P. Rivière, J. Delafont and J. Grilhé, *C.R. Acad. Sci. Paris* **299** (1984), 613

[5] C. Faivre, D. Bellet and G. Dolino, *Eur. Phys. J. B* **7** (1999), 19-36

[6] E. Molz, A.P.Y. Wong, M.H.W. Chan and J.R. Beamish, *Phys. Rev. B* **48** (1993), 5741-5750

[7] J.L. Tell and H.J. Maris, *Phys. Rev. B* **28** (1983), 5122

[8] K.M. Unruh, T.E. Huber and C.A. Huber, *Phys. Rev. B* **48** (1993), 9021-9027

[9] H.W. den Hartog, A.V. Sugonyako, D.I. Vainshtein, A.A. Turkin, S.N. Sulyanov, D.M. Kheiker and P.V. Dorovatovskii, *Phys. Stat. Sol.* (*to be published*)

[10] V.I. Dubinko, A.A. Turkin, D.I. Vainshtein and H.W. den Hartog, *J. Appl. Phys.* **86**: (11) (1999), 5957-5960

[11] V.I. Dubinko, A.A. Turkin, D.I. Vainshtein and H.W. den Hartog, *Nucl. Instr. and Meth. in Phys. Res.* **B 153** (1999), 163-166

[12] D.A. Porter and K.E. Easterling, *Phase Transitions in Metals and Alloys*, (1992)

[13] P. Haasen, *Physical Metallurgy*, Cambridge University Press, Cambridge, (1986)

[14] R. Wagner and R. Kampmann, *Mater. Sci. Technol.* **5** (1991), 213-303

[15] J. Seinen, D.I. Vainshtein, H.C. Datema and H.W. den Hartog, *J. Phys.: Condens. Matter.* **7** (1995), 705-716

[16] D.I. Vainshtein, V.I. Dubinko, A.A. Turkin and H.W. den Hartog, *Radiat. Eff. & Def. Sol.* **156** (2001), 51-57

[17] H.P. den Hartog, *Onderzoek naar de electronische eigenschappen van bestraald, gedoteerd NaCl*, Master Thesis, University of Groningen, (1994)

[18] P. Sharma, S. Ganti and N. Bhate, *Appl. Phys. Lett.* **82**: (4) (2003), 535-537

[19] E. Johnson, H.H. Andersen and U. Dahmen, *Microsc. Res. Tech.* **64** (2004), 356-372

[20] A.K. Malhotra and D.C. van Aken, *Phil. Mag. A* **71**: (5) (1995), 949-964

[21] H.W. Sheng, K. Lu and E. Ma, *Acta Mater.* **46**: (14) (1998), 5195-5205

[22] J. Zhong, Z.H. Jin and K. Lu, *J. Phys.:Condens. Mater.* **13** (2001), 11443-11452

[23] H. Trinkhaus, *Radiat. Eff. & Def. Sol.* **78**: (1-4) (1983), 189-121

[24] L.H. Zhang, E. Johnson and U. Dahmen, *Microsc. Microanal.* **10**: (Suppl 2) (2004), 332-333

[25] L.H. Zhang, E. Johnson and U. Dahmen, *Acta Mater.* **53** (2005), 3635-3642

[26] G.W. Greenwood, A.J.E. Foreman and D.E. Rimmer, *J. Nucl. Mater.* **4** (1959), 305

[27] J. Seinen, *Radiation damage in NaCl. The process of colloid formation*, PhD thesis, University of Groningen, (1994)

[28] V.I. Dubinko, A.A. Turkin, D.I. Vainshtein and H.W. den Hartog, *J. Nucl. Mater.* **304** (2002), 117-128

[29] H. de Beurs, J.A. Hovius and J.Th.M. de Hosson, *Acta metall.*, **36**: (12) (1988), 3123-3130

[30] J.H. Evans, *J. Nucl. Mater.* **68** (1977), 129

CHAPTER VI

INVESTIGATION OF SODIUM PRECIPITATES IN IRRADIATED NaCl WITH ATOMIC FORCE MICROSCOPY

6.1 Introduction

Sodium precipitates, which are created in NaCl crystals under ionizing radiation form complex systems of extended radiolytic defects. We are dealing with an interesting system consisting of metallic nanoparticles inside the insulating NaCl matrix. In terms of radiolysis this system is the counterpart of the complementary system of chlorine gas nanobubbles. The aggregates of sodium nanoparticles are assumed to be responsible for many of the interesting and unique properties of irradiated NaCl crystals, which have been observed by means of thermal analysis, electron paramagnetic resonance and Raman scattering. In order to understand the origin of the features, observed by the above-mentioned independent techniques, the direct investigation of the sodium nanoparticles in the NaCl matrix is necessary.

From this point of view one of the most powerful techniques is transmission electron microscopy (TEM). However, this method has the limitation that very small specimen thicknesses (several hundred nanometers) are required. Usual thinning procedures are polishing and ion etching. They are not easily applicable for the investigation of irradiated alkali halides because of the significant perturbations of the radiolytic defect systems in the samples caused by heating and ion bombardment, which are applied in the preparation procedures. In the case of NaCl crystals, the samples should be protected during all stages of the preparation and the measurements from water vapor in the atmosphere because of the hygroscopicity of NaCl. These limitations lead to appreciable difficulties when preparing suitable irradiated NaCl samples, and complicated technical methods are necessary for this purpose.

Another crucial difficulty of the investigation of alkali halides by means of TEM is the production of new radiolytic defects during the measurement. The high-energy electron beam from the microscope is responsible for *in-situ* radiolysis at a high reaction rate and the corresponding fast creation of radiolytic defects. As a result the existing defect systems in the sample change drastically in a short time. This makes TEM observations of the initial state of the sodium nanoparticles, i.e. which are unaffected by the measurements, hardly possible. It should be mentioned nevertheless, that successful TEM experiments on alkali halides crystals, which had been irradiated *ex-situ* (i.e. outside the TE microscope) have been performed by Hobbs et al [1]. In this work the measurements were carried out at 10 K in order to decrease the rate of *in-situ* defect production. These observations were used for studying the earliest stages of radiolysis in alkali halides.

On the other hand, Atomic Force Microscopy (AFM) is a very effective tool for the investigation of nanosized objects on flat surfaces. This method turned out to be the most suitable one for our purpose. To study nano-objects, which are located in bulk material with AFM they need to be brought to the surface of the sample. In our case of metallic particles in a crystalline NaCl sample this has been achieved by cleaving the crystal along one of its {100} planes. The embedded particles, which are assumed to remain unaffected by the cleaving procedure, will protrude from the cleaved surface, as illustrated in figure 6.1. In fact, the assumption, that the sodium particles remain unchanged, while being brought to the surface, seems to be too simple. Because of the misfit between the NaCl and Na lattice parameters, the sodium particles are expected to be stretched by the presence of the matrix (see *chapters II* and *IV*). Thus, after removing a part of the matrix surrounding the particle, its shape may be altered by uncompensated attractive forces of the residual part of the matrix.

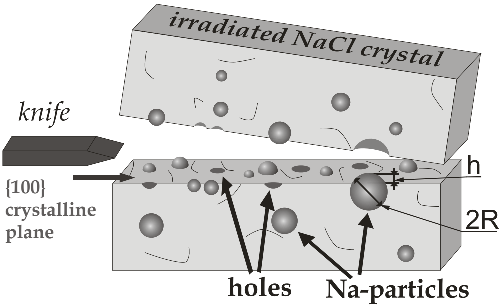

Figure 6.1: Schematic view of the cleaved irradiated NaCl sample with sodium nano-particled.

Therefore the particle might be pulled into the cavity, and flattened. Attention should be paid to the fact that because of this the particle shape and size, obtained by AFM, might be different from the corresponding properties of the particle in the bulk sample.

6.2 Experimental procedures

AFM measurements of the cleaved surface of irradiated NaCl samples have been carried out with two Omicron STM/AFM UHV microscopes. One of the microscopes was equipped with a Needle Sensor AFM system (with a quartz resonator as a driving force for the tip oscillations), operating in the non-contact mode. The other microscope was equipped with beam deflection AFM, which allows measurements in the non-contact mode with frequency modulation. Standard silicon tips with apex radius of about 10 nm were used for the microscope with beam deflection AFM system. Special tips manufactured by Omicron were used in the microscope with the needle sensor system. The radii of these tips were in the range of 10 to 30 nm.

Because of the high chemical reactivity of metallic sodium, the irradiated samples were cleaved, prepared and kept under Ultra High Vacuum (UHV) conditions ($10^{-8}\div10^{-10}$ mbar) prior to and during the experiments. The most important difficulty in the stage of the sample preparation was the cleaving procedure. It is highly important for our measurements to obtain a sufficiently flat and undistorted surface after cleaving the crystal. To achieve this goal a special cleaving device has been designed, manufactured and mounted in the UHV chamber. It allows cleaving the NaCl samples precisely along the {100} crystalline planes and avoids possible damage of the sodium particles by the cleaving knife. Sufficiently flat surfaces with clearly distinguishable crystalline steps have been obtained with this cleaving device for a variety of irradiated NaCl samples.

However, it has been found that difficulties arise when cleaving heavily irradiated samples. Above a certain level of radiation damage (about 1 J/g in terms of the LHM of radiolytic sodium in the sample) the concentration of radiation induced dislocations increases significantly. The dislocation microstructure in the crystal becomes dense and complex, which causes the cleaved surface to be jagged and irregular. Because the roughness of the surface increases drastically, it is not possible to distinguish the small Na precipitates on these samples. Unfortunately, this limits the upper dose for the samples, which are suitable for investigation with AFM. This value of the dose depends on the type of NaCl material. The best cleaving natural rock-salt crystals provide the possibility to work with samples irradiated up to 3000 MGy. On the other hand we could not obtain any acceptable surface for Br doped NaCl samples for any of the doses of interest, even though the damage level in these samples is usually rather low.

Useful AFM images were obtained for sets of natural rock-salt, KCl doped and pure moderately and heavily irradiated NaCl samples. Freshly cleaved surfaces of ionic crystals are expected to be charged. The presence of the surface charge is harmful for non-contact scanning. This gives rise to spikes and lines in the AFM scan and often it leads to the total loss of the image. Therefore, prior to AFM measurements freshly cleaved crystals have been allowed to decharge for several hours.

6.3 Observation of sodium nanoparticles

First, the surface of an unirradiated salt crystal has been investigated with AFM. Crystalline steps and dislocations are clearly seen on the cleaved surface of the sample (figure 6.2). No sign of pimple-like formations or pits have been found on the perfectly flat crystalline surfaces observed on these samples. Many separated randomly distributed spherical particles have been observed for almost all of the moderately irradiated samples. The sizes of the particles are in the range of several nanometers to several tens of nanometers (figure 6.3). The particles are distributed very inhomogeneously over the sample surface, usually they can be found accumulated in some preferred local areas, although separated from each other by several particle diameters. Similar results have been obtained by Vasile et al [2] for Pb doped KCl after electrolytic coloration. The AFM measurements presented in that work show lead metallic particles separated from each other, which are generally concentrated along macroscopic defects in the matrix. This is similar to the situation in our samples, but the concentration of defects like dislocations and disclinations in irradiated NaCl is quite high,

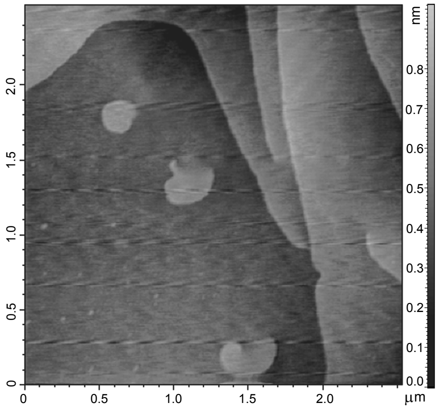

Figure 6.2: Crystalline steps and dislocations observed at the cleaved surface of unirradiated NaCl. The AFM topography image were taken under UHV conditions.

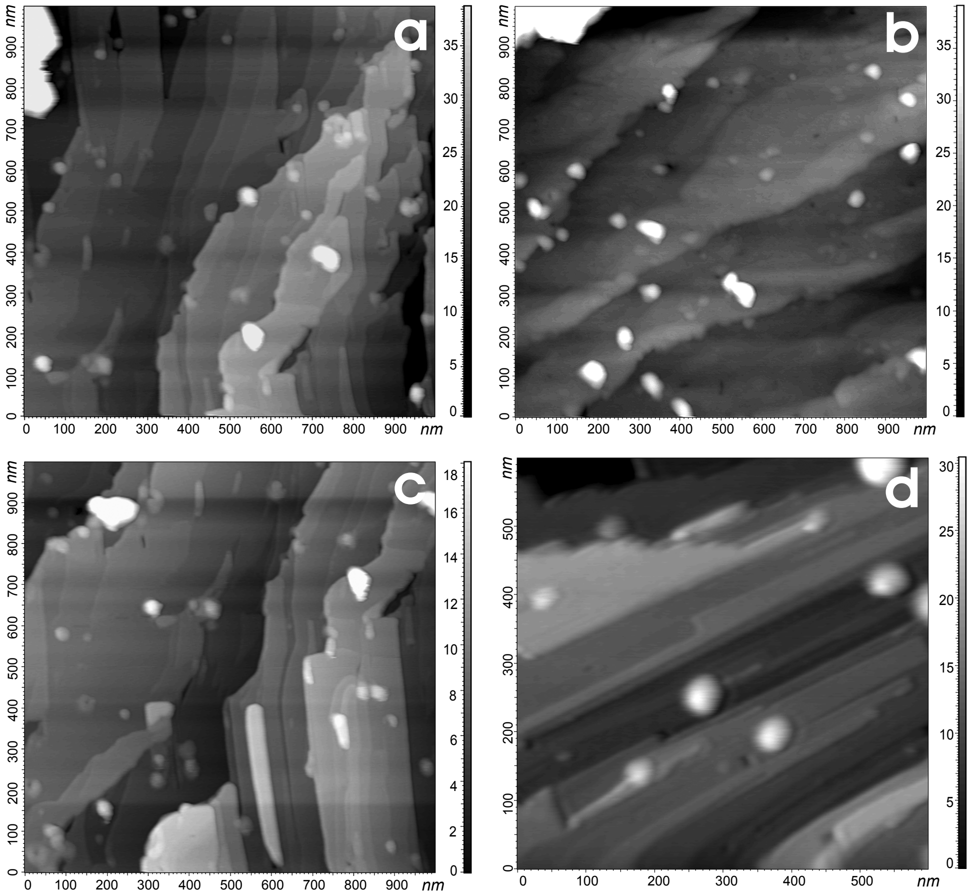

Figure 6.3: Particles and holes observed in different areas at the cleaved surface of moderately irradiated NaCl. The AFM topography images were taken under UHV conditions.

and these defects are present in almost all of the scanned areas, even when the particles have in fact not been observed (the area of a typical scan was about one to several square microns).

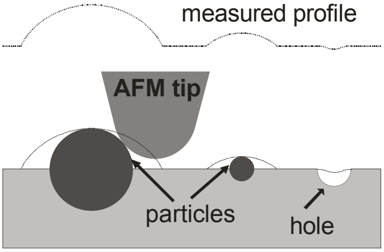

Figure 6.4: Convolution between the AFM tip and the surface.

Nanosize holes are visible in some of the images (see figure 6.3). We assume that these holes are the traces left behind by those particles, which are situated in the counter part of the cleaved crystal (as it is illustrated in figure 6.1). The average size of the holes is significantly less than the average size of the observed particles, which is due to the convolution between the tip and the surface. Convolution effects also affect the observed size of the particles. The relative effect is larger for smaller particles. The convolution effect is illustrated schematically in figure 6.4.

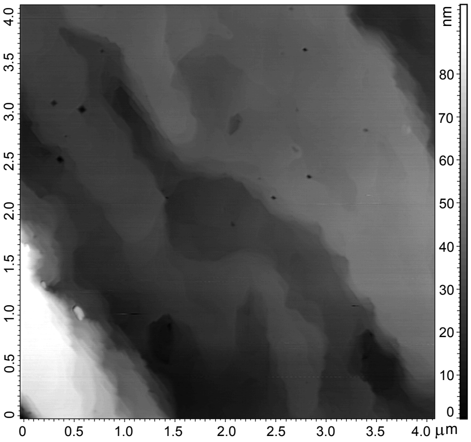

Figure 6.5: Vacancy voids holes are visible in large scanning area as black dots. The image was taken in air in the contact mode with the NT-MDT Ntegra set-up.

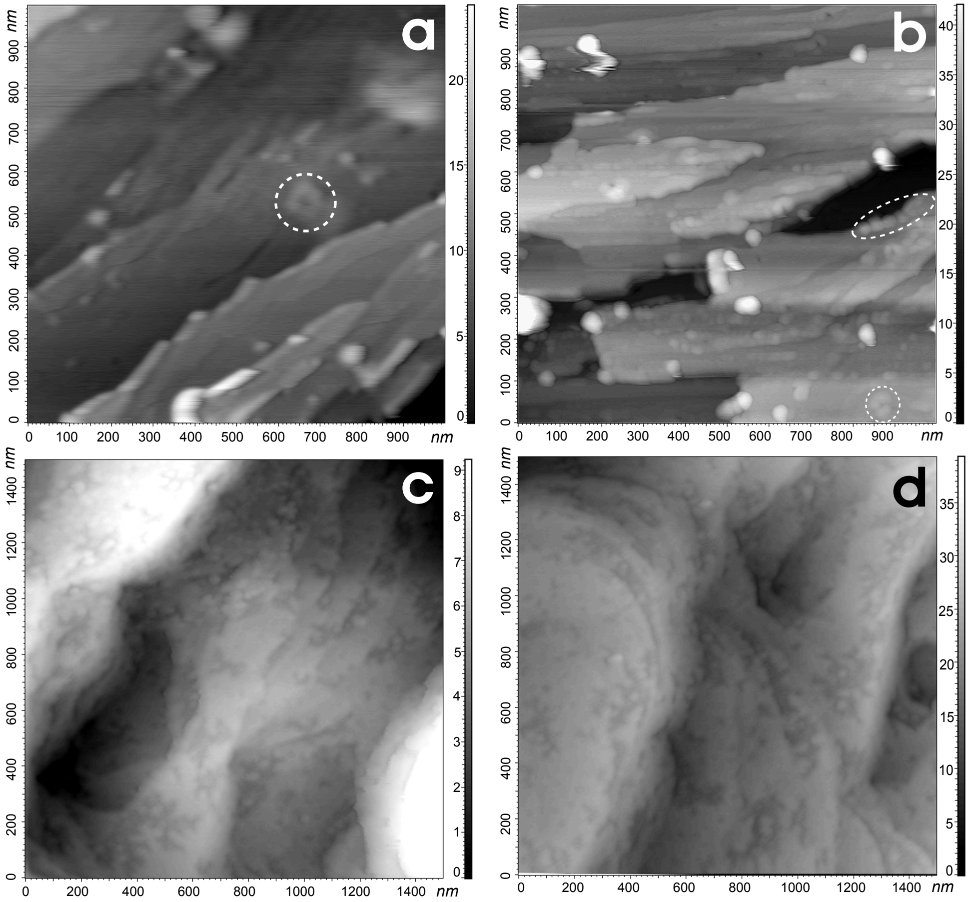

Figure 6.6: Ring- and chain-like formations (a,b) and coral-like structures (c,d) in heavily irradiated NaCl samples. The AFM topography images were taken under UHV conditions.

In addition, several irradiated crystals have been studied under ambient conditions with a NT-MDT Ntegra setup. Large square holes with a diameter of about 50 nm and about 20 nm deep were observed in the AFM images (figure 6.5). The size of the holes should be less than the real ones because of the convolution effect. The large holes are assumed to be faceted vacancy voids, which are usually observed with electron scanning microscopy (these observations are presented in the next chapter).

Interesting results have been obtained for NaCl samples, which had been irradiated up to a dose of 3000 MGy. The nanoparticles, observed in these samples show spatial arrangements, like corals, rings and lines, which consist of building blocks of small spherical particles (figure 6.6). The individual particles in these clusters have lateral sizes of typically about

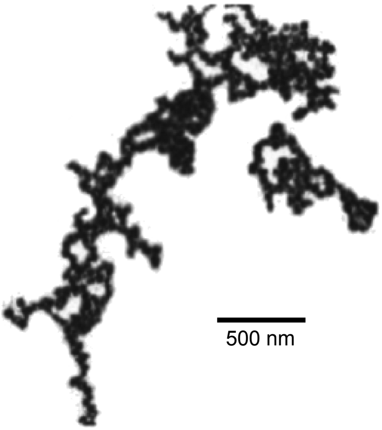

Figure 6.7: TEM image of coral-like formations of silver nanocrystals obtained in NaCl:Ag after a thermal treatment at 600°C. The image was obtained by Enculescu et al [5], the scale bar was added to the original image based on the data mentioned in [5].

10 nm and heights less than 2 nm. The overall distribution of the clusters of particles in the crystal is still very inhomogeneous. It seems that heavily irradiated crystals show a complex spatial organization of sodium nanoparticles. However, separated spherical particles have also been observed for some of heavily irradiated samples. The first visualizations of organized structures of Na precipitates in irradiated NaCl by means of AFM have been pioneered by Gaynutdinov [3]. It is interesting to note that very similar coral-like fractal structures have been observed in NaCl:Ag, KCl:Ag, KI:Ag and KBr:Ag crystals by Vasile et al [4] and Enculescu et al [5,6] by means of TEM. An example of the TEM images of coral-like arrangements of Ag particles taken from [5] is shown in fig 6.3. Silver nanocrystals were obtained by Vasile et al and Enculescu et al after electrolytic coloration and subsequent thermal annealing of the crystals.

6.4 Spatial arrangement of sodium nanoparticles

The observation of spatial structures formed by the small individual sodium particles in heavily irradiated NaCl is very significant since this appears to be a natural feature of systems of sodium and other metallic precipitates in ionic materials. Measurements of the latent heat of melting of radiolytic sodium in our samples have shown that an additional melting peak appears at temperatures higher than the equilibrium bulk melting temperature of sodium, T_{Na}^{0} when the total LHM of sodium value (which increases with irradiation dose) is higher than about 1 – 1.5 J/g. This melting peak has been observed for samples, in which spatial structures have been revealed by means of AFM. The origin of the high temperature melting peak is associated with melting of the finest sodium precipitates. The number of sodium atoms in the surface layer of these particles (i.e. the interface with the host NaCl matrix) is much larger than the number of atoms in the inner, volume part. Melting of the surface layer gives rise to the high temperature peak (see *chapter IV* of this thesis). In addition, annealing experiments, performed by Seinen [7,8] on irradiated samples at moderate temperatures (180 ^{0}C) have shown that during annealing the high temperature peak shifts to the temperatures well below the bulk melting temperature of sodium T^0_{Na}. At the same time the LHM value does not change, indicating that no changes in the amount of metallic sodium are induced. Seinen has explained this observation by smoothing of the highly irregular, jagged surface of the particles during annealing. This leads to a decrease of the surface curvature and a decrease of the melting temperature, as the latter is largely determined by the interface energy [7]. Direct AFM observations of precipitate structures with highly developed surfaces support this interpretation. Annealing of structures consisting of closely spaced individual particles, leads to coalescence of the particles and this also results in a decrease of the melting temperature.

Besides, ESR experiments carried out on heavily and ultra-heavily irradiated NaCl crystals have demonstrated anomalous magnetic properties of these samples [9-12]. The behavior of the width and intensity of the ESR line with the temperature and irradiation dose, obtained in these experiments, was unusual. It was not possible to explain these results by a simple model for a system with isolated metallic nanoparticles. On the other hand the results were very similar to those obtained for one-dimensional or quasi-one-dimensional conducting structures (for example, alkali fullerides). The results of Raman scattering experiments also support the idea of the presence of structures consisting of very small connected metallic particles in the NaCl matrix after high-dose irradiation [13,14], see also *chapter VIII*.

The results presented in this chapter have revealed formations of closely spaced metallic nanoparticles, such as strings and rings, and they can in fact be regarded as quasi-one-dimensional conductors. This is in agreement with the above mentioned ESR and Raman results, which can be explained by the presence of conducting nanowires.

6.5 Possible mechanism of the formation of the structures of nanoparticles

We will now discuss a possible mechanism of the formation of structures of agglomerates of sodium nanoparticles in heavily irradiated NaCl. It is well known for metals and alloys, which are subjected to cascade damage, that dislocations are usually decorated by high densities of small clusters of self-interstitial atoms [15,16]. Similarly, we propose that sodium particles in heavily irradiated NaCl accumulate along dislocations and dislocation loops, giving rise to the observed string- and ring-like structures. However, this explanation is in contrast with the existing models of radiolysis in NaCl [17,18], which are based on the postulate that dislocations are biased toward absorption of *H*-centers compared to *F*-centers, or more practically, the dislocation bias for *H*-centers is larger than the mean bias of the system. This means that sodium particles, which grow by the accumulation of *F*-centers, are not formed during irradiation in the vicinity of dislocations. The discrepancy can be overcome by taking into account the fact that the dislocation bias depends on the arrangement of the dislocations and total sink strength. Real dislocation structures in irradiated materials are usually very inhomogeneous and consist of various dislocation patterns such as pile-ups, walls etc. It is known that dislocation dipoles, dislocation walls and pile-ups of dislocation loops have a smaller bias than isolated edge dislocations [19]. The physical reason for this is the overlapping and mutual annihilation of the elastic fields of individual dislocations in pile-ups. When the bias of a dense dislocation pattern is smaller than the mean bias of the overall system, these structures absorb more easily *F* than *H*-centers. Excess *F*-centers arriving at the dislocation in the pattern migrate along the dislocation line and form nanoparticles associated with these dislocations. At sufficiently high doses these nanoparticles form densely-packed (chain- and ring-like) 1-D structures. The mechanism of dislocation patterning is related to the mechanism of gas bubble growth. According to a recently developed model [18] the process of growth of Cl_2 gas bubbles is accompanied by punching of dislocation loops. These loops are assumed to grow and form dislocation pile-ups. Decoration of the dislocations by self-interstitial loops may also occur in NaCl, i.e. elastic interaction of nano-size prismatic dislocation loops, punched from growing bubbles, with isolated dislocation lines may result in accumulation of these loops near the dislocation lines. One may expect that the bias of these structures is smaller that the mean bias, which results in a preferential flow of *F*-centers to these structures. Hence decoration of the dislocation forest by nanoparticles takes place, resulting in the formation of irregular fractal-like metallic structures, like those shown in figure 6.6. The mechanism of formation of sodium nanoparticle along dislocations has been discussed in [20] in terms of the spatial dependence of the dislocation bias for *H*-center absorption.

In the next section the results of combined AFM and DSC investigations on low and moderately irradiated NaCl samples are discussed. Isolated sodium particles of various sizes have been visualized in these samples by means of AFM. Differential scanning calorimetry experiments have provided us with the temperature spectra of the melting transition in these particles. An analysis of the experimental data has been carried out and the results are discussed in terms of a phenomenological model of melting of sodium precipitates.

6.6 A phenomenological model for melting of sodium precipitates

The phenomenological model of melting of the sodium nanoparticles, which will be used here, is based on the results of experiments carried out with two independent experimental techniques: differential scanning calorimetry (DSC) and AFM. Several low and moderately irradiated potassium-doped NaCl samples (see table 6.1) have been studied by means of DSC to detect the melting spectra of the sodium particles. In these samples two well-resolved melting peaks have been observed at 82 ºC (peak 1) and 92 ºC (peak 2). The temperature positions and their relative intensities of the melting peaks are typical for this type of irradiated samples (see *chapter IV* of this thesis).

Table 6.1: Parameters of the investigated samples. The irradiation doses, the irradiation temperatures, and the thermal characteristics of the samples (i.e. the LHM and the associated Na volume fraction).

Sample	Matrix and dopant	Dose	Irradiation Temperature	Latent heat of melting	Volume fraction of metallic Na
I	NaCl + 1000 ppm Potassium chloride	100 MGy (4x10^{17}e$^-$/cm^2)	120 ˚C	0.35 J/g	0.69 %
II		200 MGy (8x10^{17}e$^-$/cm^2)	100 ˚C	0.47 J/g	0.93 %
III		300 MGy (12x10^{17}e$^-$/cm^2)	100 ˚C	0.59 J/g	1.16 %
IV		400 MGy (16x10^{17}e$^-$/cm^2)	100 ˚C	0.61 J/g	1.21 %
V		400 MGy (16x10^{17}e$^-$/cm^2)	130 ˚C	0.74 J/g	1.46 %

The AFM investigations have been carried out on exactly the same samples. Randomly distributed isolated sodium particles with various sizes were visualized at the cleaved surface of the crystals. To obtain the size distribution of the particles, the heights of the protrusions, associated with the particles have been carefully measured and analyzed. The information obtained from the AFM experiments was used to reconstruct the real particle size distribution. The radius of the AFM tips used in these experiments was about 20 nm, which is larger than the particle size. As a result, because of above mentioned convolution effect between the surface and the tip, the lateral sizes of small particles will be distorted significantly, whereas lateral sizes of large particles will be displayed only slightly larger than the real ones. This results in a distortion of the measured size distribution, while the extent of the distortion depends on the particle size. To avoid this complexity, the heights of the particles were used in the analysis instead of the lateral sizes.

Thus, for each sample the distribution of the heights of the protrusions of the particles was obtained by accumulating the results from about 5 images 1000x1000 nm obtained from different areas of the sample. Some of the scans are presented in figure 6.8 and the distributions of the protrusion heights are presented in the histograms in figure 6.9 together with the corresponding DCS spectra.

Reconstruction of size distribution function

The AFM data sets obtained in this investigation have been used to reconstruct the volume size distribution of our radiation-induced sodium nanoparticles. Mathematically, the problem is formulated as follows. Let the 3D-medium (the NaCl matrix) contain spherical objects (sodium nanoparticles) with a size distribution given by the function $F(R)$, which is normalized at unity with respect to the number density of the objects

$$\int_0^\infty F(R)dR = n_V \tag{6.1}$$

where n_V is the volume fraction of the particles. Similar to the experimental procedure the crystalline medium is cleaved along one of the {100} planes such that the nanoparticles are not cleaved. Because of the symmetry of the problem, it is assumed that a particle with radius R protrudes above the surface to a maximum height $h_{max} = R$. Otherwise the particle remains in the opposite part of the cleaved matrix (see figure 6.1).

During AFM scanning of the sample surface we have collected the data, which are used to determine the shape of the distribution function of the protrusions *f(h)* normalized to the surface number density of the protrusions,

$$\int_0^\infty f(h)dh = n_S \qquad (6.2)$$

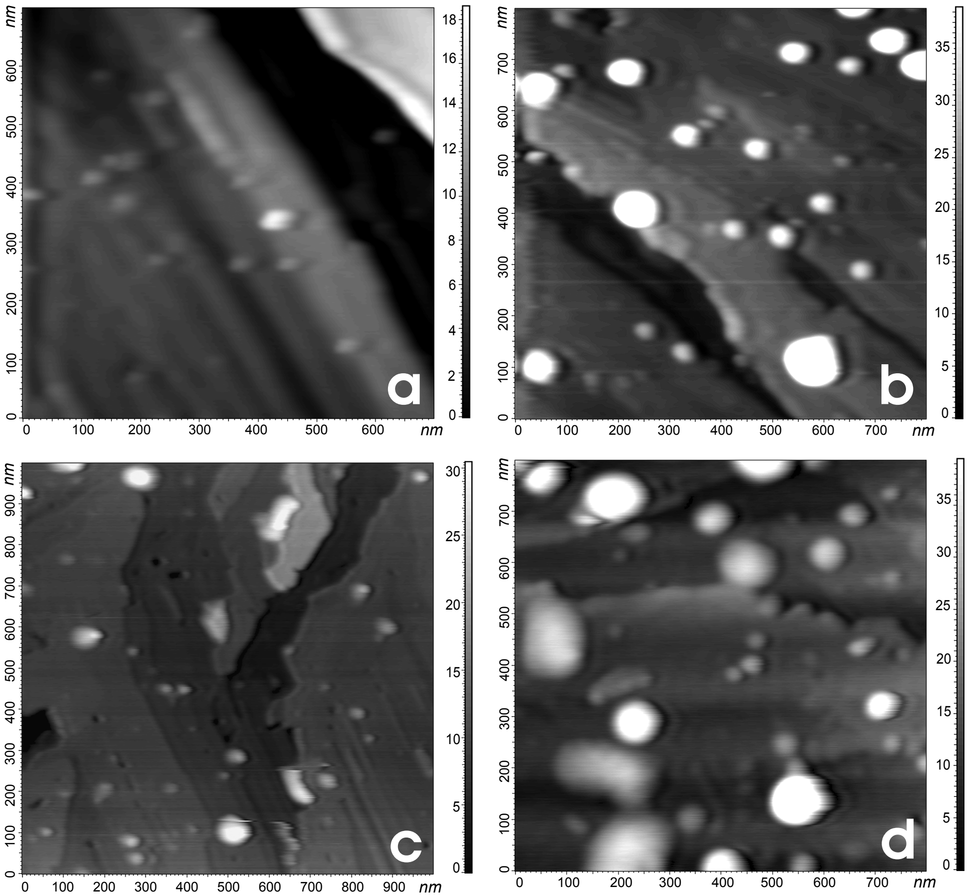

Figure 6.8: AFM images of samples irradiated up to doses 100 MGy (a), 200 MGy (b), 300 MGy (c) and 400 MGy (d).

Here, n_S is the surface concentration of the protruding nanoparticles. It can be shown that the 2D and 3D distribution functions are related by the following expressions[1]

$$f(h) = \int_h^\infty F(R)dR \qquad F(R) = -\frac{df(R)}{dR} \tag{6.3}$$

It follows from (6.3) that *f(h)* decreases monotonously with increasing *h* since the distribution function *F(R)* is positive by definition, i.e. the inequality $F(R) \geq 0$ must hold. This implies that *f(h)* has its maximum value at $h = 0$.

Experimentally, the maximum is observed at sizes larger than zero (see figure 6.9). This can be explained simply by the fact that it is not possible to measure (or to distinguish) a protrusion with zero height. Furthermore, if we are dealing with imperfect, rough surfaces, small protrusions are hardly distinguishable. So, there is a certain finite minimum height, at which the protrusions can be detected, and this minimum height depends on the surface roughness. Because we have found that the surface roughness increases with the irradiation dose, it can be concluded that with increasing amount of damage the minimum size of the precipitates that can be observed with AFM increases.

Using (6.3) one can easily find the relation between the moments of the distribution functions

$$\langle h^n \rangle n_S = \frac{1}{n+1} \langle R^{n+1} \rangle n_V \tag{6.4}$$

where the angular brackets stand for the averages of the corresponding distribution functions. Therefore the volume fraction of the nanoparticles can be written as

$$V_{col} = \frac{4\pi}{3} \int_0^\infty R^3 F(R)dR = 4\pi n_S \langle h^2 \rangle \tag{6.5}$$

This formula can be rewritten into another equation, which can be applied directly to estimate the volume fraction of the sodium nanoparticles from the AFM data

$$V_{col}^{AFM} = 4\pi \frac{N}{S} \frac{\sum_i h_i^2 n_i}{\sum_i n_i} \tag{6.6}$$

Here, N is the total number of protrusions found by means of AFM, S is the scanned surface area and n_i is the number of protrusions of height h_i. The volume fraction of metallic sodium

---

[1] The general mathematical aspects of the problem of relating the volume distributions of objects in a 3D medium to the surface distribution of cross-sections, obtained by a planar cut of the medium, are considered in [21]

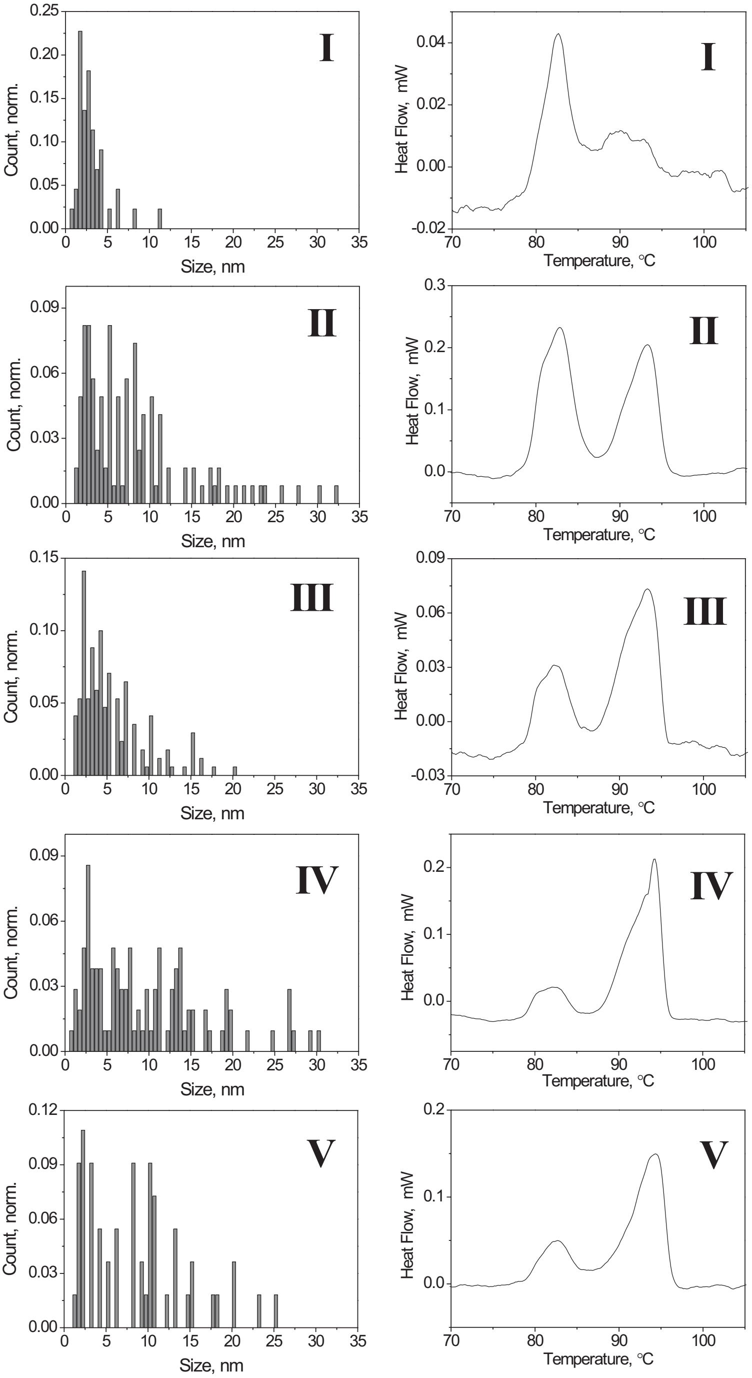

Figure 6.9: Distributions of protrusion heights and DSC-spectra for NaCl samples irradiated up to doses 100 MGy (I), 200 MGy (II), 300 MGy (III) and 400 MGy (IV and V).

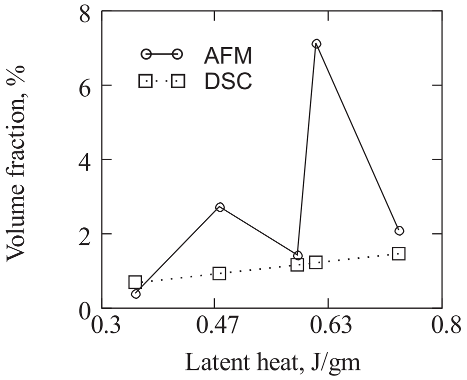

Figure 6.10: The dependence of the colloid volume fraction derived from (i) the AFM data (circles, equation 6.6) and (ii) from the LHM of the Na-colloids (squares, equation 6.7).

in the sample can be also derived from the latent heat results obtained with DSC. This means that the results from two independent experimental methods can be cross-checked. The volume fraction of metallic sodium is related to the total latent heat of melting (LHM) by

$$V_{col}^{DSC} = \frac{d_{NaCl}}{d_{Na}} \frac{Q}{H_f m} \tag{6.7}$$

where d_{NaCl} and d_{Na} are the densities of the matrix and metallic sodium, respectively; Q is the total measured LHM of metallic sodium, m is the sample weight and H_f is the specific heat of fusion. Here, it is assumed that the specific heat of fusion and the sodium density within the nanoparticles does not depend on the size of the nanoparticles. figure 6.10 shows the volume fraction of the nanoparticles as a function of (i) the corresponding LHM and (ii) the calculated results obtained from the AFM data.

It can be seen that the results obtained by two different methods correlate. However the scatter of the data points associated with the AFM experiments is quite large, probably because of the poor statistics due to appreciable inhomogeneities of the particle distribution in the samples. In order to obtain good statistics the scanned area should be very large, while at the same time by increasing the scanned area the smallest particles are harder to observe. Despite the lack of statistics we have tried to reconstruct the volume distribution functions for the samples irradiated to doses of 100 and 300 MGy, which show good agreement between the DSC and the AFM measurements (the first, third and the fifth data point in figure 6.10). The experimental results are represented by histograms, which have been fitted by the function

$$f(h) = \frac{2n_S}{\alpha\sqrt{\pi}} \exp\left(-\frac{h^2}{\alpha^2}\right) \tag{6.8}$$

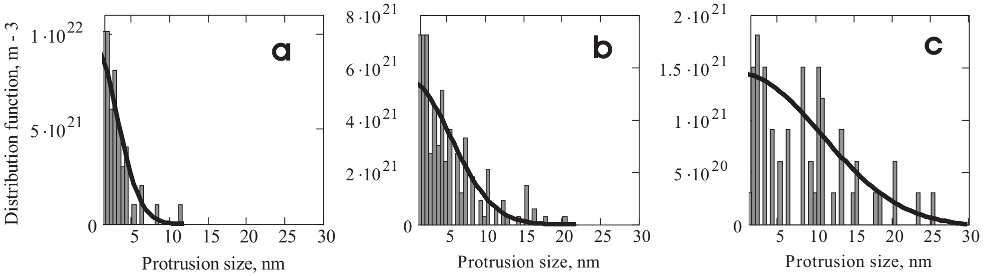

Figure 6.11: Size distribution functions of the colloid protrusions above the cleaved matrix measured by AFM after irradiation to 100 MGy (a), 300 MGy (b) and 400 MGy (c). The solid curves are the fitting functions given by equation 6.8. The distributions are normalized to the surface density (see equation 6.2).

The corresponding 3D distribution function is given by

$$F(R) = \frac{4R}{\alpha^3\sqrt{\pi}} n_S \exp\left(-\frac{R^2}{\alpha^2}\right) \tag{6.9}$$

The parameter α was adjusted to yield the same volume fractions of nanoparticles as measured with AFM, i.e.

$$\frac{4\pi}{S}\sum_i h_i^2 n_i = \int_0^\infty \frac{4\pi}{3} R^3 F_V(R)dR \tag{6.10}$$

Figure 6.11 a, b and c show the size distribution functions of the nanoparticle protrusions above the surface of the cleaved matrix along with the fitting functions. Since *f(h)* should reach its maximum value at $h = 0$, in order to obtain a good fit, the maximum values in the experimental histograms were extrapolated along x-axis to zero. The fitting functions were used to evaluate the volume size distributions of the sodium nanoparticles (figure 6.12). It is clearly seen that with increasing irradiation dose the maximum of the distribution function shifts to larger sizes.

Results and discussion

The DSC scans of the irradiated samples, which have been studied in this chapter, exhibit two melting peaks located at fixed temperature positions (82 and 92 ºC) below the melting temperature of bulk sodium (figure 6.9). The relative magnitude of the heat flow associated with the peak located at higher temperature increases with the irradiation dose. This implies the presence of two different types of particles in the NaCl matrix, which show different melting temperatures. We assume that there may be three reasons for the appearance of the two melting peaks:

1. It is known that the melting temperature of small metallic particles depends on their radius [22], and approaches the bulk melting temperature monotonically with increasing particle size. Hence, to observe two distinct well-defined melting temperatures, caused by size effects, one should assume that the particle sizes are distributed around two different values, with small deviations, because the melting peaks are quite narrow; i.e. we should be dealing with a sharp bi-modal size distribution.

2. The ensemble of particles contains two groups of precipitates with different structural states showing two different and well-defined melting temperatures. The particles can be transformed from one state to the other when they reach some critical radius during growth, without a noticeable discontinuous jump in the size.

3. The nanoparticles consist of two regions: (i) the inner part and (ii) the outer shell which is part of the NaCl-Na interface. For reasons discussed below the area of the nanoparticle close to the interface might be forced into the *fcc* structure, while the inner part has the normal *bcc* structure. This is supported by the results for Ni-nano-particles, obtained in the literature [23], which suggest that surface and core melting occurs at separate temperatures.

According to our AFM results the size distribution does not demonstrate the presence of two preferred particle sizes. The unimodal size distribution function can be obtained from the protrusions size distribution histograms with reasonable accuracy (figure 6.12). Hence we can safely rule out the first possible explanation for the existence of two melting temperatures. Our experimental observations therefore support either the second or the third possibility. With the available information it is not possible to make a choice for either option 2 or 3. Because the situation of option 2 is the simpler one with only one adjustable parameter, we will focus our attention at option 2.

Let us discuss the reason for the existence of the two different structural states mentioned in 1 and 2. At moderate temperatures the crystal structure of bulk sodium is *bcc* (with a melting temperature of 97.87ºC). It is known for free sodium that in the case of small clusters it has the *fcc* lattice structure [24,25]; our nanoparticles embedded in NaCl might also have the *fcc* structure (we emphasize that this structural state may be inherited from the NaCl-

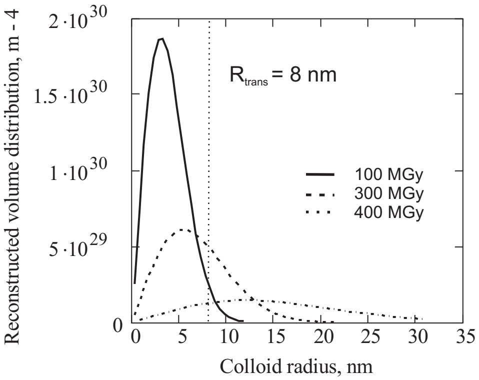

Figure 6.12: The volume size distribution functions given by equation 6.9. The meaning of R_{trans} is explained in the text.

matrix). It is likely that up to a certain radius R_{trans} the Na nanoparticle keeps its anomalous lattice structure. During irradiation the nanoparticles grow larger and their lattice structure eventually changes to *bcc* [1] [27]. This implies that the irradiated sample contains both *fcc* ($R \leq R_{trans}$) and *bcc* nanoparticles ($R > R_{trans}$), the melting temperature of which differs by a larger amount than expected on the basis of pure size effects. The melting temperature of large *bcc* nanoparticles differs from the bulk melting temperature because of size effects and the influence of the NaCl-matrix.

Strictly speaking our reasoning is valid for NaCl samples, which are subjected to irradiation at temperatures well below the temperature of the first melting peak, i.e. below 80 ºC. The samples investigated in this paper were irradiated at temperatures higher than the melting temperature of bulk sodium. This means that during irradiation the nanoparticles were in the liquid state. After irradiation the samples were cooled down to room temperature. Obviously, the size-dependent crystal structures in the nanoparticles were formed after the irradiation and during cooling. However, according to our previous results [28], the DSC scans of samples irradiated at low temperatures (T < 80 ºC) and at high temperatures (T > 100 ºC) are very similar. Moreover, the second and following DSC scans are reproducible. These remarkable facts indicate that the structural states of nanoparticles represent the equilibrium states. These states are determined by the properties of the sodium clusters and the NaCl matrix. For completeness we note that the existing experimental information does not allow us to prove whether the particles are either fully *fcc* and *bcc* or that they are hybrid systems showing surface and core melting.

---

[1] It should be mentioned that the lattice transformation of embedded particles was also observed in metallic systems. For example, ion implantation of pure aluminium with thallium gives rise to the formation of nano-sized thallium inclusions [26]. Investigations have shown that these inclusions may show either the *fcc* or *bcc* structure. Small inclusions (with diameters less than about 10 nm) are almost always *fcc* while larger inclusions (diameter larger than about 10 nm), usually are *bcc* [26]

The relative amount of heat required for complete melting of the nanoparticles of the second type (*bcc* nanoparticles) increases with increasing irradiation dose. This can be explained quite naturally by the increase of the volume fraction of *bcc* nanoparticles as a result of the increasing particle size. The melting peaks are broadened compare to the bulk melting peak, probably because of the size distribution of the particles. The combined AFM and DSC results, obtained in the present investigation, allow us to estimate the transition radius R_{trans} between the two distinct structural states of the nanoparticles. Let us assume that the melting temperatures of the nanoparticles of the two types are distributed according to the density probability functions $\rho_{1,2}(T)$

$$\rho_{1,2}(T) = \frac{1}{\sigma_{1,2}\sqrt{2\pi}} \exp\left(-\frac{(T-T_{1,2})^2}{2\sigma_{1,2}^2} \right) \tag{6.11}$$

where T_1 and T_2 are the average melting temperatures which do not depend on the particle radius; σ_1 and σ_2 are the standard deviations. The following numerical values are used below: $T_1 = 82$ ºC, $T_2 = 92$ ºC and $\sigma_{1,2} = 2$ ºC. We assume that nanoparticles with radii smaller than the transition radius R_{trans} produce the first melting peak at $T = T_1$, the other nanoparticles are responsible for the second melting peak at $T = T_2$. The heat flow as a function of the temperature is given by

$$q(T) = C\rho_1(T) \int_0^{R_{trans}} \frac{4\pi}{3} r^3 F(r)dr + C\rho_2(T) \int_{R_{trans}}^{\infty} \frac{4\pi}{3} r^3 F(r)dr \tag{6.12}$$

where $C = \frac{\beta_{DSC} H_f}{d_{NaCl} v_{Na}}$, β_{DSC} is the heating rate during the DSC measurements and v_{Na} is the molar volume of Na [29]. In equation 6.12 the first and the second terms at the right hand side represent the contributions to the heat flow associated with the nanoparticles of the first and second type, respectively.

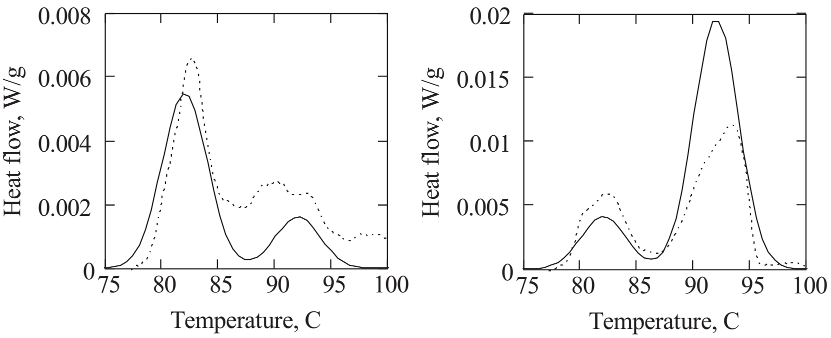

Figure 6.13: Comparison of experimental DSC curves with model DSC curves given by equation 6.12.

R_{trans} was adjusted to produce a temperature dependence of the heat flow, which is about the same as the one observed experimentally. In figure 6.13 we compare the experimental DSC curves with the reconstructed curves calculated with equation 6.12. Unfortunately, for the third sample we could not simulate a DSC curve, which is reasonably close to the experimental one. The reason for this might be the very poor statistics of the particles obtained by AFM. In fact, the lowest number of scans in the whole set of treated samples was obtained for this sample, and the number of measured particles was also quite low. Therefore a relatively large inaccuracy appears in the approximation of the size distribution of the protrusions (equation 6.8), and consequently in the reconstructed distribution of the volume of the particles sizes.

However, in those cases where the above-mentioned comparisons were successful, it was possible to estimate the transition radius R_{trans}. According to our estimations, during growth of the nanoparticle the transition from the *fcc* to the *bcc* state occurs when the particles reach the size R_{trans} = 8 nm. This estimation doesn't contradict the experimental results for melting obtained for free sodium clusters [24,25], where the transition radius has been found to be about 3.5 - 4 nm (i.e. clusters of about 10^4 atoms). We expect a larger value for R_{trans} for clusters embedded in a rigid NaCl-matrix compared with free Na-particles, since the surrounding matrix forces the Na-atoms to retain the *fcc* lattice of the Na sublattice [29], similar to small lithium precipitates in lithium fluoride [30].

6.7 Conclusions

The results of the investigations presented in this chapter deviate from those in the remaining parts of this thesis. In contrast with CESR, DSC, Raman scattering, wide angle X-ray scattering, which provide us with *indirect* information about colloidal systems of metallic Na, AFM pictures of Na colloids in NaCl might reveal details about the shape, size and geometry of these intriguing precipitate systems. In this investigation *direct* investigations of sodium precipitate systems in irradiated NaCl crystals have been carried out by means of atomic force microscopy. Radiolytic Na particles, which are situated in the bulk of the irradiated crystal, have been brought to the surface of the sample by cleaving the crystal along one of the crystalline plane. The cleaving procedure and the measurements are required to be carried out under ultra-high vacuum conditions to avoid chemical reactions between very active metallic sodium and the atmospheric water vapor and oxygen. Successive imaging of the sodium nanoparticles has been obtained with AFM facilities, which allow experiments under ultra-high vacuum conditions. Results of the AFM observation of numerous irradiated NaCl samples revealed Na particles with a rather broad size distribution. However, the radii of observed particles did not exceed hundred nanometers, and most of the particles were found to have sizes as small as only several nanometers. At the same time the spatial arrangement of the precipitates in the crystals is inhomogeneous. The particles were typically found accumulated at some preferential areas at the sample surface. In slightly and moderately irradiated NaCl samples the Na precipitates are isolated objects, embedded in the NaCl matrix.

For some of the samples we have tentatively calculated the size distributions of the Na particles. The results of these calculations have shown that with increasing irradiation dose and amount of metallic sodium in the sample the size distribution of the precipitates becomes more broadened and extends to larger particle sizes.

The next very important result of our investigation is the observation of dense coral-like and string- and ring-like organizations of Na particles in heavily irradiated NaCl samples. The sizes of the individual particles in these structures have been found to be about 2 – 5 nm. The organized structures may be formed as a result of decoration of the dislocations and dislocation loops by small metallic particles. Probably, the structures of very small Na particles in the advanced stages of the irradiation are created by rearrangements of neighboring sodium precipitates. We assume that in this process the diameter of the large precipitates is reduced, which means that the average size of the precipitates decreases drastically. This is in line with the results of CESR, SQUID and Raman spectroscopy, which indicate the presence of small interacting metallic particles, which are arranged in quasi-one-dimensional structures (*chapter VIII*). At the same time the experimental results of the differential scanning calorimetry of heavily irradiated NaCl samples (*chapter IV*) demonstrate that most of the metallic sodium in these samples is present in particles with a strong surface curvature or with ultrafine surface irregularities. These results indicate that the fine structure of the sodium precipitates, observed with AFM is not a marginal effect, but the appearance of these formations is an essential feature of later stages of radiolysis in NaCl crystals. In addition, the AFM results presented in this chapter are very relevant for the interpretation of the results of wide-angle X-ray scattering experiments, outlined in *chapter VIII*. The latter experiments seem to suggest that the size of the Na particles increases very strongly with increasing irradiation dose, while the results of independent experiments with several other techniques show the opposite. This contradiction can be understood in terms of a model, where highly organized structures of sodium nano-precipitates are formed, sowing i. a very strict orientation relation with the NaCl crystal, ii. although in general this orientation relation gives rise to 24 different, but equivalent orientations with respect to the NaCl crystal lattice, in rather large regions (several 100 nm) the orientation of the crystal axes of the individual Na-precipitates should be exactly the same and iii. the size of these regions increases with the concentration of metallic Na.

References

[1] L.W. Hobbs, A.E. Hughes and D. Pooley, *Proc. R. Soc. Lond.* **A332** (1973), 167-185

[2] E. Vasile, S. Polosan, E. Apostol, R. Trusca, V. Ciupina and V. Topa, *Phys. Stat. Sol.*: (*to be published*) (2006)

[3] R. Gaynutdinov, D.I. Vainshtein, S.J. Hak, A. Tolstikhina and H.W. den Hartog, *Radiat. Eff. & Def. Sol.* **158**: (1-6) (2003), 77-82

[4] E. Vasile, M. Datcu, S. Polosan, E. Apostol and V. Topa, *J. Cryst. Growth.* **198/199** (1999), 806-810

[5] M. Enculescu, I. Enculescu, V. Topa and E. Vasile, *Physica B* **324** (2002), 387-392

[6] M. Enculescu, V. Topa and E. Vasile, *Nucl. Instr. and Meth. in Phys. Res.* **B 191** (2002), 433-436

[7] J. Seinen, *Radiation damage in NaCl. The process of colloid formation*, PhD thesis, University of Groningen, (1994)

[8] J. Seinen, D.I. Vainshtein, H.C. Datema and H.W. den Hartog, *J. Phys.: Condens. Matter.* **7** (1995), 705-716

[9] D.I. Vainshtein and H.W. den Hartog, *Appl. Radiat. Isot.* **47**: (11/12) (1996), 1503-1507

[10] F.G. Cherkasov, R.G. Mustafin, S.G. L'vov, G.A. Denisenko, H.W. den Hartog and D.I. Vainshtein, *JETP Lett.* **67**: (3) (1998), 189-195

[11] F.G. Cherkasov, S.G. L'vov, D.A. Tikhonov, H.W. den Hartog and D.I. Vainshtein, *Radiat. Eff. & Def. Sol.* **157** (2002), 643-647

[12] F.G. Cherkasov, S.G. L'vov, D.A. Tikhonov, H.W. den Hartog and D.I. Vainshtein, *J. Phys.: Condens. Matter.* **14** (2002), 7311-7319

[13] E.I. Shtyrkov, A. Klimovitskii, H.W. den Hartog and D.I. Vainshtein, *J. Phys.: Condens. Matter.* **14** (2002), 9053-9068

[14] E.I. Shtyrkov, A. Klimovitskii, H.W. den Hartog and D.I. Vainshtein, *Radiat. Eff. & Def. Sol.* **158** (2003), 125-129

[15] N.M. Ghoniem, B.N. Singh, L.Z. Sun and T. Diaz de la Rubia, *J. Nucl. Mater.* **276** (2000), 166-177

[16] H. Trinkaus, B.N. Singh and A.J.E. Foreman, *J. Nucl. Mater.* **251** (1997), 172-187

[17] U. Jain and A.B. Lidiard, *Phil. Mag.* **35** (1977), 245-259

[18] V.I. Dubinko, A.A. Turkin, D.I. Vainshtein and H.W. den Hartog, *J. Nucl. Mater.* **277** (2000), 184-198

[19] A.A. Turkin and V.I. Dubinko, *Appl. Phys.* **A 58** (1994), 35-39

[20] A.V. Sugonyako, A.A. Turkin, R. Gaynutdinov, D.I. Vainshtein, H.W. den Hartog and A.A. Bukharaev, *Phys. Stat. Sol.* **2**: (1) (2005), 289-293

[21] L.P. Kok, *100 problems of my wife and their solution in theoretical stereology*, Coulomb Press, Leiden, (1990)

[22] E.L. Nagaev, *Phys. Rep.* **222**: (4-5) (1992), 199-307

[23] Y. Qi, T. Cagin, W.L. Johnson and W.A. Goddard, *J. Chem. Phys.* **115**: (1) (2001), 385-394

[24] R. Kusche, Th. Hippler, M. Schmidt, B. von Issendor and H. Haberland, *Eur. Phys. J. D* **9** (1999), 1-4

[25] T.P. Martin, U. Naher, H. Schaber and U. Zimmermann, *J. Chem. Phys.* **100**: (3) (1994), 2322

[26] A.H. Sorensen, E. Johnson, K.K. Bourdelle, A. Johansen, H.H. Andersen and L. Sarholt-Kristensen, *Phil. Mag. A* **75** (1997), 1533-1552

[27] S.N. Sulyanov, D.M. Kheiker, D.I. Vainshtein and H.W. den Hartog, *Sol. St. Commun.* **128**: (11) (2003), 419-423

[28] V.I. Dubinko, A.A. Turkin, D.I. Vainshtein and H.W. den Hartog, *J. Nucl. Mater.* **304** (2002), 117-128

[29] A.V. Sugonyako, D.I. Vainshtein, A.A. Turkin, H.W. den Hartog and A.A. Bukharaev, *J. Phys.: Condens. Matter.* **16** (2004), 785-798

[30] M. Lambert, Ch. Mazieres and A. Guinier, *J. Phys. Chem. Sol.* **18** (1961), 129-134

CHAPTER VII

INVESTIGATION OF VOIDS IN IRRADIATED NaCl WITH SCANNING ELECTRON MICROSCOPY

7.1 Introduction

It has been shown by earlier investigations carried out by our group [1-3] that the chemical and mechanical stability of the NaCl material under irradiation is directly connected with the development of voids. Therefore it is important to obtain information about the mechanisms that give rise to the formation of these voids. Vacancy voids, which appear in irradiated NaCl, turn out to be natural and regular products of the radiolysis process, next to Na precipitates, chlorine bubbles and dislocations. A statistical analysis of the void sizes, volume fraction and concentration provides valuable information about the radiolysis process in general and void and crack formation in the crystalline material under ionizing radiation in particular.

The results of our investigations of vacancy voids in a variety of irradiated pure and doped NaCl crystals are presented in this chapter. Voids, which are situated in the bulk of the crystal, can be visualized at the cleaved surface of irradiated NaCl samples using Scanning Electron Microscopy (SEM). Earlier investigations of vacancy voids in heavily irradiated NaCl [2,4] have revealed that the general trend for all investigated systems is that the void volume fraction increases with the irradiation dose. In the present investigations we have extended the observations of voids to much higher irradiation doses. The study of the voids in a variety of samples has helped us to observe the differences in the sizes, shapes and densities of the voids, growing in the crystals with various impurities, and ultimately to assess the consequences with regard to the radiation stability of NaCl.

The present investigations of the extremely damaged crystals show that the tendency of an increasing fraction of the void volume with the irradiation dose is observed even for ultra-high doses; no saturation of the volume of the voids has been found. However, the rate of the void growth process turned out to depend significantly on the presence of impurities. The shape of the voids was also found to be different for NaCl samples, doped with different impurities. In addition, we note that for NaCl doped with KCl the void growth rate was found to be approximately inversely proportional to the dose rate, however no such dependence was observed for Br-doped samples. Three different scenarios for the void formation process in NaCl are proposed, which are based on the analysis of observations made for crystals with various impurities. These scenarios can eventually also be considered as essential stages in the overall void formation process in crystalline NaCl.

7.2 Experimental procedures

Investigations of vacancy voids in heavily irradiated NaCl crystals have been performed with a FEI Company XL-Series Scanning Electron Microscope. To visualize voids in the bulk crystal, the samples have been cleaved in air along one of the crystalline {100} planes. After cleaving, the sample was transferred as quickly as possible to the vacuum system in order to prevent chemical degradation of the surface due to reaction with water vapor in ambient atmosphere. The freshly cleaved surfaces of irradiated samples were covered by a very thin layer of metallic palladium by means of vapor deposition. This treatment was necessary in order to avoid charging of the insulating NaCl samples during exposure to the moderately energetic electron beam of the electron microscope. The electron beam energy in our experiments was in the range 3 – 12 keV.

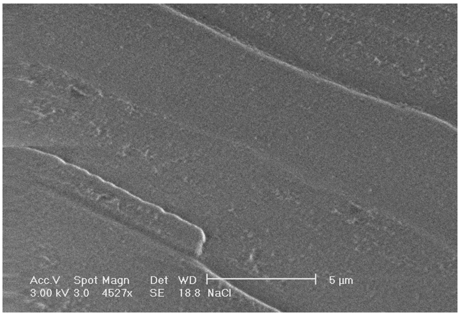

Figure 7.1: SEM image of unirradiated NaCl. Crystalline steps are observable on the flat surface with no sign of void-like formations.

As grown synthetic crystals and natural samples, which had not been irradiated, did not show any sign of void formation. The surfaces of these samples are flat, they show crystalline steps, and there is no sign of the presence of voids (see figure 7.1). Voids with sizes of tens to hundreds nanometers, showing a variety of shapes have been observed in cleaved surfaces of NaCl crystals, which had been exposed to moderate, high and ultra-high doses of irradiation[1] (figs. 7.2, 7.6, 7.7, 7.9).

Earlier experimental observations have shown that with increasing dose, relatively large voids are formed, and ultimately this formation process is followed by sudden fracture of the material. These processes are often accompanied by violent chemical reactions. We assume that in most cases the cracks are initiated by these violent local chemical reactions; the same applies to the processes leading to fracture and finally explosive decomposition of the sample

---

[1] According to our *de facto* established designation, irradiation doses of the NaCl crystals can be divided into four groups: *low* – 100 MGy and less, *moderate* – 200 to 1000 MGy, *high* – 1100 to 3000 MGy and *ultra-high* – 6000 MGy and higher (see *chapter III*).

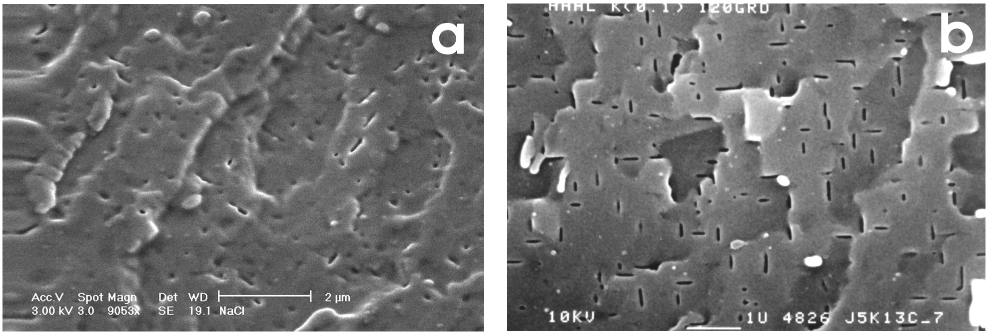

Figure 7.2: SEM image of irradiated NaCl doped with 1000 ppm KCl. (a) 'new' sample: irradiation dose 10000 MGy, dose rate 10 MGy/h, (b) 'old' sample: irradiation dose 2400 MGy, dose rate 2 MGy/h.

[1-7]. The formation of large vacancy voids correlates with the ultimate destruction of the samples under irradiation, or during heating occurs without any observable decrease of the specimen weight. This confirms that the observed cavities are vacancy voids rather than gas-filled bubbles [6]. When all radiolytic chlorine is located in voids and cracks, we would expect that during decomposition a significant fraction of this radiolysis product escapes from the sample and this leads in many cases to a measurable loss of sample mass. Therefore we have to conclude that only a small fraction of the radiation-induced chlorine atoms is captured during irradiation by the growing voids (see below). Clearly the development of vacancy voids in damaged NaCl crystals, in combination with the presence of large amounts of Na and Cl_2, affects the mechanical and chemical stability of the material under irradiation.

In this investigation SEM images have been obtained for pure and doped NaCl samples, irradiated up to 3000, 6000, 10000, 15000 and 20000 MGy at 100 ^{o}C at a dose rate of 10 MGy/h. For each dose value several samples have been investigated. The observed voids are distributed very inhomogeneously over the sample surface. The voids seem to appear preferentially in the vicinity of dislocations, and usually the concentration of voids observed on a perfectly flat surface far from the crystalline macrodefects is much smaller than the average value. Therefore, in order to obtain results, which are representative for the sample as a whole, we have investigated several areas of the sample surface for each specimen. The values of the mean void size, surface number density and surface fraction associated with the voids could be obtained only by carefully analyzing the images. However in the case of samples with a low percentage of radiolytic damage only few voids are observed on the surface of the cleaved specimen. For these samples the void statistics is poor and the values for the void concentration and surface fraction are expected to be overestimated. This is caused simply by the natural preference to choose the areas containing voids during scanning, which means that the areas without voids are underweighted in the statistical analysis. Despite the poor accuracy of the statistics and the inaccurate absolute values, all measured results are qualitatively representative.

The surface fraction of the voids has been estimated as the percentage of void area of the images. The void volume fraction has been assumed to be equal to the surface fraction. The void volume density, N_V (*vol*), was deduced from the measured density per unit surface, N_V (*surf*), and the mean size, according to the following simple relation: $N_V(vol) \approx N_V(surf)/d_V$, where d_V is the mean void size. This relation is valid for ball-shaped (or close to ball-shaped) voids, as well as and for penny-shaped voids. The error of this approximation is expected to be small compared to the statistical error.

7.3 Voids in pure and doped NaCl

An earlier investigation of voids in irradiated NaCl [4] has been carried out for samples irradiated up to 600-2400 MGy at a dose rate of 2 MGy/h. The general trend observed in [4] is that for all investigated, slightly and moderately damaged materials there are only a few, very small observable voids. The voids in these samples appear to be small and round or sometimes slightly faceted. The total volume of the voids increases with increasing dose and volume fraction of the sodium particles. Elongated or penny-shaped voids were found to develop with increasing dose [8,9].

The same tendency is observed in the present investigation. The voids grow with increasing dose and also the void concentration increases. Large elongated voids are observed mainly for potassium-doped and pure samples at high and ultra-high irradiation doses. The elongated voids are strongly aligned along the <100> crystallographic directions (see figs. 7.2, 7.7). At the same time for KBF_4 and Br-doped samples large voids are typically found to be cubic, and sometimes more or less round (figs. 7.9, 7.6). Small, round voids and large, elongated ones can be detected simultaneously in the same image (figure 7.7 a). It should be noted, that voids with sizes less than 20 nm are difficult to observe with our equipment. It is possible, that although they cannot be observed, voids with sizes less than 10 nm are also present in the early stages of the irradiation.

NaCl doped with 1000 ppm KCl

NaCl crystals doped with 1000 ppm KCl have been found to be the most unstable systems under irradiation [5,10]. The samples of this material were fractured completely and turned into very small, sometimes dust-like fragments during irradiation above 10000 MGy. According to the observations, elongated penny-shaped voids are typical for this type of samples. The void density for KCl doped samples increases significantly with increasing latent heat of melting (LHM) of sodium precipitates (i.e., with increasing volume fraction of radiation-induced metallic sodium). Two plots showing this behavior are presented in figure 7.3 a,b. The surface fraction S_v and the volume density N_v of the voids increase linearly with increasing irradiation dose (figure 7.3 c,d). Interesting results were obtained from a comparison of the previous ('old') [4] and present ('new') observations of voids. The NaCl crystals used in the 'old' investigations have been irradiated up to a maximum dose of 2400

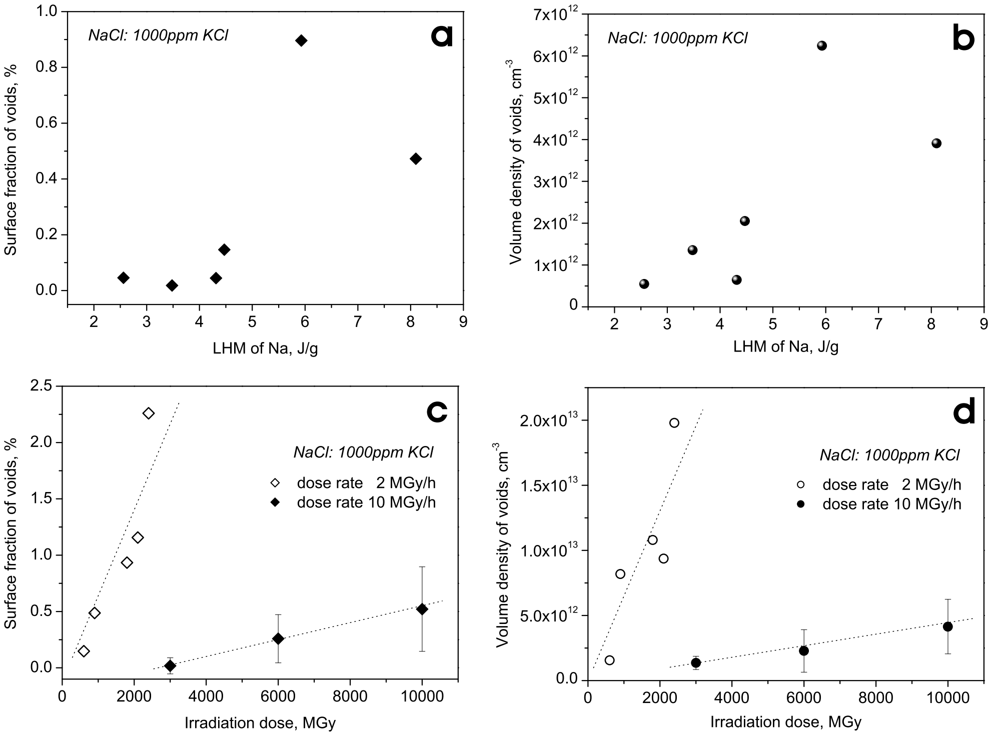

Figure 7.3: NaCl doped with 1000 ppm KCl. Void surface fraction (a) and volume density (b) versus LHM of precipitated sodium. Void surface fraction (c) and volume density (d) as a function of irradiation dose. Open circles and diamonds correspond to the 'old' irradiation, full ones – to the 'new' irradiation, respectively. The error bars show data scatter for a certain dose.

MGy at a dose rate of 2 MGy/h. The irradiation dose of the 'new' samples is in the range 3000 – 20000 MGy, the dose rate in this irradiation run was 10 MGy/h. The plots of S_v and N_v versus the irradiation dose, presented in figure 7.3 c,d show a factor of more than ten difference between the rate of increase of the concentration of voids in the 'old' and 'new' samples. The surface fraction and the volume density of the voids in previously irradiated crystals grows very steeply. The maximum 'old' N_v value exceeds almost three times the maximum N_v value for the 'new' samples, whereas the final irradiation dose is four times larger for the 'new' crystals. The large difference in the development of the voids in 'old' and 'new' KCl doped NaCl samples may be caused by the difference in irradiation dose rate – this parameter was 5 times higher in 'new' irradiation procedure.

It is likely that voids develop faster under irradiation at lower dose rates (at about 100 °C). Indeed, higher dose rates lead to an increase of the production rate of point defects (PD) – *F*- *H*- and V_F-centers and consequently to the reduction of the average distance between PD-s. This means an increase of the probability of direct back reactions between *F*- and *H*-centers and therefore a decrease of the mean path of PD in the crystal. The flux of the PD-s reaching the extended defects (ED) decreases, which leads to a decrease of the efficiency of the radiolysis process. Taking in the account that the average distance between voids is much larger than the corresponding distance between colloids or bubbles and because the total surface area of the voids is significantly smaller than for chlorine bubbles and sodium particles in the NaCl crystal, flux of PD-s to voids is reduced drastically compared with the fluxes to the chlorine bubbles and sodium particles. Hence, fewer F and V_F-centers, which are needed for void growth, reach the surface of the voids. This leads to a appreciable decrease of the growth rate of the voids at higher irradiation dose rates.

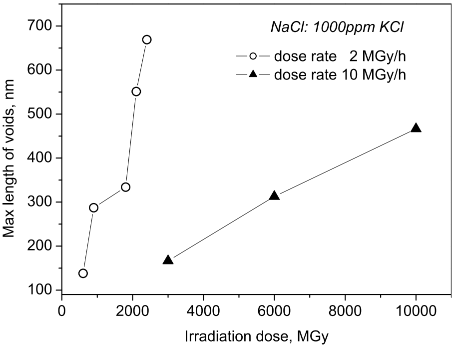

Figure 7.4: NaCl doped with 1000 ppm KCl. Maximum length of the voids. Open circles correspond to the 'old' irradiation, the full triangles – to the 'new' irradiation respectively.

We also note that higher concentrations of large elongated voids were found for the low dose rate samples (compare the images figure 7.2a and figure 7.2b). From the point of view of radiation resistance of crystalline materials, the length of elongated voids is a critical parameter for the mechanical stability of the sample under irradiation [7-9,11]. A comparison of the maximum void lengths for various sets of potassium doped NaCl samples shows larger values of the void lengths and fast growth of the void lengths with the dose for the samples irradiated at a low dose rate (figure 7.4). Hence, KCl doped samples appear to be significantly less resistant and less stable during irradiation at low dose rates.

NaCl doped with 500 ppm NaBr

Similar comparisons as for NaCl:K between 'new' and 'old' samples have been made for crystals, doped with 500 ppm NaBr. This type of NaCl materials was found to be most resistant to ionizing radiation. In contrast with the previous case, in Br doped crystals the void volume density of the 'old' samples is only slightly higher than the minimum values obtained for the 'new' ones. The growth rate of the voids is assumed to be approximately the same for dose rates of 2 and 10 MGy/hr (see figure 7.5 b). The surface fraction of the

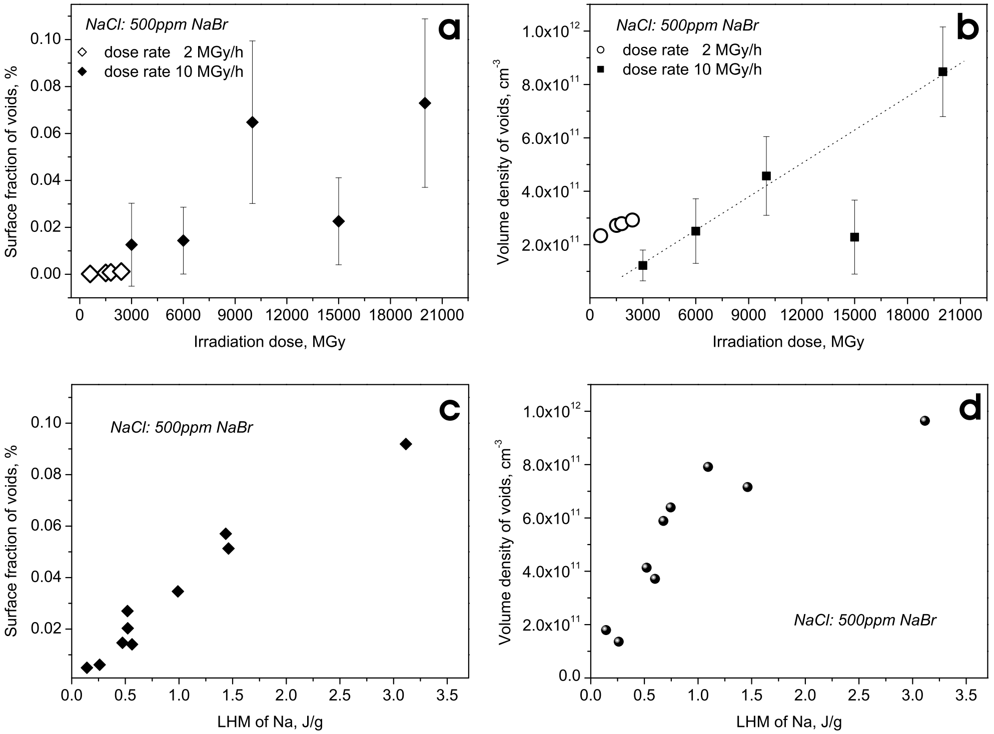

Figure 7.5: NaCl doped with 500 ppm NaBr. Void surface fraction (a) and volume density (b) as a function of irradiation dose. Open circles and diamonds correspond to the 'old' irradiation, full diamonds and squares – to the 'new' irradiation respectively. The error bars show data scatter for a certain dose. Void surface fraction (c) and volume density (d) versus LHM of precipitated sodium.

voids in these samples show good agreement between the old and new results (figure 7.5 a), although it should be noticed, that the absolute values of the surface fraction S_v for this type of material are very small (less than 0.1%) and the scatter of the data is quite large. Also the above mentioned systematic error, caused by the small number of observed voids is expected here to play a role. At the same time the general tendency of the volume density of the voids to grow with increasing LHM of sodium is also observed for Br doped samples (figure 7.5 c,d). SEM images with voids in the cleaved surface of Br doped NaCl samples are presented in figure 7.6. As discussed above, relatively small numbers of round and faceted diamond-shaped voids were found. These observations may help to understand the reason for the high mechanical stability of Br-doped samples irradiated up to ultra-high doses. The very low concentrations of voids, their small sizes and especially the absence of elongated voids indicate that the level of damage in initial matrix of the NaBr-doped samples is low, compared to KCl-doped samples.

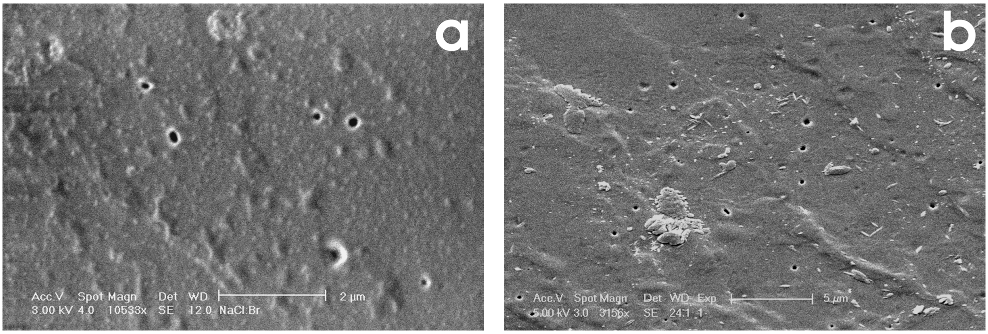

Figure 7.6: SEM image of irradiated NaCl doped with 500 ppm NaBr. Voids are typically round or faceted.

Pure NaCl

Ultra-heavily irradiated pure NaCl crystals show quite high concentrations of voids and significant void surface fractions. These pure samples show penny-shaped voids, which are more or less faceted along the preferred growth directions. These voids are strongly aligned along the <100> crystallographic directions of the NaCl matrix (figs. 7.7 a, b, c).

The increase of the void volume density with increasing irradiation dose and the LHM of Na is approximately linear for pure NaCl samples (figure 7.8). However, several individual samples have been found to show strong deviations from the normal behavior. The deviations were observed in particular for ultra-high dose irradiated samples, which show a high volume density of voids. In some cases the volume density of the voids in these samples exceeds several times the typical N_v value for the other pure NaCl samples at the same irradiation dose (figure 7.8 b). At the same time the LHM values are unusually low (figure 7.8 a). This remarkable feature can be explained by intense, but very small scale and therefore nondestructive back reactions, which occur in these NaCl crystals during irradiation. It might be that for some reason in these samples with large numbers of voids local back reactions between voids filled with Cl_2 and sodium particles are more frequent than in other samples at the same irradiation dose. The back reactions between chlorine gas in the voids and sodium particles result in a significant reduction of the fraction of metallic sodium and hence, the LHM of sodium for these ultra-heavily damaged samples is low.

Back reactions may lead to the formation of nano-sized cracks in the crystalline material [7-9,11]. Relatively small cracks (compared with those of the order of tens microns, which are typical for fractured materials [7,11]) are observed for pure NaCl, which had been irradiated up to ultra-high doses (figure 7.7 c). The observation of these cracks indicates that quite often back reactions occur in these samples, which supports the description of the crack formation processes in terms of localized back reactions, described above.

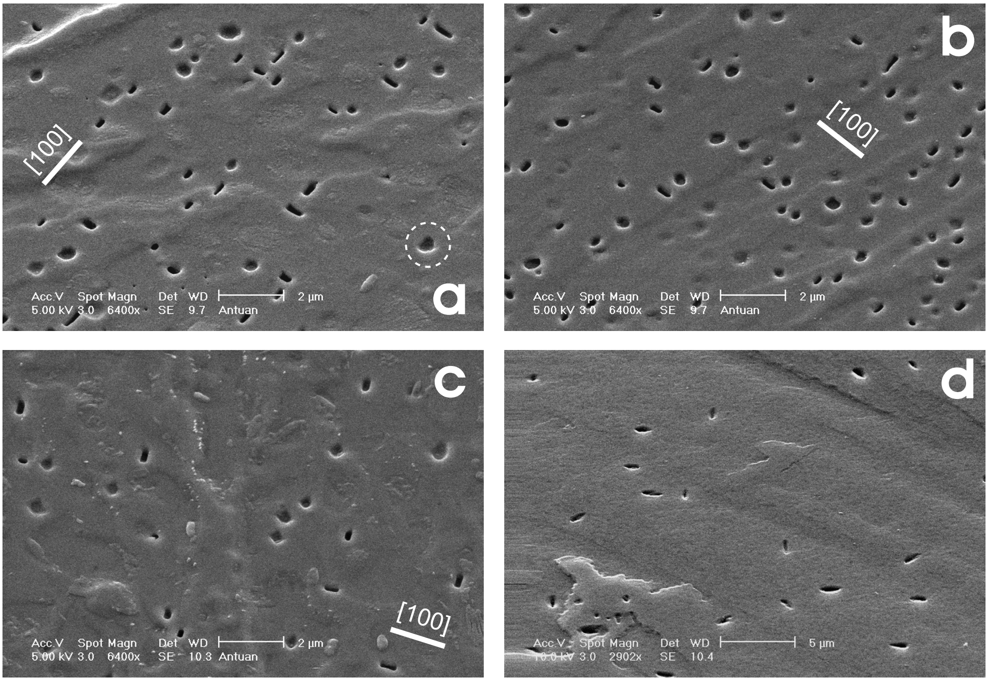

Figure 7.7: SEM image of irradiated pure NaCl. Large elongated voids are strongly aligned along the <100> crystallographic directions (a,b,c), voids with all three possible orientations are presented. Partly faceted voids can be found in the image a. (d) relatively small cracks (about a micron length) show rather rough shape. (Take notice of the different scales in the images).

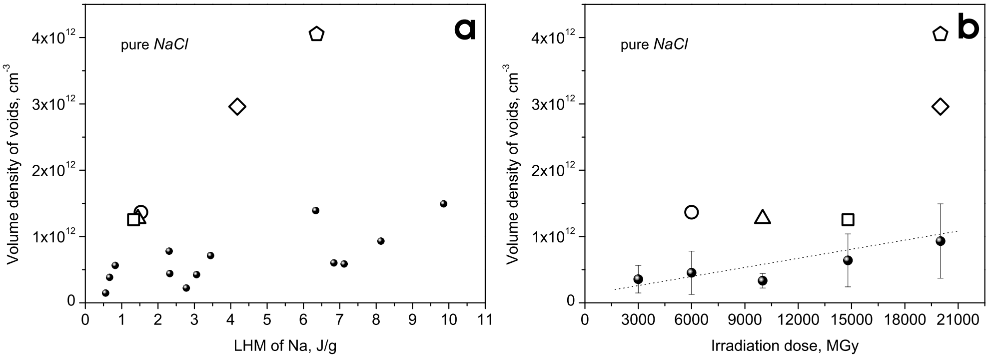

Figure 7.8: Pure NaCl samples. Void volume density versus a) the LHM of Na, b) the irradiation dose. The open figures in both plots show particular samples with untypical N_v values. The error bars in the b) plot show the data scatter for a certain dose.

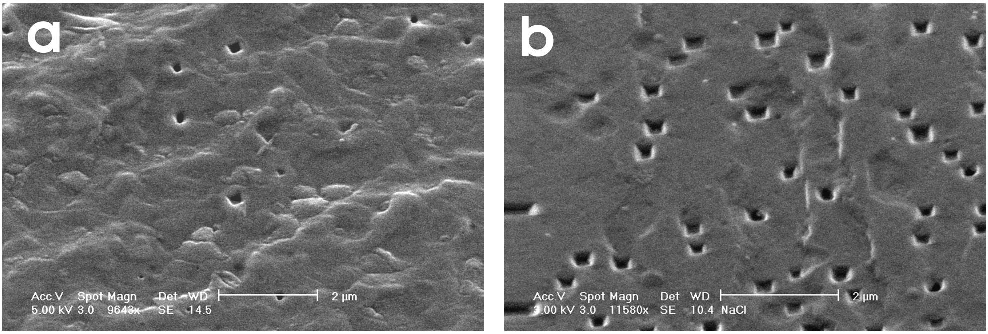

Figure 7.9: SEM image of irradiated NaCl doped with 300 ppm KBF_4. The large voids are more or less cubic.

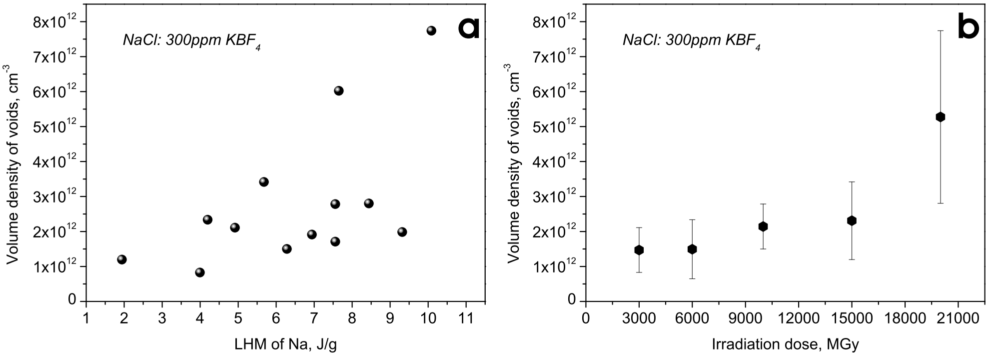

Figure 7.10: NaCl samples doped with 300 ppm KBF_4. Void volume density versus (a) the LHM of Na, (b) the irradiation dose. The error bars on the b plot show the data scatter for a certain dose. The dispersion of the data points is significant, especially for very heavily damaged samples.

NaCl doped with 300 ppm KBF_4

The voids observed in heavily damaged NaCl samples doped with 300 ppm of KBF_4 appear to be mostly faceted and more or less cubic (figure 7.9). Large elongated voids are rarely detected in this type of samples. The highest values of the void volume density obtained in this investigation were found in KBF_4 doped samples. However, the data scatter is rather large, and it increases with increasing irradiation doses, which means with increasing values of the LHM of Na. Despite the large scatter of the data it is concluded that, the characteristic behavior of the volume density of the voids is that it increases with increasing LHM of Na (i.e. with increasing irradiation dose); see the plots in figure 7.10 a and b. Again, like in pure NaCl, local back reactions in these samples may lead to a reduction of the amount of metallic sodium, which causes a large scatter of the data point in the plot N_v vs. the LHM of sodium. However, in contrast with the situation for pure NaCl, samples with very large deviations from the mean ratio of the void concentration and the LHM of sodium have not been observed for KBF_4-doped samples. This may be caused by the fact that localized back reactions don't occur as extensively as in pure NaCl. We note that in ultra-heavily irradiated KBF_4-doped NaCl localized back reactions may occur. Compared with pure NaCl samples these phenomena take place less frequently in $NaCl:KBF_4$.

7.4 Scenarios of void and crack formation

The void nucleation mechanism, which is used to understand the observations for heavily damaged NaCl has been proposed by our group (Dubinko et al [12-14]). It has been described in detail and illustrated by a scheme in *chapter II* of this thesis. In brief we can say that voids nucleate as a result of highly localized back reactions between a growing sodium particle and a chlorine nano-bubble. The energy released during the back reaction causes a highly localized temperature spike, which is accompanied by an increase of the local pressure up to several GPa. Such a high pressure induces plastic deformations in the surrounding crystalline material, which leads to the formation of an empty cavity (void nucleus) with a radius exceeding the radius of the bubble, which was present prior to the back reaction [13]. These new, small voids continue to grow by absorbing V_F and F-centers, which creates divacancies at their boundaries as a result of mutual recombination of these point defects. The scenarios of continued void and crack formation are described below and have been illustrated in the scheme shown in figure 7.11.

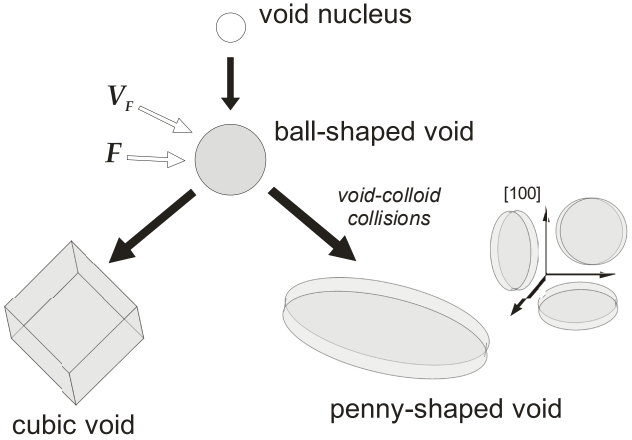

Figure 7.11: The scheme of the voids development stages.

The fate of a void nucleated as explained above depends on the fluxes of the point defects in the crystal during irradiation and the average sizes and mean distances between the extended radiolytic defects (ED-s): the sodium precipitates and the chlorine bubbles. It is important to note here that according to the usual terminology voids turn out to be tertiary radiolytic defects. This nomenclature is used on the basis of the appearance of voids due to reactions between secondary ED-s (Na-colloids and chlorine bubbles). There are three scenarios of void growth that can be used to explain the differences in the void shapes observed for the materials investigated in this thesis.

The first one is the case of high rate of the mutual recombination between the primary radiation defects (*F*- and *H*-centers), followed by slow production of V_F-centers, bubbles and colloids. According to the radiolysis model developed in our laboratory [12,15] this leads to the formation of only few voids, which have only little ‘food’ (divacancies formed by recombination of *F*- and V_F-centers) to grow and therefore they remain small and round even at high doses. This picture might be applicable to Br-doped crystals (figure 7.6). There is however a second possibility to explain the formation of preferentially small and round voids at high doses. If voids are biased to absorb *H*-centers (i.e. when the corresponding bias is larger than mean bias of the system [13]) the production of divacancies at the void boundary as a result of mutual recombination of V_F and *F*-centers will be suppressed. Besides, it should be mentioned that according to our experimental observations the round shape of the voids is typical for all crystals at rather low irradiation doses. This round shape usually related to the early stages of void growth.

The second scenario of void growth can be regarded as an extension of the growth observed in the first stage. Divacancies, which are created at the void boundary, cause the volume of the empty cavity to increase. This implies that the void size increases. From thermodynamical point of view divacancies will join the void surface such that the total void surface energy is minimized. This leads to faceting of the voids, similar to well known faceting of metallic clusters and embedded particles in crystalline hosts. We may expect a cubic shape for the empty cavities in the cubic NaCl lattice; the main axes of these cubic voids should be strongly aligned along the crystal axes of the host matrix. This situation is observed for KBF_4-doped samples (figure 7.9).

A third scenario is observed when void growth is driven by localized back reactions between radiolytic ED-s in the crystal. According to [7,9,13], chlorine bubbles are the most finely dispersed ED-s in the system (a few nanometers in size, and an average inter-bubble spacing less than 10 nm). Therefore they start to collide with large (compared with the size of the bubbles and Na-precipitates) growing voids first, and during these collisions the voids are filled with chlorine gas from the bubbles. When the voids reach an average size approximately equal to the inter-colloid spacing, the growing void collides for the first time with a colloid, which initiates a violent localized back reaction between metallic sodium of the colloid and the chlorine gas in the void. A schematic picture of the sample showing the bubbles, sodium particles and voids presented at about the same scale has been given in figure 7.12.

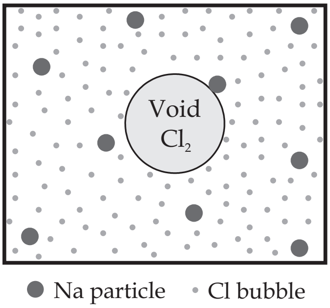

Figure 7.12: The relative sizes of the ED-s are representative for the moment of the first void-colloid collision, according to the radiolysis model, which was developed in [8].

The relative sizes of the ED-s are important parameters, which determine the moment when the first void-colloid collision takes place. This description is in accordance with the radiolysis model, which has been developed by our group, see [8]. The amount of energy released in this reaction is proportional to the energy released during the formation of one NaCl molecule and to the number of molecules formed as a result of the back reaction. The latter is approximately equal to the mean number of sodium atoms in the colloid, which is on the average close to the number of chlorine atoms accumulated in the void at the time of the collision [11,13,16]. The exothermic reaction between radiolytic Na and Cl_2 is completed extremely fastly (in the nanosecond range [16]), and this leads to a sudden and very steep rise of the temperature inside the void, which is accompanied by a very fast pressure increase [9] and thermo elastic stresses in the surrounding matrix [16]. The tangential stresses are expected to exceed the threshold value of the stress required for localized cleavage of the matrix [16], and this results in crack formation and crack propagation from the void along the {100} cleavage planes of the surrounding matrix. When the pressure drops below the threshold value the development of the crack stops. This process leads to the transition of equiaxial voids to penny-shaped nano-cracks [8], which in our SEM experiments behave like the original voids. This is why these features in heavily damaged NaCl are referred to as either voids or cracks. Obviously, these penny-shaped voids are oriented parallel to the three perpendicular {100} planes of the NaCl crystal. The penny-shaped voids in the cleaved surface of the sample look like 1D elongated voids when the sample is cleaved along a plane, which cuts the crack perpendicularly (figure 7.2); however, sometimes nearly round and very shallow holes are observed, when the cracks are oriented along the cleavage plane (figs. 7.7 a, b, c). This situation has been observed most clearly for heavily and ultra-heavily damaged pure and K doped samples. During continued irradiation the penny-shaped voids grow further by the absorption of V_F and F-centers. During this growth process the penny-shaped voids may become faceted again. Several voids in figs. 7.7 a and c are found to be partly faceted, they are presumably in the intermediate stage between the penny-shaped, present immediately after the back reaction, and the new faceted state. At the same time, during continued growth of the voids the process of bubble capture continues to take place, and this leads to new, even more violent back reactions between captured chlorine vapor and Na precipitates.

Because bubbles and colloids are distributed rather inhomogeneously in the matrix, collisions between voids and sodium particles occur more or less randomly which results in a distribution of void sizes and shapes. As long as the energy released during the back reaction is proportional to the amount of absorbed sodium and chlorine molecules, the power of the back reactions increases with the size of the voids and the colloids. This means that at sufficiently high volume fractions of the radiolytic products the propagating crack may sweep the sample volume and bring into contact adjacent chlorine and sodium precipitates, which results in self-sustained propagation of the cracks and ultimately it will lead to explosive decomposition of the sample [1,3].

It should be noted that the proposed scenarios describe only the characteristic behavior of the above-mentioned groups of samples. According to our observations voids corresponding to each of the above-mentioned three scenarios are found almost in all samples. It seems that the general trend for all investigated systems is that the average void size and the concentration increase with the irradiation dose, while the void shape transforms from round to faceted and ultimately penny-shaped are formed. From this point of view the scenarios described above are important steps in the overall void formation process. Each of these steps may be realized in all types of the NaCl materials at a certain irradiation dose, which depends on the composition of the sample, the irradiation dose and the dose rate.

7.5 Temperature enhanced nucleation of voids

Very interesting SEM pictures were obtained for NaCl samples, which had been annealed for 15 min at about 170 °C. NaCl:Br and NaCl:F crystals, which had been irradiated up to ultra-high doses, were used for the investigations. ‘As irradiated’ samples of these materials show very low concentrations of voids. After annealing the number of voids in the crystal shows a drastic increase. Very high concentrations of small voids in the annealed samples can be seen in the image presented in figure 7.13. Many tiny voids are observed with sizes, which are close to the resolution of the SEM device.

These observations clearly show that only a moderate increase of the temperature (compared to the increase to 500 °C needed for a complete annealing of all radiolytic defects in NaCl) initiates void formation process in this type of material. The temperature-induced void formation in heavily damaged samples can be understood in terms of the above described void nucleation mechanism. Indeed, by increasing the temperature during annealing the mobility of PD-s is enhanced and this causes rearrangement and coarsening of the radiolytic ED-s (chlorine bubbles and sodium particles). As a result many collisions between small chlorine bubbles and sodium particles occur. These collisions lead to localized exothermic back reactions, which, according to the model causes nucleation of voids.

Detailed investigations of temperature-induced void formation may be helpful in order to confirm the void nucleation mechanism, proposed above. Thus, measurements of the change in the LHM of sodium and chlorine before and after annealing combined with monitoring of the behavior of the void concentration and void growth with the temperature might help to find the relationship between the supposed decrease of the chlorine and sodium volume fraction on one hand and the formation of voids and the behavior of the void volume fraction on the other. By studying several types of irradiated samples one might be able to shed light on the differences in the void growth process, which leads to various void shapes, which have been observed by means of SEM.

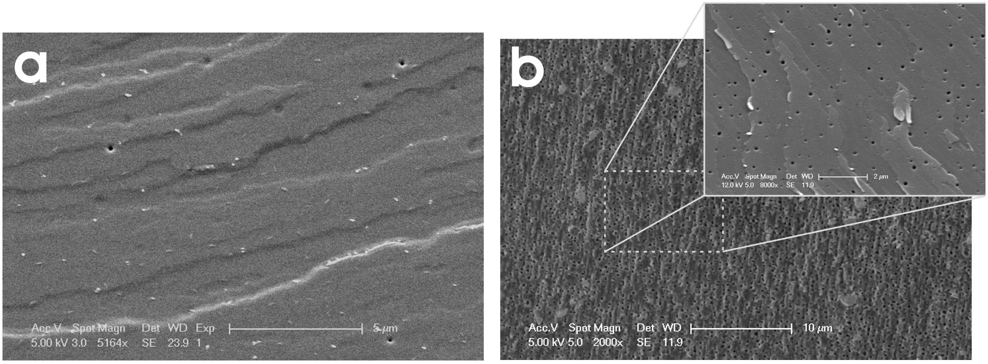

Figure 7.13: SEM images of an 'as irradiated' NaCl:Br sample (a), and an annealed at 170 °C for 15 min (b). A very large number of new voids appears in the crystal after increasing sample temperature. Please note the scale in image a is about twice that on the image b. The magnified image in b was taken from different area of the sample surface to detect the smallest voids located on a flat surface.

7.6 Conclusions

In the present investigations of voids in ultra-heavily irradiated NaCl we have shown that different impurities in the NaCl crystals lead to the formation of the voids with different shapes and sizes. Also the void concentrations and growth rates depend strongly on the presence of impurities in the samples. A detailed analysis of the SEM images, measured for large numbers of NaCl samples with various dopants allows us to draw three scenarios of the void formation process in NaCl with these impurities. A very low rate of formation of rather small spherical voids was observed to Br-doped NaCl, while the appearance of large numbers of faceted voids is typical for KBF_4-doped samples, and the presence of large numbers of elongated, penny-shaped voids is the most characteristic feature of heavily damaged pure and K-doped NaCl crystals. At the same time earlier investigations of voids in irradiated NaCl have revealed the development of small round voids in all types of NaCl crystals in earlier stages of the irradiation. In the present work rather long penny-shaped voids have been observed also for all types of the NaCl samples, including Br-doped NaCl, which had been irradiated up to ultra-high doses. In addition, faceted and partly faceted voids were found in pure and Br- and KBF_4-doped NaCl samples. Therefore, we can conclude that it is likely that the different kinds of void formation are in fact different stages of the overall process of void development. The general trend observed for all investigated systems is that the average void size and the concentration increase with the irradiation dose, while the void shape transforms from round to faceted, while finally penny-shaped voids are formed. The latter ones ultimately develop into macro-cracks, which lead to fracture and decomposition of the sample. Each of the stages of the void growth may be realized in all types of the NaCl materials at a certain irradiation dose, which depends on the composition of the sample, the irradiation dose and the dose rate.

Another interesting observation has been obtained from the comparison of earlier investigations of samples irradiated at dose rates of about 10 MGy/hr [4] and the present study where the dose rate has been increased to 100 MGy/hr. For the K-doped NaCl crystals the rate of formation of voids was found to be much larger in the case of the low dose rate experiments. In fact, for these samples the growth rate of the void volume is approximately inversely proportional to the dose rate. The concentration and volume fraction of voids are much larger in those crystals, which had been irradiated up to maximum 2400 MGy at a relatively low dose rate, while at the same time the production rate of precipitated sodium and chlorine increases much more moderately as a result of the decreased dose rate. As it was described above, because of larger flux of the PD-s to the ED-s the efficiency of the radiolysis process increases at the lower dose rate. Flux of *F*-centers, which are needed for void growth, to voids surface changes significantly with dose rate compared with the fluxes to the chlorine bubbles and sodium particles due to large average distance between voids and small total surface area of the voids in comparison with the chlorine bubbles and sodium particles. Therefore the development of the voids is enhanced significantly at low irradiation dose rate and the dose rate effect becomes much more important for the voids system, which is in agreement with our observations.

From the point of view of practical applications, i.e. storage of high-level radioactive waste (HLW) of nuclear power plants in the salt domes, the dose rate effect is very relevant since the conditions during storage are characterized by very low dose rates (typically a factor of 1.000 to 10.000 lower than the dose rate used in our laboratory experiments). Consequently, a very high efficiency of void development is expected under storage conditions, where low dose rates are combined with very high doses. With increasing growth rate of voids the stability of the irradiated NaCl will decrease drastically.

References

[1] H.W. den Hartog and D.I. Vainshtein, *Mater. Sci. Forum.* **239-241** (1997), 611-614

[2] D.I. Vainshtein, C. Altena and H.W. den Hartog, *Mater. Sci. Forum.* **239-241** (1997), 607-610

[3] D.I. Vainshtein and H.W. den Hartog, *Radiat. Eff. & Def. Sol.* **152** (2000), 23-37

[4] H.W. den Hartog, D.I. Vainshtein, V.I. Dubinko, A.A. Turkin, V.V. Gann and J. Jacobs, *Radiation Damage in NaCl. Retrievability Smart Backfill Materials Monitoring*, Report: *CORA*, University of Groningen, Groningen, (1999)

[5] H.W. den Hartog, J.C. Groote and J.R.W. Weerkamp, *Radiat. Eff. & Def. Sol.* **139** (1996), 1-19

[6] D.I. Vainshtein, V.I. Dubinko, A.A. Turkin and H.W. den Hartog, *Radiat. Eff. & Def. Sol.* **150** (1999), 173-177

[7] V.I. Dubinko, A.A. Turkin, D.I. Vainshtein and H.W. den Hartog, *Nucl. Instr. and Meth. in Phys. Res.* **B 166-167** (2000), 561-567

[8] D.I. Vainshtein, V.I. Dubinko, A.A. Turkin and H.W. den Hartog, *Nucl. Instr. and Meth. in Phys. Res.* **B 166-167** (2000), 550-555

[9] A.A. Turkin, V.I. Dubinko, D.I. Vainshtein and H.W. den Hartog, *J. Phys.: Condens. Matter.* **13** (2001), 203-216

[10] H.W. den Hartog, *Radiat. Eff. & Def. Sol.* **150** (1999), 167-172

[11] H.W. den Hartog, D.I. Vainshtein, V.I. Dubinko and A.A. Turkin, *Nucl. Instr. and Meth. in Phys. Res.* **B 191** (2002), 168-172

[12] V.I. Dubinko, A.A. Turkin, D.I. Vainshtein and H.W. den Hartog, *J. Nucl. Mater.* **277** (2000), 184-198

[13] V.I. Dubinko, A.A. Turkin, D.I. Vainshtein and H.W. den Hartog, *J. Nucl. Mater.* **289** (2001), 86-95

[14] V.I. Dubinko, A.A. Turkin, D.I. Vainshtein and H.W. den Hartog, *J. Nucl. Mater.* **304** (2002), 117-128

[15] V.I. Dubinko, A.A. Turkin, D.I. Vainshtein and H.W. den Hartog, *J. Appl. Phys.* **86**: (11) (1999), 5957-5960

[16] A.A. Turkin, V.I. Dubinko, D.I. Vainshtein and H.W. den Hartog, *Nucl. Instr. and Meth. in Phys. Res.* **B 191** (2002), 83-88

CHAPTER VIII

INVESTIGATION OF SODIUM AND CHLORINE PRECIPITATES IN IRRADIATED NaCl WITH ESR, RAMAN SCATTERING AND WIDE ANGLE X-RAY DIFFRACTION

Introduction

The major part of our experimental investigations was devoted to calorimetry and two microscopic methods (AFM and SEM), which were used to study very heavily irradiated NaCl crystals. From the results of these measurements it was clear that the properties of small radiolytic precipitates in NaCl are quite different from those of bulk sodium and chlorine. Although these experiments have provided us with valuable information about sodium and chlorine particles themselves, more detailed knowledge about the precipitated systems as a whole and their properties with the focus on the interactions with the damaged NaCl matrix are certainly worthwhile. For this reason we have carried out additional experiments, which are entirely independent from the above-mentioned ones, to improve our understanding of these highly damaged materials.

There are numerous possibilities to study the Na-precipitates, because their physical properties, such as the electronic structure, are completely different from those of the host NaCl crystal. For this reason these precipitates are very suitable for optical, magnetic and electrical investigations. Conduction electron spin resonance (CESR) and Raman Scattering (RS) experiments have provided us with a wealth of detailed information about Na-precipitates in irradiated NaCl.

The other radiolytic products, which are the counter part of the Na-precipitates, are the halogen (chlorine) gas bubbles. During the accumulation of *H*-centers, which are in fact interstitial chlorine atoms, chlorine bubbles develop, which occupy interstitial positions in the crystalline matrix. The small average size of these bubbles along with the high pressure of the chlorine gas in the bubbles are the reasons why the properties of these precipitates are quite unusual. In addition, we emphasize the importance of chlorine bubbles, because these extended defects have a dominant effect on the radiolysis process. This is why these objects are very interesting to investigate. Compared with sodium particles chlorine precipitates are far less accessible with experimental research techniques. The most important and the only experimental method, which was used until now, was calorimetry (DSC) of the melting and freezing processes in chlorine bubbles, and this method has been used extensively in this investigation, see *chapter V*. It is highly desirable to have apart from DSC at least one more independent experimental method available for the investigation of these extended defects. Optically and magnetically, chlorine bubbles are not very interesting. In contrast with Na-particles chlorine bubbles don’t possess conduction electrons, holes or trapped electrons, which may couple with electromagnetic waves or show paramagnetism. This means, that it is not possible to investigate chlorine bubbles with optical absorption/emission, electron spin resonance or AC/DC conductivity. It is not possible to study Cl_2 bubbles with AFM and

SEM, because because chlorine gas from the bubbles would escape from the bubbles when they are brought to the surface of NaCl sample. Recently, in a collaborative study Sulyanov, Kheiker, den Hartog and Vainshtein have investigated Na precipitates with wide angle X-ray scattering (WAXS). In the present study the diffraction patterns associated with solid chlorine precipitates in NaCl have been observed for the first time at 95 K. These experiments have been carried out in combination with latent heat experiments, which were required to characterize the defect state of the samples used for our investigations.

The experimental results presented in this chapter provide us with valuable additional information about the extended defects, which are formed during high dose ionizing radiation. Two sections in this chapter are devoted to conduction electron spin resonance (CESR) and Raman scattering observations of Na precipitates, the third section is devoted to the results of X-ray scattering observations of both sodium and chlorine precipitates in ultra-heavily irradiated NaCl crystals.

8A CONDUCTION ELECTRON SPIN RESONANCE (CESR) OF NA PRECIPITATES

8A.1 Introduction. CESR in small isolated Na particles

Conduction electron spin resonance measurements carried out on irradiated NaCl samples provide us with information about electronic structure of sodium precipitates, which depends on the size of these metallic particles and eventual interactions between these particles. Many experimental investigations of conduction electron spin resonance (CESR) in small sodium metallic particles have been published over the past 4-5 decades; a small selection of papers can be found in ref.'s [1-5]. At the same time a large number of theoretical papers and reviews devoted to CESR in small metallic particles has appeared in the literature since the early 60's [6-13]. When metallic particles have sizes of about one micron or smaller, the shape and the width of the resonance line are significantly different from those of bulk metal. The width of the CESR line is determined by the relaxation time of the conduction electron spins. The principal mechanisms contributing to the spin relaxation process are usually spin-flip scattering by phonons, non-magnetic impurities and surfaces. If the particles are sufficiently small scattering of the conduction electron spins by the particle surface is the dominant relaxation process. In those cases the CESR line width provides information about the size of the particles. The relaxation time T_2 due to the scattering of the conduction electrons by the surface of the particle is given by [10]:

$$\frac{1}{T_2}_{Surf.} = \frac{\varepsilon v_F S}{4V} = \frac{3\varepsilon v_F}{4R} \tag{8A.1}$$

where V is the volume, S the surface area and R the radius of particle, v_F is the Fermi velocity and ε is the probability of a spin flip each time the electron is scattered by the surface. With increasing radius of the particle the contribution of the scattering of electrons by the particle surface to the spin relaxation rate decreases. Thus, the spin relaxation time increases, which leads to a decrease of the line-width. When the radius of metallic particle is in the range between several or a few times ten nanometers, quantum size effects influence the intensity and the shape of the CESR signal. With decreasing size of the particle the energy levels in the conduction band become more and more discrete, and the separation between the levels increases. The average energy level spacing in the conduction band δ_e is given by [7,12]:

$$\delta_e = \frac{4E_F}{3N_e} \tag{8A.2}$$

where N_e is the number of conduction electrons in the particle and E_F is the Fermi energy measured from the bottom of the conduction band. When the separation between successive energy levels in the conduction band is sufficiently large, quantum size effects are observed for (i) the spin populations in the particles and (ii) the spin relaxation time. As a result quantum size effects may influence the intensity of the CESR line and its width [6-9].

The temperature dependence of the intensity of the CESR signal for small metallic particles appears to be of either Curie or Pauli type [12,14]. In the case of Curie paramagnetism the magnetic susceptibility varies inversely with the temperature, just as for simple systems with isolated paramagnetic impurity centers. The alignment of the electron spins is favored by the external magnetic field and this alignment is (partly) destroyed by thermal disorder. Pauli susceptibility is temperature independent since the number of unpaired conduction electrons at the top of the conduction band increases linearly with T. In earlier investigations [15-17] Curie-type behavior of the intensity of the resonance signal (which is proportional to the magnetic susceptibility) has been observed for low- and moderately damaged NaCl samples up to certain temperature. At this temperature, which varied in range from 140 K down to 30 K, the susceptibility behavior as a function of T shows a crossover from Curie to Pauli type paramagnetism. At the crossover temperature the energy level spacing δ_e between the electronic levels can be overcome by thermal excitations, i.e. $kT \approx \delta_e$. Using the equation 8A.2 the average numbers of electrons in the sodium particles has been estimated in [15-17] from the cross-over temperatures. Since number of conduction electrons is equal to the number of atoms in the small sodium particles, the average numbers of sodium atoms N and the average diameters of sodium particles d could be estimated to be $310 \leq N \leq 1750$ and $21 \leq d \leq 48$ Å, respectively for low- and moderately irradiated NaCl samples.

In the present observations of sodium precipitates in heavily and ultra-heavily irradiated NaCl crystals the Curie-type behavior has not been observed. Instead, the CESR line intensity as a function of T was found to increase up to a certain temperature, where the susceptibility changed to more or less Pauli behavior. At the same time the line-width showed a significant decrease. Hence, the behavior of the magnetic susceptibility at low temperatures is completely different from both Curie and Pauli-types. This behavior of the resonance signal suggests that in case of heavily- and ultra-heavily irradiated NaCl we are dealing with systems consisting of extremely small, interacting and closely spaced metallic particles rather than isolated precipitates. Interactions between the particles affect the paramagnetic resonance line, and this makes the situation far more complex than in the case of isolated and non-interacting metallic precipitates.

8A.2 Experimental techniques

The ESR experiments have been carried out in the temperature range between 4 and 300 K using an X-band Varian Centuries Series ESR spectrometer, operating at 9.25 GHz. Low temperature measurements were performed in conjunction with an Oxford Instruments flow cryostat with helium as refrigerant. The modulation frequency was 100 kHz and the modulation amplitude was 2 Gauss; the scan range was chosen to be sufficiently large to allow accurate evaluation of the line wings. In our investigations the scan range was chosen to be 800 Gauss and the scan rate was 50 Gauss/min. The microwave power was about 1 mW, and the sodium precipitates signal showed no sign of saturation.

In the present investigations we have observed the CESR signal of Na-precipitates in ultra-heavily irradiated NaCl samples as a function of the damage percentage, deduced from the DSC peak(s) associated with melting of these precipitates, see *chapter IV*. Several pure NaCl samples with an amount of metallic sodium of about 10-18 at% have been used for measuring the static magnetic susceptibility by means of a superconducting quantum interference device (SQUID). SQUID experiments have been carried with a serial SQUID-magnetometer (Quantum Design) between 5 and 200 K.

8A.3 Dependence of the CESR line on the temperature and amount of Na

The single-line CESR absorption signal associated with Na nanoparticles dispersed in irradiated NaCl crystals show a nearly symmetric Lorentzian line shape for all measured samples. The behavior of the CESR signal at room temperature (RT) with increasing irradiation dose has been determined from an analysis of the experimental data of ultra-heavily irradiated NaCl and the results of previous observations of moderately and heavily irradiated samples [16-20]. In figure 8A.1 the CESR line intensity, which is calculated by double integration of the CESR signal, is presented as a function of the latent heat of melting (LHM) of sodium for ultra-heavily irradiated NaCl samples. The LHM of sodium, which is measured by means of DSC, see *chapter IV*, is proportional to the amount of metallic sodium in the irradiated NaCl samples. The plot in figure 8A.1 shows a linear behavior, which indicates that the intensity of the CESR line is proportional to the amount of precipitated sodium in the irradiated NaCl samples, i.e. it is proportional to the damage percentage. This result for our ultra-heavily irradiated samples is in good agreement with earlier investigations of low and moderately irradiated NaCl [15].

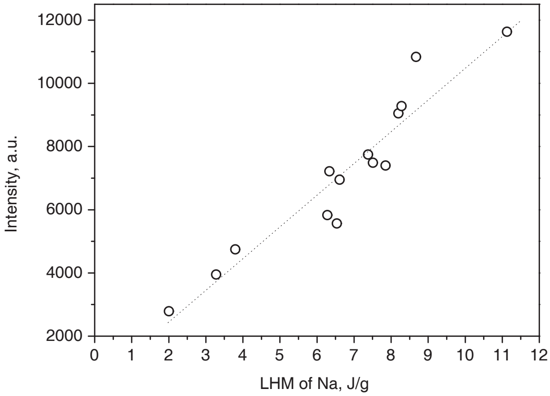

Figure 8A.1: The intensity of ESR signal vs. the latent heat of melting of precipitated sodium. The dotted line shows a linear fit of the experimental data.

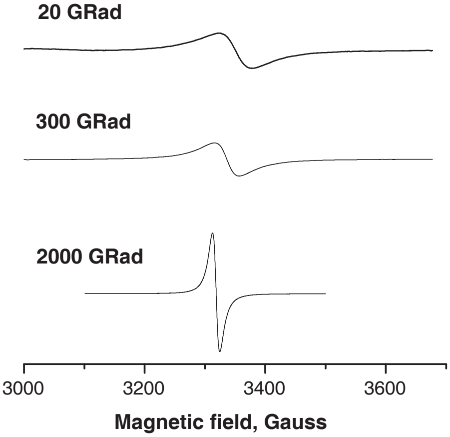

Figure 8A.2: The evolution of the ESR spectrum in NaCl with increasing irradiation dose.

The peak-to-peak linewidth (*dH*) of the CESR signal measured at RT decreases gradually with increasing irradiation dose, which corresponds with increasing amounts of metallic Na. The evolution of the CESR spectrum with increasing dose is shown in figure 8A.2 for three typical irradiated NaCl samples. The first sample has been irradiated to a dose of 20 GRad (200 MGy, the upper curve in figure 8A.2). The p-p line width is as large as 61.5 Gauss. In this dose range the p-p line width decreases rapidly with increasing irradiation dose. The second example in figure 8A.2 (curve in the center) shows the CESR signal of a sample, which had been irradiated to a dose equal to 300 GRad (3000 MGy); the line width for this sample is 43.4 Gauss. Also in this dose range the line width decreases rather rapidly with increasing irradiation dose. The third example (lower curve in figure 8A.2) was obtained for a sample, which was exposed to 2000 GRad (20000 MGy). The line width observed for this sample is 11.8 Gauss. The behavior of the width of CESR line as a function of the latent heat of melting (LHM) of sodium precipitates (which is proportional to the concentration of metallic Na in the sample) is presented in figure 8A.3. The line width decreases rapidly to about 15 Gauss with increasing concentration of metallic sodium up to about 2-4 at%, which corresponds to a LHM value of 1-2 J/g. When the LHM of Na is increased further the linewidth *dH* decreases slowly and approaches a minimum value of about 11 Gauss. This minimum linewidth is still appreciably larger than the value found for bulk sodium at room temperature, which is 6 - 7 Gauss [21,22].

The CESR signal intensity and the linewidth *dH* as a function of the temperature are shown in figure 8A.4 for several ultra-heavily irradiated pure and KBF_4 doped NaCl samples. The results are presented for samples, which had been irradiated up to 600, 1000 and 2000 Grad (6000, 10000 and 20000 MGy). The damage percentage has been measured by means of DSC and is shown expressed in terms of the LHM of the precipitated sodium. For all samples the CESR linewidth decreases with decreasing temperature from RT to about 100 K. This behavior is characteristic for both bulk sodium [21-26] and for isolated small sodium particles

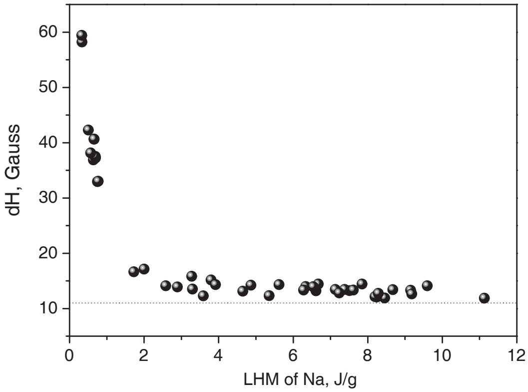

Figure 8A.3: The width of measured ESR signal as a function of the latent heat of melting of precipitated sodium. Dotted line shows the saturation value (11 Gauss).

with sizes less than about 1 µm, i.e. the skin depth for sodium at the microwave frequency of 9.25 GHz [2,4]. The slopes of the curves range from 0.016 to 0.019 Gauss/K which is close to the value of 0.018 Gauss/K, obtained by Gutowsky and Frank [23] for sodium particles with sizes ranging from 1 to 50 µm. The CESR linewidth observed in [23] is 7 Gauss at 300 K, which is attributed to bulk sodium. It is noticeable that this value is significantly smaller than 11 Gauss, which was measured for our most heavily damaged samples. In the vicinity of RT the CESR signal intensity is nearly temperature independent while showing Pauli-like susceptibility of the conduction electrons (figure 8A.4 a, b, e and f). The same behavior of the intensity around room temperature has also been observed earlier [16,17] for heavily irradiated NaCl crystals. For the most damaged samples the CESR intensity shows a slight gradual increase with decreasing temperature down to about 100 K (figure 8A.4 c, d, g and h).

Below 150-100 K the CESR line intensity starts to decrease gradually with decreasing temperature and the line-width starts to increase showing a transition occurring in a spin system of the Na precipitate system below some temperature T_C. Similar effects have been observed earlier for heavily irradiated NaCl [16,18-20]. With increasing amount of damage the transition becomes more abrupt and transition temperature T_C shifts downward to about 50 K for the most heavily damaged samples (figure 8A.4 c, d). Also for samples irradiated up to 2000 GRad (20000 MGy) there is some temperature interval above the T_C, where the linewidth is temperature independent (figure 8A.4 c, d, g and h). The origin of this temperature independent region has not been explained yet.

The increase of the CESR line-width could be evidence for a possible magnetic transition in the Na precipitates system. To verify this assumption, we have carried out SQUID measurements of the temperature dependence of the static magnetic susceptibility for several ultra-heavily irradiated samples. In some of our samples a strong peak has been observed near 50K. An example of a successful result is shown in figure 8A.5, which has been obtained for pure NaCl, which had been irradiated up to 2000 GRad (20000 MGy).

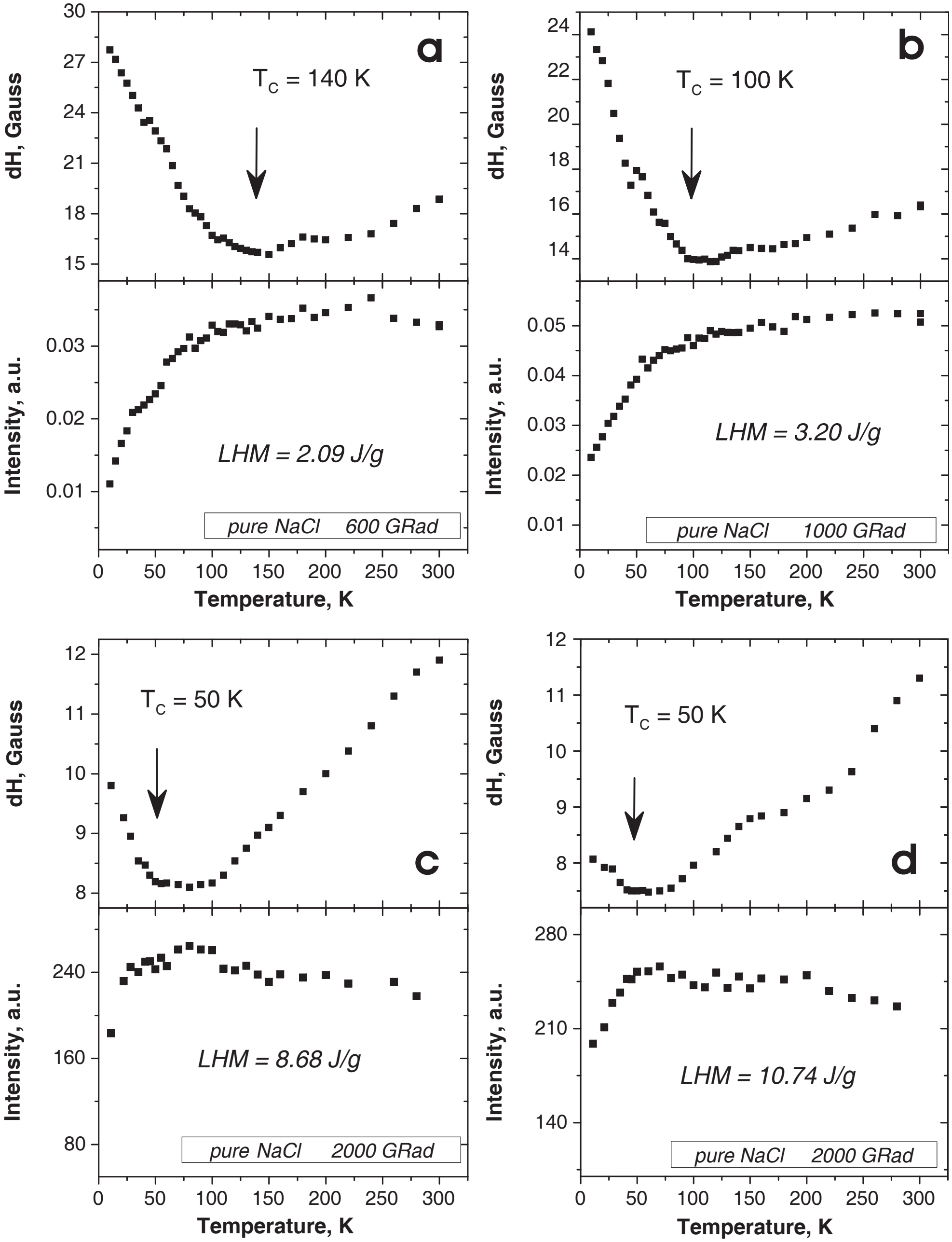

Figure 8A.4: The ESR signal width dH and intensity as a function of temperature in ultra-heavily irradiated pure NaCl samples (a, b, c and d). The temperature of transition from low-temperature to bulk metal-type behavior, T_C, shifts downwards with increasing amount of damage.

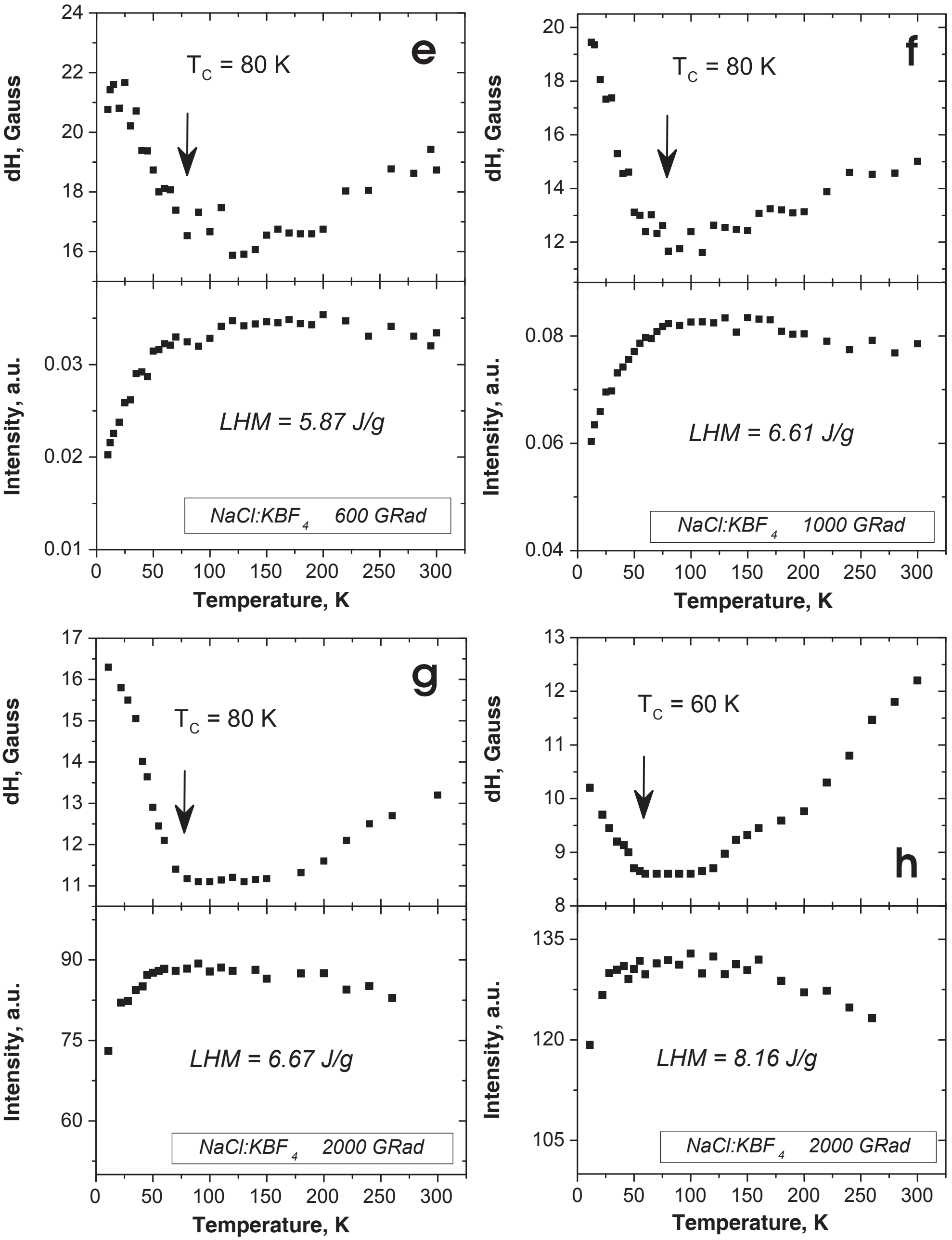

Figure 8A.4: The ESR signal width dH and intensity as a function of temperature in ultra-heavily irradiated NaCl doped with 300ppm KBF_4 samples (e, f, g and h). The temperature of transition from low-temperature to bulk metal-type behavior, T_C, shifts downwards with increasing amount of damage.

8A.4 Magnetic transition in Na precipitate systems

A decreasing CESR linewidth, measured at room temperature, have been observed by Smithard [4] for small sodium particles in X-irradiated sodium azide with increasing annealing time. During annealing the particle size was found to increase from 20 to 2000 Å. The minimum linewidth of the CESR peak of Na in sodium azide was measured to be 7.5 Gauss at 300K for particles of 2000 Å. This value for the line width is fairly close to the one for bulk sodium. In addition, an asymmetric Dysonian line shape [27] was observed when the mean particle size approached the skin depth of sodium metal (δ about 1 μm [22]). In our case of irradiated NaCl samples the decrease of the CESR linewidth, measured at room temperature, with increasing concentration of precipitated sodium can also be explained by an increase of the size of the Na particles. A symmetric Lorentzian shape of the CESR line has been observed for all, even for the most heavily damaged samples, which indicates that the Na particle radius in heavily and ultra-heavily irradiated NaCl does not reach sizes in the range of the skin depth. The CESR linewidth measured for our samples decreases with increasing Na concentration and shows saturation at about 5-6 at% metallic Na, which corresponds to a LHM value of 2.5-3 J/g. The minimum dH value, measured at room temperature is 11 Gauss, which is about 1.5 times larger than the bulk value. From the saturation behavior of the line width we conclude that the Na particles in heavily and ultra-heavily irradiated NaCl do not grow to micron sizes, but they might approach some saturation value, which is characterized by particle sizes, which are much smaller than the skin depth size δ.

The temperature dependence of the intensity of the CESR signal of heavily and ultra-heavily irradiated NaCl at low temperatures is rather unusual. It is different from the familiar Curie-like behavior, which is expected for a system of ultra-small isolated metallic particles, which has been observed for NaCl samples for doses less than 300 GRad (3000 MGy) [16-18]. It does not show the temperature independent Pauli-type behavior, like in the case of rather large particles [14] either. Instead, the susceptibility of the conduction electrons, which is proportional to the integral intensity of CESR peak and shows nearly Pauli behavior at higher temperatures, decreases with decreasing temperature below some critical temperature T_C (figure 8A.4). This indicates that an effective decrease is obtained for the number of unpaired electron spins contributing the conduction electron spin resonance line when the temperature decreases below T_C. Probably, these effects are associated with interactions between the particles, which cause the development of some spin ordered state at low temperatures. This interpretation in terms of interacting particles is supported by the fact that the observed unusual behavior of the resonance signal has been found only for samples, which had been irradiated up to 300 GRad (3000 MGy) and more, and which contain large concentrations of sodium precipitates. When the sodium concentration is high we expect a small spatial separation between the particles that leads to stronger particle-particle interactions.

Hence, the interpretation of the results obtained for NaCl samples can be given in terms of spin ordering, which occurs in nano-structured systems of extremely small interacting sodium particles. If the Na particles are sufficiently small, the energy levels in the conduction band become highly discrete. When the separation between energy levels becomes more than $4kT$, according to the model proposed by Taupin [9], the paramagnetic properties of the particles depend on whether they have an odd or even number of conduction electrons. Particles with a even or odd number of Na-atoms possess an effective spin 0 or ½, respectively. Let us now assume that these particles are situated close to each other, and that they are capable to create a variety of self-organized spatial structures. These structures could be the coral-like, wire- and ring-like formations, which have been observed by means of AFM; see *chapter VI*. At room temperature the spins, associated with the conduction electrons, are delocalized along the closely packed particles in the precipitate structures, which corresponds to the 'metallic' state of the sodium precipitate systems. The observed decrease of the spin susceptibility below transition temperature T_C might be due to spin ordering along the structure of Na particles at T_C, which removes spins from the resonance condition in the CESR experiment. This is in line with the results of several successful SQUID measurements of the static magnetic susceptibility, which show a peak for the susceptibility as a function of T at the same critical temperature (T_C, figure 8A.5) that indicates the existence of a transition of the electronic state from a paramagnetic to an anti-ferromagnetic state in the sodium precipitates systems [19,20]. The simultaneous increase of the CESR linewidth is indicative for a magnetic transition, occurring in the Na precipitate systems at T_C.

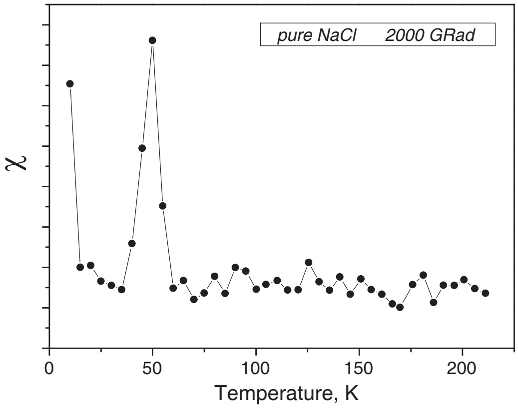

Figure 8A.5: Temperature dependence of the static magnetic susceptibility obtained from SQUID measurements.

To support this explanation we note that the behavior of the CESR signal of Na precipitates in heavily and ultra-heavily irradiated NaCl as a function of the temperature is quite comparable to that observed for systems of quasi-one-dimensional (Q1D) conductors. A very similar decrease of the CESR line intensity as in our Na-precipitates accompanied by an increase of the line width below some critical temperature have also been reported for alkali fullerides: we refer to the papers on KC_{60} [28], CsC_{60} and RbC_{60} [29,30]. The latter systems were found to exhibit Q1D metal behavior at ambient temperatures, a transition towards a spin density wave ground state has been found at about 50 K. A thermally activated paramagnetism has been observed in conducting polymer systems [31-33]. For example antiferromagnetic coupling of polaron spins was assumed to exist in the ground state along polymer chains in poly(*m*-toluidine) (PMT-HCl) [31]. A significant increase of the spin concentration was detected in this system by means of ESR by increasing the temperature above 120 ^{o}C.

The critical temperature T_C , which determines when the ordering processes in the spin system of Na precipitates takes place, depends on the average distance between neighboring particles. In real crystals the detailed structure within one sample might be variable, showing varying interparticle distances and 'defects' in the colloidal structures. These imperfections of the precipitated structure lead to a dispersion of the T_C-values, which leads to a quite smooth decrease of the intensity of the CESR line. However, we expect that with increasing irradiation dose (and correspondingly Na concentration in the sample) the precipitate structure develops into a more and more dense and well-ordered state, which cause a decrease of the distance between neighboring Na-particles and consequently a decrease of T_C. Indeed, in figure 8A.4 we observe the shift of the transition temperature towards low temperatures, while at the same time the decrease of the line intensity becomes more abrupt with increasing the LHM of sodium (figure 8A.4 a,b,c,d and e,f,g,h).

In fact this hypothesis is empirical and quite tentative yet, so more experimental data, in particular for even more heavily damaged samples, an advanced theoretical analysis are certainly needed. However, our conclusion that spin ordering occurs in precipitate structures of tiny Na-particles is in line with our AFM investigations, see *chapter VI*, where coral-like, wire- and ring-like structures of nanometer-size particles in heavily irradiated NaCl have been observed. Our interpretation is also supported by the fact that quite similar temperature effects are observed by CESR in conducting polymers and quasi-one-dimensional chains of alkali fullerides [28-33].

References

[1] R.N. Edmonds, P.P. Edwards, S.C. Guy and D.C. Johnson, *J. Phys. Chem.* **88**: (17) (1984), 3764-3771

[2] D.A. Gordon, *Phys. Rev. B* **13**: (9) (1976), 3738-3747

[3] F.J. Lopez and F. Agullo-Lopez, *Phys. Stat. Sol. (b)* **78** (1976), K81

[4] M.A. Smithard, *Sol. St. Commun.* **14** (1974), 411-415

[5] A.Ya. Vitol, E.G. Kharakhashyan, F.G. Cherkasov and K.K. Shvarts, *Fizika Tverd. Tela* **13** (1971), 2133

[6] B.W. Holland, *Magnetic Resonance and Relaxation* (1967), 468

[7] A. Kawabata, *J. Phys. Soc. Japan* **29**: (4) (1970), 902

[8] R. Kubo, *J. Phys. Soc. Japan* **17**: (6) (1962), 975

[9] C. Taupin, *J. Phys. Chem. Solids* **28** (1967), 41

[10] F.J. Dyson, *Phys. Rev.* **98** (1955), 349

[11] H.W. den Hartog, University of Groningen, (1969)

[12] A.E. Hughes and S.C. Jain, *Adv. Phys.* **28**: (6) (1979), 717-828

[13] Y. Yafet, *Solid State Phys.* **14** (1963), 1

[14] C. Kittel, *Introduction t osolid state physics*, John Wiley & Sons, New York, (1976)

[15] J. Seinen, *Radiation damage in NaCl. The process of colloid formation*, PhD thesis, University of Groningen, (1994)

[16] D.I. Vainshtein, H.P. den Hartog, H.C. Datema, J. Seinen and H.W. den Hartog, *Radiat. Eff. & Def. Sol.* **137** (1995), 73-76

[17] D.I. Vainshtein and H.W. den Hartog, *Appl. Radiat. Isot.* **47**: (11/12) (1996), 1503-1507

[18] F.G. Cherkasov, R.G. Mustafin, S.G. L'vov, G.A. Denisenko, H.W. den Hartog and D.I. Vainshtein, *JETP Lett.* **67**: (3) (1998), 189-195

[19] F.G. Cherkasov, S.G. L'vov, D.A. Tikhonov, H.W. den Hartog and D.I. Vainshtein, *Radiat. Eff. & Def. Sol.* **157** (2002), 643-647

[20] F.G. Cherkasov, S.G. L'vov, D.A. Tikhonov, H.W. den Hartog and D.I. Vainshtein, *J. Phys.: Condens. Matter.* **14** (2002), 7311-7319

[21] R.A.B. Devine and R. Dupree, *Phys. Lett.* **30 A**: (3) (1969), 211-212

[22] J.R. Asik, M.A. Ball and C.P. Slichter, *Phys. Rev.* **181**: (2) (1969), 645-661

[23] H.S. Gutowsky and P.J. Frank, *Phys. Rev.* **94** (1954), 1067

[24] R.C. McMillan, G.J. King, B.S. Miller and F.F. Carlson, *J. Phys. Chem. Solids.* **23** (1962), 1379-1380

[25] F. Vescial, N.S. Vander Ven and R.T. Schumacher, *Phys. Rev.* **134**: (5A) (1964), A1286-1290

[26] G. Feher and A.F. Kip, *Phys. Rev.* **98**: (2) (1955), 337-348

[27] J.E. Cousins, R. Dupree and R.L. Havill, *Brit. J. Appl. Phys.* **16** (1965), 1687-1692

[28] C. Coulon, A. Penicaud and R. Clerac, *Phys. Rev. Lett.* **86**: (19) (2001), 4346-4349

[29] O. Chauvet, G. Oszlanyi, L. Forro, P.W. Stevens, M. Tegze, G. Faigel and A. Janossy, *Phys. Rev. Lett.* **72**: (17) (1994), 2721-2724

[30] F. Bommeli, L. Degiorgi, P. Wachter, O. Legeza, A. Janossy, G. Oszlanyi, O. Chauvet and L. Forro, *Phys. Rev. B* **51**: (20) (1995), 14794-14797

[31] J. Anand, S. Palaniappan and D.N. Sathyanarayana, *Synth. Metals.* **66** (1994), 129-134

[32] K. Mizoguchi and K. Kume, *Sol. St. Commun.* **89**: (12) (1994), 971-975

[33] K. Mizoguchi and K. Kume, *Synth. Metals.* **69** (1995), 241-242

8B RAMAN SCATTERING AND QUANTUM CONFINEMENT EFFECTS IN NA PRECIPITATES

8B.1 Introduction

A part of our investigations of sodium precipitates in heavily irradiated NaCl, which should not be left out in this thesis, deals with Raman light scattering experiments. It is well-known that the optical properties of nano-size materials and structures are often quite different from those of the corresponding bulk samples. The unusual properties of the precipitates originate from the confinement of electrons, holes or phonons in small volumes [1-3]. Raman experiments on irradiated NaCl samples show two new high-frequency peaks, which are located beyond the cut-off frequency of NaCl [4,5]. These new peaks are not observed in unirradiated or slightly/moderately damaged NaCl crystals with rather small fractions of precipitated sodium, which were determined by means of differential scanning calorimetry measurements. These high frequency peaks are not observed either in samples, which have been annealed after irradiation. Hence, it is assumed that in heavily irradiated NaCl laser light interacts with electronic and vibrational excitations in the sodium precipitates, and these interactions give rise to new Raman scattering peaks. AFM experiments on heavily irradiated NaCl samples have revealed the presence of 'polymer'-like quasi-1D structures, which consist of small Na particles, see *chapter VI* and [6]. These observations suggest that the explanation of the appearance of the new Raman peaks should be explained in terms of electronic and vibrational excitations confined in extremely thin sodium quantum wires as proposed by Shtyrkov et al [7,8] in their investigations of the NaCl samples irradiated up to 300 GRad (3000 MGy). These authors have estimated the diameter of the wires in the framework of the proposed model of the excitations of an electron confined in metallic one-dimensional (1D) sodium nanowires. The calculated diameters of the wires are about 8.5 and 6.5 nanometers, which corresponds with the Raman scattering peaks located at 330 and 550 cm^{-1}, respectively.

The present investigations have been carried out on ultra-heavily irradiated NaCl samples. The new experimental results will be considered in the framework of the model proposed by Shtyrkov et al [7,8]. Our Raman scattering results show that in heavily damaged samples the diameter of the 1D conducting wires does not vary significantly as a function of the amount of metallic sodium in the NaCl crystal and consequently the diameter of the Na nano-wires in our samples are also about 8.5 and 6.5 nm.

8B.2 Observation of high-frequency Raman peaks

Two setups have been used for the Raman scattering measurements. In the investigations carried out by Shtyrkov et al [7,8]. The results of the Raman scattering experiments have been obtained in the temperature range of 30–200 K by means of a standard Raman setup using 90^o geometry. Prior to the measurements the samples were polished with sand paper with average grain size of 1 micron. During the experiments the samples were located in an evacuated LHe cryostat. The samples were excited by means of laser light with a wavelength of 514.5 nm (which is in the close vicinity of the plasmon-absorption band of sodium precipitates [9]) and 488 nm light. In both cases the excitation light was produced by a Spectra Physics model 171 argon-ion gas laser (operating at a power of about 50 mW) and recorded with a spectrometer equipped with a SPEX 14018 double monochromator in conjunction with a cooled EMI 9826A Photo Multiplier Tube (PMT). The slits of the monochromator were 250 μm, which results in a resolution of 3.0 cm^{-1}. The pulses, produced by the photomultiplier, were counted by a DPC 2 pulse counter. The counts were registered by means of a Nucleus 2048 MCA interface card in a personal computer.

Later Raman experiments have been carried out with a Jobin Yvon T64000 Raman Research System in the temperature range between 4 K and Room Temperature (RT). A solid-state laser operating at a wavelength of 532 nm and a power of about 10 mW was used to excite the samples.

The samples were prepared for the investigations by either cleaving of the crystals along one of the cleavage planes of the crystal or by polishing the sample surface with ultra-fine sand paper. No differences were observed between the Raman Spectra (RS) of cleaved and polished samples.

Because NaCl crystalline matrix is highly symmetric, all optical phonon excitations of the first-order spectrum of pure, undamaged NaCl are missing [10]. Therefore, one usually observes in NaCl exclusively the weak second-order RS excitations produced by inelastic scattering [11,12]. In additively and electrolytically colored NaCl second-order RS peaks have also been observed in the low-frequency range. However, rather strong first-order Raman lines in the spectra below 300 cm^{-1} have been observed by Rzepka et al and Barland et al [13,14] at 80, 100, 115, 134, 154, 205 and 230 cm^{-1}. The presence of the first-order peaks in the Raman spectrum of additively and electrolytically colored rock salt is explained by lowering of the crystal symmetry due to defects in the crystalline matrix. A similar spectrum has been observed in our irradiated NaCl samples with minor deviations of the peak positions (at most 10 cm^{-1}) from the ones mentioned above. A detailed analysis of the Raman peaks below 300 cm^{-1} has been made in [4,5] and later in more details in [7] and will be discussed below. Obviously, the crystal lattice of our irradiated NaCl samples contains large numbers of a variety of defects. As discussed in *chapters II, VI,* and *VII*, large numbers of dislocations are formed during irradiation. As shown in *chapter IV*, because of the mismatch between the NaCl and Na lattices, strain fields are generated in the NaCl matrix in the vicinity of the Na precipitates. The above- mentioned defects together with extended defects such as sodium and chlorine particles lead to lowering of the local symmetry of the ions in the host NaCl matrix. This causes the selection rules for the phonon excitations in NaCl to break down partly. Hence, those Raman lines, which were forbidden in the pure, undamaged NaCl, become (partly) allowed in our irradiated NaCl samples. An important and unique feature of the spectra of our samples is the appearance of two broad peaks at 330 and 550 cm^{-1}. These high-frequency peaks are well beyond the cut-off frequency of NaCl, which is located at 260 cm^{-1} [15]. In this investigation we were focused on the high-frequency part of the RS spectrum taken for the NaCl with a large fraction of precipitated sodium.

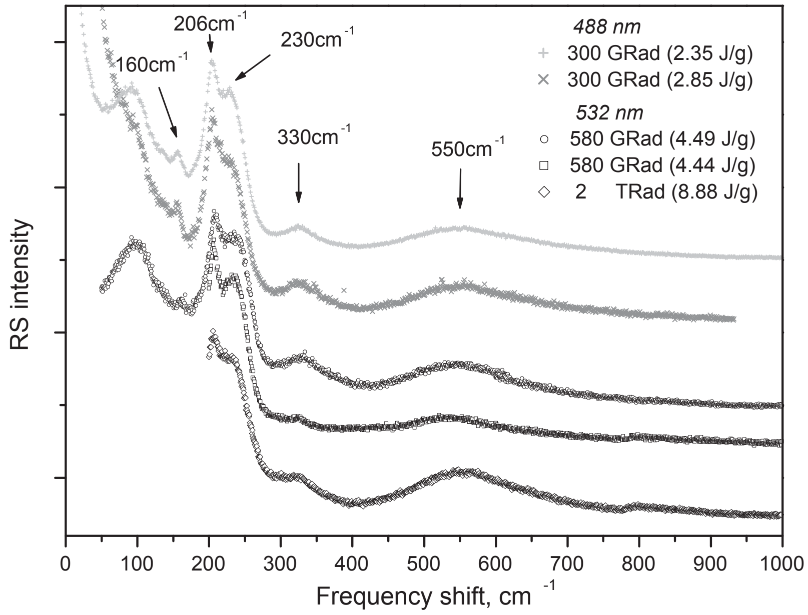

Figure 8B.1: The Raman spectra of heavily irradiated NaCl samples, measured with different setups and different excitation wavelengths. Spectra are normalized to the height of the peak at 206 cm^{-1}.

The peaks at 330 and 550 cm^{-1} have been detected for moderately damaged NaCl samples. These samples were studied by means of the setup with the Ar-ion laser. The same peaks and a weak additional feature at 800 cm^{-1} were found for ultra-heavily damaged NaCl crystals with an amount of precipitated sodium of about 20%, in these experiments excitation was carried out with the solid state laser at 532 nm. The important observation in the RS spectra is that the additional bands have not been found for low dose NaCl samples (with doses less than 10 GRad). These peaks have not been observed either in NaCl samples, which had been annealed after irradiation, to the extent that no latent heat of melting of precipitated metallic sodium could be detected by means of differential scanning calorimetry DSC, see *chapter IV* for details. Therefore, it is assumed that the high-frequency peaks are associated with metallic sodium particles [4,5]. It was proposed in [7,8] that the 330 and 550 cm^{-1} peaks are caused by light scattering of quasi-1D wires consisting of sodium precipitates and that they are associated with local excitations. Several inelastic scattering spectra of heavily irradiated NaCl samples are presented in figure 8B.1. The spectra were normalized with respect to the height of the peak at 206 cm^{-1}.

No appreciable differences have been observed for the high-frequency Raman peaks measured as a function of the temperature in the temperature range between 4 K and RT. No changes in the position, intensities and half-widths of the 330 and 550 cm^{-1} peaks have been detected within the accuracy of the measurements as a function of T. The intensities of the 330 and 550 cm^{-1} peaks (compared with the NaCl peak at 206 cm^{-1}) have been measured for a variety of irradiated samples. No correlations were found between the peak intensities and the irradiation dose, the impurity or the amount of precipitated sodium. This is in contrast with previous results, obtained for moderately irradiated NaCl [9], where a considerable increase of the intensity of 330 and 550 cm^{-1} peaks has been detected for samples with high concentrations of metallic sodium. The absolute values of the Na concentrations measured by means of DSC for the NaCl samples used for the present investigations ranged from 5 to 17 at% (LHM of sodium about 2.5 – 9 J/g). The maximum sodium concentration, in the NaCl samples obtained in [9], was about 5 at%.

We assume that the fluctuations of the peak intensities in the present investigation might be caused by the highly inhomogeneous distribution of the Na precipitates in the vicinity of the surface of the NaCl crystal. It is likely that the penetration depth of the laser beam is quite different in heavily-irradiated samples in comparison with the samples with smaller concentrations of Na, which have been used in [9]. Increasing concentrations of precipitated chlorine particles, dislocations and in particular metallic sodium precipitates in heavily-irradiated samples (see *chapters IV,V* and *VI*) lead to a drastic decrease of the penetration depth. Therefore, in our experiments on heavily damaged samples the Raman signal is produced by a very thin surface layer of the crystal. Because this layer is very thin and the sodium particles are distributed quite inhomogeneously in the sample, the number of the particles, which are excited by the laser beam and therefore give rise to the high-frequency Raman peaks, might show significant variability over the surface of the sample. This would lead to large differences in the intensities of the high-frequency Raman peaks taken from different spots at the surface.

Opposite to this, in the case of moderately damaged material, where the Raman signal is generated a rather thick surface layer, we are dealing with the situation where many particles, which are located deeper under the surface, are involved in the excitation. Because the volume of the crystal, where the Raman signal is produced, is larger, we expect that the number of the sodium particles involved in the excitations is averaged. This gives rise to rather well defined intensities of the high-frequency Raman peaks. Therefore, the intensities of these peaks in moderately damaged NaCl samples are expected to be proportional to the sodium concentration.

8B.3 Excitations of an electron confined in sodium nanowire

Our Raman scattering investigations have shown clearly the presence of the high-frequency Raman peaks at 330 and 550 cm^{-1} in the RS spectrum of heavily and ultra-heavily irradiated NaCl crystals. The relative intensities and widths of the 330 and 550 cm^{-1} peaks are close to those observed earlier for moderately damaged samples. We have considered the appearance of these peaks in the framework of a model proposed by Shtyrkov et al [7]. This explanation is outlined briefly below.

Excitations of an electron confined in sodium nanowire

A detailed analysis of the low-frequency part of the Raman spectrum has been given in [4]. It was found that in the low-frequency range the intensity of phonon spectrum shows a power-law dependence on the frequency instead of the usual Debye behavior (see figure 8B.2, which has been taken from [4]). According to the relaxation theory in disordered materials [16-19], this has led Groote et al [4] to the idea that fractal geometry characterizes the interface between the NaCl matrix and the Na metallic particles. In [7] the model of the fractal Na-NaCl interface was extended by assuming that in heavily irradiated NaCl crystals the precipitates show a dendrite-like geometry of agglomerated nano-sized metallic precipitates. This interpretation was based on the importance of surface effects, which are the predominant features, because a large fraction of the atoms in nano-sized particles is located at the surface of the particles. Also a large fraction of surface atoms is expected for the 'polymer'-like, quasi-1D fiber structures formed by the Na particles. In addition, because of the small sizes of the sodium precipitates, quantum size effects are expected to occur in the Na nano-rods and nano-wires in our irradiated samples. These effects originate from quantum confinement of the conduction electrons in narrow potential wells and wires. It is likely that small metallic precipitates behave similar to multi-electron atoms with discrete energy structures, which give rise to complex features in inelastic light scattering. The model of quantum confinement in metallic one-dimensional (1D) sodium nanowires has been proposed in [7]. The high-frequency inelastic scattering peaks at 330 and 550 cm^{-1} were assigned to excitations of electrons, which are confined to a narrow potential well.

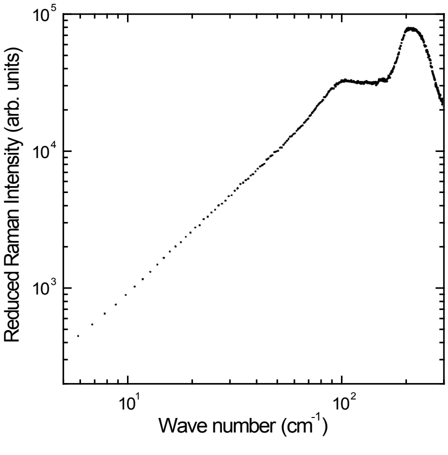

Figure 8B.2: Logarithmic plot of the Raman spectrum measured at room temperature for KBF$_4$ doped NaCl sample irradiated up to 160 GRad. The Raman intensity depends on the frequency in the low-frequency region according to a power law. Picture is taken from [4].

According to the model proposed in [7], in the case of 1D nano-structures (quantum wires along the z-direction), the motion of the electron gas is restricted to two directions (x,y). The behavior of the confined electrons in this system was described by means of the model of a rectangular cylindrical potential well with infinite walls. By solving the Schrödinger equation for a two-dimensional energy potential $U(x,y)$ with $U = 0$ outside the well and the associated boundary conditions of $\Psi_{n,m,p_z} = 0$, the spectrum of energy eigenvalues of the system was written as follows:

$$E_{n,l,p_z} = \frac{\hbar^2 j_{n,l}^2}{2m^* \rho_0^2} + \frac{p_z^2}{2m^*} \tag{8B.1}$$

where $j_{n,l}$ is the n^{th} root of the Bessel function of order l, m^* is the effective mass of the electron, $\rho_0 = d/2$ is radius of the wire. If the diameter of the nano-channel varies slowly compared with the electronic wavelength, the adiabatic approach can be used and it is possible to apply $\rho_0 = \rho_0(z)$.

Under these conditions the frequencies associated with the transitions between neighboring energy levels, expressed in wave numbers can be written as:

$$\nu_n = \frac{1}{\pi}\frac{\hbar}{cm_e}\frac{\left(j_{n+1,0}^2 - j_{n,0}^2\right)}{qd^2} \tag{8B.2}$$

where q is the ratio of the effective mass and the mass of the free electron m_e (for sodium was used $q = 1.24$), and d is the diameter of the wire (expressed in nanometers). When we choose $n = 1$ the diameter of the quantum wire is estimated to be 8.6 and 6.7 nm for the peaks at 330 and 550 cm^{-1}, respectively [7]. Therefore, these additional high-frequency peaks can be attributed to excitations of conduction electrons in quantum wires with diameters of 8.6 and 6.7 nm, which may be formed from small building blocks consisting of the metallic sodium precipitates. The rather large widths of the high-frequency Raman peaks may be caused by the distribution of the diameters of the wires. Therefore the estimated values for the diameter of the wires are the average diameters of the individual precipitates. The different values for the diameter of the wires are tentatively explained by assuming that quantum confinement does not occur in a single wire but rather in bundles consisting of a number of wires.

The similarity of the RS spectra measured for moderately and ultra-heavily damaged NaCl crystals leads us to the conclusion that some spatial structure of the sodium precipitates develops in the heavily irradiated NaCl crystals. This structure is expected to become more and more dense with increasing irradiation dose. By increasing the amount of metallic sodium, however, the characteristic size, i.e. the diameter of the individual precipitates and the nano-rods, which are the basic elements of the precipitate structure, are assumed to be approximately the same.

References

[1] S. Hayashi and H. Kanamori, *Phys. Rev. B* **26** (1982), 7079

[2] H. Reimer and F. Fischer, *Phys. Stat. Sol. (b)* **124** (1984), 61

[3] E. Rzepka, L. Taurel and S. Lefrant, *Surf. Science* **106** (1981), 345

[4] J.C. Groote, J.R.W. Weerkamp, J. Seinen and H.W. den Hartog, *Phys. Rev. B* **50**: (14) (1994), 9798-9802

[5] J. Seinen, J.R.W. Weerkamp, J.C. Groote and H.W. den Hartog, *Phys. Rev. B* **50**: (14) (1994), 9793-9797

[6] R. Gaynutdinov, D.I. Vainshtein, S.J. Hak, A. Tolstikhina and H.W. den Hartog, *Radiat. Eff. & Def. Sol.* **158**: (1-6) (2003), 77-82

[7] E.I. Shtyrkov, A. Klimovitskii, H.W. den Hartog and D.I. Vainshtein, *J. Phys.: Condens. Matter.* **14** (2002), 9053-9068

[8] E.I. Shtyrkov, A. Klimovitskii, H.W. den Hartog and D.I. Vainshtein, *Radiat. Eff. & Def. Sol.* **158** (2003), 125-129

[9] J. Seinen, *Radiation damage in NaCl. The process of colloid formation*, PhD thesis, University of Groningen, (1994)

[10] H. Poulet and J-P Mathieu, *Spectres de Vibrations et Symetrie des Cristaux*, Gordon and Breach, Paris, (1970)

[11] E. Fermi and F. Rasetti, *Z. Phys.* **71** (1931), 689

[12] E. Gross and A. Stekhanov, *Izv. Akad. Nauk SSR, Ser.: Phys.* **11** (1947), 364

[13] E. Rzepka, S. Lefrant and L. Taurel, *Sol. St. Commun.* **30** (1979), 801

[14] M. Barland, E. Duval, C. Mai, G. Mariotto, M. Montagna and G. Viliani, *Physica A* **157** (1989), 539

[15] H. Bilz and W. Kress, *Phonon Dispersion Relations in Insulators*, Springer Series in Solid State Science, *Vol. 10*, Springer-Verlag, Berlin, (1979)

[16] S. Alexander, O. Entin-Wohlman and R. Orbach, *Phys. Rev. B* **32** (1985), 6447

[17] S. Alexander, O. Entin-Wohlman and R. Orbach, *Phys. Rev. B* **33** (1985), 3935

[18] S. Alexander, C. Laermans, R. Orbach and H.M. Rosenberg, *Phys. Rev. B* **28** (1983), 4615

[19] S. Alexander and R. Orbach, *J. Phys. Lett.* **43** (1982), L625

8C WIDE ANGLE X-RAY DIFFRACTION OF HEAVILY DAMAGED NaCl

8C.1 Introduction

Small crystalline particles, which are embedded in amorphous or crystalline media, have been studied in the literature by means of wide angle X-ray diffraction (WAXS) [1-4]. From the measured diffraction patterns one obtains information about the lattice symmetry and lattice constants of each crystalline component of the investigated sample and therefore it is possible to determine which crystalline components are present in the sample. X-ray analysis also allows us to gain information about the orientation relationship between the crystalline directions of embedded particles and the surrounding matrix. In addition, information from high angular resolution X-Ray scattering experiments enables us to estimate the average size of the crystalline inclusions (see for example [1-4]).

In earlier investigations of irradiated NaCl crystals [5] sodium nano-inclusions have been detected in the host matrix of NaCl samples by means of WAXS. The inclusions were found to have a very strict orientation relationship with the host crystalline matrix. In the framework of this thesis we have studied [6] heavily and ultra-heavily irradiated NaCl samples at low temperature (95 K), which has allowed us to reveal the presence of frozen chlorine nano-precipitates in our samples, because this temperature is well below the melting temperature of chlorine bubbles, see *chapter V*. Like the Na-precipitates, also chlorine particles appear to be highly oriented with respect to the surrounding matrix. To improve the resolution significantly, synchrotron radiation has been used for the new X-Ray diffraction experiments presented in this chapter. The mean sizes of sodium and chlorine precipitates presented in this chapter have been estimated from the results of high-resolution measurements using synchrotron radiation. The calculated mean sizes of the Na particles (several hundred Ångstroms) turned out to exceed significantly the mean sizes, which were estimated earlier from the results of CESR and NMR [7-9], and Raman scattering [10,11] experiments. The latter estimations yielded mean sizes of the Na particles of a few dozen Ångstroms for heavily irradiated NaCl samples. Also calorimetry experiments for both types – heavily and ultra-heavily- irradiated NaCl samples indicate that the sodium precipitates should show very strong surface curvature and therefore small sizes, see *chapter IV*. Also here sizes of the order of ten Ångstroms are expected for our chlorine precipitates, see *chapter V*. Although there is no clear-cut and unambiguous explanation for this discrepancy at the present stage of the investigations of heavily irradiated NaCl, we assume that both the Na and the Cl_2 precipitates form highly organized structures, which consist of very fine nano-particles. Unfortunately, we were not able with the techniques applied in this chapter to reveal the ultra-fine details of these structures. In the framework of this thesis this information can only be obtained from a combined interpretation of the results of a variety of experimental techniques.

8C.2 Experimental techniques

In the investigations presented in this chapter several heavily and ultra-heavily irradiated samples with an amount of precipitated sodium up to about 20 at% have been studied by means of wide angle X-ray diffraction (WAXS); for more experimental details we refer to [6]. The single crystal experiments have been carried out by means of a Bruker Apex diffractometer with a 2D-CCD (512X512) detector. Mo K_α-radiation and a graphite monochromator were used in the setup. The NaCl single-crystal samples with a length of 5 mm and a diameter of about 0.3 mm were mounted along the φ-axis of the goniometer. 180 successive patterns with a φ-step of 1^o were registered. During each exposure the sample was rotated over $\Delta\varphi = \pm 0.5°$ to average the intensity. Furthermore, several measurements were obtained for each φ-step and the averaged results were used. This procedure allowed us to increase the dynamic range of the measurements, which was crucial for the observation of both the very weak spots from the precipitates and the strong peaks produced by the host matrix. The same method has been used in [5] for the investigations of heavily irradiated NaCl crystals at room temperature. In the present investigations the measurements have been carried out at two different temperatures: at room temperature and 95K. It was decided to investigate the samples at low temperature in order to detect the diffraction lines from solid halogen bubbles. The measuring temperature of 95K is well below the melting temperature of chlorine precipitates (which is about 170K, see *chapter V*).

Because it was not possible with the Bruker instrument to achieve an angular resolution better than 0.7^o it was not possible to determine with this setup the average particle size of the Na-inclusions from the observed line broadening. In order to improve the angular resolution of the measurements, synchrotron radiation (SR) has been used for the X-Ray diffraction experiments. In addition, the application of the super bright radiation source of the synchrotron permitted us to decrease the measuring time required to detect the very weak peaks from the precipitates. The SR source from the bending magnet at the Kurchatov Centre of Synchrotron Radiation and Nanotechnology (KCSR, Moscow, Russia) [12] was applied for this purpose in collaboration with Sulyanov, Kheiker and Dorovatovskii. The detection system was based on a MAR CCD detector operating in the 2048x2048 pixel resolution mode. The wavelength of the synchrotron radiation was λ=1.5398 Å and the angular resolution of these experiments was estimated to be $\Delta(2\theta) = 0.055°$, which is more than one order of magnitude better than the Bruker setup.

8C.3 Orientations and sizes of the precipitated nano-particles

The most intriguing result of the WAXS experiments on ultra-heavily irradiated NaCl crystals was that the crystalline matrix of these samples remains quite perfect even at highest irradiation doses. No noticeable amorphisation of the NaCl monocrystallic samples caused by irradiation has been detected in these experiments. This is in contrast with several observations reported in the literature on other inorganic materials [13,14], which show that quite often after exposure to very high irradiation doses of radiation the samples are metamict. As a result, the by far most prominent diffraction lines are those associated with the host NaCl crystal.

The diffraction patterns of the *bcc* sodium lattice have been collected, and the average lattice constant for the precipitates was calculated to be $a_{\mathrm{Na}} = 4.2795$ Å, which is slightly smaller than the value for bulk Na $a_{\mathrm{Na}} = 4.2906$ Å [15]. The diffraction patterns of orthorhombic molecular chlorine lattice could be measured at T=95K, they have not been observed at room temperature, because at this temperature the chlorine precipitates are in liquid state, see *chapter V*. The observed average values for the unit cell dimensions of the solid molecular chlorine bubbles were: $a = 6.2163$, $b = 4.4679$, $c = 8.1339$ Å, these values are reasonably close to those obtained for bulk chlorine in [16] ($a = 6.2235$, $b = 4.4561$, $c = 8.1785$ Å).

The diffraction peaks, which are associated with Na and Cl_2 precipitates, are well defined with respect to rotation of the sample around the φ-axis (which coincides with the z-axis of our sample). This means that both sodium and chlorine precipitates have strict orientation relationships with respect to the host matrix. In general, the orientation matrix (OM) is used to describe a rotation of a solid body relative to the laboratory coordinate system. If **A** is the OM for a crystal (e.g. the Na precipitate in our case), then any unit vector can be written in both the laboratory (**r**) and crystallographic unit basis (**n**) using the relation: **r = A n**. In accordance with this relation we can write $\mathbf{n}_{NaCl} = \mathbf{A}^{-1}_{NaCl}\,\mathbf{r}_{NaCl}$. Any OM can be chosen from a set of equivalent matrices. Each matrix from this set can be obtained by multiplying the OM and the matrix $\mathbf{W}_i$ representing one of the point group rotation operators for the crystal under investigation. Any vector $\mathbf{n}_{Na}$ corresponding to a reflection from Na precipitate, can be written in 'NaCl' coordinates as $\mathbf{n}_{Na} = \mathbf{W}_i\mathbf{U}\mathbf{n}_{NaCl}$ ($i = 1, N_w$). Here $N_w = 24$ for the point group $m\bar{3}m$ of the Na lattice and $\hat{\mathbf{U}}$ is any matrix connecting the NaCl and Na systems. Obviously, if p is the multiplicity factor for a particular crystallographic coordinate plane of the precipitate, and N_w is the number of **W**-matrices for the host crystal, then the total number of possible reflections in the diffraction pattern can be $P = pN_w$. So if we use *hkl*-type reflections for the Na precipitates, then in general as many as 48×24 = 1152 reflections are possible. The 200-type reflections ($p = 6$) from the Na precipitates have been chosen in [5] to determine their orientations. All vectors corresponding to the observed 200-type Na reflections in the coordinate system of NaCl are presented in figure 8C.1.

It has been found in [5] that the orientation of all Na nanoparticles relative to the NaCl matrix in our irradiated crystals belongs to Kurdjumov-Sachs orientation relationship [17]. This orientation relationship (OR) is well known for *bcc-fcc* interfaces (see for example [18,19] for the case of metal-metal precipitation) and can be written in terms of the following expressions: $(1\bar{1}1)_{fcc}\|(101)_{bcc}$, $[101]_{fcc}\|[1\bar{1}1]_{bcc}$. Our case of the Na-NaCl *bcc-fcc* interface has been considered in [5] in terms of the theory of epitaxy. According to the model calculation proposed in [20], one can achieve a good match along the closest packed row of the {111} plane of the fcc crystal and the {110} plane of the bcc crystal by a rotation over an angle $\Theta = 5.26^{\circ}$ if the ratio of the atomic distances for these planes has the special value: $r = a/b = 1.0887$, where a is equal to the nearest neighbor distance in the {111} plane of the fcc

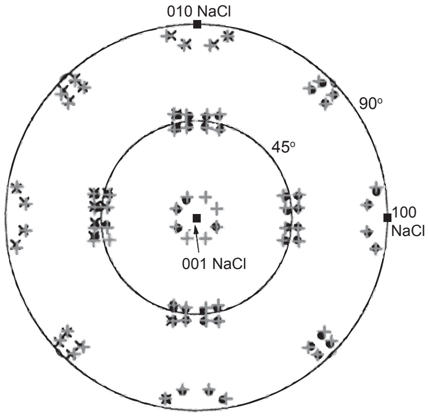

Figure 8C.1: Projection of the <001> directions of Na precipitates in the unit cell coordinate system of NaCl crystal. Here solid circles and x-es are measured 200-type Na reflections corresponding to the vectors in the upper and bottom half-sphere respectively, crosses are all vectors generated for K-S OR.

crystal and with b equal to the corresponding value in the {110} plane of the bcc crystal. This situation corresponds to the K–S OR. The nearest neighbor distance of the Na sub-lattice in the Na {111} plane of the NaCl crystal is *a* = 3.984 Å and the corresponding distance in the Na precipitate is *b* = 3.706 Å. This implies that the ratio is r = 1.075, which is quite close to the value required for the K–S OR mentioned above. A schematic picture, illustrating this OR of the Na-NaCl interface is presented in figure 8C.2.

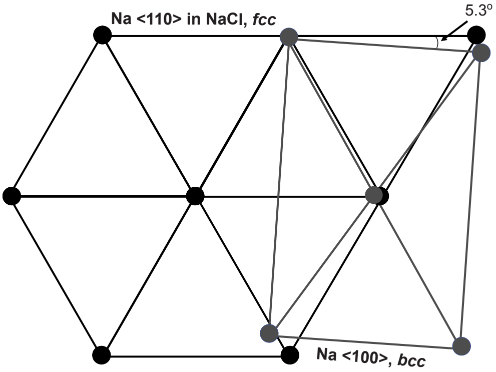

Figure 8C.2: Orientation of Na precipitate lattice to the host NaCl matrix. {110} plane of Na nanoparticle is rotated through the angle 5.26° with respect to {111} plane of NaCl.

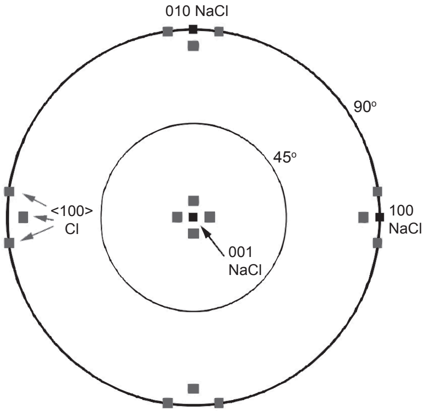

Figure 8C.3: Projection of the <100> directions of Cl_2 precipitates in the unit cell coordinate system of NaCl crystal.

Analogous to Na precipitates, the vectors corresponding with the observed Cl_2 reflections in the coordinate system of NaCl are presented in figure 8C.3. The following orientation relationship was found between frozen Cl_2 bubbles and the host NaCl matrix: $\{001\}_{Cl_2} \| \{001\}_{NaCl}$, $<110>_{Cl_2} \| <110>_{NaCl}$. A schematic picture of the matching of the crystal lattices in the 001 planes of solid Cl_2 and NaCl is shown in figure 8C.4. The rotation angle for $<100>_{Cl_2}$ with respect to $<100>_{NaCl}$ found from the experiments is 9.10°, while the angle calculated from the measured cell parameters which is required for coincidence of the cubic and orthorhombic cell diagonals is 9.30°. Note that the inter-atomic distances along the rows $<110>_{Cl_2}$ and $<110>_{NaCl}$, which are equal to 3.82Å and 3.99Å respectively, differ by less than 4.5%, which means that the atomic positions along these rows reveal only a slight misfit.

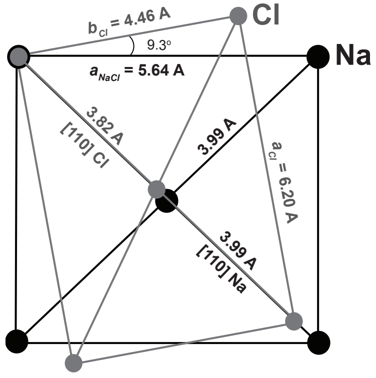

Figure 8C.4: Orientation of Cl_2 precipitate lattice to the host NaCl matrix. {001} planes of NaCl and Cl_2 lattices, $<001>_{Cl}$ and $<100>_{NaCl}$ directions coincide.

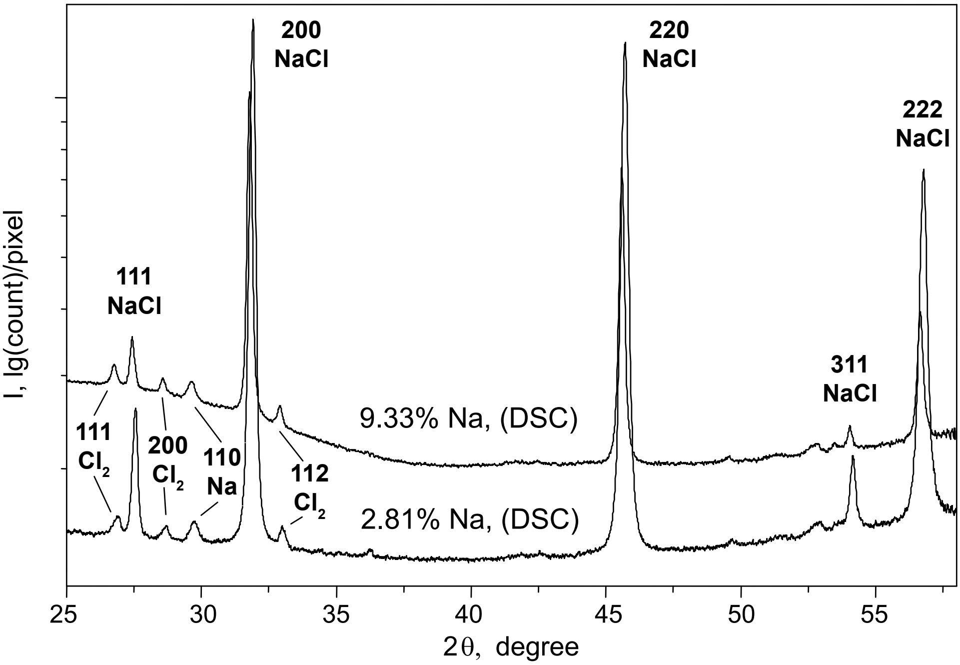

Figure 8C.5: X-ray pseudo-powder spectra of ultra-heavily irradiated NaCl samples, NaCl, Na and Cl_2 diffraction peaks are observed.

Some typical powder diffraction spectra of heavily irradiated NaCl samples are shown in figure 8C.5. The diffraction peaks of the NaCl, Na and Cl_2 crystal lattices are observed in the $I(2\theta)$ plot in figure 8C.5. Close-ups of the 110 Na and 200 Cl_2 peaks are presented in figure 8C.6 a and b respectively. The solid line in both plots shows the instrumental resolution function (IRF)[1] for the synchrotron experiment. The observed Na and Cl_2 Bragg diffraction peaks are broadened significantly. The broadening of Bragg peaks in the X-Ray diffraction pattern may be caused by several reasons: (i) instrumental effects, (ii) effects of the finite size of the crystallites, (iii) strain accommodated in the matrix and (iv) extended defects in the crystal. The second point provides us with a possibility to calculate the mean size of the embedded small particles from the measured width of the diffraction peaks (see for example [2,3]). We have used the Scherrer formula [21] to estimate mean sizes of sodium and chlorine particles:

---

[1] The IRF has been obtained with a reference powder (zeolite or LaB_6 N660a NIST standard) inserted into a glass capillary with an inner diameter of D = 0.3 mm. The full width at half-maximum of the Bragg peaks was measured to be of 0.055° and it shows a very weak dependence on 2θ in the range of our measurements. The mean angular difference between the measured and reference Bragg angles did not exceed 0.001°. The peak profile of the IRF was well described by the symmetric Pearson-VII (PVII) or the pseudo -Voigt (pV) function [6].

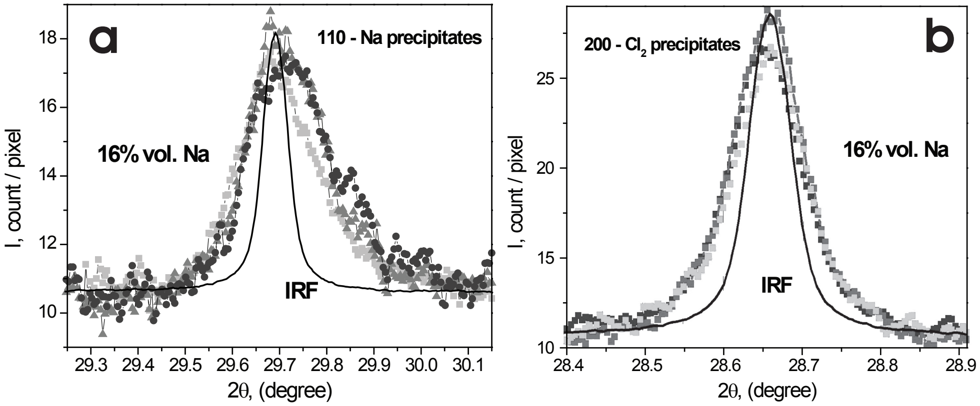

Figure 8C.6: X-ray spectra of ultra-heavily irradiated NaCl samples, (a) 110-peaks of Na precipitates (b) and 200-peaks of Cl2 precipitates. Solid line in both plots is the instrumental resolution function (IRF).

$$L = \frac{K\lambda}{\cos\theta \; B} \qquad (8C.1)$$

where λ is the wavelength of the incident X-ray beam, L is the linear dimension of the particle, θ is the Bragg angle, B is width of the diffraction peak at half-maximum, and K is a numerical constant. The contribution to the peak broadening caused by lattice distortions in the small particles has not been taken into account in these rather tentative estimations. We have also assumed that there are no extended defects such as dislocations in our small precipitated particles, which could lead to the broadening of Bragg peaks of these particles.

The mean sizes of the Na and Cl_2 precipitates in our heavily irradiated NaCl samples have been estimated to be of order of several hundred Ångstroms, and the results suggest that the average sizes increase with the damage percentage, see figure 8C.7. It has been found [6], that the Bragg peaks for chlorine bubbles show different widths for different matrix orientations. The difference in the peak widths for 002 and 200 peaks was found to be about a factor of two, even though the Bragg angles do not differ much. From the measured differences of the widths of the Bragg peaks it can be concluded that chlorine bubbles in heavily damaged NaCl are not spherical, and that they show a significant reduction of the size along the crystal *c*-axis. Hence, the ellipsoid model proposed in [22] has been used for calculating the mean size of the chlorine bubbles. In terms of the model, chlorine bubbles are 3-axial ellipsoids in the host NaCl crystal lattice. The *a,b,c* axes of these ellipsoids can be obtained from the following equation [22]:

$$L_{hkl} = (3/2)/(b_{11}h^2 + b_{22}k^2 + b_{33}l^2 + b_{12}hk + b_{13}hl + b_{23}kl)^{1/2}\, d_{hkl} \qquad (8C.2)$$

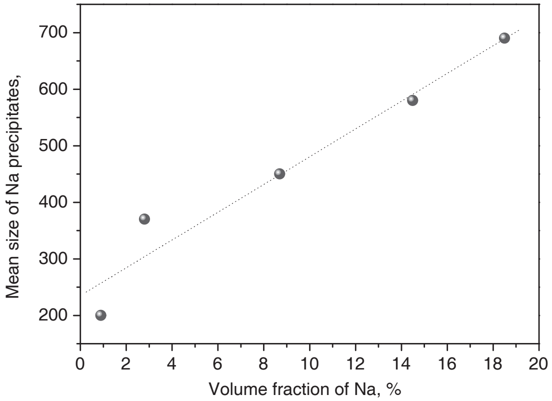

Figure 8C.7: The average sizes of Na precipitates estimated from X-ray diffraction experiments vs. volume percentage of precipitated sodium obtained by means of DSC (*chapter IV*).

where L_{hkl} is diameter of the crystallite along the [*hkl*] direction, d_{hkl} is the interplanar distance, and the ellipsoid radii *a,b,c* are connected with the size values as $r_{abc} = (2/3)\ L_{abc}$. In our particular case of precipitates with an orthorhombic cell, the values b_{12}, b_{13}, b_{23} are zero. The b_{11}, b_{22}, b_{33} parameters were calculated by means of least squares fitting taking into account the widths of all observed chlorine reflections. In the evaluation of the experimental results we have applied IRF deconvolution. The two radii of the oblate ellipsoid, which served as a model for the average chlorine bubble in irradiated NaCl samples, were estimated and the mean sizes are presented in table 8C.1. In addition, the volume fractions of metallic sodium have been estimated from the intensities of the Na and NaCl diffraction peaks of the investigated samples, the results of these estimations have been presented in table 8C.1 together with the volume fractions calculated from calorimetry measurements (latent heat of melting).

Table 8C.1: The average sizes of the ellipsoidal chlorine bubbles in ultra-heavily irradiated NaCl samples.

Dose, GRad	V_{Na} / V, % (DSC)	Estimated Cl_2 precipitate size, Å		Estimated Na precipitate size, Å	V_{Na} / V, % (X-Ray)
		c	*a, b*		
300	0.9	190	470	200	1.1
300	2.8	310	830	370	3.5
300	8.7	340	830	450	7.1
2000	14.5	460	1070	580	10.3
2000	18.5	–	–	690	–

8C.4 Discussion of the mean sizes of the Na and Cl_2 particles

The mean size of the Na particles in heavily irradiated NaCl has been estimated from the results of X-ray diffraction experiments to be several hundred Ångstroms and it increases almost linearly with the volume fraction of metallic sodium in the irradiated sample, figure 8C.7. At the same time the estimations, which were obtained from the results of CESR and NMR experiments for the samples irradiated up to 300 Grad (3000 MGy) and with about the same Na volume fraction yield mean Na particle sizes of about 5-10 nm [7-9]. The mean size of the precipitates in ultra-heavily irradiated samples is also expected to not exceed significantly these estimations. Raman scattering on heavily and ultra-heavily irradiated NaCl has shown mean sizes of 7-9 nm [10,11], see *section 8B* of this chapter. The particle size, which has been estimated from AFM measurements for the 300 Grad-irradiated NaCl samples, were a few nanometers [23,24], *chapter VI*. Also calorimetry (DSC) investigations of the melting process in sodium precipitates indicate that a very strong curvature of the interface between Na particles and the host matrix exists, which suggests that the sodium particles are very small or they form structures with ultra fine surface irregularities, *chapter IV*. Quantitative estimations can be obtained from earlier observations [25,26]. These results show that the mean size of the Na particles in heavily irradiated NaCl samples is always less than 10 nm. Typical sizes of only several nanometers are also expected for our chlorine bubbles, *chapter V*.

Hence, the sizes of sodium and chlorine precipitates obtained from X-ray diffraction appear to be considerably overestimated. This discrepancy is not fully explained at the present stage of the investigations. We note however that according to the above-mentioned AFM experiments sodium precipitates in heavily irradiated NaCl samples form highly organized and compact structures (i.e. rings and strings and coral-like formations). Spherical particles, which form these structures, have sizes less than 10 nm. It is probable that local details of these highly organized Na precipitate formations are missed in our X-ray diffraction measurements. The rather crude size estimations, obtained with X-ray diffraction, are assumed to provide us with the overall size of relatively large blocks of strongly arranged sodium particles with exactly the same alignment. A similar situation is expected to exist for the chlorine precipitate system. Therefore the information obtained by WAXS can be considered to be complementary to that obtained by means of CESR, NMR, AFM and Raman scattering, which all probe primarily the local structure of the precipitates.

References

[1] W. Fan, M. O'Brien, M. Ogura, M. Sanchez-Sanchez, C. Martin, F. Meneau, K. Kurumada, G. Sankar and T. Okubo, *Phys. Chem. Chem. Phys.* **8** (2006), 1335–1339

[2] G. Kellermann and A.F. Craievich, *Phys. Rev. B* **65**: (13) (2002), 134204

[3] Ch. Kumpf, *Appl. Phys. A* **85** (2006), 337–343

[4] V. Swamy, D. Menzies, B.C. Muddle, A. Kuznetsov, L.S. Dubrovinsky, Q. Dai and V. Dmitriev, *Appl. Phys. Let.* **88** (2006), 243103

[5] S.N. Sulyanov, D.M. Kheiker, D.I. Vainshtein and H.W. den Hartog, *Sol. St. Commun.* **128**: (11) (2003), 419-423

[6] S.N. Sulyanov, D.M. Kheiker, P.V. Dorovatovskii, A.V. Sugonyako, D.I. Vainshtein and H.W. den Hartog, *to be published* (2006)

[7] F.G. Cherkasov, R.G. Mustafin, S.G. L'vov, G.A. Denisenko, H.W. den Hartog and D.I. Vainshtein, *JETP Lett.* **67**: (3) (1998), 189-195

[8] D.I. Vainshtein, H.P. den Hartog, H.C. Datema, J. Seinen and H.W. den Hartog, *Radiat. Eff. & Def. Sol.* **137** (1995), 73-76

[9] D.I. Vainshtein and H.W. den Hartog, *Appl. Radiat. Isot.* **47**: (11/12) (1996), 1503-1507

[10] E.I. Shtyrkov, A. Klimovitskii, H.W. den Hartog and D.I. Vainshtein, *J. Phys.: Condens. Matter.* **14** (2002), 9053-9068

[11] E.I. Shtyrkov, A. Klimovitskii, H.W. den Hartog and D.I. Vainshtein, *Radiat. Eff. & Def. Sol.* **158** (2003), 125-129

[12] D.M. Kheiker, *Crystallography Reports (to be published)*

[13] A. Benyagoub, *Nucl. Instr. and Meth. in Phys. Res. B* **225** (2004), 88-96

[14] C. Fillet, T. Advocat, F. Bart, G. Leturcq and H. Rabiller, *C. R. Chimie* **7** (2004), 1165-1172

[15] E. Aruja and H. Perlitz, *Z. Kristallogr. Kristallgeom. Kristallphys. Kristallchem.* **100** (1939), 195

[16] B.M. Powell, K.M. Heal and B.H. Torrie, *Molecular Physics* **53** (1984), 929

[17] G.V. Kurdjumov and G. Sachs, *Z. Phys.* **64** (1933), 325

[18] J.K. Chen, D. Farkas and W.T. Reynolds, *Acta mater.* **45**: (11) (1997), 4415-4421

[19] C.P. Luo and U. Dahmen, *Acta mater.* **46**: (6) (1998), 2063-2081

[20] A. Zangwill, *Physics at Surfaces*, Cambridge University Press, London, (1996)

[21] A.L. Patterson, *Phys. Rev.* **56** (1939), 978-982

[22] T.B. Zunic and J. Dohrup, *Powder. Diffr.* **14**: (3) (1999), 203-207

[23] R. Gaynutdinov, D.I. Vainshtein, S.J. Hak, A. Tolstikhina and H.W. den Hartog, *Radiat. Eff. & Def. Sol.* **158**: (1-6) (2003), 77-82

[24] A.V. Sugonyako, A.A. Turkin, R. Gaynutdinov, D.I. Vainshtein, H.W. den Hartog and A.A. Bukharaev, *Phys. Stat. Sol.* **2**: (1) (2005), 289-293

[25] J.C. Groote and J.R.W. Weerkamp, *Radiation damage in NaCl. Small particles*, PhD thesis, University of Groningen, (1990)

[26] J. Seinen, *Radiation damage in NaCl. The process of colloid formation*, PhD thesis, University of Groningen, (1994)

Conclusions

The results obtained with the experimental methods given in this chapter have provided us with valuable information about precipitated sodium and chlorine systems in irradiated NaCl crystals. The information presented in this chapter has helped us decisively in understanding important aspects of the organization in the structures of extended radiolytic defects in heavily and ultra-heavily irradiated NaCl. The experimental results obtained for Na-precipitates by means of CESR show that systems of small interacting metallic particles are formed in NaCl when the irradiation dose reaches values of 300 GRad (3000 MGy) and higher. The concentrations of radiolytic Na in these samples are higher than about 2 at%. Detailed measurements of the temperature dependence of the CESR signal revealed that a magnetic transition occurs in the Na-precipitated system at temperatures below 100K. The results can be explained by anti-ferromagnetic ordering of conduction electron spins in the precipitate systems, taking place along the quasi-linear structures of tiny sodium particles at sufficiently low temperatures. This hypothesis is supported by a similar temperature behavior of the electron spin system, which has been observed in several conducting polymers and alkali fullerides, which were shown to form quasi-one-dimensional conducting systems. In our samples presence of sodium precipitate structures with quasi-1D geometry have been confirmed by the AFM experiments on heavily irradiated NaCl crystals, where various coral-like, string- and ring-like formations of small nanoparticles have been observed, *chapter VI*.

Raman scattering experiments on heavily- and ultra-heavily irradiated NaCl samples have revealed at least two additional high-frequency peaks, which were explained by quantum confinement of the conduction electrons in sodium nano-rods. In the framework of this explanation the average diameters of sodium nano-wires have been estimated to be 67 and 86 Å. Although these interpretations of the results of Raman scattering experiments have a certain degree of arbitrariness, they are in line with the CESR and AFM results, presented in this thesis (*chapter VIII,A* and *chapter VI*).

The WAXS results reported in this chapter show unambiguously that in heavily irradiated NaCl *bcc* Na particles are formed. Our observations for solid Na precipitates are in good agreement with earlier results. In addition, our WAXS experiments have revealed for the first time the presence of solid particles of molecular chlorine in irradiated NaCl samples at 95K. Our measurements have shown that a very strict relationship between the orientation of the crystal lattice of sodium and chlorine precipitates with respect to the crystal lattice the host NaCl matrix exists. However, the average size of the radiolytic particles obtained from X-ray diffraction is at least one order of magnitude larger than the values obtained with CESR and RS. The discrepancy between the average sizes of precipitates estimated from the X-Ray and other measurements results can be explained, if we assume that we are dealing with highly organized structures of Na- and Cl_2-precipitates. Within a certain distance the crystal lattice of each part of the precipitate structure has exactly the same orientation and also the correct position with respect to the host NaCl matrix.

Acknowledgements

The work, discussed in this chapter, is the result of a fruitful cooperation with my colleagues and friends: Aidar Validov, who carried out and analyzed most of the CESR and SQUID experiments, David Vainshtein, who explained to me the ins and outs of the ESR spectrometer, sustained full-time support and contributed by valuable discussions, and who provided inspiration and encouragement for this part of the project. Sergey Klimin, who facilitated gaining understanding of the Raman setup and related optics and helped me to carry out the measurements. Alexander Klimovitskii, who implemented an important part of the Raman experiments and supplied me with useful information gained during our discussions, where I also would like to mention the important contributions made by Prof. Dr. E. Shtyrkov. Sergey Sulyanov has carried out a large number of wide-angle X-Ray scattering measurements and accomplished an intricate analysis of the data. The collaboration with Sergey and his group at the Kurchatov Centre of Synchrotron Radiation and Nanotechnology allowed us to perform the necessary high-resolution X-Ray diffraction experiments with their synchrotron radiation source. As a result several papers have been prepared.

CHAPTER IX

MODIFICATION OF THE DEFECT STRUCTURE OF IRRADIATED NaCl

9.1 Introduction

Recent experimental studies on radiation damage in NaCl crystals have shown that changes in the irradiation temperature dramatically affect the evolution of size distributions of sodium colloids and chlorine bubbles. It has been observed by means of DSC that the latent heat of melting of sodium decreases during low-temperature irradiation (18 °C) of samples, which have been irradiated before at high temperature (100 °C), while in contrast with this the stored energy increases slowly, implying that the amount of radiation damage, including the Na and Cl_2 precipitates, increases slowly with increasing dose. This experimental observation can be explained by dissolution of large colloids, which are visible for melting, while large numbers of small precipitates are found, which do not contribute to the melting peaks of Na and Cl_2. In other words, we assume that the observations should be explained by significant changes in the colloids size distribution. In the present chapter we will consider a possible mechanism of dissolution of relatively large Na-colloids during low temperature irradiation.

9.2 Two-steps irradiation procedure and calorimetry of the samples

Synthetic NaCl single crystals doped with 300 ppm KBF_4 have been used for the experimental investigations presented in this chapter. The irradiation has been carried out with 0.5 MeV electrons by means of a linear accelerator (see *chapter III* for details). After an initial high temperature irradiation at 100 °C up to 320 Grad the samples were irradiated in the second stage at 18 ºC up to a maximum additional dose of 550 Grad. For each set of samples, which had been irradiated to the same initial dose of 320 Grad, the SE and the LHM of radiolytic sodium and chlorine precipitates have been measured. Figure 9.1 shows the dose dependence of the sodium LHM and the SE during the two-stage irradiation experiment. The LHM of sodium increases with the dose during the initial high temperature irradiation, whereas during the second stage of the irradiation experiment at 18 ºC a clear decrease of the LHM of sodium can be seen (figure 9.1a).

In figure 9.1b the dose dependence of the SE is plotted. The SE released during DSC measurements due to the back reaction between the radiolytic products, Na and Cl_2 is proportional to the total number of neutral sodium atoms created by irradiation in the NaCl crystal lattice. The LHM of sodium/chlorine is proportional to the amount of sodium/chlorine agglomerated in sufficiently large particles, which exhibit the above-described melting behaviour. The left part of figure 9.1b shows the increase of the SE during irradiation at 100 °C. The SE values after low temperature irradiation demonstrate a significant sample to sample variability.

Nevertheless a small increase of the SE with the irradiation dose can be noticed (at least there is definitely no consistent decrease of the SE, figure 9.1b), at the same time the LHM of sodium decreases appreciably. Obviously, the decrease of the LHM is due to dissolution of large colloids. The slow growth of the SE with the low-temperature dose can be explained by nucleation of small-sized Na clusters and possibly *F*-centers and small aggregates of these defects (which do not contribute to the melting peaks observed in these experiments), which appear to replace the above-mentioned large, shrinking colloids. This means that under low temperature irradiation the size distribution of the colloids changes appreciably. As for the LHM of chlorine, there is a large scatter of experimental data points; therefore we are not in the position to conclude that the LHM of chlorine decreases in the same proportion as the LHM of sodium (figure 9.2).

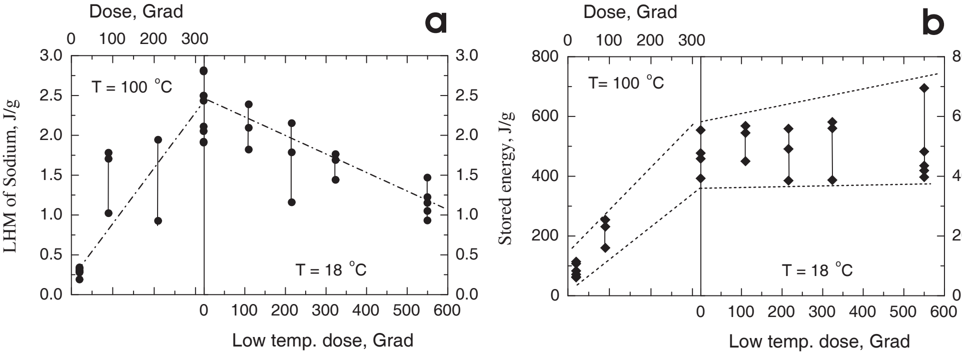

Figure 9.1: The LHM of sodium colloids (a) and the stored energy (b) versus the dose in the two-stage irradiation experiment. The dashed-dotted lines in (a) are plotted as a guide for the eyes. The data points connected by the solid lines correspond to sets of samples irradiated to the same high and low-temperature dose. The dashed lines in (b) show the general trends for the minimum and maximum SE values.

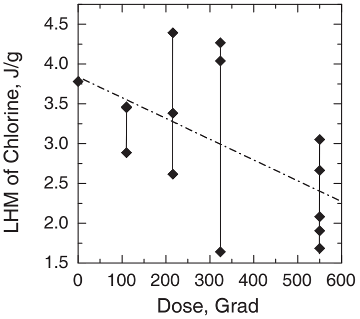

Figure 9.2: The LHM of chlorine precipitates versus the low temperature dose. The dashed-dotted lines are fitted to the data points. Data points connected by the solid lines correspond to sets of samples irradiated to the same high and low-temperature dose.

9.3 Modeling of the size distributions of the precipitates

The model for radiolysis in NaCl [1], which is used for the interpretation of our experimental findings, has been outlined in *chapter II*. The advantage of this model over the Jain-Lidiard model [2,3] is that it can explain the formation of voids in NaCl during radiolysis. According to [4,5], voids in NaCl grow due to absorption of F centers and V_F-centers, which are produced at dislocations because of the dislocation bias for H centers (V_F-center in NaCl is an electro-neutral Schottky pair occupied by a Cl atom). In the model calculations of ref. [1] the authors have simulated the dose dependence of the mean values for the concentrations and precipitate sizes of colloids, gas bubbles and voids; the evolution of size distributions of these defects has not been addressed. In order to understand the experimental results, obtained for the second stage at low temperature, we need a more detailed description of the populations of the colloids and bubbles, i.e. it is necessary to consider formation and evolution of particle size distributions as a function of the temperature.

Below we will formulate a set of chemical rate equations for the average concentrations of mobile *F*- and *H*-centers and immobile clusters of these defects. We assume that Na colloids nucleate homogeneously via coagulation of *F*-centers. Chlorine bubbles are assumed to nucleate heterogeneously, i.e. the traps for *H*-centers are introduced in the model, in accordance with [6,7]. Trapping of *H*-centers is a necessary element of the model, because the rate of homogeneous nucleation of chlorine bubbles is small due to the low concentration of highly mobile *H*-centers [6,7]. The nature of the traps for *H*-centers will not be specified. In principle, the NaCl crystal may contain various types of traps with different binding energies with point defects. Crystal lattice defects, which may serve as traps for *H*- and *F*-centers, include impurity ions and complex defects, dislocation jogs, grain boundaries etc. At present we have no detailed information about the nature of these trapping centers in NaCl. Possibly a series of special low dose irradiation experiments involving samples with different concentrations of dopants could help to answer the questions regarding the relation between defect traps and doping. However, this task is beyond the scope of the present work. The aim of this chapter is to find a physical mechanism for the dissolution of large Na-colloids during low temperature irradiation, using a minimum set of assumptions. For this reason voids, dislocations and V_F-centers are not included in the model. This approach can justified by the fact that the sink strengths of voids and dislocations are smaller than the sink strengths of colloids and bubbles [4,5]. This means that V_F-centers and voids are secondary defects, which do not influence essentially the evolution of colloids and chorine precipitates. Several remarks should be made about this simplification. In most of the existing models [2-7] dislocations are considered to be necessary microstructural elements of the radiolysis process. However, we will see from the treatment presented below that radiolysis is also possible in dislocation-free material. The driving force is the asymmetry of the absorption of *H*- and *F*-centers by clusters of various sizes and types. On the other hand, dislocations may provide nucleation sites for both bubbles and colloids [8].

The following reactions between traps, F-centers, H-centers and their clusters, F_n and H_n, are considered:

$$\begin{aligned}
&F_n + F \leftrightarrow F_{n+1}\\
&F_n + H \rightarrow F_{n-1}\\
&Trap + H \leftrightarrow H^T\\
&H^T + H \rightarrow H_2^T\\
&H_n^T + H \rightarrow H_{n+1}^T\\
&H_n^T + F \rightarrow H_{n-1}^T
\end{aligned} \tag{9.1}$$

The concentrations of F- and H-centers change with time according to

$$\begin{aligned}
\frac{dC_F}{dt} &= K - \beta D_H C_H C_F - 4\beta D_F C_F^2 - \beta D_F C_F C_{TH} + W_C^-(2)C_2 - \\
&\quad D_F C_F k_F^2 + D_F \frac{4\pi}{\omega}\sum_{n=2}^{\infty} r_n C_n Z_{CF}(n) C_F^e(n)
\end{aligned} \tag{9.2}$$

$$\frac{dC_H}{dt} = K - \beta D_H C_H C_F - \beta D_H C_H \left(C_T - C_{HT} - \sum_{n=2}^{\infty} B_n \right) - \beta D_H C_H C_{HT} - D_H C_H k_H^2 + \nu_{HT} C_{HT}$$

where K is the production rate of F- and H-centers expressed in terms of displacements per atom per second (dpa/s), β is the F-H recombination rate constant, D_H and D_F are the diffusion coefficients of H- and F-centers, respectively, C_T is the concentration of traps for H-centers, C_{HT} is the concentration of trapped H-centers, C_n is the concentration of F_n clusters, B_n is the concentration of H_n clusters, W_C^- is the shrinkage rate coefficient of colloids (see below), ω is the molecular volume of the host lattice, r_n is the radius of the cluster containing n point defects, ν_{HT} is the de-trapping rate of the H-center

$$\nu_{HT} = \beta D_H \exp\left(-\frac{E_{HT}}{k_B T} \right) \tag{9.3}$$

$C_F^e(n)$ is the thermal concentration of F-centers in equilibrium with colloids containing n sodium atoms

$$C_F^e(n) = \exp\left(\frac{2\gamma\omega}{k_B T r_n} - \frac{E_{Ff}}{k_B T} \right) \tag{9.4}$$

where γ is the colloid-matrix interface energy, E_{Ff} is the formation energy of F-centers.

The total sink strength for absorption of point defects k_i^2 is given by

$$k_i^2 = \frac{4\pi}{\omega}\sum_{n=2}^{\infty} r_n \left(C_n Z_C(n) + B_n Z_{Bi}(n)\right), \qquad i = F, H \tag{9.5}$$

where Z_{Ci} and Z_{Bi} are the point defect capture efficiencies of sodium clusters (colloids = C) and chlorine clusters (bubbles = B).

Nucleation of chlorine precipitates starts with trapping of mobile H-centers by trapping centers; the concentration of H-centers collected at the traps obeys the equation

$$\begin{aligned}\frac{dC_{HT}}{dt} &= \beta D_H C_H \left(C_T - C_{HT} - \sum_{n=2}^{\infty} B_n \right) + W_B^-(2) B_2 - \\ &\beta C_{HT}\left(D_H C_H + D_F C_F\right) - \nu_{HT} C_{HT}\end{aligned} \tag{9.6}$$

where W_B^- is the shrinkage rate coefficient of chlorine precipitates (see below).

Continued trapping of F- and H-centers by dimers, trimers and higher aggregates leads to formation of a distribution of cluster sizes

$$\frac{dC_2}{dt} = 2\beta D_F C_F^2 - \left(W_C^-(2) + W_C^+(2)\right) C_2 + W_C^-(3) C_3 \tag{9.7}$$

$$\frac{dC_n}{dt} = W_C^+(n-1) C_{n-1} - \left(W_C^-(n) + W_C^+(n)\right) C_n + W_C^-(n+1) C_{n+1} \tag{9.8}$$

$$\frac{dB_2}{dt} = \beta D_H C_H C_{HT} - W_B^-(2) B_2 - W_B^+(2) B_2 + W_B^-(3) B_3 \tag{9.9}$$

$$\frac{dB_n}{dt} = W_B^+(n-1) B_{n-1} - W_B^-(n) B_n - W_B^+(n) B_n + W_B^-(n+1) B_{n+1} \tag{9.10}$$

Sodium and chlorine clusters nucleate and evolve due to absorption of F- and H-centers, respectively. We also take into account the thermal ‘evaporation’ of F-centers from sodium clusters. The corresponding growth and shrinkage rate coefficients are defined as follows

$$W_C^+(n) = \frac{4\pi}{\omega} r_n D_F Z_{CF}(n) C_F \tag{9.11}$$

$$W_C^-(n) = \frac{4\pi}{\omega} r_n \left(D_H Z_{CH}(n)\, C_H + D_F Z_{CF}(n) C_F^e(n)\right) \tag{9.12}$$

$$W_B^+(n) = \frac{4\pi}{\omega} r_n D_H Z_{BH}(n) C_H \tag{9.13}$$

$$W_B^-(n) = \frac{4\pi}{\omega} r_n D_F Z_{BF}(n) C_F \tag{9.14}$$

Growth rate coefficient of cluster of n PD-s is proportional to the concentration of the same PD-s in the vicinity of the cluster and PD-s diffusion coefficient in one hand, and corresponding capture efficiency $Z_{Ai}(n)$ and cluster size in other hand. In the same way, in the expression for the shrinkage coefficient the same parameters appear for the 'opposite sign' PD-s. The second term in the shrinkage coefficient of colloids (equation 9.12) is responsible for thermal evaporation of F-centers from the colloid.

The driving force of radiolysis is the difference of the fluxes of F- and H-centers to the different sinks, i.e., on the average, bubbles should be biased to absorption of H-centers. The efficiency of a specific defect cluster to capture particular point defects depends on the interaction of these point defects with the cluster. The interaction results in a net drift of point defects to the cluster in addition to the diffusion flux. The flux of point defects to the defect cluster is given by

$$J_A = 4\pi R Z_{Ai} D_i C_i \ , \qquad A = Bubble,\ Colloid \qquad i = F\ , H \tag{9.15}$$

The calculation of the capture efficiencies is a separate and complicated task. For metals this problem has received much attention in the past in connection with the problem of vacancy swelling of structural materials of nuclear reactors. Generally, the capture efficiency of an isolated spherical macro-defect of radius R is given by [5,9]

$$Z_{Ai}(R) = 1 + \alpha_{Ai}^{(1)} \frac{a}{R} + \alpha_{Ai}^{(2)} \frac{\sigma_n}{\mu} + \alpha_{Ai}^{(3)} \left(\frac{\sigma_n}{\mu} \right)^2 \tag{9.16}$$

where a is the lattice constant, $\alpha_{Ai}^{(n)}$ are dimensionless constants which depend on the material properties and the temperature, σ_n is the normal stress at the cluster-matrix interface and μ is the shear modulus of the matrix. The origin of various terms in this formula is discussed in [5,9]. In dense pile-ups or bunches of macrodefects the capture efficiencies also depend on arrangement of microstuctural defects, since the elastic field of neighboring clusters may overlap, i.e. point defect may interact with several clusters simultaneously [10]. We assume that the different behaviour of the LHM after low temperature irradiation is associated with the differences in the aggregation states of the sodium colloids during irradiation. It is known that the main driving force for the microstructural evolution under irradiation is the difference between the capture efficiencies of H- or F-centers by extended defects of various kinds and/

or sizes (Na colloids, chlorine inclusions and dislocations) [2,4,5]. During irradiation at high temperature (100 °C) the large colloids are in the liquid state, but at room temperature these colloids are in the solid state. For this reason their capture efficiencies differ, which might lead to observed dissolution of large colloids. Rather than going into the details of the capture efficiency calculations, we will use in our simulations the modeled temperature dependent capture efficiencies and cluster sizes (figure 9.3) [1].

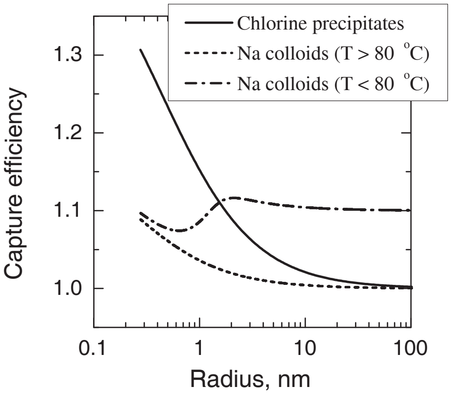

Figure 9.3: Capture efficiencies of *H*-centers. It is assumed that small colloids (R<1 nm) are always solid and their capture efficiencies do not depend on the irradiation temperature.

Schematically, the mechanism of colloid dissolution at low temperature can be described as follows. The number of *F*-centers *n* in a large colloid changes as a function of the time

$$\frac{dn}{dt} \propto \left(\delta_{mean} - \delta_C(n)\right) D_F C_F \tag{9.17}$$

where the bias of colloids for absorption of *H*-centers $\delta_C(n)$ is defined by

$$\delta_C(n) = 1 - \frac{Z_{CF}(n)}{Z_{CH}(n)} \tag{9.18}$$

and the mean bias of the system δ_{mean} is determined by all macro-defects present in the system

$$\delta_{mean} = 1 - \frac{k_F^2}{k_H^2} \tag{9.19}$$

During irradiation at a high temperature the large colloids are in the liquid state (according to DSC the melting temperatures of colloids are distributed in the interval from 80 to 140 ^{o}C [7]). At high temperatures the condition $\delta_{mean} - \delta_C(n) > 0$ is true; i. e. $dn/dt > 0$. At low temperatures, because we are dealing with solid sodium precipitates, the absolute value of the size misfit of these colloids increases. This means that at low temperatures the bias for absorption of *H*-centers by large colloids may become larger than the mean bias of the system, i.e. large colloids should shrink, i.e. $\delta_{mean} - \delta_C(n) < 0$ and $dn/dt < 0$. The linear expansion of bulk sodium as a result of melting is about 0.9%. Assuming that the liquid colloid has no or a very small misfit, which does not contribute significantly to the capture efficiencies ($\alpha_{Ai}^{(2)}\sigma_n/\mu < 1$), and taking into account the linear thermal expansion of the NaCl-matrix and the colloid, the size misfit of the solid colloid with the BCC-lattice of bulk sodium is about -1%. This negative misfit results in tensile stresses within the colloid and in a stronger interaction of *H*-centers with the colloid compared with *F*-centers. I.e. at low temperatures large colloids are expected to absorb preferentially *H*-centers instead of *F*-centers. This assumption is suggested by our experimental observations, showing dissolution of the colloids during irradiation at low temperatures. The term $\alpha_{Ai}^{(2)}\sigma_n/\mu$ in the expression for the capture efficiency (16) is responsible for this effect. The normal stress at the cluster-matrix interface is given by

$$\sigma_n = \frac{12\mu K_C}{4\mu + 3K_C}\varepsilon \qquad \sigma_n/\mu = -0.011 \tag{9.20}$$

In metals the value of the coefficient $\alpha_{Ai}^{(2)}$ is usually between about 1 and 10 [9]. We assume that we are dealing with similar values in the case of NaCl. This means that the colloid bias might change considerably after cooling down the sample from 100 ^{o}C to room temperature. With regard to very small colloids, we can say that it is likely that they do not exhibit melting, since the surrounding matrix forces the Na-atoms to retain the FCC lattice of the Na sublattice [11], similar to small lithium precipitates in lithium fluoride [12]. This would explain two aspects of our experimental observations: (i) the LHM peak of metallic Na decreases during low temperature irradiation and (ii) the temperature dependence of the bias of very small Na precipitates is weak.

In the simulations we have used a standard set of material parameters [5-7] (table 9.1). We have found that the rate of colloid nucleation depends strongly on the colloid-matrix interface energy. To overcome this difficulty we have used the temperature dependent surface energy of the colloids (table 9.1). This can be justified by the following known facts [13-15]: (i) with increasing temperature the surface energy of solids decreases by about 0.5 mJ/m^2 K for many metals; and (ii) the surface energy of solids is higher than the surface energy of liquids.

Table 9.1: Material parameters used in calculations.

Parameter	*Value*
Absorbed energy required per primary *F-H* displacement, eV	100
Dose rate, *K*, Mrad/hour (dpa/s)	480 ($8x10^{-6}$)
Irradiation dose at 100 °C, Grad (dpa)	320 (19.4)
Irradiation dose at 20 °C, Grad (dpa)	550 (33.3)
Diffusion coefficient of H-centers, D_H, m^2s^{-1}	$10^{-6}exp(-0.1eV/k_BT)$
Diffusion coefficient of F-centers, D_F, m^2s^{-1}	$10^{-6}exp(-0.78eV/k_BT)$
Formation energy of F-centers, E_{Ff}, eV	1
Recombination rate constant, β, m^{-2}	$3x10^{20}$
Atomic volume of the host lattice, ω, m^{-3}	$4.4x10^{-29}$
Concentration of traps for H-centers, c_T	10^{-5}
Binding energy of an H center with the trap, E_{HT}, eV	0.6
Colloid-matrix interface energy, $\gamma(T) = \gamma_0 + a(T - T_0)$, mJ/$m^2$	$430 - 0.4\ (T - 373\ K)$
Colloid bulk modulus, K_C, GPa	6.3
Shear modulus of NaCl, μ, GPa	12.61

9.4 Simulation of the two-steps irradiation experiment

Figure 9.4 shows the simulated formation of point defect clusters at 100 °C. Because of the high mobility of the *H*-centers, chlorine clusters nucleate first. The leading edges of both distributions advance with time.

The model sample, which was irradiated at 100 °C to a dose 320 Grad, has been allowed to anneal for 1 week at 20 °C; no changes in volume fraction were observed, only the small-sized clusters ($n < 10$) annealed. Subsequently, the second stage irradiation at 18 ºC to a maximum dose of 550 Grad was simulated using the “low temperature” capture efficiency of the colloids (dash-dotted line in figure 9.3). The results are plotted in figure 9.5.

Because of the high mobility of the *H*-centers, in the early stages of the low temperature irradiation a new population of chlorine clusters nucleates at the available traps (which gives rise to the peak in figure 9.5b at about 3 nm), but the contribution of the clusters, associated with this peak, to the total volume fraction is small. It can be seen that large colloids dissolve, while very large number densities of small colloids are predicted to exist in these materials.

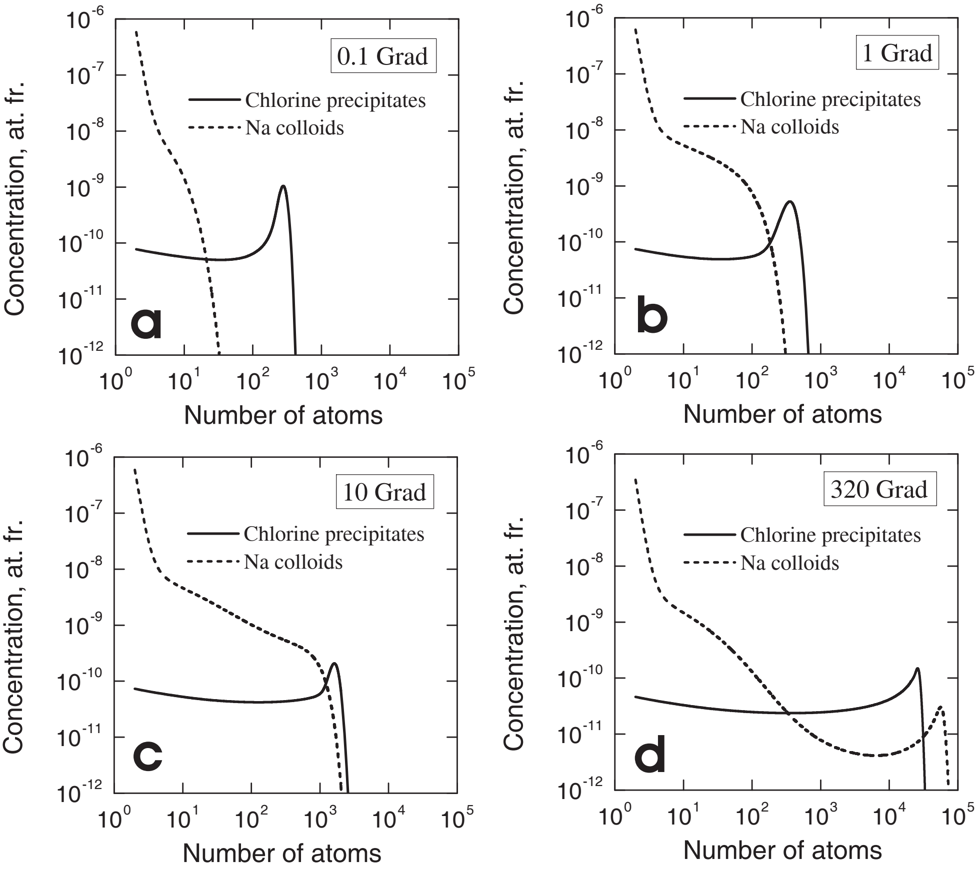

Figure 9.4: The development of the size distribution of the precipitates as a function of the irradiation dose. The concentrations of clusters C_n and B_n, denoted in the figure as Na colloids and chlorine precipitates, versus the number of atoms n in the clusters. The simulations correspond to irradiation at 100 °C up to 320 Grad (using the "high temperature" capture efficiency for colloids, shown by dashed line in figure 9.3).

Our explanation of the decrease of the LHM of sodium after low temperature irradiation is based on the different properties of solid and molten colloids. At low temperature (when the Na precipitates are in the solid state) we assume that the large colloids show an increased efficiency to capture *H*-centers, which leads to a decrease of the size of these colloids.

In figure 9.6 the results of the calculations are compared with experimental data. The model sample was "irradiated" at 100 °C to a dose of 320 Grad. Subsequently, the second stage irradiation is given to the sample at 18 °C to a dose of 550 Grad in a simulation using the "low temperature" capture efficiency of the colloids. According to figure 9.6, the agreement between the experimental results and the model predictions is satisfactory.

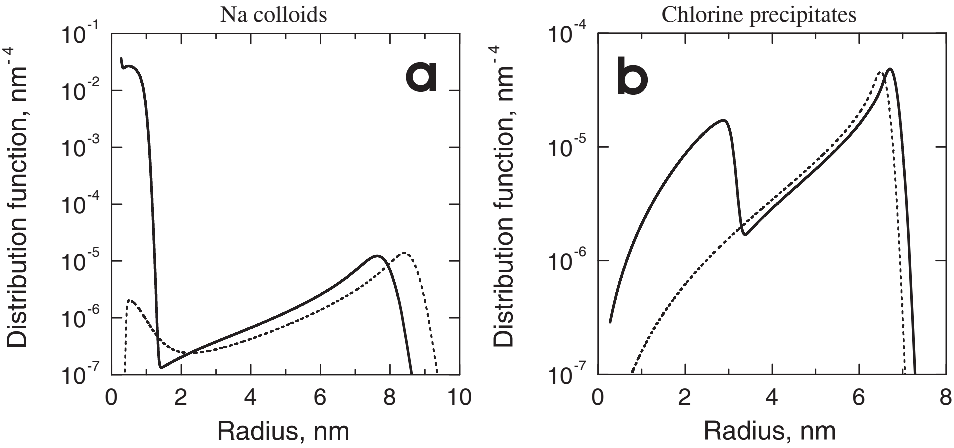

Figure 9.5: The simulated evolution of the distribution functions of Na colloids (a) and chlorine precipitates (b) after a second stage irradiation to 550 Grad at 18 °C. The initial distribution functions (dashed lines) were obtained by simulation of irradiation to 320 Grad at 100 °C. The solid lines correspond to calculations with the "low temperature" capture efficiency of the colloids (dash-dotted line in figure 9.3).

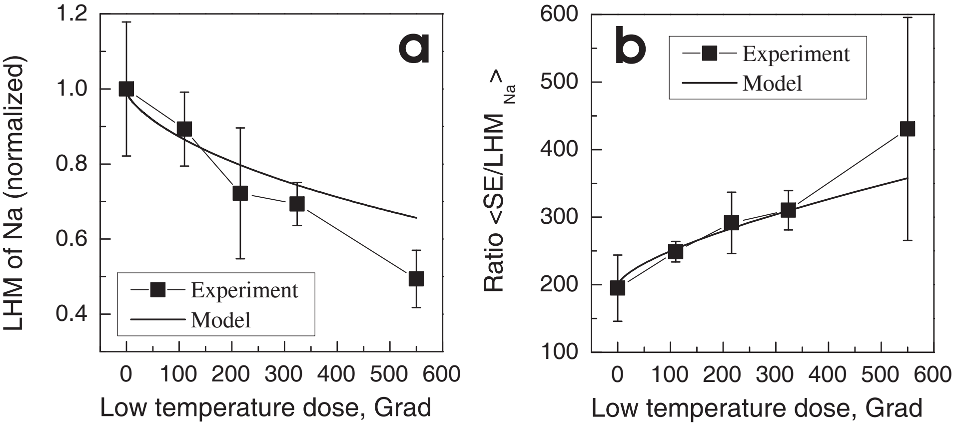

Figure 9.6: Comparison of the simulation results and the experimental data. The data points have been obtained by averaging the data depicted in figure 9.1a over a set of samples irradiated to the same high and low-temperature dose. The error bars show the standard deviations for each set of experimental data.

(a) the LHM (experiment) and the simulated volume fraction of large colloids ($R > 1$ nm). Both the experimental data and the data from simulations are normalized to the corresponding maximum values.

(b) the ratio of SE to LHM of sodium (experiment) and the ratio of total amount of radiolytic Na to the amount of Na in large colloids ($R > 1$ nm). The latter is multiplied by the ratio SE/LHM = 195 (see reference [6,7]) measured in samples before low temperature irradiation.

9.5 Conclusions

The experimental observations along with the model simulations, presented in this chapter, show that the change of the irradiation temperature has a drastic effect on the evolution of the radiolytic nanoprecipitates. The decrease of the temperature during irradiation results in a reorganization of the defect structure. Large colloids are dissolved under irradiation at low temperature, and very small colloids arise instead. From the increase of the SE we can conclude that the overall volume fraction of the newly nucleated colloids and the isolated *F*-centers is slightly larger than the part of the large colloids, which was dissolved during low temperature irradiation. The model, formulated to describe the nucleation kinetics and the evolution of the size distribution of chlorine precipitates and sodium colloids in NaCl under irradiation, shows remarkable agreement with the experimental results. The calculations show a significant renewal of the colloid size distribution and a shift of its maximum to smaller sizes caused by the decreased irradiation temperature. The difference in the capture efficiency of the colloids in the liquid and solid state is assumed to be the reason of the differences of the size distributions of the colloids, nucleated above and below the melting point.

Obviously, other causes, like the temperature dependence of the mobility of the PD's and the temperature dependent de-trapping processes also influence the colloid size distribution. However, these effects are assumed to be weaker; they did not cause dissolution of the colloids [1].

In addition, it should be noted, that we can expect to find different colloid size distributions in the NaCl crystals, which had been irradiated at different temperatures without changing the temperature during irradiation run. A detailed study of the temperature dependence of the ED-s distribution would be worthwhile. Although the AFM observations of colloids shows a considerable statistical error in the measurement of the colloid sizes distributions (*chapter VI*), extensive AFM experiments for a vast number of NaCl samples, irradiated at different temperatures would be helpful to study of the temperature dependence of the distribution of colloids sizes.

References

[1] A.A. Turkin, A.V. Sugonyako, D.I. Vainshtein and H.W. den Hartog, *J. Phys.: Condens. Matter.* **18** (2006), 5655-5668

[2] U. Jain and A.B. Lidiard, *Phil. Mag.* **35** (1977), 245-259

[3] A.B. Lidiard, *Phil. Mag.* **39** (1979), 647-659

[4] V.I. Dubinko, A.A. Turkin, D.I. Vainshtein and H.W. den Hartog, *J. Nucl. Mater.* **277** (2000), 184-198

[5] V.I. Dubinko, A.A. Turkin, D.I. Vainshtein and H.W. den Hartog, *J. Nucl. Mater.* **304** (2002), 117-128

[6] J.C. Groote and J.R.W. Weerkamp, *Radiation damage in NaCl. Small particles*, PhD thesis, University of Groningen, (1990)

[7] J. Seinen, *Radiation damage in NaCl. The process of colloid formation*, PhD thesis, University of Groningen, (1994)

[8] A.V. Sugonyako, A.A. Turkin, R. Gaynutdinov, D.I. Vainshtein, H.W. den Hartog and A.A. Bukharaev, *Phys. Stat. Sol.* **2**: (1) (2005), 289-293

[9] V.A. Borodin, A.I. Ryazanov and C. Abromeit, *J. Nucl. Mater.* **207** (1993), 242-254

[10] A.A. Turkin and V.I. Dubinko, *Appl. Phys.* **A 58** (1994), 35-39

[11] A.V. Sugonyako, D.I. Vainshtein, A.A. Turkin, H.W. den Hartog and A.A. Bukharaev, *J. Phys.: Condens. Matter.* **16** (2004), 785-798

[12] M. Lambert, Ch. Mazieres and A. Guinier, *J. Phys. Chem. Sol.* **18** (1961), 129-134

[13] A.W. Adamson and A.P. Gast, *Physical chemistry of surfaces*, Wiley, (1997)

[14] J.M. Howe, *Interfaces in materials: Atomic structure, kinetics and thermodynamics of solid-vapor, solid-liquid and solid-solid interfaces*, Wiley, (1997)

[15] V.K. Kumikov and Kh. B. Khokonov, *J. Appl. Phys.* **54** (1983), 1346-1350

SUMMARY

The interest in the formation of radiation damage in alkali halides and in particular, in NaCl, is stimulated by the fact that rock-salt in stable geological formations is a prominent candidate medium for storage of high-level waste (HLW) of nuclear power plants. As a result of the interaction between the ionizing radiation, emitted by HLW, and the neighboring rock salt crystals, the $Na^+ Cl^-$ ions in the crystal are transformed partly into neutral sodium and chlorine atoms and molecules, respectively. This process of transformation and successive separation of sodium and chlorine atoms in NaCl by means of radiation is similar to the well known process called electrolysis. For this reason the production of radiation induced defects in NaCl and many other ionic compounds is often referred to as radiolysis. As a result, a fraction of the energy, emitted by HLW, is stored in crystalline rock salt by introducing radiolytic products, among which metallic sodium and molecular chlorine.

Although NaCl has been investigated both experimentally and theoretically very extensively, many observations made in radiation damage studies are not understood. To mention just a few: The first question is related with the very remarkable observation, that for very high doses (produced in the laboratory by means of a 0.5 or 1.35 MeV electron beam) more than 20 at% of the NaCl molecules in the crystal can be transformed into Na and Cl_2. The second important question is why in many samples the presence of minor fractions (a few 100 ppm) of impurities has so drastic effects on the production of radiolytic Na and Cl_2, even in the range of 20 at% and higher. And why are the individual precipitates in NaCl extremely small, although it appears from the results obtained from experiments on moderately damaged samples that the average particle size increases with increasing amount of precipitates. Although this thesis is not aimed at providing clear-cut answers on all these questions, we think that we were able to present some new ideas, which might help to find solutions.

Apart from this, we have found intriguing new results, showing that with heavily damaged NaCl we have discovered a new class of exotic materials showing interesting and unexpected structural, chemical, stability, electrical, magnetic and optical properties. These properties have almost nothing in common with the bulk properties of NaCl, metallic sodium or molecular chlorine and are often largely determined by the nano- or microstructure of the heavily damaged samples. Probably the most remarkable and technologically relevant property of many of our heavily damaged NaCl crystals is that they might even be powerful explosives.

In many cases the concentrations of Na and Cl_2 increase without any sign of saturation as a function of the irradiation dose. Accumulation of very large amounts of the radiolytic products in the crystalline material leads to a significant decrease of the chemical and mechanical stability of the rock salt and ultimately to explosive decomposition of NaCl crystal as a result of spontaneous exothermic recombination of radiolytic Na and Cl_2. Good understanding of the radiolysis process in alkali halides and its consequences for the materials, which are exposed to ionizing radiation for a very long time period, is crucial for safe storage of high-level nuclear waste in salt mines. The main purpose of this thesis is to provide an insight into the radiolysis process in crystalline NaCl in very advanced stages, where extremely high concentrations of radiolytic products have been accumulated.

A detailed analysis of the structure and properties of the radiolytic sodium and chlorine precipitates systems and the host crystalline matrix at very high irradiation doses is required to explain the behavior of extremely heavily irradiated NaCl crystals. Comprehensive experimental observations of the natural rock salt and synthetic pure and doped NaCl samples, which have been irradiated to extremely high doses by means of electron beams, have been carried out in combination with the application of newly developed theoretical models describing the radiolysis process and the development of the main extended defects in NaCl.

A variety of experimental methods has been applied to study sodium and chlorine precipitate systems in very heavily irradiated NaCl. Differential Scanning Calorimetry has been utilized to measure the concentrations of the radiolytic products accumulated in the NaCl samples by using the energy associated with the phase transition of sodium and chlorine in the precipitates as a measuring probe. The results, obtained from these calorimetry experiments have shown that the general trend for all NaCl samples is a continuous increase of the amount of precipitated sodium in the irradiated NaCl crystals with increasing dose. However the rate of the increase varies from sample to sample depending on the impurities present in the samples. We have observed that compared with pure NaCl, the radiolysis process is slowed down appreciably in Br-doped samples. On the other hand the percentage of precipitated sodium increases significantly in K- and KBF_4-doped crystals compared to pure NaCl samples. There is only exception, which is pure NaCl, irradiated up to 2×10^3 GRad (2×10^{10} Gy or 8×10^{19} e^-/cm^2), where for the highest dose reached in our investigation – the amount of metallic sodium increases steeply and reaches the highest values among all investigated NaCl samples. In addition it should be noted, that in these samples no saturation of the amount of precipitated Na with increasing irradiation dose is observed, just as for all other types of NaCl samples (i.e. doped and natural crystals). However, our experimental results show that the presence of small amounts of NaBr has a significant effect on the radiation resistance of NaCl in particular for ultra-high doses. The amount of precipitated sodium in the 400 ppm NaBr doped samples remains less than 4 at% even for samples exposed to a ultra-high dose of 2×10^3 GRad (2×10^{10} Gy or 8×10^{19} e^-/cm^2). On the other hand, the amount of precipitated sodium in these samples shows small but almost linear growth with the increasing dose, therefore we cannot make the inference about saturation of radiation damage for the NaBr doped NaCl crystals either.

An analysis of the melting spectra, which are in fact the plots of the heat flow in the differential scanning calorimetry experiments as a function of the temperature, of precipitated sodium has shown that in moderately irradiated NaCl samples (with doses less than 3×10^2 GRad or 3×10^9 Gy, or 12×10^{18} e^-/cm^2) sodium particles may exist showing two different structural states – (1) a *fcc* or octahedral lattice structure, which has been observed for free small sodium clusters, and (2) a *bcc* lattice structure, which is typical for bulk sodium. Two melting peaks, located at two different temperatures below the melting temperature of bulk sodium, are associated with melting of the *fcc*- and *bcc*-sodium particles, respectively. We cannot exclude the possibility that the nano-particles consist of two regions: the inner and outer region, where the latter is part of the NaCl-Na interface. The area of the nanoparticle close to the interface might inherit the *fcc* structure from the NaCl-matrix, while the inner part has the normal *bcc* structure. Surface and core melting in such particles may occur at separate temperatures.

In heavily irradiated NaCl samples (with doses of 3×10^2 GRad or 3×10^9 Gy, or 12×10^{18} e^-/cm^2 and higher) a third and wide melting peak appears at temperatures higher than the melting temperature of bulk sodium. At the same time first and second melting peaks disappear. The concentration of radiolytic metallic sodium in these samples is higher than about 2 at%. The location of the melting peak at high temperature suggests that for this type of samples the curvature of the interface between the Na particles and the host matrix is very large. This led us to the conclusion, that in advanced stages of the irradiation the sodium precipitates are converted into very small particles or structures with ultra fine surface irregularities. Indeed, dense and coral-like structures, which consist of building blocks of small spherical particles, have been observed in heavily irradiated NaCl crystals by means of Atomic Force Microscopy. The sizes of the individual particles in these structures have been found to be about 2 – 5 nm. In some of these samples highly organized string- and ring-like formations of tiny Na particles have also been found. The organized structures may be formed in the crystalline NaCl matrix as a result of decoration of dislocations and dislocation loops by small metallic particles. Probably, the structures of very small Na particles in advanced stages of the irradiation are created by rearrangements of neighboring sodium precipitates and short-range exchange of sodium atoms between the precipitates during continuous irradiation.

At the same time experimental results obtained for Na-precipitates by means of Conduction Electron Spin Resonance spectroscopy show that systems of small interacting metallic particles are formed in NaCl when the irradiation dose reaches values of 3×10^2 GRad (3×10^9 Gy, or 12×10^{18} e^-/cm^2) and higher. Detailed measurements of the temperature dependence of the spin resonance signal revealed that a magnetic transition occurs in the Na-precipitated system at temperatures below 100K. The results can be explained in terms of anti-ferromagnetic ordering of conduction electron spins in the precipitate systems, taking place along the quasi-linear structures of tiny sodium particles at sufficiently low temperatures. It should be mentioned that a similar temperature behavior of the electron spin system has been observed in several conducting polymers and in some alkali fullerides, which were shown to form quasi-one-dimensional conducting systems.

The formation of highly organized structures of radiolytic particles in heavily irradiated rock salt crystals may also explain the high capacity of NaCl crystals to accumulate very large amounts of precipitated sodium. Indeed, self-organization of radiolytic precipitates might be the reason why sodium and chlorine precipitates are separated highly effectively. This also suggests that similar highly organized structures of the other radiolytic products, including the halogen (chlorine) gas bubbles, which are the counter part of the Na-precipitates, are also formed. Unfortunately, compared with sodium particles, chlorine precipitates are far less accessible with experimental research techniques. The most important experimental method, which was used to investigate these chlorine objects, is differential scanning calorimetry of the melting and freezing processes.

It has been found by means of calorimetry measurements that in relatively low damaged samples a large fraction of the radiolytic chlorine in the NaCl matrix does not exhibit melting behavior. However, when the overall fraction of radiolytic Na (and Cl_2) in the sample reaches values of 3-4 at% about the full amount of Cl_2 is 'visible' in melting experiments, which implies that all Cl_2 molecules contribute to the melting peak. This could be deduced from the ratio of the latent heat of melting of Na and Cl_2. The results of these experiments on heavily damaged materials indicate that the numbers of chlorine and Na atoms in heavily damaged NaCl are the same, i.e. no chlorine atoms or molecules escape during irradiation; the chlorine, located in the bubbles, represents almost all the radiolytic Cl_2 in the sample. Also the fact, that we have not observed any evidence for specific heat effects associated with condensation or evaporation of chlorine in the bubbles population, indicates that the pressure in the chlorine bubbles should be higher than the critical value for chlorine (i.e. 76 bar); it is therefore assumed that the chlorine in these bubbles is in the liquid state.

A detailed analysis of the melting spectra associated with chlorine in the bubbles shows that the pressure in the bubbles changes when they undergo the solid-liquid phase transition. From the temperature shift of the freezing temperature compared to the melting temperature of chlorine we have found that the pressure in the bubbles changes in about 0.9 kbar. At the same time the maximum pressure in a bubble with a radius of 2 nm (which is the most probable size of the bubbles, according to the theoretical calculations) was estimated to be about 15 kbar. This estimation is of the same order of magnitude as the one obtained for halogen bubbles in metals.

Surprisingly, the X-Ray scattering experiments on ultra-heavily irradiated NaCl crystals revealed that the crystalline matrix of these samples remains quite perfect even at highest irradiation doses. No noticeable amorphisation of the NaCl monocrystallic samples, caused by irradiation, has been detected in these experiments. This is in contrast with several observations reported in the literature on other inorganic materials, which show that quite often after exposure to very high irradiation doses of radiation the samples are metamict (amorphous). The X-Ray results prove that in heavily irradiated NaCl *bcc* Na particles are formed. Solid particles of molecular chlorine have also been observed in irradiated NaCl samples at 95K (this temperature is well below the melting temperature of chlorine in the bubbles). Our experimental results show that a very strict relationship between the orientation of the crystal lattices of sodium and chlorine precipitates with respect to the crystal lattice of the host NaCl matrix exists.

The X-Ray results seem to suggest that the size of the sodium and chlorine particles increases very strongly with increasing irradiation dose, while the results of independent experiments using several other techniques such as Atomic Force Microscopy, Conduction Electron Spin Resonance spectroscopy, and also Raman scattering spectroscopy and differential scanning calorimetry on the same samples show the opposite. I.e. in very heavily damaged NaCl the particles should be extremely small. This contradiction can be understood in terms of a schematic model, where well-organized structures of sodium nano-precipitates are formed, which show (i) a very strict orientation relation with the NaCl crystal, (ii) although in general this orientation relation gives rise to 24 different, but equivalent orientations with respect to the NaCl crystal lattice, in rather large regions (several 100 nm) the orientation of the crystal axes of the individual Na-precipitates should be exactly the same and (iii) the size of these regions increases with the concentration of metallic Na. This description is supported by the observation that the perfection of the crystalline NaCl matrix is high, even for the most heavily damaged samples.

Direct chemical reactions between sodium and chlorine nano-precipitates are assumed to be responsible for the development of nano- and micro-cracks (voids) in the host NaCl matrix. Voids, which are situated in the bulk of the crystal, can be visualized at the cleaved surface of irradiated NaCl samples by means of Scanning Electron Microscopy. Their sizes are tens to hundreds nanometers, and these voids show a variety of shapes. The present investigations of voids in ultra-heavily irradiated NaCl show that the shapes and sizes of the voids, and also the void concentrations and growth rates depend on the presence of impurities in the NaCl crystals. A detailed analysis of the void images, carried out for large numbers of NaCl samples with various dopants show a very low rate of formation of rather small spherical voids for Br-doped NaCl, while the appearance of large numbers of faceted voids is typical for heavily damaged KBF_4-doped samples. The presence of large numbers of elongated, penny-shaped voids is the most characteristic feature of heavily damaged pure, K-doped NaCl crystals and natural rock salt samples. However, the general trend observed for all investigated systems is that the average void size and the concentration increase with the irradiation dose, while the void shape transforms from round to faceted ones, while finally penny-shaped voids are formed, which are in fact nano-cracks produced by instantaneous chemical reactions. The nano-cracks develop into macro-cracks, which ultimately leads to fracture and decomposition of the sample. Each of these stages of void growth may be realized in all types of the NaCl materials at a certain irradiation dose, which depends on the composition of the sample, the irradiation dose, the dose rate and the irradiation temperature.

An interesting observation has been obtained from a comparison of the results for NaCl samples, which had been irradiated at different dose rates. For the K-doped NaCl crystals the rate of formation of voids was found to be much larger in the case of the low dose rate experiments. In fact, for these samples the growth rate of the void volume is approximately inversely proportional to the dose rate. The concentration and volume fraction of the voids are much larger in those crystals, which had been irradiated at low dose rate, while at the same time the production rate of precipitated sodium and chlorine increases much more moderately at decreased dose rates. From the point of view of practical applications, i.e. storage of high-level radioactive waste of nuclear power plants in the salt domes, the dose rate effect is very relevant since the conditions during storage are characterized by very low dose rates (typically a factor of 1000 to 10000 lower than the dose rate used in our laboratory experiments). Consequently, a very high efficiency of void development is expected under storage conditions, where low dose rates are combined with very high doses. With increasing growth rate of voids the stability of the irradiated NaCl decreases drastically, because especially at high doses the presence of voids and nano-cracks (penny-shaped voids) reflects the occurrence of the above-mentioned instantaneous back reactions between radiation-induced Na and Cl_2.

In addition, we have investigated the modifications of the precipitate systems cause by variation of the irradiation temperature. For this purpose we have carried out two-stage irradiation experiments, where in the first stage the irradiation temperature is about 100 °C, which corresponds approximately with the maximum production rate of radiation damage. In the second stage the irradiation temperature was lowered to room temperature and the behavior of the latent heat of melting of sodium and the stored energy were measured as a function of the dose added at room temperature. The results strongly indicate that during the second stage irradiation the nano-structured precipitates are modified appreciably. Large colloidal fragments are split up under irradiation at low temperature, which leads to fragmentation of sodium colloids and the production of very small colloids and even *F*- and *F*-aggregate centers. A fraction of these colloidal fragments in the samples might be reduced in size such that the melting peak cannot be observed anymore or otherwise the very wide size distribution leads to an extremely wide latent heat peak, which cannot be observed as a result of the small value of the signal-to-noise ratio. In agreement with this observation, the simulations by means of the radiolysis model used in this thesis show that reduction of the irradiation temperature in the second stage of the experiments leads to drastic reductions of the average size of sodium colloids.

SAMENVATTING

De interesse in het ontstaan van stralingsschade in alkali halogeniden en in het bijzonder, in NaCl, wordt versterkt door het feit dat natuurlijk steenzout in stabiele geologische formaties een prominente kandidaat is om te dienen als opslagmedium voor hoogwaardig kernsplijtingsafval (KSA) van kerncentrales. Door de interactie tussen de ioniserende straling, uitgezonden door het KSA, en de naastgelegen steenzoutkristallen, worden de Na^+ en Cl^- ionen in de kristallen gedeeltelijk getransformeerd in neutrale natrium atomen en chloor moleculen. Het proces van transformatie en de daaropvolgende scheiding van de natrium en chloor atomen, respectievelijk moleculen in de NaCl kristallen door inwerking van straling is vergelijkbaar met een meer algemeen bekend proces dat elektrolyse wordt genoemd. Daarom wordt de produktie van defecten in NaCl en vele andere zouten ten gevolge van straling vaak radiolyse genoemd. Als gevolg van radiolyse wordt een deel van de energie, die door het KSA wordt uitgezonden, in kristallijn steenzout in de vorm van radiolytische produkten, zoals onder andere metallisch natrium en moleculair chloor, opgeslagen.

Ook al zijn er wereldwijd vele experimentele en theoretische onderzoeken naar stralingsschade in NaCl uitgevoerd, toch ontbreekt nog steeds de verklaring voor verscheidene waarnemingen, die in deze onderzoeken verricht zijn. Recent onderzoek aan grote aantallen NaCl monsters, die bestraald waren met hoge stralingsdoses, heeft uitgewezen dat in veel gevallen de concentratie natrium en chloor zonder enig teken van verzadiging met de bestralingsdosis toeneemt. Ophoping van groter wordende hoeveelheden radiolytische produkten in het kristallijne materiaal leidt tot een drastische afname in chemische en mechanische stabiliteit van het steenzout en uiteindelijk tot explosieve ontbinding van het NaCl kristal als gevolg van spontane, exotherme recombinatie van radiolytisch Na en Cl_2 (knalzout). Een beter begrip van de radiolytische processen in alkali halogeniden en de consequenties voor de materialen, die gedurende zeer lange periodes worden blootgesteld aan ioniserende straling, is van cruciaal belang voor veilige opslag van KSA in zoutmijnen. Het hoofddoel van het onderzoek in dit proefschrift is inzicht te verkrijgen in de radiolytische processen in kristallijn NaCl in vergevorderde stadia van bestraling, waar extreem hoge concentraties van radiolytische produkten zijn opgebouwd. Een gedetaileerde analyse van de structuur en de eigenschappen van radiolytisch natrium en chloor en die van de kristallijne NaCl matrix bij zeer hoge doses is nodig om het gedrag van intensief bestraalde NaCl kristallen te verklaren. Experimentele waarnemingen aan bestraald natuurlijk steenzout en zuivere en eveneens bestraalde verontreinigde, synthetische NaCl monsters, zijn uitgevoerd en vergeleken met de resultaten, verkregen met nieuw ontwikkelde theoretische modellen die de radiolytische processen en de ontwikkeling van de meest belangrijke defecten in NaCl beschrijven.

De resultaten van Differential Scanning Calorimetry experimenten van de fase overgang van natrium en chloor in de precipitaten laten zien dat de algemene trend voor alle NaCl monsters is dat de concentratie van de radiolytische precipitaten in de bestraalde NaCl kristallen toeneemt naarmate de dosis toeneemt. De snelheid van de toename verschilt echter per monster, afhankelijk van het type en de hoeveelheid verontreiniging die in het monster aanwezig is. We hebben gezien dat vergeleken met zuiver NaCl de snelheid van het radiolytisch proces behoorlijk afnam voor de Br-verontreinigde monsters. Aan de andere kant nam het percentage van metallisch natrium in K- en KBF_4- verontreinigde kristallen significant toe. In zuiver NaCl, dat in ons onderzoek was bestraald tot de hoogst behaalde doses – 2×10^{3} Grad (2×10^{10} Gy of 8×10^{19} e^{-}/cm^{2}), nam vanaf een zekere waarde van de dosis de hoeveelheid metallisch natrium zeer snel toe en bereikte de hoogste waarden van alle onderzochte NaCl monsters. Verder kan worden gezegd dat er voor geen enkel van de onderzochte NaCl monsters (zuivere, verontreinigde en natuurlijke kristallen) met toenemende bestralingsdosis echte verzadiging van de hoeveelheid precipitaat Na is waargenomen. De verkregen resultaten geven aan, dat het aanbrengen van met natriumbromide gedoteerd NaCl rondom de opslagcontainers mogelijk leidt tot een drastische beperking van de hoeveelheid stralingsschade onder opbergomstandigheden. Gericht vervolgonderzoek, om vast te stellen wat de mogelijkheden van een dergelijke opslagstrategie zijn, is noodzakelijk.

Een analyse van de ‘smeltspectra’, welke in feite de grafieken van de warmtetoevoer naar het monster, gemeten in de Differential Scanning Calorimetry experimenten als functie van de temperatuur zijn, laat zien dat voor natrium precipitaten in zwaar bestraalde NaCl monsters (bij doses van 3×10^{2} Grad (3×10^{9} Gy of 12×10^{18} e^{-}/cm^{2} en hoger) de kromming van het scheidingsvlak tussen de Na deeltjes en de NaCl matrix erg sterk is. Dit heeft ons tot de conclusie geleid dat in vergevorderde stadia van de bestraling de natrium precipitaten erg kleine deeltjes zijn of dat ze gekarakteriseerd worden door min of meer aaneengesloten structuren met ultra fijne oppervlakte onregelmatigheden. Inderdaad zijn in sterk bestraalde NaCl kristallen met behulp van Atomic Force Microscopy (AFM) dichte, koraal-achtige structuren waargenomen, die bestaan uit de kleine bolvormige deeltjes. Met deze techniek is de grootte van deze deeltjes bepaald op 2 – 5 nm. In sommige preparaten zijn ook hoog-georganiseerde buis- en ringvormen gevonden, die uit kleine Na deeltjes zijn opgebouwd. Deze georganiseerde structuren zijn mogelijk in het NaCl kristalrooster gevormd als gevolg van decoratie van dislocaties en dislocatie loops door kleine natrium metaaldeeltjes. Experimentele resultaten verkregen door middel van Geleidingselectron Spin Resonantie (Conduction Electron Spin Resonance (CESR)) spectroscopie aan NaCl kristallen met bestralingsdoses van 3×10^{2} GRad (3×10^{9} Gy, or 12×10^{18} e^{-}/cm^{2}) of hoger, hebben laten zien dat de defect systemen bestaan uit grote aantallen zeer kleine metallische Na precipitaten, die als gevolg van onderlinge wisselwerkingen niet meer als geisoleerde deeltjes beschouwd kunnen worden. Gedetailleerde temperatuur afhankelijke metingen van het electron spin resonantie signaal laten zien dat een magnetische faseverandering optreedt beneden 100K. De resultaten kunnen worden verklaard in termen van anti-ferromagnetische ordening van geleidingselectronen in de precipitaat systemen, die bij voldoende lage temperatuur als gevolg van de interacties tussen de kleine Natrium deeltjes langs de hierboven genoemde quasi-lineaire structuren ontstaat. De vorming van sterk georganiseerde structuren van radiolytische deeltjes in zwaar bestraalde steenzout kristallen verklaart ook het grote gemak waarmee NaCl kristallen gedurende bestraling Natrium precipitaten kunnen opslaan. Inderdaad, het lijkt er sterk op dat zelf-organisatie van radiolytische precipitaten de reden is waarom Natrium en Chloor precipitaten zeer effectief gescheiden kunnen worden, waardoor terugreacties bemoeilijkt worden. Dit geeft aan dat vergelijkbare sterk georganiseerde structuren van andere radiolytische producten, waaronder de halogeen (Chloor) gas bubbels, dus de tegenhanger van de Na precipitaten, ook aanwezig zijn.

Met Differential Scanning Calorimetry is bepaald dat in relatief weinig beschadigde preparaten een groot deel van het radiolytische Chloor in het kristalrooster van NaCl geen smeltgedrag vertoont. Niettemin, als de concentratie van radiolytisch Na (and Cl_2) in de preparaten een waarde van 3 of 4 at% teboven gaat, draagt de volledige hoeveelheid Cl_2 bij tot de waargenomen smeltpiek. De resultaten van deze experimenten aan sterk beschadigde materialen geven aan dat de hoeveelheden Chloor en Natrium atomen in sterk beschadigd NaCl hetzelfde zijn, of in andere woorden: er ontsnappen tijdens de bestraling geen Chloor atomen of moleculen; het Chloor, dat in bubbels gelokaliseerd is, omvat al het radiolytische Cl_2 in het monster. Ook het feit, dat we geen bewijs hebben gevonden voor een veranderende warmtecapaciteit welke veroorzaakt zou kunnen worden door condensatie of verdamping van Chloor in de bubbel populatie, geeft aan dat de druk in de Chloor bubbels hoger moet zijn dan de kritische waarde voor Chloor (76 bar). We nemen daarom aan dat de Chloor moleculen in de bubbels zich in de vloeibare fase bevinden. Een gedetailleerde analyse van de smeltspectra, welke het smeltgedrag van Chloor in de bubbels toont, laat zien dat de druk verandert wanneer zij de vaste stof–vloeistof faseovergang ondergaan. Uit de verschuiving van het vriespunt ten opzichte van het smeltpunt van Chloor hebben we berekend dat de druk in de bubbels 0.9 kbar is. Verder merken we op, dat de geschatte maximum druk in de Chloor bubbels, volgens een theoretisch model uitkomt op een waarde rond 15 kbar. Deze schatting is van dezelfde orde van grootte als de waarde, die gevonden is voor halogeen bubbels in metalen.

Verrassend genoeg laten Röntgen Diffractie experimenten aan ultra sterk bestraalde NaCl kristallen zien dat het kristalrooster van deze preparaten perfect blijft, zelfs bij de hoogste stralingsdosis. Er zijn in onze experimenten geen aanwijzingen gevonden voor amorfisatie van de kristallijne NaCl preparaten, die het gevolg zou kunnen zijn van de blootstelling aan de zeer hoge stralingsdoses. Dit is in tegenstelling tot de vele waarnemingen, die in de literatuur voor verschillende andere anorganische materialen gerapporteerd zijn, en die aantonen dat na blootstelling aan een erg hoge stralingsdosis de preparaten vaak metamict (amorf) worden. De resultaten van de Röntgen Diffractie experimenten bewijzen dat in sterk bestraald NaCl Natrium deeltjes aanwezig zijn. Daarnaast zijn in bestraalde NaCl preparaten bij een temperatuur van 95 K (deze temperatuur is ver beneden het smeltpunt van Chloor in de bubbels) vaste deeltjes bestaande uit moleculair Chloor gevonden. Onze experimentele resultaten tonen aan dat er een zeer sterke relatie bestaat tussen de orientatie van de kristalroosters van de Natrium en Chloor precipaten en het rooster van het NaCl kristal.

Directe chemische reacties tussen Natrium en Chloor nano-precipitaten zijn waarschijnlijk verantwoordelijk voor het ontstaan van de waargenomen nano- en microscheurtjes in het NaCl kristalrooster. Deze scheurtjes tonen een verscheidenheid aan vormen en zijn tientallen tot honderden nanometers groot. De vormen en groottes van deze scheurtjes, alsmede de concentratie en groeisnelheid tijdens de bestraling hangen sterk af van de aanwezigheid van onzuiverheden in de NaCl kristallen. Niettemin is de algemene trend voor alle onderzochte systemen dat de gemiddelde grootte van de scheurtjes en de concentratie ervan toenemen bij toenemende bestralingsdosis, terwijl de vorm van rond naar gefacetteerd tendeert. Uiteindelijk ontstaan muntvormige scheurtjes (penny-shaped cracks). Deze nano-scheurtjes ontstaan instantaan door locale chemische reacties tussen Natrium en Chloor. De nano-scheurtjes ontwikkelen zich bij toenemende dosis tot grotere, micro-scheuren, en uiteindelijk leidt het proces tot het breken en volledig uiteenvallen van het monster, hetgeen gepaard gaat met zeer krachtige chemische reacties. Elk van de stadia van groei van de nano en micro-scheurtjes kan gerealiseerd worden in alle typen NaCl materialen bij een zekere bestralingsdosis, die afhankelijk is van de samenstelling van het monster, de bestralingsdosis, de intensiteit van de bestraling en de bestralingstemperatuur. Bovendien is gevonden dat de groeisnelheid van het volume van de scheurtjes ongeveer omgekeerd evenredig is met de stralingsintensiteit, d.w.z. de concentratie en volume fractie van de scheurtjes zijn veel groter in de kristallen die bestraald zijn bij lage stralingsintensiteit. Voor praktische toepassingen, oftewel de opslag van hoog radioactief afval van kerncentrales in zoutmijnen, zijn de effecten van de stralingsintensiteit zeer relevant, omdat de omstandigheden gedurende de opslag van KSA gekarakteriseerd worden door een combinatie van hoge doses en lage stralingsintensiteiten. Hierdoor wordt een hoge efficientie verwacht bij het creeëren van de genoemde scheurtjes onder opslagomstandigheden. Met toenemende hoeveelheden nano- en microscheurtjes vermindert de stabiliteit van het bestraalde NaCl drastisch, omdat de aanwezigheid van steeds groter wordende holtes, nano- en microscheurtjes (penny-shaped cracks of voids) de kracht van de chemische reactie tussen Na en Cl_2 wordt vergroot, waardoor de kristallen uiteindelijk volledig uiteenspatten en omgevormd worden tot een verzameling stofdeeltjes.

Tenslotte hebben we hebben de veranderingen van het systeem van precipaten bestudeerd, die veroorzaakt worden door een sterke verlaging van de bestralingstemperatuur. We hebben daarbij gevonden, dat een dergelijke verlaging van de bestralingstemperatuur een drastisch effect heeft op de evolutie van de radiolytische nano-precipaten. Grote colloïdale deeltjes worden onder bestraling bij lage temperaturen opgesplitst, hetgeen leidt tot fragmentatie van de Natrium colloïden en de productie van zeer kleine colloïden en zelfs F- and F-aggregaat centra. Ook de modelberekeningen wijzen op een significante verandering in de distributie van de grootte van colloïden en een verschuiving van de maximale grootte naar kleinere colloiden door de verlaging van de bestralingstemperatuur. De experimentele resultaten laten zien, dat ook bij een verlaging van de bestralingstemperatuur de productie van stralingsschade doorgaat. Desondanks lijkt het er op, dat een geforceerde verlaging van de bestralingstemperatuur in een opbergplaats zou kunnen bijdragen tot het vergroten van de stabiliteit van de bestraalde zoutkristallen, omdat de afmetingen van de Na-deeltjes sterk wordt gereduceerd. Als gevolg hiervan is de energie, die gepaard gaat met de locale reacties tussen Na en Cl_2 eveneens aanmerkelijk kleiner dan voor de monsters, die niet bij lage temperaturen nabestraald waren.

LIST OF PUBLICATIONS

A.V. Sugonyako, D.I. Vainshtein, A.A. Turkin, H.W. den Hartog, A.A. Bukharaev,
Melting of sodium clusters in electron irradiated NaCl,
Journal of Physics: Condensed Matter, 16 **6**, p. 785-798, (2004)

A.V. Sugonyako, A.A. Turkin, R. Gaynutdinov, D.I. Vainshtein, H.W. den Hartog,
A.A. Bukharaev,
Systematic UHV-AFM experiments on Na nano-particles and nano-structures in NaCl,
Physica Status Solidi C, 2 **1**, p. 289-293, (2005)

A.V. Sugonyako, D.I. Vainshtein, H.P. den Hartog, A.A. Turkin, H.W. den Hartog,
Melting properties of radiation-induced Na and Cl_2 *precipitates in ultra-heavily irradiated NaCl*,
Physica Status Solidi C, 2 **1**, p. 362-366, (2005)

V.I. Dubinko, A.A. Turkin, A.S. Abyzov, A.V. Sugonyako, D.I. Vainshtein,
H.W. den Hartog,
Nucleation and growth of sodium colloids in NaCl under irradiation: Theory and experiment,
Physica Status Solidi C, 2 **1**, p. 438-443, (2005)

A.A. Turkin, A.V. Sugonyako, D.I. Vainshtein, H.W. den Hartog,
Radiolysis of NaCl at high and low temperatures: Development of size distribution of bubbles and colloids,
Journal of Physics: Condensed Matter, 18, p. 5655-5668, (2006)

H.W. den Hartog, A.V. Sugonyako, D.I. Vainshtein, A.A. Turkin, S.N. Sulyanov,
D.M. Kheiker, P.V. Dorovatovskii,
Characterization of ultra-heavily damaged NaCl
submitted for publication

S.N. Sulyanov, D.M. Kheiker, P.V. Dorovatovskii, A.V. Sugonyako, D.I. Vainshtein and
H.W. den Hartog,
Characterization of the size and orientation of Na and Cl nanocrystals in electron irradiated NaCl crystals by means of synchrotron radiation (SR)
to be published

ACKNOWLEDGEMENTS

This book is the result of four long years of my research work and my everyday life. These years brought me plenteous experience and made me grow as a researcher, and not to a less extent as a personality. These years are very important and unforgettable for me, as well as important and unforgettable are those people who, in one way or another, helped me to make this book possible. To all these people I owe my hearty thanks and my deep appreciation.

In the first place, I would like to express my gratitude to my promoter Henry den Hartog for his invaluable guidance, encouragement and support throughout all the stages of the completion of my thesis. I am thankful to him for providing an excellent opportunity of a challenging research, for his patience and a constant readiness for discussions. His admirable persistence and his passion for science inspired me during all these years and helped me stay motivated and overcome the toughest obstacles and the difficulties encountered during the research.

I gratefully thank David Vainshtein for his advice, supervision and continuous support during all these years. I cannot thank him enough for his vital contribution to this project and his assistance, which goes beyond the scientific research. I would also express special thanks to his family – Rita, Liya and Ilya for their warmest care during my first days in Groningen.

I am especially indebted to Anastas Bukharaev, who brought this project under my attention and encouraged me to apply. This thesis would not have come into existence without his support in the very beginning of my Ph.D. project.

My deep appreciation goes to Vladimir Dubinko and Anatoly Turkin for providing computer modeling and theoretical basis for this research. Anatoly, my utmost thanks for the fruitful discussions and essential contribution to almost all parts of this thesis.

I am very grateful to the members of the reading committee, Jeff de Hosson, Daniel Khomskii and Paul Blom for their constructive comments on this thesis.

I would like to thank Arend Heeres for being the first person who taught me how to work with ultra-high vacuum. To Gert ten Brink, thank for your brief but ample training course for operating the scanning electron microscope. I convey special acknowledgement to Sjoerd Hak for helping me to get the expertise in UHV-AFM and Henk Bruinenberg for his technical assistance for the device.

I am also thankful to Harry Jonkman for giving me the opportunity to work on his UHV equipment. To Sergey Sulyanov, thanks for fruitful collaboration in the most intricate X-Ray experiments. I also gratefully acknowledge Jacob Baas for helping me in using SQIUD magnetometer. Many thanks to Alexander Klimovitskii for his crucial contribution to the Raman experiments and always being ready to help. I have also benefited from the assistance and advice in my Raman measurements from Sergey Klimin. I am always pleased with our scientific discussions, which sometimes after working time transferred into more philosophical conversations over a glass of beer. I would like to thank Paul van Loosdrecht for letting me use their optical facilities.

I am grateful to Renate, Sonja, Annette and Margriet for their indispensable help dealing with travel declarations and all bureaucratic matters. Special thanks to Margriet for her 'rescue mission' on Ameland.

It is a pleasure to acknowledge Jeff de Hosson for an opportunity to work on scanning microscopes and also for kind hospitality in MK-group. Alessio, Swami and Emiel, I kindly appreciate the friendly atmosphere in our office. My grateful thanks extend to all members of MK-group: Gopi, Maarten, Tony, Uzi, Bart, Paul, Alex, Changqiang Chen, Yutao, Sriram, Dave, Vasek, George, Pim, Damiano, Sasha Klimovitskii, Sasha Fedorov, Peter, Kalpak, Willem and Elly.

Great respect and many thanks to Bram and Emiel for making the summary of this thesis into the samenvatting.

My hearty thanks go to Olya, Aidar, Dima Efremov, Katja, Gala and Alexey Kalinov, for our unforgettable evening-parties and weekends. To Ans van Doorsen for the wonderful dinner-parties on Saturnuslaan. Mylene, Oana, Silviu, Sandra, Marius, Gwilherm, Roberto, Daniele, thank you all for the very pleasant days spent on Ameland and not a whit less pleasant evenings in Groningen. I am immensely thankful to Monika, Tamara, Carlijn, Zanna, Dima Mazurenko for their moral support and for the great fun we had together. To Sasha, who always fancied a short coffee-chat, thank you for enjoyable conversations and valuable advice. My sincere thanks to Oksana. To Patricio and Anita, to Suzi, Stas, Sami.

My wholehearted gratitude to Dimka and Denis for being good friends and for all that time we have spent together. My warmest thanks to Adrianka for showing the way of peaceful happiness.

I also want to extend much gratitude to Mike, Nathalie, Max, Tatiana, Filippo, Dan, Olenka, Volodia, Sasha Michnenko, Ramunas, Natalya, Irina and to Szili, Lacra, Mirela, Ana, Yura, Vadim and Alya for providing a really friendly and fun atmosphere.

I would like to say my grateful thanks to my parents and my brother for their unconditional love and support, their constant encouragement and persistent confidence in me.

It is hardly possible to name everyone, who helped me during my research and my time in Groningen, I would like to express my apology and hearty thanks to those, whom I could not mention here.

Anton

27 February 2007, Groningen